

Analysis of Advanced Sodium-cooled Fast Reactor Core Designs with Improved Safety Characteristics

THÈSE N° 5480 (2012)

PRÉSENTÉE LE 3 SEPTEMBRE 2012

À LA FACULTÉ DES SCIENCES DE BASE

LABORATOIRE DE PHYSIQUE DES RÉACTEURS ET DE COMPORTEMENT DES SYSTÈMES

PROGRAMME DOCTORAL EN ENERGIE

ÉCOLE POLYTECHNIQUE FÉDÉRALE DE LAUSANNE

POUR L'OBTENTION DU GRADE DE DOCTEUR ÈS SCIENCES

PAR

Kaichao SUN

acceptée sur proposition du jury:

Prof. R. Schaller, président du jury

Prof. R. Chawla, directeur de thèse

Dr J. Krepel, rapporteur

Dr A. Pautz, rapporteur

Prof. J. Wallenius, rapporteur



ÉCOLE POLYTECHNIQUE
FÉDÉRALE DE LAUSANNE

Suisse
2012

Abstract

In order to meet the steadily increasing worldwide energy demand, nuclear power is expected to continue playing a key role in electricity production. Currently, the large majority of nuclear power plants are operated with thermal-neutron spectra and need regular fuel loading of enriched uranium. According to the identified conventional uranium resources and their current consumption rate, only about 100 years' nuclear fuel supply is foreseen. A reactor operated with a fast-neutron spectrum, on the other hand, can induce self-sustaining, or even breeding, conditions for its inventory of fissile material, which effectively allow it – after the initial loading – to be refueled using simply natural or depleted uranium. This implies a much more efficient use of uranium resources. Moreover, minor actinides become fissionable in a fast-neutron spectrum, enabling full closure of the fuel cycle and leading to a minimization of long-lived radioactive wastes.

The sodium-cooled fast reactor (SFR) is one of the most promising candidates to meet the Generation IV International Forum (GIF) declared goals. In comparison to other Generation IV systems, there is considerable design experience related to the SFR, and also more than 300 reactor-years of practical operation. As a fast-neutron-spectrum system, the long-term operation of an SFR core in a closed fuel cycle will lead to an equilibrium state, where both reactivity and fuel mass flow stabilize. Although the SFR has many advantageous characteristics, it has one dominating neutronics drawback, viz. there is generally a positive reactivity effect when sodium coolant is removed from the core. Furthermore, this so-called sodium void effect becomes even stronger in the equilibrium closed fuel cycle.

The goal of the present doctoral research is to improve the safety characteristics of advanced SFR core designs, in particular, from the viewpoint of the positive sodium void reactivity effect. In this context, particular importance has been given to the dynamic core behavior under a hypothetical unprotected loss-of-flow (ULOF) accident scenario, in which sodium boiling occurs. The proposed improvements address both neutronics and thermal-hydraulics aspects. Furthermore, emphasis has been placed on not only the beginning-of-life (BOL) state of the core, but also on the beginning of closed equilibrium fuel cycle (BEC) state.

An important context for the current thesis is the 7th European Framework Program's Collaborative Project for a European Sodium Fast Reactor (CP-ESFR), the reference 3600 MWth ESFR core being the starting point for the conducted research. The principally employed computational tools belong to the so-called FAST code system, viz. the fast-reactor neutronics code ERANOS, the fuel cycle simulating procedure EQL3D, the spatial kinetics code PARCS and the system thermal-hydraulics code TRACE. The research has been carried out in essentially three successive phases.

The first phase has involved achieving a clearer understanding of the principal phenomena contributing to the SFR void effect. Decomposition and analysis of sodium void reactivity have been carried out, while considering different fuel cycle states for the core. Furthermore, the spatial distribution of void reactivity importance, in both axial and radial directions, is investigated. For the reactivity decomposition, two methods – based on neutron balance considerations and on perturbation theory, respectively – have been applied. The sodium void reactivity of the reference ESFR core has been, accordingly, decomposed reaction-wise, cross-section-wise, isotope-wise and energy-group-wise. Effectively, the neutron balance based method allows an in-depth understanding of the “consequences” of sodium voidage, while the perturbation theory based method provides a complementary understanding of the “causes”.

The second phase of the research has addressed optimization of the reference ESFR core design from the neutronics viewpoint. Four options oriented towards either the leakage component or the spectral effect have been considered in detail, viz. introducing an upper sodium plenum and boron layer, varying the core height-to-diameter (H/D) ratio, introducing moderator pins into the fuel assemblies, and modifying the initially loaded plutonium content. The sensitivity of the principal safety and performance parameters, viz. void reactivity, Doppler constant, nominal reactivity and breeding gain, has been evaluated with respect to each of the options. Finally, two synthesis core concepts – representing different selected combinations of the optimization options – have been proposed.

The third and last phase has been to test the proposed optimized designs in terms of the dynamic core response to a representative ULOF accident, in which sodium boiling occurs. Such a hypothetical transient is of prime importance for SFR safety demonstration, since it may lead to a severe accident situation, where both cladding and fuel melt. As compared to the response of the reference ESFR core, certain improvements are indeed achieved with the static neutronics optimization carried out. However, these are found, in themselves, to be insufficient as regards the prevention of cladding and fuel melting. Thermal-hydraulic optimization has thus been considered necessary to: 1) prevent sodium flow blockage in the fuel channels and 2) avoid boiling instabilities caused by the vaporization/condensation process in the upper sodium plenum. Following implementation of appropriate thermal-hydraulics related design changes, one arrives at a final configuration of the SFR core in which – for the selected accident scenario – a new “steady state” involving stable sodium boiling is shown to be achievable, with melting of neither cladding nor fuel. Such satisfactory behavior has been confirmed not only for the beginning-of-life core state, but also for the equilibrium closed fuel cycle.

Keywords: Sodium-cooled Fast Reactor (SFR), Generation IV, FAST code system, ERANOS, TRACE, PARCS, SERPENT, neutronics, thermal-hydraulics, 3D-kinetics, sodium boiling, sodium void effect, reactivity decomposition, core optimization, ULOF transient analysis, wrapper design.

Résumé

Pour faire face à la demande croissante d'énergie à travers le monde, l'énergie nucléaire doit continuer à jouer un rôle clef dans la production d'électricité. Aujourd'hui la grande majorité des centrales nucléaires utilisent des neutrons avec un spectre dit thermiques et nécessitent de fréquents rechargements de combustible à l'uranium enrichi. La quantité des ressources d'uranium identifiées ainsi que leurs consommations actuelles suggèrent que les besoins en combustible des centrales nucléaires actuelles sont seulement couverts pour les 100 prochaines années. A l'opposé les réacteurs ayant un spectre de neutrons rapides utilisent le combustible beaucoup plus efficacement et peuvent même augmenter l'inventaire de matière fissile. Ainsi, après le chargement initial, ces réacteurs peuvent être rechargés avec de l'uranium naturel ou appauvri maximisant l'utilisation des ressources d'uranium. De plus, les actinides mineurs sont fissiles dans ces réacteurs à neutrons rapide ce qui permet de fermer le cycle du combustible et de minimiser les déchets radioactifs à vie longue.

Le réacteur à neutrons rapides refroidi au sodium (Sodium Fast Reactor; SFR) est l'un des concepts de réacteur les plus prometteurs pour satisfaire les critères du forum international Génération IV (GIF). A la différence des autres concepts de réacteurs de quatrième génération, les réacteurs refroidis au sodium bénéficient d'un large retour d'expérience tant au niveau du design que de l'opération avec plus de 300 ans-réacteur de fonctionnement. En tant que réacteurs à neutrons rapides, leurs opérations à long terme dans un cycle du combustible fermé permettront d'atteindre un état d'équilibre aussi bien en terme de réactivité que de masse de combustible. Bien que les réacteurs refroidis au sodium aient de nombreux avantages, ils souffrent cependant d'un désavantage neutronique majeur : ils ont généralement un coefficient de vide positif, c'est à dire un effet en réactivité positif lors d'une vidange accidentelle du sodium. Cet effet est encore plus marqué lorsque l'état d'équilibre du cycle du combustible est atteint.

L'objectif de ce travail de thèse est d'améliorer les paramètres de sûreté des concepts avancés de SFR, et en particulier de réduire l'effet en réactivité positif associé à la vidange du sodium. Dans ce contexte, une importance particulière a été attachée au comportement dynamique du cœur en cas d'une perte accidentelle de la circulation du sodium sans arrêt du réacteur (Unprotected Loss-Of-Flow Accident: ULOF) ce qui entraîne l'ébullition du sodium. Les améliorations proposées sont liées à la fois aux aspects neutronique et thermohydraulique. En outre on a considéré non seulement le cœur avec son chargement initial (BOL) mais aussi lorsque l'état d'équilibre du cycle du combustible est atteint (BEC).

Un contexte important de ce travail de thèse est le projet de collaboration dédiée au SFR européen (CP-ESFR) du 7^{ème} programme cadre européen. Ainsi le point de départ de cette recherche est le cœur ESFR de référence ayant une puissance de 3600 MWth. Les codes de calculs utilisés dans cette thèse font principalement partie du formulaire de calcul FAST. Ce sont principalement le code de neutronique pour réacteurs à neutrons rapides ERANOS, la procédure EQL3D simulant le cycle du

combustible, le code de cinétique spatiale PARCS et le code de thermohydraulique TRACE. Le travail de thèse est divisé en trois parties.

La première partie vise à mieux comprendre les phénomènes physiques contribuant au coefficient de vide du SFR. L'effet en réactivité due à la vidange du sodium a été décomposé et analysé pour des cœurs représentatifs des différentes étapes du cycle combustible. En outre, les distributions axiales et radiales de l'importance de l'effet en réactivité sont étudiées. Pour la décomposition de réactivité, deux méthodes ont été appliquées, l'une basée sur le bilan neutronique, l'autre sur la théorie des perturbations. Ainsi l'effet en réactivité de la vidange du cœur ESFR de référence a été décomposé selon le type de réaction, le type de section efficace, le type d'isotope et le groupe d'énergie des neutrons. En effet, la méthode basée sur le bilan neutronique permet de comprendre les « conséquences » de la vidange du sodium alors que celle basée sur la théorie des perturbations permet d'en comprendre les « causes. »

Dans la seconde partie le cœur ESFR de référence a été optimisé sur la base d'études neutroniques. Quatre options visant à optimiser soit les fuites neutroniques soit les effets spectraux ont été considérées en détails. Ces options sont : l'introduction d'un plenum de sodium et d'une couche de bore dans la partie supérieure du réacteur, l'ajustement du rapport diamètre sur hauteur du cœur, l'introduction de crayons modérateurs dans les assemblages, et l'ajustement de la quantité de plutonium utilisé lors du chargement initial. La variation des principaux paramètres de sûreté et de performance, tel que le coefficient de vide, le coefficient Doppler, la réactivité nominale et le gain de surgénération, ont été évalués pour les quatre options ci-dessus. Finalement, deux designs de cœur résultant de l'optimisation des différents paramètres ont été proposés.

La troisième et dernière partie est consacrée à l'étude du comportement dynamique des deux designs de cœur optimisés pendant un scénario accidentel ULOF de référence qui entraîne l'ébullition du sodium. Un tel transitoire hypothétique est primordial pour démontrer la sûreté d'un SFR car il peut entraîner un accident sévère incluant la fonte de la gaine et du combustible. Comparé au comportement du cœur ESFR de référence, ceux des cœurs optimisés précédemment du point de vue de neutronique démontrent des améliorations significatives. Cependant celles-ci ne suffisent pas à prévenir la fonte de la gaine et du combustible. Des améliorations thermohydrauliques doivent être apportées afin 1) de prévenir le blocage de la circulation du sodium dans les canaux combustibles et 2) d'empêcher les instabilités du cœur dues aux phénomènes de vaporisation et de condensation du sodium dans le plenum. Des modifications appropriées ont été implémentées dans le design thermohydraulique, ce qui a permis, à la suite du scénario d'accident considéré, d'atteindre un nouvel état d'équilibre caractérisé par une ébullition du sodium stable où le combustible et sa gaine restent intacts. Un tel comportement est satisfaisant et a été démontré non seulement pour le cœur avec son chargement initial (BOL) mais aussi pour l'état d'équilibre du cycle du combustible fermé (BEC).

Mots clés : Réacteur à neutrons rapides refroidi au sodium (SFR), Génération IV, formulaire de calcul FAST, ERANOS, TRACE, PARCS, SERPENT, neutronique, thermohydraulique, cinétique spatiale, ébullition du sodium, effet de la vidange du sodium, décomposition de réactivité, optimisation du cœur, analyse de transitoire ULOF, design de l'enveloppe de l'assemblage.

Contents

Chapter 1	Introduction	1
1.1	Nuclear energy today	1
1.2	Main advantages of fast reactors	4
1.3	Generation IV	6
1.4	World-wide SFR activities	8
1.5	Goals and scope of the present research	11
1.6	Outline of the thesis	14
	References	17
Chapter 2	Thesis Background	21
2.1	Collaborative Project - European Sodium Fast Reactor	21
2.1.1	Framework of the CP-ESFR	21
2.1.2	ESFR safety objectives and design principles	22
2.1.3	ESFR core description and general design features	24
2.2	Computational tools	27
2.2.1	The FAST code system	27
2.2.2	SERPENT	40
	References	42
Chapter 3	Void Reactivity Decomposition and Analysis	45
3.1	Verification of ERANOS calculations against SERPENT	45
3.2	Selected fuel cycle states for the ESFR core	47
3.2.1	Evolution towards open and closed equilibrium fuel cycle conditions	47
3.2.2	Void reactivity at different fuel cycle states	50
3.3	Spatial distribution of void reactivity importance	51
3.4	Reactivity decomposition methods	53
3.4.1	Neutron balance based method	54
3.4.2	Perturbation theory based method and sensitivity coefficients	58
3.5	Void reactivity decomposition	59
3.5.1	Reaction-wise decomposition (neutron balance based method)	59

3.5.2	Cross-section-wise decomposition (perturbation theory based method)	62
3.5.3	Isotope-wise decomposition (neutron balance based method)	63
3.5.4	Isotope-wise sensitivity coefficients (perturbation theory based method) ..	68
3.5.5	Energy-group-wise decomposition (neutron balance based method)	71
3.6	Chapter summary	73
	References	75
Chapter 4 Neutronics Optimization of the ESFR Core		77
4.1	Considered optimization options and parameters	77
4.1.1	Leakage oriented optimization options	78
4.1.2	Spectrum oriented optimization options	80
4.1.3	Considered safety and performance parameters	81
4.1.4	Void reactivity decomposition and equilibrium fuel cycle methodologies ..	81
4.2	Optimization study at BOL	82
4.2.1	Upper sodium plenum and boron layer	82
4.2.2	Core H/D ratio	86
4.2.3	Moderator pins	87
4.2.4	Initial plutonium content	91
4.3	Results for the equilibrium fuel cycle	93
4.3.1	Upper sodium plenum and boron layer	93
4.3.2	Core H/D ratio	94
4.3.3	Moderator pins	95
4.3.4	Initial plutonium content	96
4.4	Main findings and proposed optimized cores	97
4.4.1	Summarized discussion of the results	97
4.4.2	Proposed optimized cores	99
4.5	Chapter summary	101
	References	102
Chapter 5 Impact of Optimization on Transient Behavior		103
5.1	The PARCS/TRACE model and selected transient	104
5.1.1	Description of the PARCS/TRACE model	104
5.1.2	Verification of the PARCS/TRACE model	105
5.1.3	Description of the ULOF transient	107
5.2	Core behavior during the ULOF transient at BOL	108
5.2.1	The reference ESFR core behavior at BOL	109
5.2.2	Behavior of the SC1 core at BOL	111

5.2.3	Behavior of the SC2 core at BOL	113
5.2.4	Summary and discussion.....	115
5.3	Thermal-hydraulics optimization: wrapper openings.....	116
5.3.1	Description of the innovative wrapper design	116
5.3.2	Behavior of the SC1 core with wrapper openings at BOL	118
5.3.3	Behavior of the SC1 core with wrapper openings at BEC.....	120
5.3.4	Behavior of the SC2 core with wrapper openings at BOL	122
5.3.5	Behavior of the SC2 core with wrapper openings at BEC.....	125
5.3.6	Summary and discussion.....	127
5.4	Stabilization of conditions in the upper plenum.....	129
5.4.1	The alternative sodium plenum design	129
5.4.2	Final-configuration core behavior at BOL.....	130
5.4.3	Final-configuration core behavior at BEC.....	133
5.4.4	Summary and discussion.....	136
5.5	Chapter summary.....	136
	References.....	139
Chapter 6 Conclusions and Recommendations for Future Work....		141
6.1	Chapter-wise summary	141
6.2	Main achievements	143
6.3	Recommendations for future work	150
6.4	Concluding remarks.....	153
	References.....	154
Appendix A Monte Carlo Verification of ERANOS Calculations ..		157
A.1	Background.....	157
A.2	Benchmark results	158
A.3	Investigation of the unresolved resonance treatments.....	162
A.4	Conclusions	163
	References.....	164
Appendix B Sensitivity Study with respect to Plenum Height		165
B.1	Background.....	165
B.2	Studied cases and results	165
B.3	Conclusions	167

Appendix C Study on Sodium Boiling Oscillations.....	169
C.1 Theoretical background	169
C.2 Sodium boiling experiment considered [C.05]	171
C.3 Comparison of simulated flow rate oscillations with experimental data	173
C.4 Conclusions	174
References.....	176
Acknowledgements.....	177
Curriculum Vitae	179

Nomenclature

Abbreviations

1D, 2D, 3D	One, two, and three dimensional
AC	Active Core
ACS	Above Core Structure
ADS	Accelerator Driven System
ALARP	As Low As Reasonably Practicable
ANS	Advanced Nuclear Systems
ASTRID	Advanced Sodium Technological Reactor for Industrial Demonstration
AXI	AXIal expansion effect
B1	Buckling search for $k_{eff} = 1$
BEC	Beginning of Equilibrium closed fuel Cycle
BG	Breeding Gain
BOL	Beginning-Of-Life
BOC	Beginning of equilibrium Open fuel Cycle
BWR	Boiling Water Reactor
CDA	Core Disruptive Accident
CEA	Commissariat à l'énergie atomique (France)
CEFR	China Experimental Fast Reactor
CDFR	China Demonstration Fast Reactor
CFD	Computational Fluid Dynamics
CPFR	China Prototype Fast Reactor
CMFD	Coarse Mesh Finite Difference
CP	Collaborative Project
CR	Control Rod
CSD	Control and Shutdown Device
DAC	Coolant Density effect in Active Core region
DC	Doppler Constant
DHR	Decay Heat Removal

DOP	DOPpler effect
DSD	Diverse Shutdown Device
DSP	Coolant Desity effect in Sodium Plenum region
E.C.	External Characteristics
EDF	Electricité de France
EEC	End of Equilibrium closed fuel Cycle
EFPD	Equivalent Full-Power Day
EFR	European Fast Reactor
EFPY	Equivalent Full-Power Year
EISOFAR	European Innovative SOdium-cooled FAst Reactor
EOC	End of equilibrium Open Cycle
EOL	End-Of-Life
EOS	Equation-Of-State
EPFL	Ecole Polytechnique Fédérale de Lausanne (Switzerland)
EPR	European Pressurized Reactor
ERANOS	European Reactor ANalysis Optimized calculation System
ESFR	European Sodium Fast Reactor
EURATOM	EUROpean ATOMIC energy community
FAST	Fast-spectrum Advanced Systems for power production and resource managemenT
FBR	Fast Breeder Reactor
FIMA	Fission per Initial Metal Atom
FP	Fission Product
FP	Framework Program
FR	Fast Reactor
GCR	Gas-Cooled Reactor
GFR	Gas-cooled Fast Reactor
GIF	Generation-IV International Forum
H/D	Height-to-Diameter
HM	Heavy Metal
HTSTR	HeaT STRucture
IAEA	International Atomic Energy Agency
I.C.	Internal Characteristics
IGCAR	Indira Gandhi Centre for Atomic Research (India)

IHX	Intermediate Heat eXchanger
IPPE	Institute of Physics and Power Engineering (Russia)
JAEA	Japan Atomic Energy Agency (Japan)
LFR	Lead-cooled Fast Reactor
LMFBR	Liquid-Metal Fast Breeder Reactor
LOCA	Loss-Of-Coolant Accident
LRS	Laboratory for Reactor Physics and Systems Behavior (Switzerland)
LWGR	Light-Water-cooled Graphite-moderated Reactor
LWR	Light Water Reactor
MA	Minor Actinide
MCNP	Monte Carlo N-Particle
MOX	Mixed OXide
MSR	Molten Salt Reactor
NPP	Nuclear Power Plant
NRC	Nuclear Regulatory Commission (USA)
ODS	Oxide Dispersion Strengthened
PARCS	Purdue Advanced Reactor Core Simulator
PBMR	Pebble Bed Modular Reactor
PFBR	Prototype Fast Breeder Reactor (India)
PHWR	Pressurized Heavy Water Reactor
PSI	Paul Scherrer Institute (Switzerland)
R&D	Research and Development
RAD	RADial expansion effect
RIA	Reactivity Insertion Accident
SC	Synthesis Core
SCWR	Supercritical-Water-Cooled Reactor
SETS	Stability-Enhancing Two-Step
SFR	Sodium-cooled Fast Reactor
TPEN	Triangular Polynomial Expansion Nodal
TRACE	TRAC/RELAP Advanced Computation Engine
TRU	TransUranic nuclides
UK	United Kingdom
ULOF	Unprotected Loss-Of-Flow
ULOHS	Unprotected Loss-Of-Heat-Sink

UR	Unresolved Resonance
USA	United States of America
UTOP	Unprotected Transient Over Power
VAC	Coolant Void effect in Active Core region
VHTR	Very-High-Temperature Reactor
VSP	Coolant Void effect in Sodium Plenum region
XS	cross-section

Parameters

C	Conversion ratio	[-]
D	Diffusion coefficient	[cm]
D	Diameter	[cm]
g	Gravitational acceleration	[m/s ²]
h	Enthalpy	[kJ/kg]
H	Height	[cm]
k_{inf}	Infinite multiplication factor	[-]
k_{eff}	Effective multiplication factor	[-]
\dot{m}	Mass flow rate	[kg/s]
p	Pressure	[Pa]
ΔP	Pressure drop	[Pa]
Q	Mass flow rate	[kg/s]
q''	Heat flux	[W/m ²]
q'''	Power density	[W/m ³]
t	Time	[s]
T	Temperature	[°C]
u	Stagnation energy	[kJ/kg]
v	Velocity	[m/s]
η	Number of neutrons produced per neutron absorbed in fuel	[-]
ν	Average number of neutrons released per fission	[-]
σ	Microscopic cross-section	[cm ²]
Γ	Volumetric production	[m ³ /s]
τ	Tensor of viscous stresses	[Pa]
Φ	Neutron flux	[n/cm ² /s]
Σ	Macroscopic cross-section	[cm ⁻¹]
ρ	Reactivity	[-]
ρ	Density	[kg/m ³]
$\Delta\rho_v$	Void reactivity	[-]
χ	Fission spectrum	[-]

Indices

A	Absorption
C	Capture
e	Electrical
F	Fission
fin	Final
g	Energy group
ini	Initial
L	Leakage
N	Nominal
P	Production
S	Scattering
th	Thermal
V	Voided
+	Adjoint

Chapter 1

Introduction

This opening chapter is structured as follows. Section 1.1 provides a general introduction to the status of nuclear energy today. Section 1.2 presents the main advantages of fast reactor (FR) technology. It is in this context that five out of the six so-called Generation IV nuclear energy systems have fast neutron spectra associated with them (Section 1.3). Almost all the FRs which have been built and operated to date have employed sodium as the primary coolant, the worldwide activities related to sodium-cooled fast reactors (SFRs) being briefly presented in Section 1.4. The goals and scope of the present doctoral research – pertaining to the improvement of the safety characteristics of advanced SFR core designs – are described in Section 1.5. Finally Section 1.6 gives the structure of this thesis.

1.1 Nuclear energy today

At the end of 2010, there were 441 nuclear power reactors in operation worldwide (see Table 1.1), providing around 14% of the global electricity, which corresponds to a total capacity of 375 GWe [1.01]. The large majority (82%) of existing nuclear power plants (NPPs) feature Generation II light water reactors (LWRs), where water is used both to moderate neutrons and to remove the heat generated from the nuclear fuel [1.02]. The worldwide LWRs, which can be divided into two broad categories, consist of 269 pressurized water reactors (PWRs), where the primary coolant remains in the liquid phase and steam is generated in a secondary loop, and 92 boiling water reactors (BWRs), where steam is generated in the primary loop and directly drives a turbine. In comparison to light water, heavy water has a much lower neutron absorption cross-section, and hence certain advantages as coolant and moderator in a nuclear reactor. There are currently 46 pressurized heavy water reactors (PHWRs) operating in the world, mainly in Canada, India and the Republic of Korea. The rest of the existing NPPs consist of 18 gas-cooled reactors (GCRs) in the UK, 15 graphite-moderated light-water-cooled reactors (LWGRs) in Russia and 1 FR^{1.1}, also in Russia.

More than 75% of the above mentioned NPPs have been operating for over 20 years, so that many will soon be requiring either replacement or life-time extension. There are currently 67 NPPs under construction, with a total capacity of 64 GWe [1.01]. Fifteen countries are involved, and the details

^{1.1} Phénix in France had its final shutdown at the end of 2009. MONJU in Japan, which was restarted in May 2010 after a long shutdown period, was forced to shutdown once again, following a second accident in August 2010. More detailed information can be found in Section 1.4.

Chapter 1: Introduction

can be found in Table 1.1. As seen, China is the most active country with 28 NPPs under construction in parallel, Russia and India having 11 and 6, respectively. In Europe and the USA, the boom of nuclear power from the 1960s to the late '70s was obstructed by the nuclear accidents of Three Mile Island in 1979 and Chernobyl in 1986. As a result, almost no new NPPs have been built in these regions since then. Following the recent nuclear renaissance, there are now 8 reactors under construction in Europe (w/o Russia) and 1 in the USA.

Table 1.1. Nuclear power reactors in operation and under construction worldwide [1.03]

Country	Reactors in operation		Reactors under construction	
	No. of units	Total MWe	No. of units	Total MWe
Argentina	2	935	1	692
Armenia	1	375		
Belgium	7	5 926		
Brazil	2	1 884	1	1 245
Bulgaria	2	1 906	2	1 906
Canada	18	12 569		
China	13	10 058	28	28 230
Czech Republic	6	3 678		
Finland	4	2 716	1	1 600
France	58	63 130	1	1 600
Germany	17	20 490		
Hungary	4	1 889		
India	19	4 189	6	3 766
Iran, Islamic Republic of			1	915
Japan	54	46 821	2	2 650
Korea, Republic of	21	18 698	5	5 560
Mexico	2	1 300		
Netherlands	1	482		
Pakistan	2	425	1	300
Romania	2	1 300		
Russian Federation	32	22 693	11	9 153
Slovakia	4	1 816	2	782
Slovenia	1	666		
South Africa	2	1 800		
Spain	8	7 514		
Sweden	10	9 303		
Switzerland	5	3 238		
Ukraine	15	13 107	2	1 900
United Kingdom	19	10 137		
United States of America	104	101 240	1	1 165
Total	441	375 267	67	64 064

Chapter 1: Introduction

Each year, the International Atomic Energy Agency (IAEA) prepares low and high projections of future nuclear capacity development in the world [1.04]. In the latest reported high projection, the global nuclear power capacity increased from 375 GWe in 2010 to 803 GWe in 2040 and to 1415 GWe by 2050, which is an almost fourfold increase during 40 years. In the low projection, the capacity increased to 546 GWe in 2030 and to 590 GWe by 2050. Figure 1.1 shows the regional breakdown of both high and low projections. As can be seen, the highest growth is expected in the Far East and is dominated particularly by the nuclear expansion plans in China.

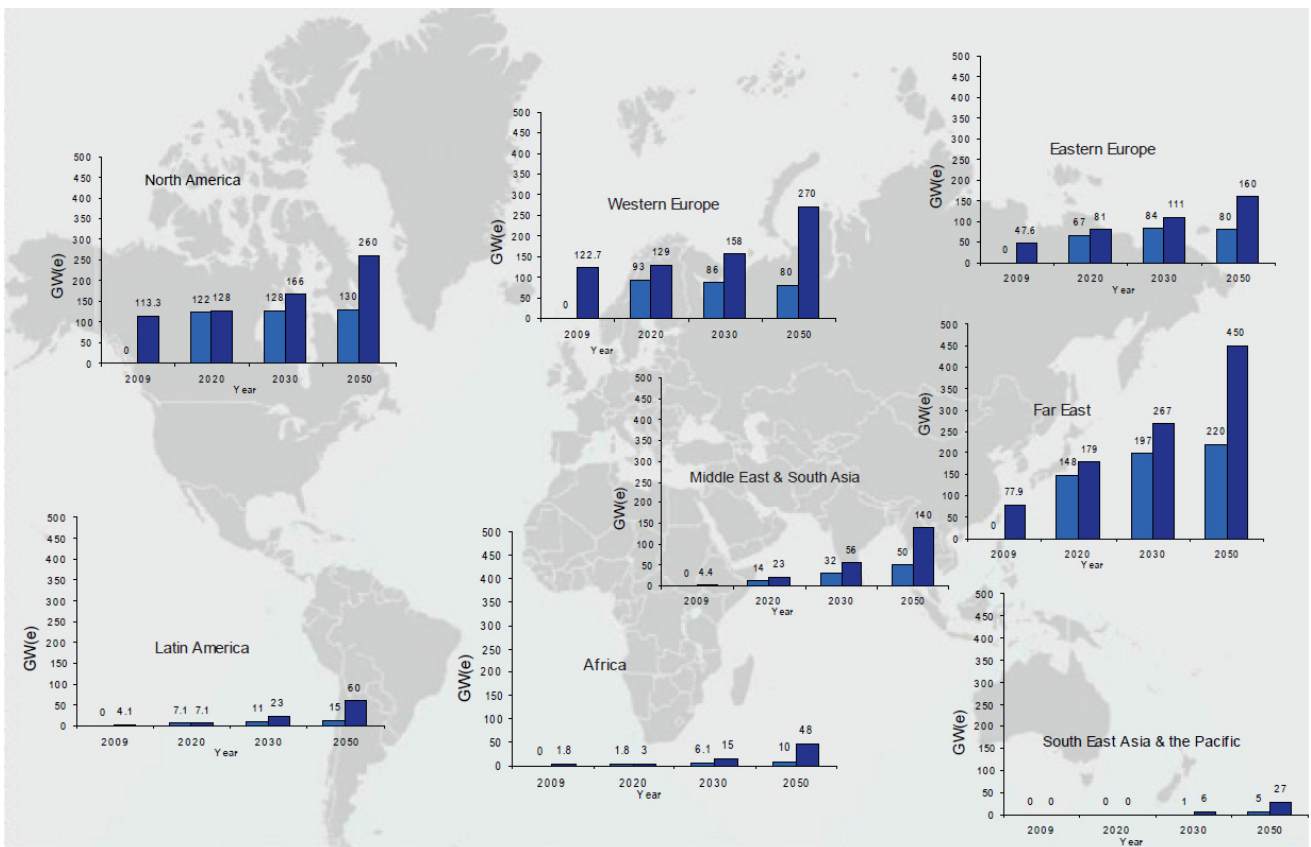


Figure 1.1. The regional breakdown of the IAEA updated low and high projections in 2010 [1.04].

On March 11th 2011, the Fukushima Dai-ichi NPP site was subjected to one of Japan's worst-ever natural disasters – an earthquake of record severity (magnitude 9.0 M_w) and correspondingly high tsunamis. The assessment of the resulting severe accident events is still in progress, and it is expected that the final conclusions will significantly influence the above described projections of future nuclear power development.

The shorter term impact of the Fukushima accident has been felt most strongly in Switzerland. Three new NPPs had been projected in the country before the accident [1.05], the intention having been to

replace and/or extend the existing ones at Mühleberg, Beznau and Gösgen. The final authorizations for these new NPPs were expected around 2020. However, almost immediately after the Fukushima accident, the Swiss government announced the suspension of all preparatory activities. This was followed by a decision to phase-out nuclear power by around 2034, when the last of the existing NPPs is expected to end its operation. Viewed globally, the reaction to Fukushima in Switzerland has been more of an exception than the rule. Thus, many countries – such as the USA, China, France and the UK – have declared that they will maintain their plans for nuclear power development, with an even greater emphasis to be placed on enhancing safety.

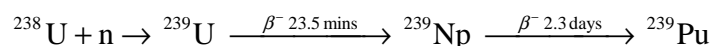
Currently, the world population continues to increase steadily. This needs to be effectively supported by both basic electricity production and other primary energy needs. An ideal energy supply should be able to ensure the sustainability of humanity's development and hence have clean, safe and cost effective features. Prominent among the possible resources is nuclear energy. It has not only a strong potential to help meet the increasing energy demand while avoiding an excessive increase of greenhouse-gas emissions, but also features competitive economics in the light of its relatively low fuel cycle costs.

1.2 Main advantages of fast reactors

The large majority of the existing NPPs use uranium based fuel, since ^{235}U is the only fissile nuclide which nature has provided. However, the latter exists to the extent of as little as 0.72% in natural uranium. The rest consists of mainly ^{238}U , which is a fertile nuclide. It is almost non-fissionable in the current Generation II NPPs.

Identified conventional uranium resources (U), recoverable at a cost of less than \$130/kg U, are currently estimated at 5,700,000 tonnes. There are an additional 700,000 tonnes U of identified conventional resources recoverable at costs between \$130/kg U and \$260/kg U [1.01]. The global natural uranium requirements of NPPs are presently 68,000 tonnes per year. Thus, only about 100 years' nuclear fuel supply can be foreseen if a constant consumption rate is taken into account [1.06]. Obviously, this cannot ensure a sustainable contribution to the world's energy demand.

In reality, the large amount of the fertile nuclide ^{238}U occurring in natural uranium can be converted to ^{239}Pu , which is fissile and thus provides an alternative to ^{235}U . The conversion occurs through neutron capture, followed by a short series of beta minus (β^-) decays:



where the values indicated after " β^- " are the corresponding half-lives. The conversion of ^{238}U to ^{239}Pu occurs in all nuclear power plants, but the conversion ratio C , i.e. the ratio of fissile material produced to that destroyed, is only about 0.5 in LWRs. If C is greater than 1.0, the reactor becomes a

“breeder” of fissile material, and this is the basic concept which can enable a drastic improvement in uranium utilization.

The parameter η , defined as $\nu \cdot \sigma_f / \sigma_a$, represents the number of neutrons produced per neutron absorbed in a fissile nuclide, where ν is the average number of neutrons released per fission, and σ_f and σ_a are the microscopic cross-sections for fission and absorption, respectively. The breeding condition can be met if the η value of the fissile isotope is greater than 2, i.e. more than two neutrons are produced from a single neutron absorption. This means that, while one produced neutron is needed to maintain the chain reaction, there is still at least one extra neutron which can be used for breeding.

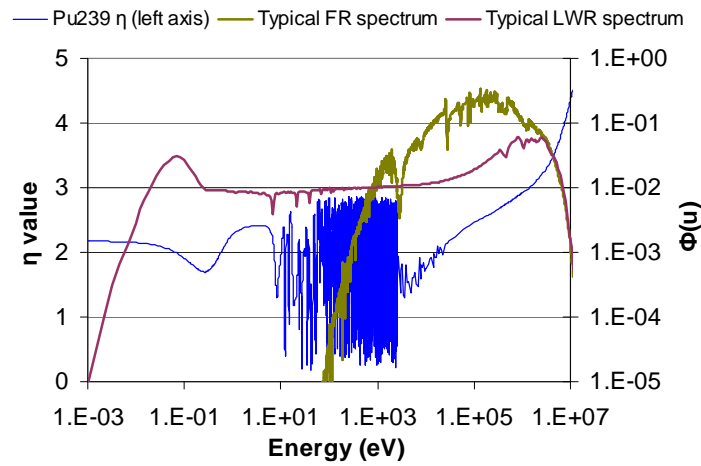


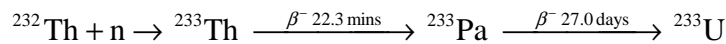
Figure 1.2. η value of ^{239}Pu , together with typical FR and LWR neutron spectra^{1,2}.

In Figure 1.2, the ^{239}Pu η value is shown as a function of energy, together with typical FR and LWR neutron spectra. It can be seen that, on the one hand, the typical LWR neutron spectrum has two significant peaks: one in the thermal neutron range and the other in the fast neutron range. Consequently, almost all the ^{239}Pu fissions will occur in the former region (due to the much higher fission cross-section value there), where the η value is just around 2. On the other hand, the typical FR neutron spectrum mainly covers the range from 10 keV to 1000 keV. This corresponds to the energy region where the ^{239}Pu η value is significantly greater than 2, which means that the fission source is able not only to provide one neutron to maintain the chain reaction and one for capture in the fertile material (^{238}U), but also to take into account some other losses. Consequently, LWRs need to be loaded regularly with additional fissile material, whereas a FR neutron spectrum can enable self-sustaining, or even breeding, conditions as regards fissile material requirements. Effectively,

^{1,2} The η value has been calculated using cross-sections from the JEFF-3.1 nuclear data library [1.07]. The typical FR spectrum is from ERANOS calculations for one of the currently studied SFR fuel assemblies [1.08]. The data of the presented typical LWR spectrum is obtained from [1.09].

such conditions allow a reactor – after the initial loading – to be refueled using simply natural or depleted uranium. This implies a much more efficient use of uranium resources. Moreover, minor actinides become fissionable in a FR neutron spectrum, which enables full closure of the fuel cycle and leads to a minimization of long-lived radioactive wastes.

For the sake of completeness, it should be mentioned here that another fertile material, viz. thorium (100% ^{232}Th), can also be used for breeding nuclear fuel. Thorium occurs even more abundantly than uranium, and certain countries, e.g. India, have very large reserves [1.10]. In an analogous manner to ^{238}U , ^{232}Th can be converted to the fissile nuclide ^{233}U through a neutron capture and a short series of beta minus decays:



Such conversion, however, can be conducted more effectively in thermal and intermediate neutron spectra, rather than in a fast neutron spectrum. As a result, the thorium fuel cycle is not considered as the reference for FR technology but rather adopted for other reactor concepts such as the molten salt reactor, one of the so-called Generation IV systems (see next section).

1.3 Generation IV

Thirteen participating partners – Argentina, Brazil, Canada, China, EURATOM, France, Japan, the Republic of Korea, Russia, South Africa, Switzerland, the UK, and the USA – have agreed on a framework for international cooperation in research for a future generation of nuclear energy systems, known as Generation IV. Figure 1.3 shows the evolution of nuclear energy system generations. The first generation of nuclear energy systems consists of mainly the early prototype reactors, which were built in the 1950s and '60s. Nowadays, most of the worldwide commercial NPPs in operation belong to the second generation, which were constructed mainly in the 1970s. Generation III was developed more recently in the 1990s, with a number of evolutionary designs that offer significant advances in safety and economics. More advanced versions of Generation III systems (so-called Generation III+) are currently available as near-term deployable plants and are being constructed in several countries. New NPPs built till 2030 will likely be chosen from this generation. It is for the period beyond 2030 that innovative advances through renewed R&D have stimulated worldwide interest in Generation IV systems.

The earlier mentioned thirteen partner countries have formed the Generation IV International Forum (GIF) to meet the R&D challenges in developing the next generation of innovative nuclear energy systems. The major goals of these systems defined in the GIF roadmap are [1.11]:

Sustainability–1: Generation IV nuclear energy systems will provide sustainable energy generation that meets clean air objectives and promotes long-term availability of systems and effective fuel utilization for worldwide energy production.

Chapter 1: Introduction

Sustainability–2: Generation IV nuclear energy systems will minimize and manage their nuclear waste and notably reduce the long-term stewardship burden, thereby improving protection for the public health and the environment.

Economics–1: Generation IV nuclear energy systems will have a clear life-cycle cost advantage over other energy sources.

Economics–2: Generation IV nuclear energy systems will have a level of financial risk comparable to other energy projects.

Safety and Reliability–1: Generation IV nuclear energy systems operations will excel in safety and reliability.

Safety and Reliability–2: Generation IV nuclear energy systems will have a very low likelihood and degree of reactor core damage.

Safety and Reliability–3: Generation IV nuclear energy systems will eliminate the need for offsite emergency response.

Proliferation Resistance and Physical Protection: Generation IV nuclear energy systems will increase the assurance that they are a very unattractive and the least desirable route for diversion or theft of weapons-usable materials, and provide increased physical protection against acts of terrorism.

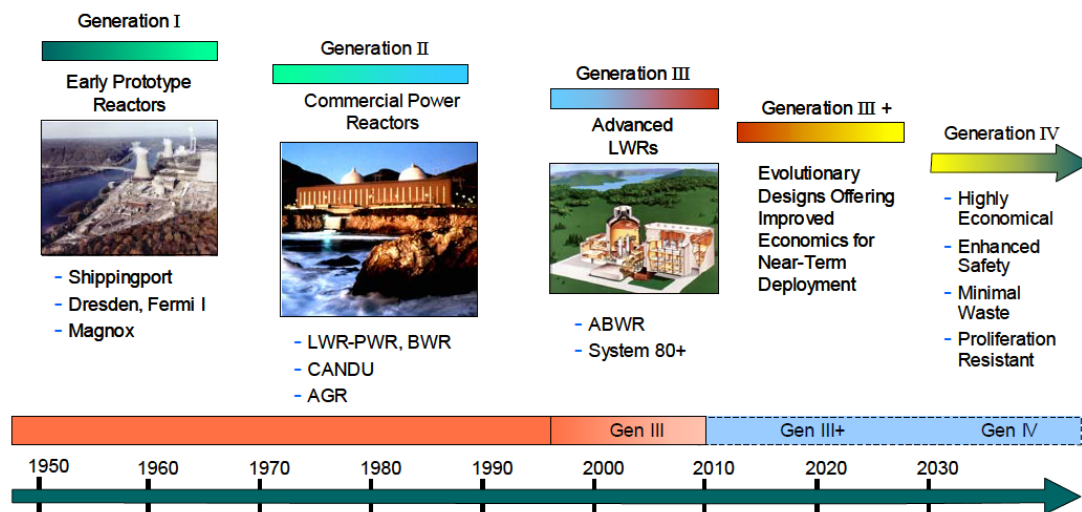


Figure 1.3. Schematic showing the evolution of nuclear energy systems [1.11].

The early phase of the Generation IV exercise culminated in the selection of six candidate nuclear energy systems, and these are listed in Table 1.2. As discussed previously, FR technology is highly favored because of its sustainability in terms of high fuel utilization and the minimization of long-lived wastes. Thus, in the context of a long-term energy strategy, five out of the six selected Generation IV systems have fast neutron spectra associated with them, thus enabling full closure of the fuel cycle.

Table 1.2. Overview of the six Generation IV nuclear energy systems [1.11]

Generation IV System	Neutron Spectrum	Selected Coolant	Temperature (°C)	Fuel Cycle	Size (MWe)
VHTR (very-high-temperature reactor)	Thermal	Helium	900 – 1000	Open	250 – 300
SFR (sodium-cooled fast reactor)	Fast	Sodium	550	Closed	30 – 150, 300 – 1500, 1000 – 2000
SCWR (supercritical water-cooled reactor)	Thermal / Fast	Water	510 – 625	Open / Closed	300 – 700, 1000 – 1500
GFR (gas-cooled fast reactor)	Fast	Helium	850	Closed	1200
LFR (lead-cooled fast reactor)	Fast	Lead	480 – 800	Closed	20 – 180, 300 – 1200, 600 – 1000
MSR (molten salt reactor)	Fast / Thermal	Fluoride salts	700 – 800	Closed	1000

1.4 World-wide SFR activities

In comparison to other Generation IV systems, there is considerable design experience related to the SFR, and also more than 300 reactor-years of practical operation [1.11]. As such, the SFR is one of the most promising candidates to meet the declared goals of the GIF in a timely manner.

Since the very beginning of the nuclear era, scientists have considered almost everything available as possible primary coolant for a nuclear reactor, viz. gases, water, liquid metals, fluid fuel, etc. Due to the relatively high power density in a fast reactor core, liquid metals have generally been considered to be the most suitable. This is because of their high thermal conductivity and heat capacity [1.12], as well as the useful temperature range they offer under atmospheric pressure conditions. Eventually, the testing of different alternative coolants demonstrated that sodium has marked advantages and, as such, has been chosen as the primary coolant in almost all the fast reactors constructed to date.

Experimental SFRs [1.13]

BR-5, operated in the Soviet Union with an output of 5 MW thermal (MW_{th}), was the first reactor in the world using sodium as a coolant and plutonium oxide as a fuel. The main purpose of the reactor was to obtain burnup data on PuO₂ and other fuel types, and to gain experience in the operation of

Chapter 1: Introduction

systems with radioactive sodium in the primary circuit. Its first criticality was reached in 1958, and it operated at full power from the following year. During 1971-72, the BR-5 plant was modified and enlarged to permit a power level of 10 MWth, being called BR-10 thereafter.

The Enrico Fermi Nuclear Generating Station is located on the shores of Lake Erie in Michigan, USA. It is named after the Italian nuclear physicist Enrico Fermi, most known for his work on the development of the first nuclear reactor, as well as for many other major contributions to nuclear physics. The first unit, Fermi-1, was an SFR and its first criticality was reached in 1963. It was specifically designed with a power of 60 MWe (200 MWth). Fermi-1 was built and operated, at that time, to evaluate the economics of a commercial prototype fast reactor for electricity generation.

The Rapsodie experimental sodium-cooled reactor was the first French fast reactor. Its construction was started in 1962, under a collaboration between CEA and EURATOM. The reactor went critical in 1967, reaching 20 MWth in the same year. The core and equipment were modified in 1970 to increase the power level to 40 MWth. The irradiation results obtained by Rapsodie were extrapolated to the Phénix reactor.

In 1979, Japan's first fast reactor JOYO commenced operation with its MARK I core at a power of 75 MWth. In 1983, the plant started operating with the MARK II core at a power level of 100 MWth. Initial criticality of the MK-III core was achieved in 2003, which was followed by the successful operational demonstration up to the rated power of 140 MWth. JOYO has shown excellent performance as an experimental fast reactor for more than 26 years; 64,000 pins with solid pellets have been irradiated in the core, with a maximum burnup level of around 15 at. %.

The China Experimental Fast Reactor (CEFR) is the first step in the Chinese development of fast reactor technology. It is a 20 MWe (65 MWth) pool-type SFR. Criticality of this reactor was reached in 2010, and the full power operation started recently in 2011. The CEFR will be used as a tool for qualification of computer codes, for studying safety characteristics and safe operation, and for applied research for the fast reactor prototype and demonstrator which are to follow. The latter represent the next two stages in the Chinese fast reactor development program, viz. the construction of a 600 MWe prototype fast reactor (CPFR), for which design work started in 2005, and a 1000-1500 MWe demonstration reactor (CDFR).

Prototype SFRs [1.14] [1.15] [1.16]

Phénix was the prototype SFR in France, located at the Marcoule nuclear site. It was of pool-type design and generated 255 MWe (565 MWth) power, with a gross thermal efficiency of 45%. Construction of Phénix began in 1968, the first grid connection being in 1973. The reactor was generally operated at the power tolerated by the equipment, with comparatively high load factor. It provided about 100,000 hours of grid-connected operation representing 3,900 equivalent full power days at operating temperatures of 560°C for the reactor hot structures. The plant, when finally

Chapter 1: Introduction

shutdown at the end of 2009, had achieved all the objectives of demonstration of fast reactor technology which had been set for it at the time of construction.

BN-350 was a small-scale prototype SFR located in Aktau, Kazakhstan. In addition to providing power for the city (150 MWe), BN-350 was also used for producing plutonium and for desalination to supply fresh water to the city. Construction of the BN-350 began in 1964, the plant's first grid connection was in 1973, and final shutdown in 1999. For more than 25 years, the operation of the BN-350 reactor promoted the exploration of the new industrial region of Kazakhstan, which is rather rich in natural resources.

BN-600 has been operating since 1980 as the Beloyarsk-3 nuclear power plant and is currently still in operation. Its power was designed at 600 MWe (1470 MWth), and full power operation was reached at the end of 1981. Reactor operation has been stable with a load factor of ~75% and a turbine efficiency of ~43%. At the end of 2009, the total BN-600 power operation time had amounted to ~ 7870 EFPD (Equivalent Full Power Days), and ~ 112 billion kWh of electricity had been generated. Based on the demonstration experience of BN-600, a commercial size SFR – the BN-800 – was designed, and this is expected to reach first criticality in 2012.

MONJU is a prototype SFR, located in Tsuruga, Japan. Construction started in 1986 and first criticality was reached in 1994. The reactor is of loop-type design, with a power level of 280 MWe (714 MWth). MONJU was forced to shutdown in 1995, during its pre-operational testing phase (at 40% power). This was due to a sodium leak in the non-radioactive secondary heat transport system, which caused a major fire. Considerable effort had to be invested before public understanding and acceptance could be regained. After appropriate modifications, MONJU was restarted in May 2010. However, another accident, involving dropped machinery, occurred in August 2010, and this has led to the plant being shutdown once again.

The Prototype Fast Breeder Reactor (PFBR) is currently under construction in Kalpakkam, India. The Indira Gandhi Centre for Atomic Research (IGCAR) is responsible for the design of this reactor. PFBR is of 500 MWe capacity and is a pool-type SFR with 2 primary pumps, 4 intermediate heat exchangers and 2 secondary loops. As of April 2011, it was expected to be commissioned in 2012. India has a strong interest in proving the viability of the SFR, since it can – in the long term – use the thorium fuel cycle. The world's second largest proven reserves of thorium are situated in India. At the current stage, however, it is planned to use ^{238}U , and not thorium, as fertile material in PFBR. The new bred fissile material will thus initially be plutonium, not ^{233}U .

Commercial size SFRs [1.16] [1.17] [1.18]

As mentioned above, a commercial power unit – the BN-800 reactor – was contemplated in Russia as an advanced version of BN-600. Its capacity is 870 MWe (2100 MWth). In order to obtain the largest economical benefit, most of the BN-600 design solutions were retained. Moreover, it was planned to create a small series of such plants, all sharing a single complex of fuel cycle facilities. Construction

of BN-800 started in 1987, but protests halted progress in 1988. The license for restarting construction was issued in 1997. However, due to financial difficulties, the progress with BN-800 has been slow. The power plant is currently still under construction, with first criticality expected in 2012.

Super-Phénix was the first large SFR worldwide, located on the Rhône River at Creys-Malville in France. It had a power level of 1242 MWe (2990 MWth). The reactor was connected to the grid in January 1986 and full power was reached in December of the same year. It was definitively shutdown, for political reasons, in 1997, 20 years before the end of the plant's designed lifetime. Viewed as a whole, the operation of Super-Phénix was beset with interruptions: over a period of 11 years, the total operational time of the power plant sums up to just 53 months, during which it produced 7.9 billion kWh. Nevertheless – and in spite of having been decommissioned early – Super-Phénix succeeded in demonstrating that a large-scale, commercial size SFR is easy to operate from the neutronics point of view, the large thermal inertia being a real advantage in limiting reactivity feedback effects. Furthermore, the operational experience gained for large components remains significant. The knowledge acquired from Super-Phénix has been integrated into the European Fast Reactor (EFR) project.

EFR is a 1500 MWe reactor concept, based largely on the experience gained with Super-Phénix. With France in the leading role, the project was launched in 1988. It essentially represents a synthesis of the extensive experience acquired with pool-type, oxide-fuelled SFRs as operated in France, Germany and the UK. One of the outstanding achievements of the EFR project has been to make firm and reliable cost estimates. Even though the construction of a reactor with such a design may not be possible in the near future, the project has helped establish a well-validated way forward towards the commercial utilization of fast reactors, especially of the SFRs.

More recently, viz. since 2007, a new R&D program – being conducted jointly by CEA, EDF and Areva – has been underway in France. This has, as objective, the development and implementation, by 2020, of a prototype reactor with promising innovations representative of a new generation of SFRs. The prototype, called ASTRID (Advanced Sodium Technological Reactor for Industrial Demonstration), sets out to demonstrate the progress made in SFR technology on an industrial scale by qualifying innovative options (some of which still remain open in the areas requiring improvements, especially safety and operability). The new reactor is expected to serve as the precursor of a first-of-its-kind commercial system, which can largely meet the declared GIF goals.

1.5 Goals and scope of the present research

As discussed above, the SFR has many advantages. However, it has a dominating neutronics drawback, viz. there is generally a positive reactivity effect when sodium coolant is removed from the core. In other words, one has a positive reactivity coefficient associated with sodium voidage. The overriding aim of the present doctoral research is to analyze and optimized advanced SFR core

Chapter 1: Introduction

designs with improved safety characteristics, particularly from the viewpoint of the sodium void reactivity effect and its impact on SFR dynamic behavior in hypothetical accident scenarios.

As indicated earlier, the SFR – as a fast spectrum system – enables full closure of the fuel cycle, and thus an optimal management of fuel resources and minimization of long-live radioactive wastes. The long-term operation of an SFR core in a closed fuel cycle will lead to an equilibrium state, where both reactivity and fuel mass flow stabilize. This assumes constant periodic fuel treatment. Also for an open cycle (once-through) operation, a certain equilibrium state can be obtained. Several investigations of the sodium void effect have been reported earlier for the beginning-of-life (BOL) conditions of an SFR or, at most, for beginning of open equilibrium (BOC) conditions, e.g. [1.19, 1.20, 1.21]. Emphasis has accordingly been placed in the present research not only on analysis of the BOL and BOC states, but also on the beginning of closed equilibrium (BEC) state.

The reference SFR core design used in this doctoral study is based on the present “working horse” core of the Collaborative Project on the European Sodium Fast Reactor (CP-ESFR) [1.22]. This 3600 MWth SFR concept was proposed by the French CEA [1.23]. The EQL3D procedure [1.24], developed in the framework of the FAST project at the Paul Scherrer Institute (PSI), and based on the ERANOS code [1.25], has been applied to obtain the two equilibrium states (BOC and BEC) for the analyzed core.

The first step in the present research has been to arrive at a clearer understanding of the principal contributing phenomena for the SFR void effect. This has been achieved by carrying out a detailed void reactivity decomposition study.

Following this, different ways have been investigated for improving the neutronics safety parameters of the reference ESFR core design in the equilibrium closed fuel cycle, those at BOL being considered as the starting point. In the process, the principal neutronics performance parameters have been considered in parallel, in order to ensure basic feasibility for operation as also to preserve the iso-breeding feature of the core. Based on the specific optimization options identified, two “synthesis” core concepts have been proposed, each featuring improved safety characteristics relative to the reference core.

In the final phase of the research, the transient behavior of the synthesis cores has been compared to that of the reference ESFR design. This has been done in the context of a representative unprotected loss-of-flow (ULOF) accident scenario, i.e. flow run-down without SCRAM. During such a hypothetical transient, sodium boiling is anticipated to occur and, as such, the consequences of the accident depend strongly on the sodium void formation and the corresponding reactivity feedback effects, i.e. on closely coupled neutronics/thermal-hydraulics phenomena.

Specific aspects of each of the above three phases of the present research are described below.

1) *Sodium void reactivity decomposition and analysis*

Reactivity decomposition is commonly applied in reactor physics analysis, and the related methodologies are well developed. These are based on either neutron balance considerations or on perturbation theory, applications having been reported for both thermal and fast reactors. The perturbation theory based method is widely used to assess the impact of different contributing factors to a given reactivity change and to quantify the corresponding sensitivity coefficients. It requires direct and adjoint flux calculations. The neutron balance based method employs two direct flux calculations, viz. for the nominal and the perturbed cases (with the relevant changes being made in the perturbed core). Accordingly, it assumes that the individual components of the reactivity change are independent.

The neutron balance based method can be used for detailed reactivity decompositions in terms of different reactions, nuclides or energy groups. However, the nominal and perturbed fluxes should be correctly normalized to ensure consistency in the comparison. The normalization is often made to the neutron production rate. This corresponds, in practical terms, to the same power level in the nominal and perturbed cores. An alternative approach, as adopted currently, is to normalize the neutron balance to the integral flux.

2) *Neutronics optimization of the ESFR core*

As indicated earlier, the overriding aim of the present doctoral research is to achieve an improvement of the safety characteristics of advanced SFR core designs. The comprehensive neutronics study carried out in this context has aimed at assessing the optimization potential for the reference ESFR core, in terms of the principally considered safety parameters, viz. void reactivity ($\Delta\rho_v$) and Doppler constant (DC), as also the main performance parameters, viz. nominal reactivity (ρ) and breeding gain (BG).

There are several different SFR optimization options recommended in the literature [1.26, 1.27, 1.28], and four of these have been selected currently, viz. introducing an upper sodium plenum and boron layer, varying the core height-to-diameter (H/D) ratio, introducing moderator pins into the fuel assemblies, and modifying the initially loaded plutonium content. The sensitivity of the considered safety and performance parameters is investigated with respect to each of the different optimization options. In all cases, the void reactivity has been analyzed in detail, via its decomposition in terms of reaction-, isotope- and/or energy-group-wise components.

Finally, as mentioned, two synthesis core concepts have been proposed by combining different optimization options. In each case, having a positive nominal reactivity at the End of Equilibrium closed fuel Cycle (EEC) has been set as the boundary condition.

3) *Impact of optimization on transient behavior*

In a hypothetical SFR ULOF accident scenario, sodium boiling will occur at the ambient low pressure if the sodium coolant flow through a given channel is too low for the heat to be removed in the liquid phase. A positive reactivity will be inserted due to the sodium void effect. Although this is partly compensated by certain negative feedbacks, viz. Doppler and thermal expansion effects, the overall reactivity change usually remains positive. The reactor power will thus increase following the onset of sodium boiling.

The following reference ULOF scenario has been considered in the present research for analyzing the different SFR core designs: flow run-down without SCRAM, with a half-time (time after which the flow is reduced by 50%) of 10 seconds and an asymptotic flow rate of 20% of the initial (nominal) flow.

The transient analysis has been carried out using PSI's FAST code system, which employs a number of individual codes in coupled mode to analyze the dynamic behavior of different advanced fast reactor concepts [1.29]. Most recently, the thermal-hydraulics code TRACE in the FAST code system has been extended and validated for sodium two-phase flow calculations [1.30, 1.31]. This has allowed an accurate simulation of the strong interaction, under transient conditions, between the positive sodium void reactivity and two-phase thermal-hydraulics.

The starting point for the transient analysis is the reference ESFR core design. For the selected ULOF scenario, it is found that the reactor power goes up rapidly, causing both cladding and fuel to melt. The two proposed synthesis core designs are then tested. Here, it is found that – although the neutronics optimization leads to certain improvements of the dynamic core behavior – thermal-hydraulic design modifications are needed 1) to avoid sodium flow blockage and 2) to reduce boiling instabilities caused by the vaporization/condensation process in the upper sodium plenum. Following implementation of appropriate assembly design changes in this context, one arrives at a final core configuration, in which, for the selected accident scenario, a new “steady state” involving stable boiling is found to be achievable, with melting of neither cladding nor fuel.

1.6 Outline of the thesis

The present doctoral thesis is organized in six chapters.

Following this introductory chapter, the second chapter provides a more specific general background for the thesis. As mentioned, an important context for this doctoral research is the 7th European Framework Program's CP-ESFR. Accordingly, more details are given about this project, and the main design features of the reference 3600 MWth ESFR core are presented. The computational tools

Chapter 1: Introduction

employed are also introduced in this chapter. More specifically, these include the FAST code system and the Monte Carlo neutronics code SERPENT [1.32]. The FAST code system essentially consists of the fast-reactor neutronics code ERANOS, as well as the EQL3D procedure (ERANOS based) for the fuel cycle calculation, the 3D spatial kinetics code PARCS, the in-house routine ERANOS2PARCS for converting the cross-section format, the 1D thermal-hydraulics code TRACE, and the thermal-mechanics code FRED. Except for the last one, all the other codes have been applied in this doctoral work. The use of SERPENT has mainly been for benchmarking some of the ERANOS calculations.

Chapter 3 focuses on the sodium void effect. At first, various voiding scenarios and the spatial distribution of void reactivity importance are investigated. Then, the neutron balance based methodology of void reactivity decomposition – as developed and applied currently – is described. The ability to breakdown a reactivity change in terms of the contributions of individual reactions, nuclides and/or energy groups is shown to be most useful in providing a deeper understanding of the sodium void effect in the reference ESFR core. It also proves to be a valuable tool for the optimization studies described in the following chapter. As mentioned earlier, the other widely applied approach for reactivity effect investigations is that based on perturbation theory and corresponding sensitivity analysis. This approach is introduced as well, and it is shown that the corresponding decomposition results for the void effect provide useful complementary information to that obtained from the neutron balance based method.

The neutronics optimization study for the reference ESFR core design is detailed in Chapter 4. As mentioned earlier, there are various SFR optimization options recommended in the literature. Most of these were given some preliminary consideration at the start of the study, a down-selection finally resulting in the four options currently given detailed analysis, viz. introducing an upper sodium plenum and boron layer, varying the core H/D ratio, introducing moderator pins into the fuel assemblies, and modifying the initially loaded plutonium content. The sensitivity of the void reactivity, Doppler constant, nominal reactivity and breeding gain has been evaluated with respect to each of the four optimization options. In doing so, focus has been placed not only on BOL conditions, but also on the BEC state. Finally, the two “synthesis” cores – representing different selected combinations of the optimization options – are described, the common boundary condition set being to have a positive nominal reactivity margin at EEC.

Chapter 5 discusses the testing of the synthesis cores, in terms of their dynamic response to the onset of sodium boiling under the highly challenging conditions of the postulated ULOF. It is first shown how, in the case of the reference ESFR core, this hypothetical accident scenario leads to rapid melting of both cladding and fuel. Certain improvements are achieved with the neutronics optimization carried out for the synthesis cores. However, these are found, in themselves, to be insufficient as regards the prevention of the severe core accident. An additional need is indicated, viz. that for improving the sodium flow behavior during the accident. The corresponding modifications carried out in the thermal-hydraulic design of the fuel assemblies are the introduction (at an appropriate axial elevation) of small openings in the wrapper tube and the adoption of an extended upper fission gas

Chapter 1: Introduction

plenum. The former is shown to prevent sodium blockage, while the latter helps reduce boiling instabilities caused by the vaporization/condensation process in the upper sodium plenum. As a result, one succeeds in achieving a core configuration, in which, melting of neither cladding nor fuel occurs during the stipulated accident.

Finally, Chapter 6 provides the main conclusions to be drawn from the present doctoral research, as well as the recommendations for future work.

References

- [1.01] IAEA nuclear technology review, issued by IAEA, 2011.
- [1.02] Nuclear power reactors in the world, issued by IAEA, 2011.
- [1.03] Power reactor information system: <http://www.iaea.org/pris>.
- [1.04] IAEA annual report 2010, issued by IAEA, 2011.
- [1.05] Jahresbericht 2010, Nuklearforum Schweiz, 2011.
- [1.06] Uranium 2009: Recourses, Production and Demand. Issued by NEA, 2010.
- [1.07] Java-based nuclear data display program: <http://www.oecd-neo.org/janis/>.
- [1.08] K. Sun, J. Krepel, K. Mikityuk, S. Pelloni, R. Chawla. Void reactivity decomposition for Sodium-cooled Fast Reactor in equilibrium fuel cycle. *Annals of Nuclear Energy*, vol. 38(12): pp. 1645-1657, 2011.
- [1.09] International Handbook of Evaluated Criticality Safety Benchmark Experiments, issued by NEA, 2009.
- [1.10] Thorium fuel cycle – Potential benefits and challenges, issued by IAEA, 2005.
- [1.11] A Technology Roadmap for Generation IV Nuclear Energy Systems, issued by U.S. DOE and GIF, 2002.
- [1.12] GIF R&D Outlook for Generation IV Nuclear Energy Systems, issued by GIF, 2009.
- [1.13] Status of liquid metal cooled fast breeder reactors, Technical Reports Series, No. 246, p. 89, issued by IAEA, 1985.
- [1.14] T. Fanning. Sodium as a Fast Reactor Coolant, Topical Seminar Series on Sodium Fast Reactors, 2007.
- [1.15] N. N. Oshkanov O. M. Saraev, M. V. Bakanov, P. P. Govorov, O. A. Potapov, Yu. M. Ashurko, V. M. Poplavskii, B. A. Vasil'ev, Yu. L. Kamanin, V. N. Ershov. Thirty years of experience in operating the BN-600 sodium-cooled fast reactor. *Atomic Energy*, vol. 108(4): pp. 234-239, 2010.
- [1.16] IAEA Fast Reactor Database: <http://www-frdb.iaea.org/>, 2006.
- [1.17] The Hindu, <http://www.thehindu.com/sci-tech/technology/article1981270.ece>, 2011.
- [1.18] P. Le Coz, J. F. Sauvage, J. P. Serpantie. Sodium-cooled Fast Reactor: the ASTRID plant project. In ICAPP 2011, paper 11249.

Chapter 1: Introduction

- [1.19] P. Sciora, L. Buiron, G. Rimpault, F. Varaine, E. Hourcade, A.C. Scholer, D. Ruah, D. Verrier, S. Massara, D. Lecarpentier, T. Jourdeuil. A Break Even Oxide Fuel Core for an Innovative French Sodium-Cooled Fast Reactor: Neutronic Studies Results. In GLOBAL 2009, Paper 9528.
- [1.20] Yu. S. Khomyakov, V. A. Eliseev, I. V. Malysheva, V. I. Matveev, A. M. Tsiboulya. Optimization of Parameters of MOX Fuel Core of Sodium Cooled Large Size Fast Reactor. In GLOBAL 2009, Paper 9235.
- [1.21] J. Tommasi, P. Archier, J. M. Ruggieri. Validation of the sodium void reactivity effect prediction using JEFF-3.1 nuclear data. *Annals of Nuclear Energy*, vol. 37(11): pp. 1534-1553, 2010.
- [1.22] G. L. Fiorini and A. Vasile. European Commission – 7th Framework Programme The Collaborative Project on European Sodium Fast Reactor (CP ESFR). In ICAPP 2009, Paper 9064.
- [1.23] A. Vasile G. L. Fiorini, Ph. Dufour, J.M. Bonnerot, Ch. Latgé. The Collaborative Project on European Sodium Fast Reactor (CP ESFR) European Commission – 7th Framework Programme. In ICAPP 2011, Paper 11297.
- [1.24] J. Krepel, S. Pelloni, K. Mikityuk, P. Coddington. EQL3D: ERANOS based equilibrium fuel cycle procedure for fast reactors. *Annals of Nuclear Energy*, vol. 36(5): pp. 550-561, 2009.
- [1.25] J. M. Ruggieri, J. Tommasi; J. F. Lebrat; C. Suteau; D. Plisson-Rieunier; C. De Saint Jean; G. Rimpault; J. C. Sublet. ERANOS 2.1: International Code System for GEN IV Fast Reactor Analysis. In ICAPP 2006, Paper 6360.
- [1.26] H. S. Khalil and R. N. Hill. Evaluation of Liquid-Metal Reactor Design Options for Reduction of Sodium Void Worth. *Nuclear Science and Engineering*, vol. 109: pp. 221-266, 1991.
- [1.27] L. Buiron, Ph. Dufour, G. Rimpault, G. Prulhiere, C. Thevenot, J. Tommasi, F. Varaine, A. Zaetta. Innovative Core Design for Generation IV Sodium-cooled Fast Reactors. In ICAPP 2007, paper 7383.
- [1.28] P. Sciora, D. Blanchet, L. Buiron, B. Fontaine, M. Vanier, F. Varaine, C. Venard, S. Massara, A.C. Scholer, D. Verrier. Low void effect core design applied on 2400 MWth SFR reactor. In ICAPP 2011, Paper 11048.
- [1.29] K. Mikityuk, S. Pelloni, P. Coddington, E. Bubelis, and R. Chawla. FAST: An advanced code system for fast reactor transient analysis. *Annals of Nuclear Energy*, vol. 32(15): pp. 1613-1631, 2005.
- [1.30] A. Chenu, K. Mikityuk, and R. Chawla. TRACE simulation of sodium boiling in pin bundle experiments under loss-of-flow conditions. *Nuclear Engineering and Design*, vol. 239(11): pp 2417-2429, 2009.

Chapter 1: Introduction

- [1.31] A. Chenu. Single- and two-phase flow modeling for coupled neutronics / thermal-hydraulics transient analysis of advanced sodium-cooled fast reactors. Swiss Federal Institute of Technology, Lausanne (EPFL), doctoral thesis No. 5172 (2011).
- [1.32] J. Leppänen. PSG2/Serpent – a continuous-energy Monte Carlo reactor physics burnup calculation code (user's manual). Version September 5, 2011.

Chapter 2

Thesis Background

The general background of the thesis is described in this chapter. Section 2.1 introduces the Collaborative Project for a European Sodium Fast Reactor (CP-ESFR). The “working horse” core design of this project has served as the reference core for the present doctoral research, i.e. is effectively the starting point for the studies carried out on SFR safety improvement. The basic computational tools used are detailed in Section 2.2. Thereby, emphasis is given to the FAST code system, developed in the framework of PSI’s FAST project and consisting of the core neutronics codes ERANOS (statics) and PARCS (dynamics), the system thermal-hydraulics code TRACE and the fuel thermal-mechanics code FRED. In addition, the Monte Carlo code SERPENT – used currently for benchmarking some of the sodium void effect results obtained with the deterministic code ERANOS – is also described.

2.1 Collaborative Project - European Sodium Fast Reactor

The Collaborative Project for a European Sodium Fast Reactor (CP-ESFR, Contract Nr: 232 658) follows the 6th European Framework Program project called “Roadmap for a European Innovative Sodium cooled Fast Reactor - EISOFR” [2.01].

2.1.1 Framework of the CP-ESFR

The CP-ESFR merges the contribution of 23 European partners. It has been realized under the aegis of the 7th Framework Program, in the Advanced Nuclear Systems (ANS) area, with a total budget of 11.55 M€ (50% being by the European Commission). The project started in 2009 and is scheduled to end in 2012. The CP-ESFR is devoted to the identification and study of innovations to be considered for the future in SFR core design, safety, reactor architecture and components, as also to the dissemination of knowledge related to this technology among young European professionals [2.02].

The major research objectives addressed by the fourth generation of European sodium-cooled fast reactors can be summarized as the following three items: an improved safety, a reduced economics risk, and a flexible and robust nuclear material management. In addition to the above mentioned items, the project is also a platform for helping to rebuild the European expertise in the SFR field with the

participation of young professionals. It should be noted it is in this context that the present doctoral work received partial financing from the ESFR project.

The CP-ESFR is structured into different main technical sub-projects, the overriding common objective being to improve the efficiency and safety of current-day SFR systems and fuels. Moreover, in order to ensure full technical and administrative coherency, the management activities are also explicitly indicated in the project structure. As described in [2.03], a strong commitment within CP-ESFR is to look for complementarities with Generation IV activities. As such, the results of the project could represent the contribution to the Generation IV SFR of the European Union member states (under the aegis of the European Commission).

2.1.2 ESFR safety objectives and design principles

Safety is always the most crucial issue for reactor design. The principal safety objectives, relevant for all current and future nuclear plants, have been defined by the IAEA [2.04] as the following:

- General safety objective: to protect individuals, society and environment from radiological hazards.
- Radiation protection objective: to ensure that radiation exposure is kept below prescribed limits and as low as reasonably achievable.
- Technical safety objective: to take all reasonably practicable measures to prevent accidents and to mitigate their consequences should they occur.

For Generation IV systems, and the SFR in particular, technical guidelines considered for the French EPRTM [2.05] are considered as a basis [2.06]. The practical safety objectives for CP-ESFR, defined in consistency with the European safety framework, are the following [2.07]:

- The individual and collective exposure of workers, and the impact on public and environment, during normal operating conditions and in the case of frequent transients, have to meet the European and national regulatory requirements.
- The number of significant faults, which could occur frequently under normal operating conditions, has to be reduced.
- The global occurrence frequency of the potentially most severe “dealt with” accident has to be made lower than 10^{-5} per plant-year, by taking into account uncertainties and all types of failures and hazards.
- A significant limitation of radioactive releases that may result from any “dealt with” event has to be achieved.

In order to enhance robustness, the practical safety objectives are addressed within CP-ESFR R&D studies as follows [2.07]:

Chapter 2: Thesis Background

- The safety approach has to be developed and implemented in the design at an early stage of the project, i.e. safety has to be “built in” rather than “added on”.
- The operational and licensing background of SFR technology has to be considered.
- An ALARP (As Low As Reasonably Practicable) approach is applied for doses to the public and workers, for both normal operating conditions and the case of accidents.
- The targeted design provisions should in particular avoid the risk of an important mechanical energy release. Moreover, protective measures for people living in the vicinity of the damaged power plant should be minimized.
- The protection of the public with respect to chemical releases (due to sodium reactions with air, water and concrete) has to be assessed. For the associated sodium aerosols releases, the objective is to minimize the need for emergency measures.

The earlier listed, principal safety objectives for current and future NPPs are achieved through the application of the defense-in-depth principle, which ensures the safety of the public and protects the environment. In [2.08] are defined five levels of defense-in-depth for the currently operating LWRs. These are being extended to meet the declared safety objectives of future reactors [2.07], especially Generation IV systems, in a technology neutral context (see Table 2.1). It should be noted here that the final goal of the current doctoral research focuses on defense-in-depth level 3, i.e. preventing ESFR core damage under the conditions of a reference ULOF accident scenario.

Table 2.1. Levels of defense-in-depth for future reactors

Levels of defense-in-depth	Objective	Essential means
Level 1	Prevention of abnormal operation and failure	Conservative design and high quality in construction and operation
Level 2	Control of abnormal operation and failure	Control, limiting and protection systems and other surveillance features
Level 3	Control of accidents to limit radiological releases and prevent escalation to: 1) Core damage 2) Whole core accident	Engineered safety features and accident procedures
Level 4	Control of whole core accident to limit radiological releases and prevent escalation to situation that could lead to early or large radiological releases.	Complementary features and accident management
Level 5	Mitigation of significant radiological releases by implementation of off-site emergency measures.	Off-site emergency response

2.1.3 ESFR core description and general design features

The reference ESFR is designed as a commercial-size unit with a thermal power of 3600 MW and 1500 MW electrical output. There are two working-horse core designs which have been proposed as initial concepts in CP-ESFR: one is based on oxide fuel and the other on carbide fuel [2.09]. Their core parameters are listed in Table 2.2 and their schematic views are given in Figure 2.2.

Table 2.2. ESFR core parameters for the oxide and carbide versions.

ESFR core version	Oxide	Carbide
Thermal power	3600 MWth	3600 MWth
Volume	17.5 m ³	10.5 m ³
Lattice pitch	20.08 cm	18.32 cm
Fuel type	Pins / Pellets	Pins / Pellets
Nr. of fuel assemblies	453	414
Diameter	4.72 m	4.10 m
Height	1.00 m	0.80 m
H/D ration	0.21	0.19
Actinides	74.1 tons	39.5 tons
Plutonium	11.6 tons (15.7%)	8.5 tons (21.5%)
Core management	5 x 410 = 2050 EFPD	3 x 533 = 1600 EFPD
Average burn-up	~10 % FIMA ~100 GWd/tHM	~15 % FIMA ~150 GWd/tHM
Coolant	Sodium	Sodium
Inlet coolant temp.	395 °C	395 °C
Outlet coolant temp.	545 °C	545 °C

The working-horse cores have provided the basis for optimization studies. Currently, the project (2009-2012) is in its final year. The optimized core designs have already been decided, e.g. introducing a 60 cm upper sodium plenum with a 30 cm boron layer above it, replacing the lower reflector by fertile blanket, and increasing the initially loaded plutonium content correspondingly in order to ensure core criticality. The present doctoral work – although representing a Swiss contribution to the CP-ESFR [2.09] – is nevertheless independent of the project. The principal emphasis currently has been on optimization of the ESFR core, such that improved core behavior can be demonstrated for a representative unprotected loss-of-flow accident.

It should be mentioned that the carbide working-horse core in the ESFR project is considered to be a plutonium burner. Thus, only the oxide core is considered in the present research. The active core has a pancake shape, 4.7 meters in diameter and 1.0 meter in height (see Figure 2.2 left). Above the active core, there is a fission gas plenum (11 cm) and then an upper steel reflector (70 cm). Below the active core, there is firstly a lower reflector (30 cm), and this is followed by a second fission gas plenum (91

cm). The fuel assemblies, consisting of pins with mixed U-Pu oxide pellets and steel cladding, are loaded into the inner and outer core zones with different plutonium contents (14.6% and 17.0%, respectively). In the current assembly design, the fuel-to-sodium ratio is significantly increased by enlarging the fuel pin diameter (as compared to the Super-Phénix fuel). This is advantageous for all the key parameters, i.e. void reactivity, Doppler constant and breeding gain. The sodium inlet and outlet temperatures are 395°C and 545°C, respectively, and the estimated average fuel temperature is 1227°C.

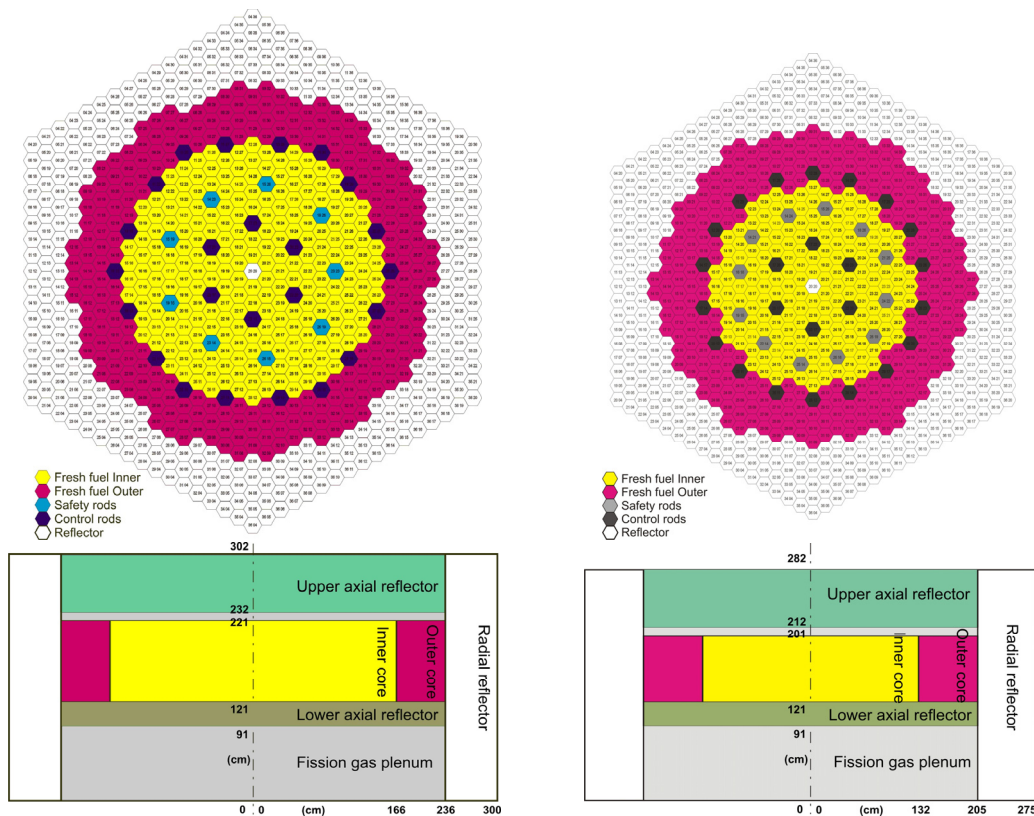


Figure 2.2. Horizontal and vertical sections of the oxide (left) and carbide (right) ESFR [2.09].

A pool type SFR is the reference system considered in CP-ESFR [2.10] (see Figure 2.3). The entire reactor is immersed in a sodium “pool”. Due to the sodium/oxygen chemical reaction, this pool is isolated from air and covered by argon gas. Besides the reactor core, the ESFR has 3 primary pumps maintaining the sodium flow, 6 intermediate heat exchangers (IHX) extracting the heat from the primary cycle under normal operating condition, and 6 decay heat removal (DHR) systems providing efficient heat removal capacity under accident conditions. The “above core structure” (ACS) is located on the top of the core, its main functions being the support of the control rod drive mechanisms and the control of the primary sodium flow distribution. The reactor core (reflectors and shields included) is supported by a diagrid, which rests on the strongback. The latter is a box-type structure comprising

two circular plates. It rests on the main vessel bottom (no welding), to which it transfers the total core weight. Space has been provisioned at the bottom of the pool for core catchers within and outside the primary vessel (named internal and external core catchers, respectively). These are devices to catch the molten core material (mainly corium) in case of a core meltdown and prevent it from escaping the containment building. The internal core catcher could be a circular tank of small capacity located below the strongback. The external core catcher could be a circular open tank of high capacity, enough to contain the corium and sodium, which may require extra cooling.

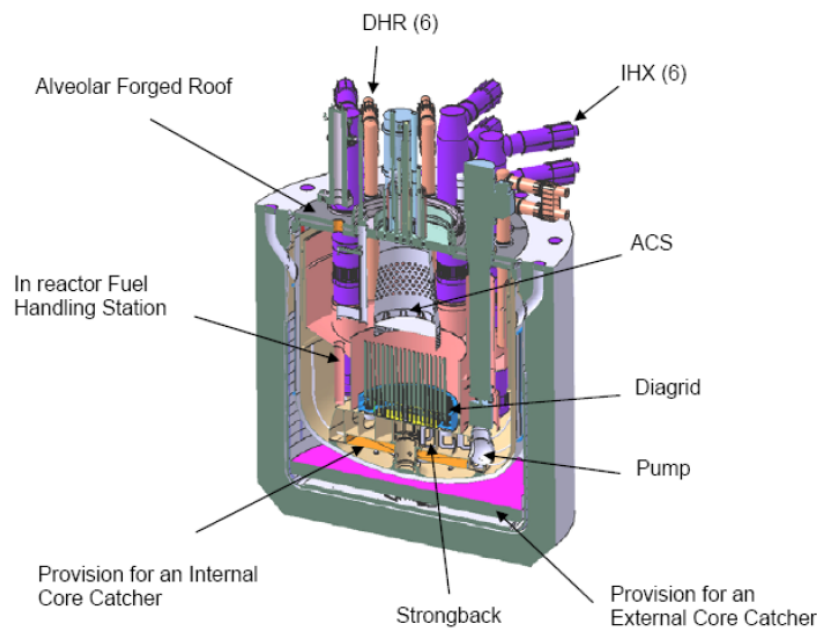


Figure 2.3. 3D view of the reference pool design [2.10].

The ESFR design strategy and the approach taken with respect to the containment functions follow previous European concepts, i.e. Super-Phénix and EFR. A schematic view of the ESFR containment is shown in Figure 2.4. Double concrete walls protect against radiological releases: the inner one closely surrounds the primary vessel; the other is the outer containment wall. Such a design may effectively prevent escalation of a situation that could lead to early or large radiological releases. Current-day designs of nuclear power plants are characterized by an enhanced safety level. In particular, Generation IV systems have to be highly safe and able to withstand extremely severe external events such as floods, tsunamis, tornadoes, fires and, in particular, aircraft crashes and earthquakes. On the one hand, the ESFR adopts a thick steel layer in the containment shell to guard against an aircraft crash. On the other hand, at the bottom of the reactor building, special features (e.g. seismic raft, isolators and bearing pads) have been incorporated to mitigate the seismic risk [2.11].

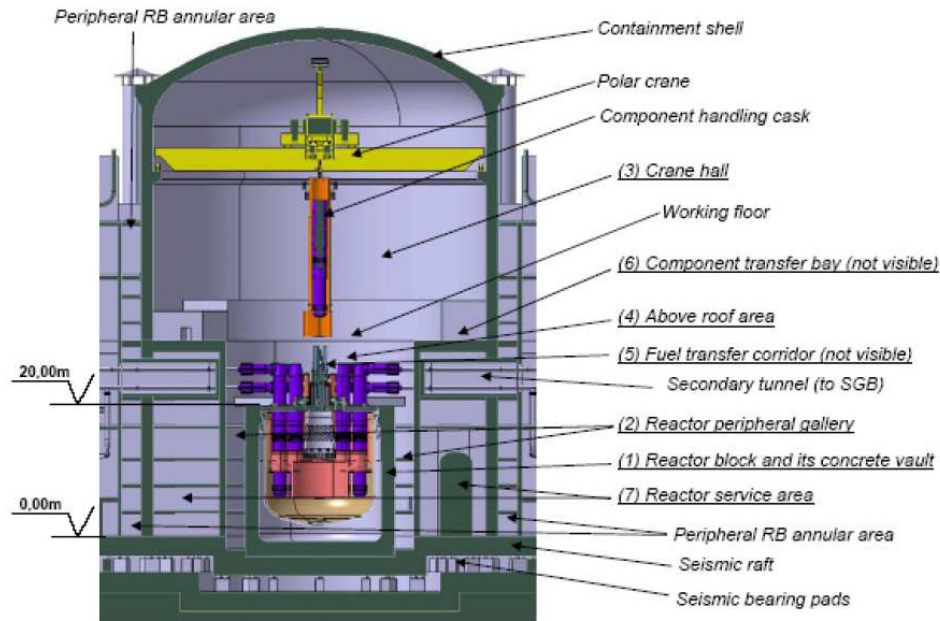


Figure 2.4. Schematic view of the ESRF containment [2.11].

2.2 Computational tools

The basic computational tools used in the current doctoral research are presented in this section. Subsection 2.2.1 describes the FAST code system, in particular the neutronics codes ERANOS (statics) and PARCS (dynamics), and the system thermal-hydraulics code TRACE. The Monte Carlo code SERPENT, used for benchmarking sodium void effect results obtained with ERANOS, is described briefly in Subsection 2.2.2.

2.2.1 The FAST code system

FAST, standing for Fast-spectrum Advanced Systems for power production and resource management, is a research project of the Laboratory for Reactor Physics and Systems Behavior (LRS) at PSI. Within different international frameworks, the comparative analysis of GIF-proposed fast-spectrum reactor systems, viz. SFR, GFR and LFR, is carried out in this project. More specifically, the research activity focuses on three main areas, viz. neutronics, thermal-hydraulics and fuel thermal-mechanics.

One of the major objectives of the FAST project is to develop and maintain a code system, also called FAST, as a general tool for analyzing core statics and dynamics behavior for various fast-spectrum systems, in multi-domains as mentioned above [2.12]. This code system consists of well established

existing codes, viz. ERANOS for static neutronics, PARCS for reactor kinetics, TRACE for system thermal-hydraulics, and FRED for fuel thermal mechanics. Some of these codes have been extended for specific purposes. Besides, an EQL3D procedure has been programmed – based on the ERANOS code – for fuel cycle calculations. Furthermore, an in-house routine ERANOS2PARCS has been developed in order to convert ERANOS output cross-sections into the format needed for input to PARCS.

A flow chart of the FAST code system is presented in Figure 2.5, showing the main codes used as well as the information exchanged through couplings. For the statics part, ERANOS is directly responsible for the neutronics calculation; for the dynamics part, it provides input in terms of macroscopic cross-sections and their derivatives (with respect to fuel temperature, coolant density, and dimension expansions) to PARCS. The latter then solves the steady state and time-dependent, multi-group neutron diffusion or transport equation to provide power distribution information to TRACE and FRED. In the meantime, TRACE solves the balance equations for mass, momentum and energy for the liquid and vapor phases to obtain the corresponding material temperature and density values. FRED solves the strain-stress equations to derive the thermal-mechanical behavior of fuel and structural elements. The internally coupled TRACE and FRED codes can derive the best-estimate temperature information and then send this back to PARCS through another internal coupling. At each time step, PARCS re-calculates the resulting reactivity changes and updates the power distribution.

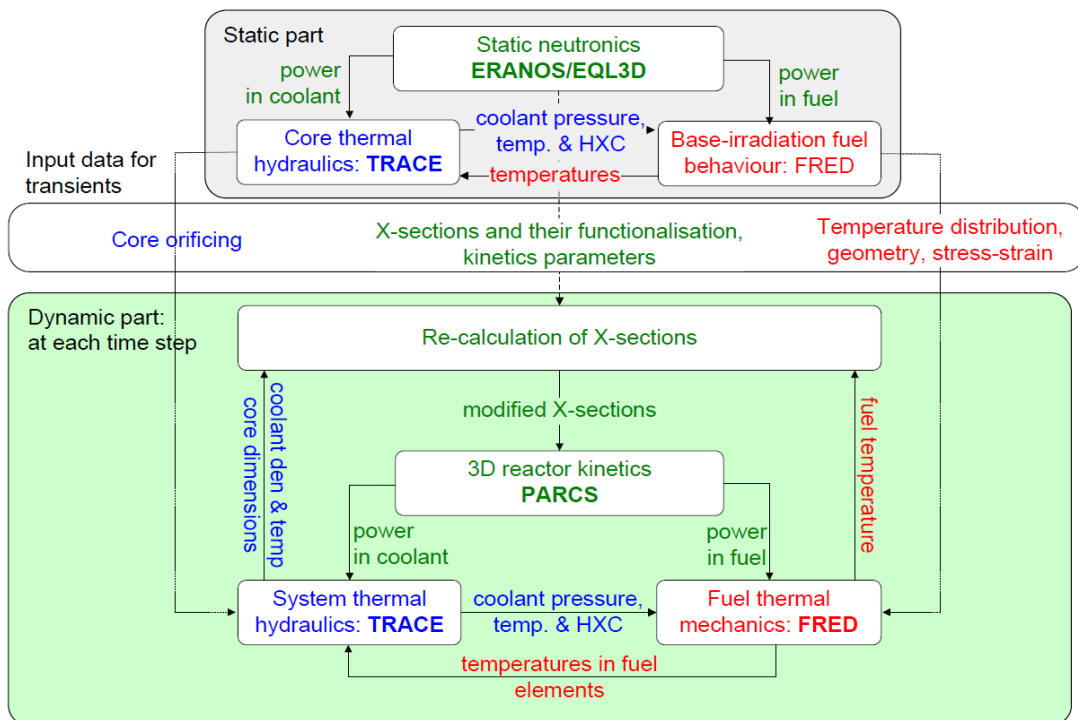


Figure 2.5. FAST code system flow chart [2.12].

More comprehensive descriptions for each individual code are detailed below:

ERANOS code: static neutronics

ERANOS, standing for European Reactor ANalysis Optimized code System, is used in this doctoral study for the static neutronics calculation. This deterministic code system consists of data libraries, individual codes and calculation procedures that have been developed and validated within the European collaboration on fast reactors over the past 20 years. The most recent version is ERANOS-2.2, which was released by the French CEA in 2010. However, this doctoral work started in 2008; therefore, all the calculations have been carried out using the second latest version ERANOS-2.1, which was released in 2007.

Five nuclear data libraries are available in ERANOS-2.1 [2.13]: JECCOLIB2, ERALIB1, JENDL-3.1, JEFF-3.1, and ENDFB-6.8. The first two libraries were already available in ERANOS-2.0; the first is based on JEF-2.2 data, while the second is a library which was adjusted on the basis of integral experiments. The latter three libraries have been newly included in ERANOS-2.1. In particular, JEFF-3.1, which was released in May 2005 under the auspices of the OECD/NEA's JEFF project [2.14], is recommended as the reference nuclear data library for fast-spectrum reactor calculations. Accordingly, it is the ERANOS library which has been selected for the present doctoral study. It consists of data sets which have been condensed appropriately into ERANOS-specific energy structures, viz.

- a 1968-energy-group library for the most important 103 nuclides and 9 compounds,
- a 172-energy-group library (XMAS structure) for the “103 + 9” (condensed from the previous fine library), as well as for additional 277 nuclides,
- a 33-energy-group library for the “103 + 9 + 277” (condensed from the XMAS-structure library), as well as for 57 pseudo-fission-products,
- a 175-energy-group library (VITAMIN-J structure) for 380 nuclides.

The ERANOS code system contains all the functions required for reference and design calculations of Liquid Metal Fast Reactor (LMFR) cores (as well as blankets, reflectors and shields), with extended capabilities for treating advanced reactor fuel assemblies and cores, Accelerator Driven Systems (ADSs) and GFRs. Nevertheless, applications for SFRs remain of greatest interest. Most validations of this code system have been carried out using results from sodium reactors, viz. MASURCA (CEA-Cadarache), ZPPR (Idaho), Phénix (Marcoule) and Super-Phénix (Creys-Malville) [2.15]. The verifications focus on both data libraries and computational algorithms, which finally make ERANOS a suitable basis for reliable neutronic calculations, for both current-day and advanced SFRs.

An advantage of the ERANOS code system is its modular structure, which can provide high flexibility for different calculation features. In most cases, the objective of ERANOS calculations is either the generation of appropriately self-shielded cross-sections or the determination of the effective multiplication factor k_{eff} . These objectives can be met by employing the deterministic methods implemented in ERANOS for solving the Boltzmann transport equation, which governs the behavior

of the neutron population. The commonly applied procedure can usually be separated into two major steps: (1) cross-section preparation using the cell/lattice code, and (2) the core calculation using these cross-sections to determine reactor characteristics. This separation normally corresponds to a two-level description of the geometry. The former deals with the assembly level, e.g. fuel, blanket, control rod, reflector, etc., whereas the latter looks at the entire reactor.

ECCO, standing for European Cell COde, is adopted in ERANOS for the preparation of self-shielded cross-sections and scattering matrices. In order to meet the specific requirements for the characteristics of fast neutron reactor cells, ECCO uses the subgroup method associated with the slowing down treatment in many energy groups, more specifically, 1968 for the current data library. The collision probability method is selected to deal with the highly heterogeneous lattices. Many types of geometries are available in ECCO, among which a 2D hexagonal lattice of cylindrical pins within a hexagonal wrapper is commonly used for describing the studied ESRF fuel assembly. From one geometry unit j to another i , the collision probability is given by [2.16]:

$$p_{j \rightarrow i} = \frac{1}{V_j} \iint \Sigma_i \cdot n(\vec{r}_j \rightarrow \vec{r}_i) dV_i dV_j \quad \text{Eq. 2.1}$$

where Σ_i is the macroscopic total cross-section in geometry unit i , $n(\vec{r}_j \rightarrow \vec{r}_i)$ is the corresponding transport kernel, and V represents the volume of the geometry unit. By taking into account the resonance structure for heavy nuclides and the complex geometry of the heterogeneous lattice, the self-shielded macroscopic cross-section for any partial reaction x (e.g. transport, capture, fission, scattering, etc.) in the geometry unit i in a given fine energy group g , i.e. $\bar{\Sigma}_{x,i}^g$, can be obtained by means of the subgroup method, assuming a uniform neutron source within this subgroup [2.17]:

$$\bar{\Sigma}_{x,i}^g = \frac{\sum_j S_j^g \cdot \sum_k \alpha^{g,k} \cdot p_{j \rightarrow i}^{g,k} \cdot \Sigma_{x,i}^{g,k}}{\sum_j S_j^g \cdot \sum_k \alpha^{g,k} \cdot p_{j \rightarrow i}^{g,k}} \quad \text{Eq. 2.2}$$

where S represents the uniform neutron source, j and k are the geometry unit index and probability index respectively, and α is the probability weight. The prepared self-shielded cross-sections and scattering matrices in the fine energy-groups are condensed according to a broader energy-group scheme, e.g. the 33-group structure in ERANOS. The condensation process is described as following:

$$\bar{\Sigma}_{x,i}^G = \frac{\sum_{g \in G} \Phi_i^g \cdot \Sigma_{x,i}^g}{\sum_{g \in G} \Phi_i^g} \quad \text{Eq. 2.3}$$

where g represents the fine energy-group within a broad energy-group G . Φ is the neutron flux and is determined by the integral transport equation:

$$\Phi_i^g = \frac{1}{V_j} \iint \left(\sum_{g'} \Sigma_{s,j}^{g' \rightarrow g} \Phi_j^{g'} + S_j^g \right) \cdot n(\vec{r}_j \rightarrow \vec{r}_i) dV_i dV_j \quad \text{Eq. 2.4}$$

where $\Sigma_s^{g' \rightarrow g}$ is the macroscopic scattering cross-section from energy group g' to g and S represents the neutron source term.

The condensed cross-section data are used further for the full-core calculation. In ERANOS, two modules – BISTRO and TGV/VARIANT – are available for the purpose of computing the neutron flux in the whole core by solving the eigenvalue (i.e. the effective multiplication factor k_{eff}) problem. The former is a finite difference code using the S_n (or discrete ordinates) method. Thereby, the Boltzmann equation is solved in two-dimensional (2D) geometries (XY or RZ) for a number of directions and each direction is associated to a weight. The latter is implemented in the VARIANT code using a variational nodal method. It can model Cartesian and hexagonal geometries.

Since the ESFR core consists of hexagonal fuel assemblies, it is the TGV/VARIANT module that has been selected as the flux solver in the present research. This variational nodal method is based on the second-order form of the even-parity transport equation [2.18]. The solution is computed in the form of even and odd parity flux expansions. More specifically, the basis functions are orthogonal polynomials for the spatial variables and spherical harmonics for the angular variables. The full transport option consumes considerable computational time; accordingly, a transport option with simplified spherical harmonics, i.e. neglecting the high-order cross-terms in the angular developments, has been implemented in the method. It should be mentioned here that the currently conducted fuel cycle analysis requires a large amount of flux solving calculations. In order to achieve a reasonable computational time, the simplified transport option has been selected as the reference route. In addition, a diffusion option is available in the VARIANT code, and this has been employed during the verification of the kinetics code PARCS (see below).

The ERANOS code system also contains a burnup computation module. The isotope evolution is calculated by solving the Bateman equations with the necessary input data, consisting of the energy-group-wise neutron flux, the reactor power level and the pre-defined evolution chain. The Bateman equations are solved using the exponential resolution method (also called matrix exponential method) in ERANOS [2.19]. The evolution chain adopted in this doctoral research for the heavy nuclides is shown in Figure 2.6. Further details regarding the burnup calculation are given later while describing the EQL3D procedure.

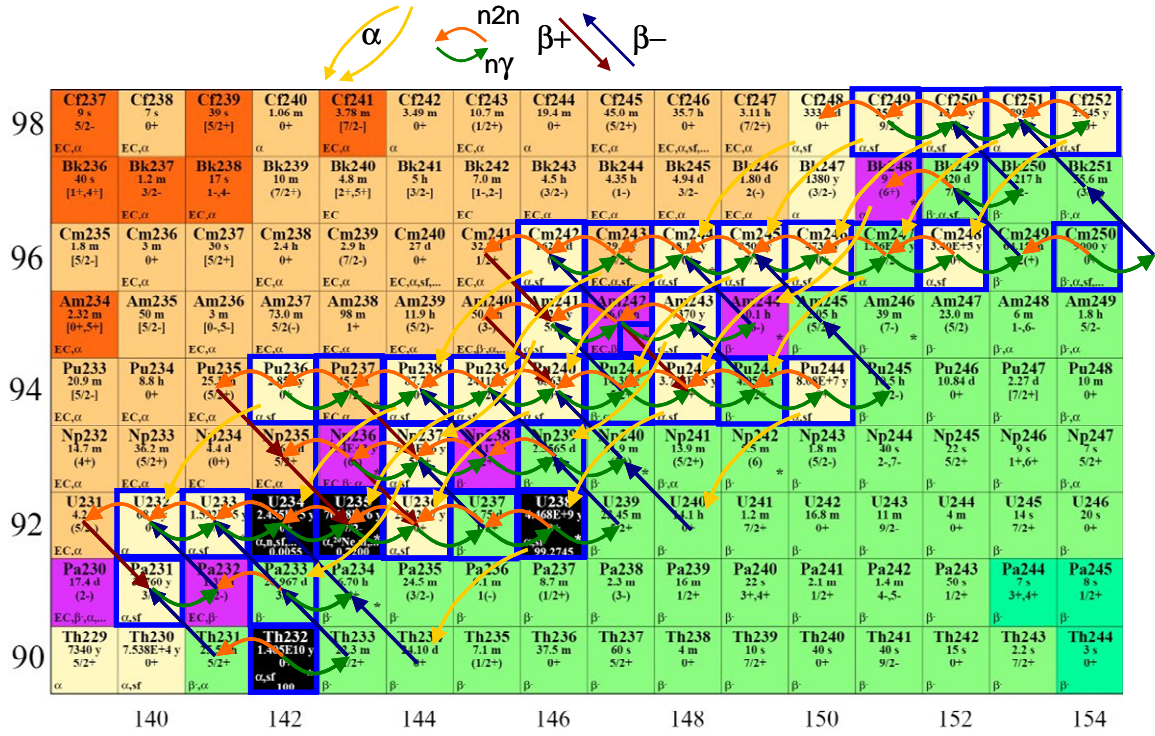


Figure 2.6. Evolution chain for the heavy nuclides adopted in this doctoral research [2.20].

ERANOS is able to provide useful information on fuel composition via a material balance module. Thanks to this option, the fuel composition, as well as the breeding gain (BG) value, can be evaluated for any given fuel cycle state. The latter is an important performance parameter from the point of view of fast reactor core design, which characterizes the excess fissile material produced relative to the consumed quantity. It is defined as:

$$BG = \sum_n \sum_i \omega_i \frac{C_{i-1}^n + D_{i-1}^n - (A_i^n + D_i^n)}{F} \quad \text{Eq. 2.5}$$

where the index n stands for the core region, i denotes the fuel isotope, F is the total fission rate in the core, A and C are the absorption and capture rates, respectively, while the two decay rates D_{i-1} and D_i represent, respectively, the production and destruction rates of isotope i by all possible radioactive decays. It should be noted that the fuel isotope $i-1$ can be transmuted, via a neutron capture, to fuel isotope i . The parameter ω_i is a weighting factor used in ERANOS, characterizing the reactivity of each isotope i on a scale where the “importance” of ^{239}Pu is 1 and that of ^{238}U is 0, the basis being provided by the following equation [2.21]:

$$\omega_i = \frac{(v\sigma_f - \sigma_a)_i^n - (v\sigma_f - \sigma_a)_{\text{U238}}^n}{(v\sigma_f - \sigma_a)_{\text{Pu239}}^n - (v\sigma_f - \sigma_a)_{\text{U238}}^n} \quad \text{Eq. 2.6}$$

where ν represents the number of neutrons produced per fission, and σ_f and σ_c are the microscopic cross-sections for fission and capture, respectively.

The ERANOS code system is capable of providing reaction rate information via a neutron balance module. Different types of reaction rates, e.g. fission, capture, production, leakage and scattering, can be generated for each computational node, and these can also be considered in terms of isotope-wise, energy-group-wise and combined isotope- and energy-group-wise contributions. In the next chapter, a neutron balance based reactivity decomposition method will be introduced and the used reaction rates are provided by this ERANOS module.

Another ERANOS feature applied in the present doctoral work is the possibility to perform sensitivity analysis based on perturbation theory, e.g. to carry out a reactivity breakdown and quantify its sensitivity to individual variables. Both linear and generalized perturbation theory can be applied using the implemented module in ERANOS. The former neglects the effect of flux variations caused by the perturbation, so that this approach is accurate for “small” changes. The latter is valid for reactivity effects in a more general sense and has therefore been adopted currently. It should be noted that using perturbation theory requires not only the direct flux, but also the adjoint flux (i.e. the neutron importance). The assessment of the void reactivity sensitivity to individual variables has been done in this doctoral work mainly with respect to isotope-wise reactions, the corresponding mathematical formulation being presented in greater detail in Subsection 3.4.2.

Figure 2.7 illustrates the ERANOS calculation routes applied in the present doctoral research.

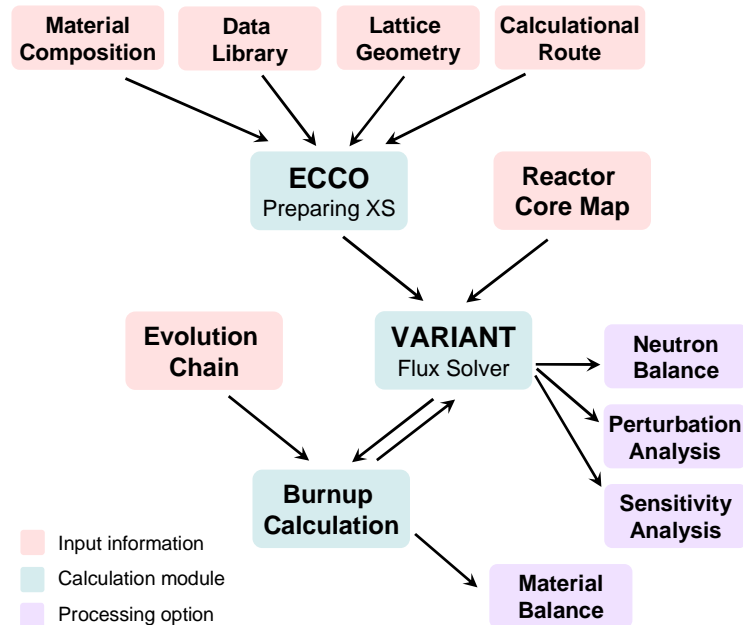


Figure 2.7. Schematic showing the ERANOS calculation routes applied in this doctoral work.

EQL3D procedure

As mentioned earlier, the focus in the present research is not only on the beginning-of-life (BOL) state of the core, but also on the beginning of equilibrium closed fuel cycle (BEC). The corresponding fuel cycle calculations for the studied SFR core have been carried out using the ERANOS based EQL3D procedure, which was developed in the FAST group of the Laboratory for Reactor Physics and Systems Behavior (LRS) at PSI. The methodology has been extensively described in [2.20].

In general, the EQL3D procedure can be used to yield the description of two basic situations: 1) the equilibrium of an open fuel cycle (result of periodic operation with fresh fuel without any recycling) and 2) the equilibrium of a closed fuel cycle (the asymptotic state resulting from the reactor's operation with a fixed fuel management scheme involving recycling of its own fuel). In both cases, the explicit cycle-by-cycle operation under specified periodic fuel management is simulated until the equilibrium state is reached. The methodology focuses on the actinides (including uranium) and their evolution in an iso-breeding reactor [2.22]. The fundamental assumptions are to keep the actinides mass in the manufactured fuel constant and to impose constant reactor power.

The basic logic of the EQL3D fuel treatment is illustrated in Figure 2.8. Fuel cycle equilibrium is defined as the state where the actinide composition evolution during two successive fuel cycles is identical. The actinides treatment is comprehensively programmed. During a given simulation, it is constantly repeated after each fuel cycle (or batch). More specifically, the spent fuel is unloaded and cooled for a given time to decrease its temperature and radioactivity, and the reactor core is reshuffled. Then, the actinides in the unloaded spent fuel are extracted and recycled, following the removal of the fission products (and a fraction of the actinides, if reprocessing losses are optionally specified). In order to preserve the mass, the reprocessed fuel is mixed with specified feed and finally loaded back into the reactor core.

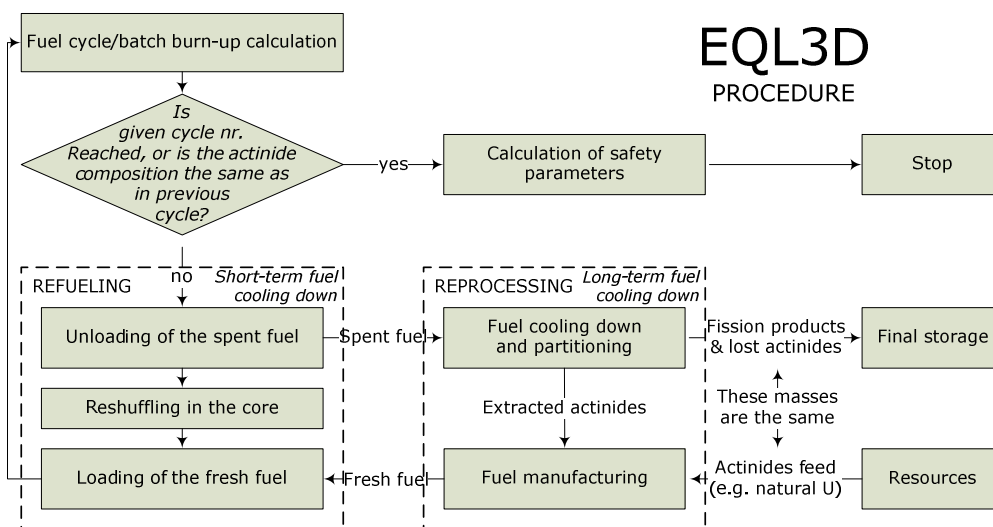


Figure 2.8. Flow chart of the actinides treatment within EQL3D [2.20].

For obtaining the closed fuel cycle equilibrium state of the ESFR core (as well as for the core designs with improved safety characteristics), the design-specific fuel cycle length of 2050 Equivalent Full Power Days (EFPDs) and its division into 5 batches (each of 410 EFPDs) have been considered in the simulations. It is assumed that the reshuffling and refueling period takes 30 days and that the cooling time before reprocessing is of one cycle duration ($5 \times (410 + 30) = 2200$ days). During the reprocessing, only fission products (FPs) from the discharged fuel, which represent about 10% of the loaded mass, are replaced by natural uranium feed. The remaining uranium, plutonium and minor actinides (MA) are recycled, the recycling losses being assumed to be zero.

PARCS code

PARCS, standing for Purdue Advanced Reactor Core Simulator, is a 3D reactor core simulator which solves the steady state and time-dependent, multi-group neutron diffusion and simplified P_3 (SP3^{2.1}) transport equations in square and hexagonal geometries [2.23]. As indicated previously, PARCS is integrated into the FAST code system for the purpose of spatial kinetics calculations. It is directly coupled to the thermal-hydraulics code TRACE, which provides to PARCS the material temperatures and coolant densities information. After each defined time step, PARCS re-calculates the macroscopic cross-sections and then sends the resulting power distribution back to TRACE.

PARCS can predict reactor behavior under both steady state and transient conditions. In order to establish the initial steady state, an eigenvalue calculation has to be performed. PARCS obtains the eigenvalue using the Wielandt eigenvalue shift method, which adjust the ν value in the subsequent transient calculation to make the initial state critical. Under transient conditions (i.e. the primary function of PARCS), PARCS solves the time-dependent neutron diffusion equations involving both delayed and prompt neutrons. The temporal differencing is based on the exponential transform and theta method. At each time step, it yields a transient fixed source problem, which is solved by the nonlinear coarse-mesh finite difference (CMFD) method. This is a nodal method discretizing the core into coarse meshes. Typically, the mesh size is that of a fuel assembly.

A hexagonal-geometry core calculation has been implemented in PARCS, based on a higher order hexagonal nodal coupling kernel which utilizes the triangular polynomial expansion nodal (TPEN) method. The non-transverse-integrated TPEN method solves a 2D problem directly, rather than solving two coupled 1D problems in each plane as in the Cartesian nodal method. Effectively, the 3D problem is decoupled into a radial and an axial problem that are coupled through transverse-leakages. Radially, the 2D problem for each hexagon is solved by first splitting the hexagon into six triangles and then expanding the 2D flux solution for each triangle into a 2D third order polynomial.

In PARCS, the macroscopic cross-sections are used for creating the reference state, and their derivatives with respect to state variables (assuming a linear dependency of the different effects) are used for accounting for the reactivity feedbacks. Originally, PARCS was developed for LWR

^{2.1} SP3 stands for the third-order simplified spherical harmonics (P_N) approximation.

Chapter 2: Thesis Background

applications. In order to enable the fast-neutron-spectrum system analysis, its cross-section parameterization has been modified within the framework of PSI's FAST project [2.12]. More specifically, a different (logarithmic) dependence of the Doppler reactivity on the fuel temperature is functioned, the boron regulation is removed, and reactivity can be additionally influenced by control rod position, as well as core dimensions and effective fuel density change (through changes in neutron leakage). The 33 energy-group ERANOS/ECCO structure has mostly been used in the present study.

Eq. 2.7 represents the current procedure for re-calculating the macroscopic cross-sections in every calculational node during transients:

$$\begin{aligned} \Sigma(T_f, \rho_c, R, H, Z) = \Sigma_0 &+ \left[\frac{\partial \Sigma}{\partial \ln T_f} \right]_{T_{f_0}} (\ln T_f - \ln T_{f_0}) + \left[\frac{\partial \Sigma}{\partial \rho_c} \right]_{\rho_{c_0}} (\rho_c - \rho_{c_0}) \\ &+ \left[\frac{\partial \Sigma}{\partial R} \right]_{R_0} (R - R_0) + \left[\frac{\partial \Sigma}{\partial H} \right]_{H_0} (H - H_0) + \left[\frac{\partial \Sigma}{\partial Z} \right]_{Z_0} (Z - Z_0) \end{aligned} \quad \text{Eq. 2.7}$$

where Σ , T_f , ρ_c , R , H and Z represent the macroscopic cross-section, the fuel temperature, the coolant density, the average core radius, the average core height and the control rod position, respectively. The subscript 0 stands for the nominal state. As can be seen, linear dependence is considered in each case, except for the Doppler effect where a logarithmic dependency on the fuel temperature is assumed.

As indicated previously, the cell code ECCO is used to produce the self-shielded macroscopic cross-sections (as well as the scattering matrix) and their derivatives. The data format is converted from ECCO (ERANOS) output to PARCS input through an interface, viz. the in-house routine ERANOS2PARCS [2.24]. The complementary kinetics parameters, viz. the delayed neutron spectra, and the six-group delayed neutron fractions β_i and corresponding decay constants λ_i , are also provided by ERANOS.

Since for some transients, it is possible that reactivity feedbacks are not predicted with sufficient accuracy due to their strong interactions, a new cross-section generation model has recently been built into the FAST code system [2.25]. This is based on a background cross-section, or sigma-zero (σ_0), model [2.26]. The main idea behind this new model is that of preparing sets of microscopic instead of macroscopic cross-sections. At each time step of the transient simulation, a newly developed set of PARCS subroutines and input specifications enable one to explicitly calculate the average macroscopic cross-sections to be used by suitably interpolating microscopic cross-sections from the pre-generated tables. This method, however, is not used in the current doctoral work, since it has still not been validated for transients such as a ULOF in which sodium boiling is anticipated to occur.

TRACE code

TRACE (standing for TRAC/RELAP Advanced Computation Engine), formerly called TRAC-M, is the latest in a series of best-estimate reactor system codes developed by the U.S. Nuclear Regulatory Commission (NRC). The current version of TRACE combines the capabilities of the NRC's four main

system codes, viz. TRAC-P, TRAC-B, RELAP5 and RAMONA, into a single modernized computational tool [2.27]. TRACE has been designed to perform best-estimate analysis of loss-of-coolant accidents (LOCAs), operational transients and other accident scenarios in LWRs. It can also model phenomena occurring in experimental facilities designed to simulate transients in reactor systems. TRACE employs the models of multi-dimensional two-phase flow, non-equilibrium thermodynamics, generalized heat transfer, reflood, level tracking and reactor kinetics. The code also provides the functions of automatic steady state and restart.

For single-phase calculations, the classic three-equation hydrodynamics model is adopted in TRACE. The three conservation equations govern the balance of mass, momentum and energy, respectively [2.28], and they are:

$$\begin{aligned}
 1) \text{ Mass conservation equation} \quad & \frac{\partial \rho}{\partial t} + \nabla(\rho \vec{v}) = 0 \\
 2) \text{ Momentum conservation equation} \quad & \frac{\partial}{\partial t} \rho \vec{v} + \nabla(\rho \vec{v} \otimes \vec{v}) = \rho \vec{g} + \nabla \cdot \boldsymbol{\tau} - \nabla p \\
 3) \text{ Energy conservation equation} \quad & \frac{\partial}{\partial t} \rho u^0 + \nabla(\rho h^0 \vec{v}) = \rho \vec{g} \cdot \vec{v} + \nabla(\boldsymbol{\tau} \cdot \vec{v}) + q''' - \nabla \bar{q}''
 \end{aligned}$$

where ρ , \vec{v} , \vec{g} , $\boldsymbol{\tau}$, p , u^0 , h^0 , q''' and \bar{q}'' represent fluid density, fluid velocity, gravitational acceleration, tensor of viscous stresses, coolant pressure, coolant stagnation energy, coolant enthalpy, power density and heat flux, respectively. Certain closure laws have to be applied to the last two equations, viz. wall friction factor for momentum conservation and heat transfer coefficient for energy conservation.

The above described differential equations are solved using finite-volume numerical methods. The heat transfer equations are evaluated using a semi-implicit time-differencing technique. The fluid-dynamics equations in the spatial 1D, 2D and 3D components use a multi-step time-differencing procedure by default; a more straightforward semi-implicit time-differencing method is also available. The finite-difference equations for hydrodynamic phenomena form a system of coupled, nonlinear equations and are solved by the Newton-Raphson iteration method. The resulting linearized equations are solved by direct matrix inversion.

Steam-water two-phase flow is represented in TRACE by a non-equilibrium, non-homogeneous hydrodynamics model. Each phase is considered separately in terms of two sets of conservation equations. Thus, the basic volume- and time-averaged, two-phase, two-fluid model consists of six partial differential equations [2.29]. The jump conditions of the two phases are:

$$\begin{aligned}
 1) \text{ Mass exchange (vaporization)} \quad & \Gamma_v = -\Gamma_l \\
 2) \text{ Momentum exchange (friction)} \quad & \Gamma_v (\{v_v\}_j - \{v_l\}_i) + (\{\tau\}_{i,v} - \{\tau\}_{i,l}) \cdot P_i = 0 \\
 3) \text{ Energy exchange (heat exchange)} \quad & \Gamma_v (h_{i,v}^0 - h_{i,l}^0) = (\Phi_{i,v} + \Phi_{i,l}) \cdot a_i
 \end{aligned}$$

Chapter 2: Thesis Background

where Γ , P_i , Φ and a_i represent volumetric production, interface perimeter, heat flux and concentration of interfacial area, respectively. The subscripts v, l and i stand for vapor, liquid and interface of vapor and liquid, respectively.

As mentioned previously, TRACE was originally designed for LWR applications, considering light water as the main working fluid. Nevertheless, the TRACE database contains the physical properties of not only light water (liquid-gas), but also several other coolants, viz. heavy water (liquid-gas), sodium (liquid), lead-bismuth (liquid) and CO₂ (gas). Furthermore, a number of non-condensable gases are also included: air, hydrogen, helium, argon, nitrogen, xenon and krypton. In the context of this doctoral study, sodium is the main working fluid. However, only single phase flow is available in the original TRACE version, which is highly limiting for applications in which sodium boiling is anticipated.

Within the framework of an earlier EPFL doctoral thesis carried out at PSI [2.30], the TRACE code has been extended to enable sodium two-phase simulation. Appropriate closure relations, which represent the interfacial and wall-to-fluid transfer mechanisms specific to sodium coolant, have been implemented in the extended model. This two-phase flow model^{2.2} was benchmarked through a code-to-code comparison and the simulation of three relevant sets of experiments. SIMMER, a reference state-of-the-art code for the analysis of LMFR severe accidents, was selected for the code-to-code comparison. The three different sets of experiments chosen were: 1) pressure drop measurements in quasi steady state sodium boiling, 2) dryout measurements in quasi steady state sodium boiling and 3) sodium boiling experiments under loss-of-flow conditions. From the validation study carried out, it was possible to demonstrate that the implemented sodium two-phase flow model is capable of predicting, with satisfactory accuracy, boiling inception, void fraction, radial and axial expansion of the boiling region, pressure evolution, coolant and cladding temperature, etc. For the sake of completeness, the set of closure relations implemented in TRACE is summarized in Table 2.3 [2.30].

^{2.2} The implemented sodium two-phase flow model considers annular flow as the dominant regime from boiling onset up to dryout.

Table 2.3. Summary of the set of closure relations for sodium flow modeling, as currently implemented in TRACE [from 2.30].

Flow regime	Single-phase	Pre-dryout	Post-dryout
Void fraction (α)	$\alpha = 0$	$0 < \alpha < 0.957$	$\alpha \geq 0.957$
Flow quality (x)	$x = 0$	$0 < x < 0.3$	$x \geq 0.3$
<i>Interfacial closure-relations</i>			
Interfacial area (a_i)	-	$4 \frac{\sqrt{\alpha}}{D_h}$	$4 \frac{\sqrt{\alpha}}{D_h}$
Interfacial friction (f_i)	-	$a_i \frac{\rho_v}{2} (0.005(1 + 150(1 - \sqrt{\alpha})))$	$f_{i,pre-dryout} \left/ \left(\frac{1 - \alpha}{1 - 0.99} \right) \right.$
Interfacial-to-liquid heat transfer (h_{il})	-	$\frac{2\sigma}{2 - \sigma} \cdot \sqrt{\frac{M}{2\pi R}} \cdot \frac{h_{fg}^2 MP_s(T_l)}{RT_s^{2.5}}$	$h_{il,pre-dryout} \cdot \left(\frac{1 - \alpha}{1 - 0.99} \right)$
Interfacial-to-gas heat transfer (h_{iv})	-	10^8	10^8
<i>Wall-to-fluid closure-relations</i>			
Wall-to-liquid friction (f_{wl})	$8 \cdot \left(\left(\frac{8}{Re} \right)^{12} + \frac{1}{(a+b)^{1.5}} \right)^{1/12}$	$\phi_l^2 \cdot f_{wl,Single-phase}$	$Cf_{wl} \cdot f_{wl,pre-dryout}^*$
Wall-to-gas friction (f_{wv})	-	0	$(1 - Cf_{wl}) \cdot f_{wl,Single-phase}^*$
Wall-to-liquid heat transfer (h_{wl})	$0.047 \cdot \left(1 - e^{-3.8 \left(\frac{p}{D} \right)} \right) \cdot (Pe^{0.77} + 250) \cdot \frac{k_l}{D_h}$	$h_{wl,Single-phase}$	$Cf_{wl} \cdot h_{wl,pre-dryout}^*$
Wall-to-gas heat transfer (h_{wv})	-	0	$(1 - Cf_{wl}) \cdot 0.023 Re^{0.8} Pr^{0.4}^*$

* Fraction of liquid in contact with the wall: $Cf_{wl} = \left(\frac{0.9999 - \alpha}{1 - 0.957} \right)^{0.5} \cdot \left(\frac{1 - x}{1 - 0.3} \right)^{b_0}$

The motivation for the code extension has of course stemmed from the dominating SFR neutronics drawback referred to earlier, viz. positive sodium void reactivity. This renders it very important to be able to predict the strong interaction between sodium two-phase thermal-hydraulics and the core reactivity under transient conditions. On the one hand, the sodium void reactivity effect is largely dependent on sodium-flow phenomena, e.g. the onset of boiling, vapor generation, pressure drop change, etc. On the other hand, the power change caused by this reactivity effect has strong influence on the two-phase flow development.

TRACE takes a component-based approach to model a reactor system. Each physical piece of equipment in a flow loop can be represented in terms of certain components. Each component can be further nodalized into a number of cells over which the fluid, conduction and kinetics equations are averaged. In TRACE, there are a large number of different component types available so that a wide range of applications can be covered. In the TRACE modeling carried out currently (core region of the

primary circuit), it is only the following components which have been required: PIPE, FILL, BREAK, HTSTR (heat structure) and POWER. PIPE is a hydraulic component modeling the fluid flow in a 1D element. The inlet and outlet can be connected to FILL and BREAK, respectively. These apply the desired coolant-flow and pressure boundary conditions. HTSTR is a 2D element (cylindrical geometry in the case of the SFR fuel rod model) for modeling a component producing heat, and this is normally linked to a hydraulic component, e.g. a PIPE. The energy distribution in the core is specified with the POWER component.

The computational time for TRACE is highly problem dependent. It is a function of the total number of mesh cells, the maximum allowable time step size and the information exchange rate between the coupled neutronics and thermal-hydraulics. Furthermore, the two-phase flow simulation is much more time consuming than that of single phase. The stability-enhancing two-step (SETS) numerics in hydraulic components allows the material Courant limit to be exceeded. Thus, very large time steps can be used in slow transients, and this leads to a significant speedup (by one or two orders of magnitude) of the corresponding simulations.

FRED code

The thermal-mechanics code FRED, which is the last part of the FAST code system, has not been used in the current doctoral work. However, a short introduction is given here for the sake of completeness.

The FRED code is currently being developed for the thermal and mechanical simulation of FR and LWR fuel rod behavior under base-irradiation and accident conditions [2.31]. In the framework of the FAST code system, it has been coupled with TRACE as a subroutine [2.32]. At each time step, TRACE sends information to FRED in terms of axial power density distribution, cladding-coolant heat exchange coefficient, coolant temperature and coolant pressure for all simulated fuel pins. With these data, the current version of the code calculates the fuel rod temperature distribution, stress-strain conditions for the cladding, fuel deformation, fuel-cladding gap conductance and fuel rod inner pressure. At the same time, it sends back to TRACE the temperature distribution in the fuel pin, and the coupled transient simulation proceeds.

2.2.2 SERPENT

SERPENT is a 3D continuous-energy reactor physics burnup calculation code based on the Monte Carlo method [2.33]. It has been under development at the VTT Technical Research Centre in Finland since 2004. SERPENT is written in standard ANSI-C language and has been mainly developed for the Linux operating system. Originally, the main purpose of this code was to have a simplified Monte Carlo neutron transport method for group constant generation.

At the moment, the suggested applications of SERPENT include:

- generation of homogenized multi-group constants for deterministic reactor calculations,

Chapter 2: Thesis Background

- fuel cycle studies involving detailed assembly-level burnup calculation,
- validation of deterministic lattice transport codes,
- full-core reactor physics and burnup calculations for research reactors,
- educational purposes and demonstration of reactor physics phenomena.

SERPENT reads continuous-energy cross-sections from ACE-format data libraries based on JEF-2.2, JEFF-3.1, JEFF-3.1.1, ENDF/B-VI.8 and ENDFB/B-VII, then reconstructs them to a uniform lethargy-width energy grid. The nuclear data is available for 432 nuclides at six temperatures between 300K and 1800K. It should be noted that the data format is shared with the widely-used Los Alamos code MCNP, and any continuous-energy MCNP data library can be used with SERPENT as well.

SERPENT uses a universe-based geometry model (similar to MCNP and Keno-VI), which allows the description of practically any 2D or 3D fuel or reactor configuration. The geometry consists of material cells, defined by elementary and derived surface types. The SERPENT geometry routine for the neutron transport is based on a combination of conventional surface-to-surface ray-tracing and the Woodcock delta-tracking method [2.34], which has proven efficient and well suited for lattice calculations. The combination of two tracking methods overcomes the efficiency problems normally encountered with delta-tracking in the presence of localized heavy absorbers [2.35].

SERPENT has fully-automated, built-in depletion routines for burnup calculations. The transmutation cross-sections are calculated during the transport cycle and the decay/transmutation chains are then generated automatically.

In the current doctoral work, this Monte Carlo code is mainly used for providing code-to-code benchmark comparisons for the static neutronics calculations performed using the reference deterministic methodology of ERANOS, emphasis being placed on the sodium void effect evaluation. The comparisons have been carried out at both lattice/cell and full-core levels. SERPENT can generate homogenized group constants, and the predefined energy grid types include the 1968-group and 33-group structures used in ERANOS/ECCO. This feature enables the comparison of not only the multiplication factors and reactivity effects, but also the neutron spectrum and homogenized energy-group-wise cross-sections. Furthermore, the produced group constants include all input parameters needed for few-group nodal diffusion calculations, e.g. scattering matrices, effective delay neutron fractions, power distributions, point-kinetics parameters, etc. In the context of future applications of the FAST code system, SERPENT can thus be considered as an alternative code for providing neutronics data to TRACE (point-kinetics) and PARCS (3D-kinetics).

References

- [2.01] G. L. Fiorini and A. Vasile. European Commission – 7th Framework Programme The Collaborative Project on European Sodium Fast Reactor (CP ESFR). In ICAPP 2009, Paper 9064.
- [2.02] A. Vasile, G. L. Fiorini, Ph. Dufour, J.M. Bonnerot, Ch. Latgé. The Collaborative Project on European Sodium Fast Reactor (CP ESFR) European Commission – 7th Framework Programme. In ICAPP 2011, Paper 11297.
- [2.03] European Commission Work Programme 2008.
- [2.04] Safety of nuclear power plants: design - IAEA safety standards series n° NS-R-1, 2001.
- [2.05] Technical guidelines for the design and construction of the next generation of nuclear power plants with pressurized water reactors, 2004.
- [2.06] European utility requirements for LWR nuclear power plants. Revision C, 2001.
- [2.07] Safety objectives and design principles, CP-ESFR, deliverable SP3.1 D1, Revision 0, 2010.
- [2.08] INSAG 12 basic safety principles for nuclear power plants 75-INSAG-3 Revision 1, 1999.
- [2.09] CP-ESFR working horses – core concept definition, CP-ESFR, deliverable SP2.1 D1, Revision 0, 2009.
- [2.10] ESFR working horse pool concept description, CP-ESFR, deliverable SP4.1 D1, Revision 0, 2009.
- [2.11] Guidelines and recommendations of techniques and methods for the reduction of seismic vulnerability, CP-ESFR, deliverable SP3.2 D4, Revision 0, 2011.
- [2.12] K. Mikityuk, S. Pelloni, P. Coddington, E. Bubelis, R. Chawla. FAST: An advanced code system for fast reactor transient analysis. *Annals of Nuclear Energy*, vol. 32(15): pp. 1613-1631, 2005.
- [2.13] J. M. Ruggieri, J. Tommasi, J. F. Lebrat, C. Suteau, D. Plisson-Rieunier, C. De Saint Jean, G. Rimpault, J. C. Sublet. ERANOS 2.1: International Code System for GEN IV Fast Reactor Analysis. In ICAPP 2006, Paper 6360.
- [2.14] The JEFF-3.1 library: http://www.nea.fr/html/dbdata/projects/nds_jef.htm, the JEFF team.
- [2.15] J. Tommasi, P. Archier, J. M. Ruggieri. Validation of the sodium void reactivity effect prediction using JEFF-3.1 nuclear data. *Annals of Nuclear Energy*, vol. 37(11): pp. 1534-1553, 2010.

Chapter 2: Thesis Background

- [2.16] F. Giust. Methods of steady-state nuclear reactor calculations. Lecture in “Special topics in reactor physics”, ETH Zurich, Switzerland, 2009.
- [2.17] G. Rimpault. Physics documentation of ERANOS: the ECCO cell code. Technical report, RT–SPRC–LEP–97–001, CEA, France.
- [2.18] G. Palmiotti et al. VARIANT: Variational anisotropic nodal transport for multi-dimensional Cartesian and hexagonal geometry calculations. Technical report, ANL-95/40, Argonne National Laboratory, 2005.
- [2.19] J. Y. Doriath. ERANOS manuel des méthodes – les calculs d’évolution. Technical report, NT–SPRC–LEPH–96–204, CEA, France.
- [2.20] J. Krepel, S. Pelloni, K. Mikityuk, P. Coddington. EQL3D: ERANOS based equilibrium fuel cycle procedure for fast reactors. *Annals of Nuclear Energy*, vol. 36(5): pp. 550-561, 2009.
- [2.21] M. Salvatores. Principles and challenges for future fast reactor designs. Lecture at Frédéric Joliot / Otto Hahn Summer School, Karlsruhe, Germany, 2009.
- [2.22] S. Pelloni, J. Krepel, K. Mikityuk. EQL3D: methodology for simulation of equilibrium cycle for advanced fast reactors. In *PHYSOR 2008*, paper log402.
- [2.23] T. Downar et al. PARCS v2.7 U.S. NRC core neutronics simulator: user manual. Purdue University, August, 2006.
- [2.24] E. Bubelis et al. Enhancement of the PARCS, TRAC/AAA and ERANOS codes for use within the FAST code system. Technical report. TM-41-05-21, Paul Scherrer Institut, 2005.
- [2.25] S. Pelloni and K. Mikityuk. A new cross-section generation model in the FAST code system and its application to gas- and sodium-cooled Generation-IV fast reactors. *Annals of Nuclear Energy*, vol. 38(1): pp. 1-13, 2011.
- [2.26] R. E. MacFarlane et al. The background cross-section method as a general tool for reactor analysis. Technical report. LA-UR-78-1004, Los Alamos National Laboratory, USA, 1978.
- [2.27] F. Odar et al. TRACE V5.0 USER’S MANUAL. U.S. Nuclear Regulatory Commission, Office of Nuclear Regulatory Research, 2006.
- [2.28] E. Royer. Thermal hydraulics of LWRs – basic module. INSTN course, Saclay, France.
- [2.29] J. W. Spore et al. TRAC-M/FORTRAN 90 (version 3.0) Theory Manual. LA-UR-00-910, Los Alamos National Laboratory, USA, 2000.
- [2.30] A. Chenu. Single- and two-phase flow modeling for coupled neutronics / thermal-hydraulics transient analysis of advanced sodium-cooled fast reactors. Swiss Federal Institute of Technology Lausanne (EPFL) doctoral thesis, 2011. N° 5172.

Chapter 2: Thesis Background

- [2.31] K. Mikityuk and A. Shestopalov. FRED fuel behavior code: main models and analysis of Halden IFA-503.2 tests. *Nuclear Engineering and Design*. Vol. 241(7): pp. 2455-2461, 2011.
- [2.32] P. Petkevich. Development and application of an advanced fuel model for the safety analysis of the Generation IV gas-cooled fast reactor. Swiss Federal Institute of Technology Lausanne (EPFL) doctoral thesis, 2008. N° 4180.
- [2.33] J. Leppänen. PSG2/Serpent – a continuous-energy Monte Carlo reactor physics burnup calculation code (user's manual). Version September 5, 2011.
- [2.34] E. R. Woodcock. Techniques used in the GEM code for Monte Carlo neutronics calculations in reactors and other systems of complex geometry. Technical report, ANL-7050, Argonne National Laboratory, USA, 1965.
- [2.35] J. Leppänen. Performance of Woodcock delta-tracking in lattice physics applications using the SERPENT Monte Carlo reactor physics burnup calculation code. *Annals of Nuclear Energy*, vol. 37: pp. 715-722, 2010.

Chapter 3

Void Reactivity Decomposition and Analysis

The main focus of the current chapter is to achieve a clear understanding of the principal phenomena contributing to the SFR void effect. Decomposition and analysis of sodium void reactivity have been carried out, emphasis being placed on the equilibrium closed fuel cycle. At first, a verification of the deterministic code ERANOS has been carried out against a Monte Carlo code, viz. SERPENT (Section 3.1). The evolution of nominal reactivity and fuel composition, while approaching open and closed equilibrium fuel cycle conditions for the ESFR core, is presented in Section 3.2. Void reactivity values for different fuel cycle states are also given. In Section 3.3, the spatial distribution of void reactivity importance is presented, in terms of both axial and radial directions. In this context, the possible additivity of the spatial void importance is investigated.

Section 3.4 introduces reactivity decomposition methods. These are based on either neutron balance considerations or on perturbation theory, the former approach being the one taken principally in the current research. Effectively, a neutron balance based method for void effect decomposition allows an in-depth understanding of the “consequences” of sodium voidage, while a perturbation theory based method provides a complementary understanding of the “causes”. The ESFR sodium void reactivity has been decomposed reaction-wise, cross-section-wise, isotope-wise and energy-group-wise, the results being detailed in Section 3.5. Finally, a chapter summary is given in Section 3.6.

It should be mentioned that, for most of the simulations presented in this chapter, the ESFR control rods have been assumed to be located at the upper parking position. For the complementary studies using the perturbation theory based method and the corresponding sensitivity analysis, the control rods were inserted 20 cm into the active core in order to make it critical. Furthermore, it should be noted that the voiding of the entire active core (both inner and outer fuel zones) is effectively the most conservative case, i.e. that with the highest void reactivity. Accordingly, this is the voiding scenario which has currently been selected as reference for the detailed void reactivity decomposition studies carried out.

3.1 Verification of ERANOS calculations against SERPENT

As mentioned in Subsection 2.2.1, the deterministic code system ERANOS is generally adopted in this doctoral study for the steady state neutronic calculations. The constituent data libraries, individual codes and calculation procedures have been developed and validated within the European

collaboration on fast reactors over the past 20 years. In particular, ERANOS was initially developed for sodium-cooled fast reactor systems operating with MOX fuel, so that it can be considered quite appropriate as computational tool for the current ESFR-related research. Nevertheless, a validation study for the ERANOS calculations – particularly in the context of the void reactivity – is clearly desirable. This can be achieved, to a significant extent, via comparisons with a reference neutronic analysis methodology, and the Monte Carlo code SERPENT (see Section 2.2.2) has currently been selected for the purpose.

The same basic nuclear data, viz. JEFF-3.1, have been used in ERANOS and SERPENT for the benchmark calculations. The average material compositions of the fuel pellets, cladding, assembly wrapper, coolant, control rod, reflector, etc. are completely consistent in the models used with the two codes. However, ERANOS has a heterogeneous description for the fuel assembly only (homogeneous descriptions for the rest), whereas SERPENT simulates all the components heterogeneously. The resulting comparison has been carried out on two different scales: 1) at the cell level and 2) at the full reactor core level. For the cell/lattice calculation, both codes select reflective boundary condition (i.e. infinite lattice) and switch off the B1-method option (buckling search for $k_{eff} = 1$). In ERANOS, the reference computational route is adopted, viz. treatment of the heterogeneous cell geometry using collision probabilities and applying the subgroup method in the fine energy-group structure.

Table 3.1. Comparison of SERPENT and ERANOS results for the ESFR core – in terms of multiplication factor, void reactivity and Doppler constant – at both cell and full-core levels.

Cell level benchmark	SERPENT	ECCO/ERANOS	Difference
Inner fuel k_{inf} (1500K)	1.11237 ± 0.00004	1.10767	470 ± 4 pcm
$\Delta\rho_v$ (90% voided)	2736 ± 6 pcm	2667 pcm	69 ± 6 pcm
DC (1500K→900K)	-1219 ± 11 pcm	-1322 pcm	103 ± 11 pcm
Outer fuel k_{inf} (1500K)	1.20836 ± 0.00004	1.20319	517 ± 4 pcm
$\Delta\rho_v$ (90% voided)	2559 ± 6 pcm	2508 pcm	51 ± 6 pcm
DC (1500K→900K)	-956 ± 11 pcm	-1020 pcm	64 ± 11 pcm
Full-core benchmark	SERPENT	ERANOS	Difference
k_{eff} (1500K)	1.01397 ± 0.00005	1.01006	391 ± 5 pcm
$\Delta\rho_v$ (90% voided)	1486 ± 7 pcm	1505 pcm	-19 ± 7 pcm
DC (1500K→900K)	-1284 ± 14 pcm	-1329 pcm	45 ± 14 pcm

Table 3.1 shows the comparative results in terms of multiplication factor (i.e. k_{inf} and/or k_{eff}), void reactivity ($\Delta\rho_v$) and Doppler constant (DC). As can be seen, SERPENT obtains higher multiplication factor values than ERANOS at both cell and full core levels, the difference being found to be around 400 pcm ($1 \text{ pcm} = 10^{-5}$). This discrepancy may be largely attributed to using different treatments of the unresolved resonance region. In this region, ECCO derives effective cross-sections through computing self-shielding factors using the narrow resonance approximation, whereas SERPENT employs

probability distributions for the total cross-section along with the corresponding elastic, fission, and capture cross-section distributions. A very relevant study [3.01] has shown that the different unresolved resonance data treatments in Monte Carlo and deterministic codes can, in certain situations, yield discrepancies in multiplication factor of more than 1000 pcm. Thus, the current observed differences seem to be acceptable. Some further discussion on this topic is provided in Appendix A. It is important to note here, however, that – even though the multiplication factors computed by SERPENT and ERANOS differ significantly – the results obtained for reactivity effects, e.g. $\Delta\rho_v$ and DC, show very good agreement (differences of less than ~105 pcm). This observation provides convincing justification for assuming that ERANOS is capable of predicting the principal safety parameters considered in this doctoral research with adequate accuracy.

Further ERANOS-to-SERPENT comparisons can be found in Appendix A. The results considered thereby include not only the multiplication factors and reactivity effects, but also the neutron spectra and group constants (viz. macroscopic fission and capture cross-sections, etc.).

3.2 Selected fuel cycle states for the ESFR core

3.2.1 Evolution towards open and closed equilibrium fuel cycle conditions

The long-term operation of the SFR core in a closed fuel cycle will lead to an equilibrium state, where both reactivity (or k_{eff}) and fuel mass flow stabilize. This assumes constant periodic fuel treatment. Similarly, equilibrium can be obtained also for open (once-through) cycle operation. The present void reactivity study focuses not only on the beginning-of-life (BOL) condition of the SFR core, but also on the beginning of open and closed equilibrium (BOC and BEC, respectively) fuel cycle states. Several investigations of the sodium void effect can be found in the open literature for BOL or, at most, BOC conditions. Emphasis has accordingly been placed here on analyzing also the BEC state.

Equilibrium conditions for the SFR core can be obtained using the PSI procedure EQL3D, which allows the description of two basic situations, viz. 1) the equilibrium of an open fuel cycle (the result of periodic fresh fuel introduction without any recycling), and 2) the equilibrium of a closed fuel cycle (the asymptotic state of the reactor with a fixed fuel management scheme involving recycling of its own fuel). A brief description of the EQL3D procedure is given in Subsection 2.2.1, more details being available in [3.02].

It should be mentioned here that the original core design (see Subsection 2.1.3) with 453 fuel assemblies (225 inner / 228 outer) was modified to enable the subdivision into five batches (see Figure 3.1a). The modified core has three assemblies less in the outer fuel zone. The equilibrium closed fuel cycle was calculated for the design of a specific five-batch cycle. The assemblies were divided into ten groups, as shown in Figure 3.1b, viz. five for the inner zone and five for the outer zone (5×45 / 5×45). This reloading pattern was adopted from [3.03].

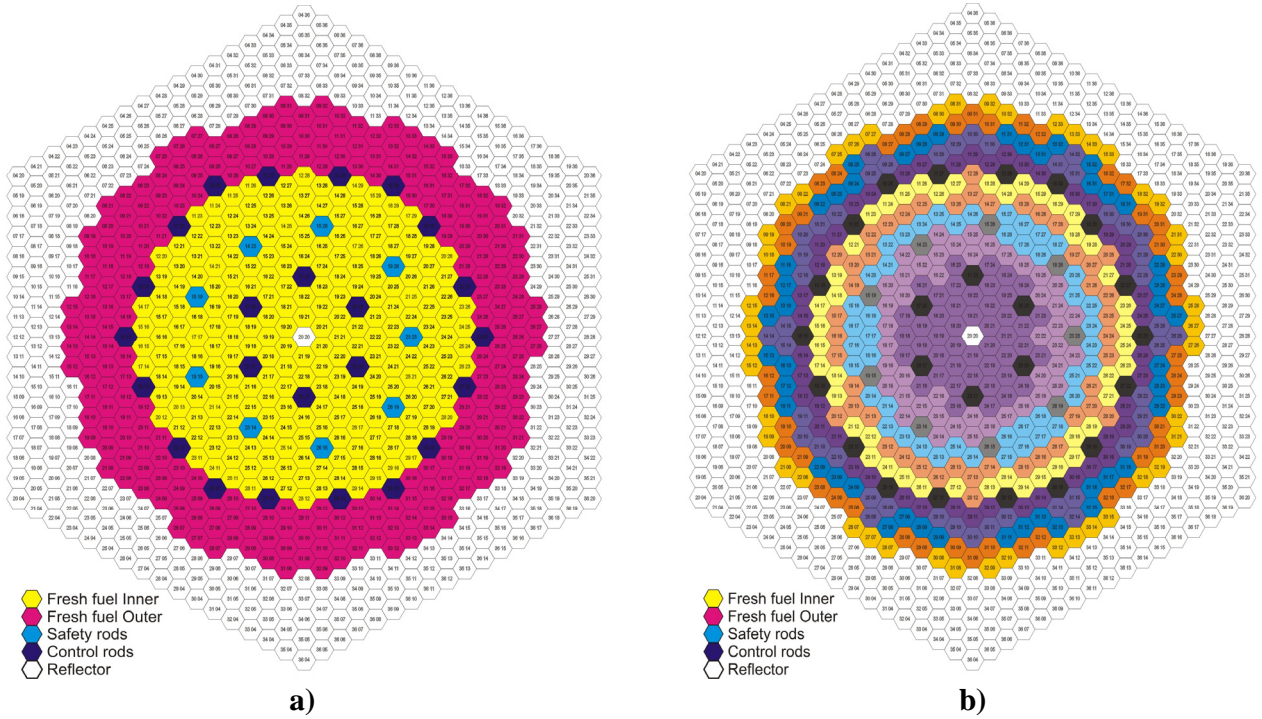


Figure 3.1. Horizontal cross-sections of a) the modified core design with 450 assemblies and b) the five-batch reloading pattern.

The evolutions of k_{eff} towards open and closed equilibrium fuel cycle conditions are presented in Figure 3.2. The equilibrium state can be clearly distinguished once the k_{eff} variation between two successive fuel cycles remains constant. Thus, for the open fuel cycle, the equilibrium is reached within less than 10 Equivalent Full-power years (EFPY), whereas the period required for the closed fuel cycle is more than 40 EFPY. Although the approach paths for reaching equilibrium are interesting and could be discussed in greater detail, the main objective currently is to compare the reactivity level at each of the considered fuel cycle states. Thus, it is seen that the BOL and BOC reactivities are quite comparable, the observed difference being a few hundreds of pcm. On the other hand, the BEC reactivity is higher by more than 4000 pcm. This increased nominal reactivity is caused by the higher plutonium content in the equilibrium closed fuel cycle, which is related to the core's breeding capability.

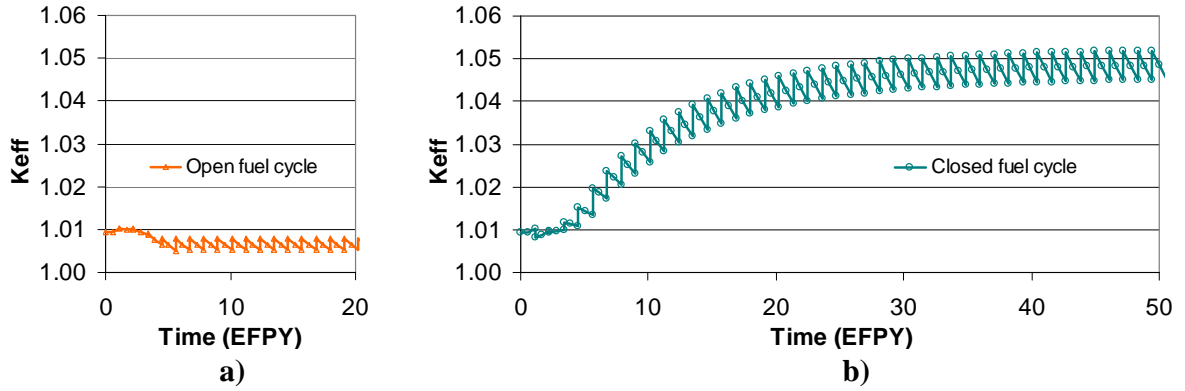


Figure 3.2. Evolutions of the nominal ESFR core k_{eff} towards a) open and b) closed equilibrium fuel cycles. EFY represents Equivalent Full-Power Years.

Later in this chapter and in Chapter 5, respectively, the spatial distribution of the void importance and the spatial propagation of sodium boiling are discussed. These features are strongly correlated to the neutron flux distribution (and/or the power map), which is considerably different for the different fuel cycle states. In this context, the neutron flux distributions at BOL, BOC and BEC are shown in Figure 3.3. As can be seen, the flux is suppressed in the inner fuel zone at BOL, since the initial plutonium content in this region is relatively low in comparison to that in the outer fuel zone. When the equilibrium state (either for the open or the closed fuel cycle) is reached, more plutonium has been generated at the core center, and at the same time, deeper burnup levels have been achieved in the outer core region. The reactor cores in equilibrium states thus have a more uniform plutonium distribution. This results in significantly changed radial flux distributions at BOC and BEC, viz. with a relatively flat plateau in the central region and monotonic reduction towards the core periphery.

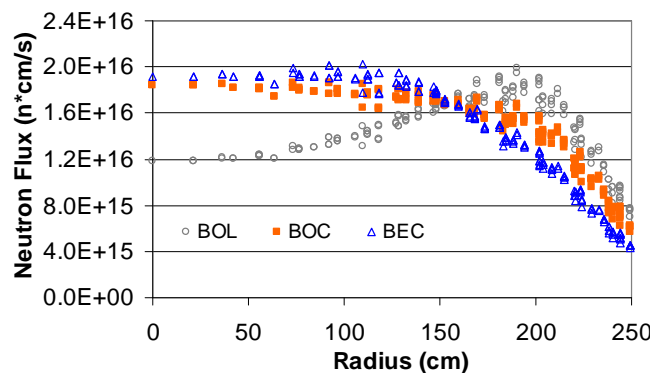


Figure 3.3. Comparison of radial flux distributions of fuel-assembly integrated values at BOL, BOC and BEC, respectively.

3.2.2 Void reactivity at different fuel cycle states

The evolution of the sodium void reactivity, i.e. of the difference between the reactivities of the nominal and voided cores, is shown in Figure 3.4. It is seen that the BOL void reactivity is lower than the BOC and BEC values, which are close to each other.

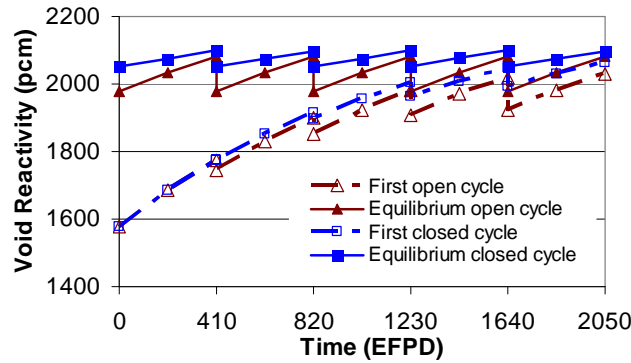


Figure 3.4. Evolutions of the sodium void reactivity during the first and the equilibrium (open and closed) fuel cycles. EFPD represents Equivalent Full-Power Days.

Table 3.2 gives the values of the void reactivity ($\Delta\rho_v$) for different fuel cycle states together with the corresponding global fuel composition in terms of uranium (U), plutonium (Pu), minor actinide (MA) and fission product (FP) masses. One can see an increase of plutonium mass from BOL to BOC, and then further to BEC, which results in correspondingly higher nominal reactivity. Furthermore, the void reactivity increases from 1578 pcm at BOL to 1978 pcm at BOC, and then further to 2050 pcm at BEC. These differences will be analyzed and explained later in Section 3.4.

Table 3.2. Void reactivity and global fuel composition for five selected fuel cycle states.

Fuel cycle state	$\Delta\rho_v$ (pcm)	U (t)	Pu (t)	MA (t)	FP (t)	Sum (t)
Beginning of life (BOL)	1578	61.98	11.54	0.09	0.00	73.61
Beginning of equilibrium open cycle (BOC)	1978	58.83	11.78	0.24	2.76	73.61
End of equilibrium open cycle (EOC)	2081	57.21	11.85	0.30	4.25	73.61
Beginning of equilibrium closed cycle (BEC)	2050	57.82	12.42	0.63	2.74	73.61
End of equilibrium closed cycle (EEC)	2099	56.32	12.43	0.61	4.25	73.61

The void reactivity analysis for the BEC state is a principal goal in the current chapter. Comparisons with BOL and BOC are also made for the various results, obtained applying both the neutron balance and perturbation theory based methods for reactivity decomposition.

3.3 Spatial distribution of void reactivity importance

There are several possible scenarios for considering the coolant voiding in the SFR core, i.e. the specific core regions assumed to have been voided in a given situation. Local voiding scenarios, either node- or assembly-wise, can help to understand the spatial distribution of the void reactivity importance, as also to investigate the possible additivity of the effects of individual voided volumes and/or their correlation with flux worth, i.e. with the product of flux and adjoint flux.

Via step-by-step, assembly- or node-wise local voiding, radial and axial void reactivity importance maps have been created. The radial distribution, in terms of axially integrated assembly-wise values, is presented in Figure 3.5, where one third of the symmetrical core is shown. The manner in which assembly- and node-wise voiding has been considered, and the corresponding map in terms of the spatial distribution of the node-wise void reactivity importance, are given for a central vertical cut of the core in Figure 3.6. It should be noted that BEC is considered as the reference fuel cycle state in this section.

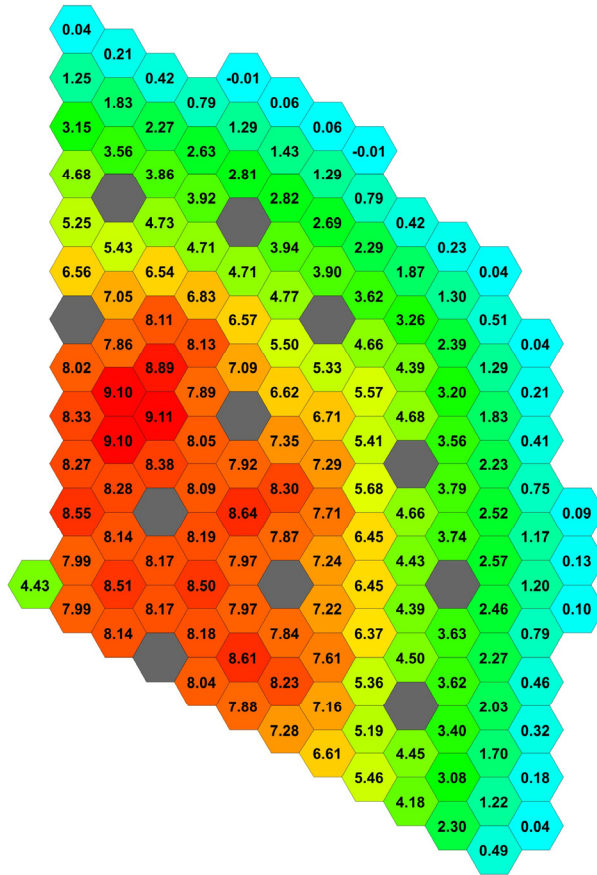


Figure 3.5. Radial void reactivity importance map at BEC (units: pcm), created by step-by-step assembly-wise voiding. Results are shown for a third of the symmetrical core.

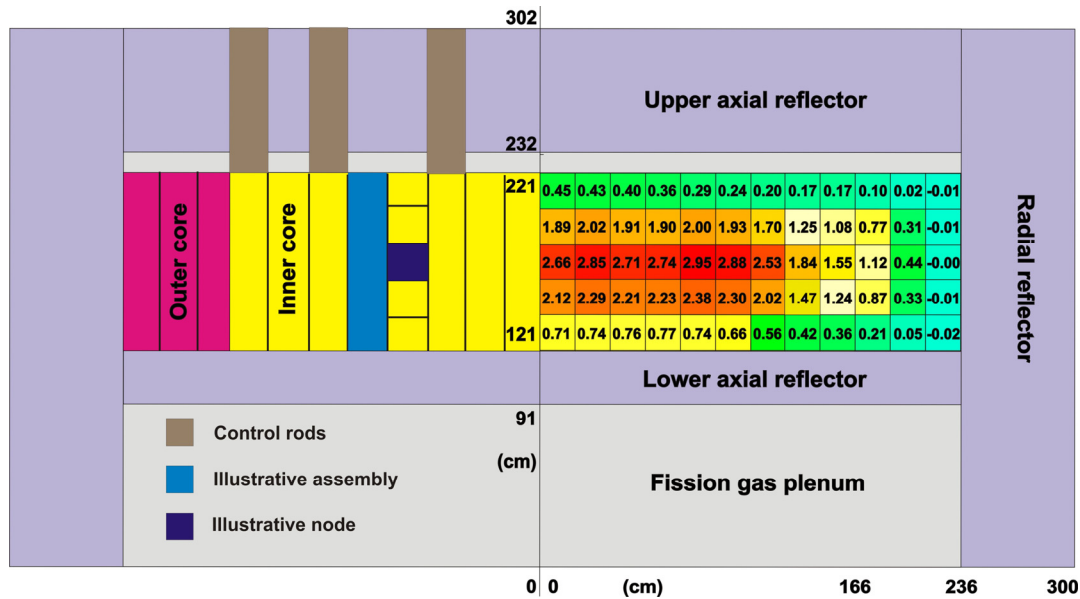


Figure 3.6. Void reactivity importance map at BEC (units: pcm), created by step-by-step node-wise voiding. Results for a central vertical cut of the core are given on the right, the left-hand side of the figure showing a schematic of the modeling carried out.

The two maps clearly show that high void worths occur at the center of the active core, with much lower values at the core periphery. The fact that the local void reactivity importance is strongly correlated with the neutron flux worth (product of flux and adjoint flux) distribution is confirmed by Figure 3.7. This compares the radial assembly-wise distributions of the flux worth and of the void reactivity importance, local values being expressed, in each case, relative to the average value over the volume of the active core (the regions containing fuel).

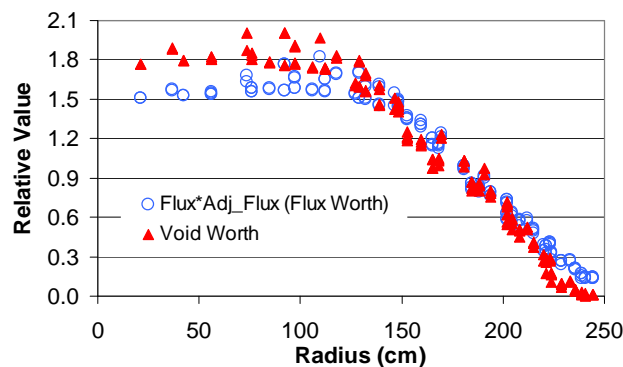


Figure 3.7. Radial assembly-wise correlation of flux worth and void reactivity importance at BEC.

Clearly, a check on the additivity of the local void worths is of considerable interest. The reference voiding scenario, viz. voiding of the complete active core (435 fuel assemblies and 2175 calculational nodes), has been considered for the purpose. The results are presented in Table 3.3. As can be seen, the sum of assembly-wise void reactivity values is practically identical to the reference void reactivity, i.e. voiding of the active core. The difference is only 10 pcm. Also, the sum of node-wise void reactivity worths is in relatively good agreement with the reference void reactivity. The difference of ~ 80 pcm is probably caused by the non-linear behavior of the leakage effects at the core periphery and/or numerical effects related to the perturbations caused by node-wise voiding.

Table 3.3. Additivity check for assembly- and node-wise voiding effects, with respect to voiding of the complete active core (i.e. the regions where fuel is present).

Voided volume	Active core	Assembly	Node
Number of volumes in active core	1	435	2175
Average void reactivity (pcm)	2050.2	4.69	0.91
Sum over active core (pcm)	2050.2	2040.0	1970.3

3.4 Reactivity decomposition methods

The neutron balance method [3.04, 3.05] and the perturbation theory method [3.06, 3.07, 3.08] represent the two principal approaches one may adopt for reactivity decomposition. Both of these have been applied in the current doctoral work. From the basic definitions of these two methods, one sees that 1) the reactivity decomposition obtained by perturbation theory corresponds to the effects of individual reaction cross-sections and thus mainly provides an understanding of the causes of the void effect, while 2) the neutron balance method derives the reactivity components in terms of the changes in neutron productions and losses, and thus mainly provides an understanding of the consequences. The information obtained is thus different but strongly complementary.

Sensitivity analysis, based on the perturbation theory method, has also been carried out currently, the results serving to underline the isotopes which are the most important for the void effect. Moreover, it has been found that the sensitivity coefficients obtained in this context for the major neutron absorbing isotopes are, in relative terms, quite consistent with the isotope-wise results of the neutron balance based decomposition.

It should be noted that the numerical analysis for both neutron balance and perturbation theory based methods has been carried out using appropriate modules of the ERANOS code system. In all cases, the flux calculations were done for hexagonal-Z 3D geometry in 33 energy groups. The perturbation theory based method was applied with direct and adjoint flux solutions based on diffusion theory, the standard 3D approach within ERANOS, whereas the neutron balance based method employed a

transport-theory flux solution. For the sake of simplicity of the mathematical notation, a diffusion theory description is used below for both methods. Thus, the static diffusion equation for $G=33$ energy groups may be written as:

$$\begin{aligned}
 & -\nabla D(g, \vec{r}) \nabla \Phi(g, \vec{r}) + \Sigma_c(g, \vec{r}) \Phi(g, \vec{r}) + \Sigma_f(g, \vec{r}) \Phi(g, \vec{r}) + \\
 & + \Sigma_s(g, \vec{r}) \Phi(g, \vec{r}) = \sum_{g'=1}^{g-1} (\Sigma_{g' \rightarrow g}(\vec{r}) \Phi(g', \vec{r})) + \frac{1}{k_{eff}} \chi(g) \sum_{g'=1}^G (v_{g'} \Sigma_f(g', \vec{r}) \Phi(g', \vec{r}))
 \end{aligned} \quad \text{Eq. 3.1}$$

where the neutron flux Φ [n/cm²/s], diffusion coefficient D [cm] and macroscopic cross-sections for neutron capture Σ_c [1/cm], fission Σ_f [1/cm], scattering Σ_s [1/cm] and down scattering from higher energy groups $\Sigma_{g' \rightarrow g}$ [1/cm] are all functions of the energy group g (or g') and position \vec{r} . The steady state fission spectrum $\chi(g)$ being used in the ERANOS calculations is a function only of the energy group.

3.4.1 Neutron balance based method

As indicated above, the neutron balance based method for reactivity decomposition has been widely used in the past and has currently been adopted as the principal approach for in-depth analysis of the sodium void reactivity effect. The developments carried out have been described in [3.09], as well as in [3.10].

The method is based on consideration of the integral neutron reaction rates in the active core (AC). Eq. 3.1 is, in this case, summed over the energy groups and integrated over space. For a consistent definition of the leakage term, the active core, consisting of all fuel zones, has been considered as the reference volume. Accordingly, the neutron balance equation can be written as:

$$\begin{aligned}
 & - \int_{AC} \sum_{g=1}^G (\nabla D(g, \vec{r}) \nabla \Phi(g, \vec{r})) dV + \int_{AC} \sum_{g=1}^G (\Sigma_c(g, \vec{r}) \Phi(g, \vec{r})) dV + \int_{AC} \sum_{g=1}^G (\Sigma_f(g, \vec{r}) \Phi(g, \vec{r})) dV \\
 & = \frac{1}{k_{eff}} \int_{AC} \sum_{g=1}^G (v_g \Sigma_f(g, \vec{r}) \Phi(g, \vec{r})) dV
 \end{aligned} \quad \text{Eq. 3.2}$$

where the sum of two integrals from the scattering terms is zero and has thus been omitted. The first integral on the left-hand side of Eq. 3.2 represents the leakage from the active core (L). The second and third terms represent the capture (C) and fission (F) rates, respectively. (The absorption rate A is the sum of C and F). The integral on the right-hand side of the equation represents the production rate (P). All these reaction rates have units of 1/s and relate to the active core. It should be noted that the net leakage from the active core is equal to the absorption rate outside this reference volume (i.e. in the reflector, the control rods, etc.). Using the space-energy integral of the flux (with units of n-cm/s) over the active core:

$$\Phi_{AC} = \int_{AC} \sum_{g=1}^G \Phi(g, \vec{r}) dV, \quad \text{Eq. 3.3}$$

the one-group core-average cross-section (with units of 1/cm) can be expressed as:

$$\bar{\Sigma}_i = \frac{R_i}{\Phi_{AC}} \quad \text{Eq. 3.4}$$

R (as also the corresponding reaction index i) represents the selected reaction rate (L , C , F or P). Clearly, the one-group core-average cross-section can be understood as the average probability per centimeter for a neutron travelling in the active core to leave it forever (L), to be absorbed (C and F), or to produce new neutrons due to fission (P).

The neutron balance equation, i.e. Eq. 3.2, can be rewritten using the defined notation for the reaction rates. Replacing simultaneously k_{eff} by the reactivity ρ and considering it as a function of parameter x (e.g. sodium voidage, fuel temperature, etc.), one obtains:

$$\rho(x) = 1 - \frac{1}{k_{eff}(x)} = 1 - \frac{L(x) + C(x) + F(x)}{P(x)} \quad \text{Eq. 3.5}$$

It should be noted that the four reaction rates directly depend on the neutron flux (see Eq. 3.2), which can be broadly characterized by the following three parameters: amplitude, energy spectrum and spatial distribution. When one considers integration over the energy spectrum and the spatial distribution, i.e. normalizes to unity in each case, Φ_{AC} is simply equivalent to the amplitude. The latter, however, is an arbitrary constant, which effectively cancels out in Eq. 3.5. Thus, the four reaction rates may be considered as depending on the average spectrum and the spatial distribution, i.e. on the corresponding cross-sections, which, however, are also interdependent. For instance, the variation of the capture cross-section can change not only the capture rate, but also other cross-sections through the impact on the average spectrum and the spatial distribution. This, in a way, suggests a certain limitation of perturbation theory based decomposition, which seeks to quantify the effects of individual cross-sections. Differently, the neutron balance based method focuses on the consequence of the perturbation, which is represented by the impact on the reaction rates themselves.

By assuming the independency of the four reaction rates, i.e. by neglecting the mutual dependencies, e.g. $\partial C / \partial L$, the derivative of the reactivity ρ with respect to the parameter x can be written as:

$$\frac{d\rho}{dx} = \frac{\partial \rho}{\partial L} \frac{dL}{dx} + \frac{\partial \rho}{\partial C} \frac{dC}{dx} + \frac{\partial \rho}{\partial F} \frac{dF}{dx} + \frac{\partial \rho}{\partial P} \frac{dP}{dx} \quad \text{Eq. 3.6}$$

The increment $\Delta \rho$ from a nominal state x_0 to perturbed state x_1 can be expressed as the integral of Eq. 3.6, and the corresponding reaction-wise decomposition components can be derived as follows:

$$\begin{aligned}
 \Delta\rho &\equiv \rho(x_1) - \rho(x_0) = \int_{x_0}^{x_1} \frac{d\rho}{dx} dx = \int_{x_0}^{x_1} \frac{\partial\rho}{\partial L} \frac{dL}{dx} dx + \int_{x_0}^{x_1} \frac{\partial\rho}{\partial C} \frac{dC}{dx} dx + \int_{x_0}^{x_1} \frac{\partial\rho}{\partial F} \frac{dF}{dx} dx + \int_{x_0}^{x_1} \frac{\partial\rho}{\partial P} \frac{dP}{dx} dx \\
 &= \int_{x_0}^{x_1} -\frac{1}{P} \frac{dL}{dx} dx + \int_{x_0}^{x_1} -\frac{1}{P} \frac{dC}{dx} dx + \int_{x_0}^{x_1} -\frac{1}{P} \frac{dF}{dx} dx + \int_{x_0}^{x_1} \frac{1}{P \cdot k_{eff}} \frac{dP}{dx} dx \quad \text{Eq. 3.7} \\
 &= \Delta\rho_L + \Delta\rho_C + \Delta\rho_F + \Delta\rho_P
 \end{aligned}$$

For most perturbations, the exact courses of the functions $\frac{1}{P}$ and $\frac{1}{P \cdot k_{eff}}$ from state x_0 to x_1 are unknown. Although the exact values of the integrals cannot be derived without knowing the evolution paths, one can assume monotonic variations and no sign change of these functions, then the minimum and maximum estimates for each integral can be determined. The value of the integral can then be approximated by averaging the minimum and maximum estimates. In the present study, which is dedicated mainly to the void effect, the removal of sodium from the active core is considered as the perturbation. In this particular case, the variations of the functions $\frac{1}{P}$ and $\frac{1}{P \cdot k_{eff}}$ are of the type shown in Figure 3.8.

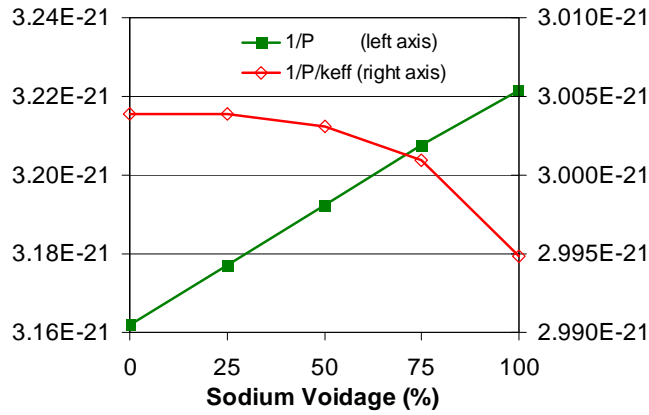


Figure 3.8. Dependence of considered functions on sodium voidage. The production rates P (units: n/s) correspond to the nominal core power.

According to the above monotonic behavior of these functions – from the nominal state x_0 to perturbed state x_1 (caused by the sodium voiding) – one can express the maximum and minimum estimates as:

$$\begin{aligned}
 \frac{1}{P_0} &\leq \frac{1}{P} (x \in \langle x_0, x_1 \rangle) \leq \frac{1}{P_1} \\
 \frac{1}{P_1 \cdot k_{eff1}} &\leq \frac{1}{P \cdot k_{eff}} (x \in \langle x_0, x_1 \rangle) \leq \frac{1}{P_0 \cdot k_{eff0}}
 \end{aligned} \quad \text{Eq. 3.8}$$

where P_0 , k_{eff0} and P_1 , k_{eff1} stand for the production rates and multiplication factors at x_0 and x_1 states, respectively. As the next step, the maximum and minimum estimates of the four reaction-wise components (corresponding to leakage, capture, fission and production) are derived as follows:

$$\begin{aligned}
 \Delta\rho_{L,\min} &= -\frac{L_1 - L_0}{P_0} \leq \Delta\rho_L = \int_{x_0}^{x_1} -\frac{1}{P} \frac{dL}{dx} dx \leq -\frac{L_1 - L_0}{P_1} = \Delta\rho_{L,\max} \\
 \Delta\rho_{C,\min} &= -\frac{C_1 - C_0}{P_0} \leq \Delta\rho_C = \int_{x_0}^{x_1} -\frac{1}{P} \frac{dC}{dx} dx \leq -\frac{C_1 - C_0}{P_1} = \Delta\rho_{C,\max} \\
 \Delta\rho_{F,\min} &= -\frac{F_1 - F_0}{P_0} \leq \Delta\rho_F = \int_{x_0}^{x_1} -\frac{1}{P} \frac{dF}{dx} dx \leq -\frac{F_1 - F_0}{P_1} = \Delta\rho_{F,\max} \\
 \Delta\rho_{P,\min} &= \frac{P_1 - P_0}{P_1 \cdot k_{eff1}} \leq \Delta\rho_P = \int_{x_0}^{x_1} \frac{1}{P \cdot k_{eff}} \frac{dP}{dx} dx \leq \frac{P_1 - P_0}{P_0 \cdot k_{eff0}} = \Delta\rho_{P,\max}
 \end{aligned}
 \tag{Eq. 3.9}$$

Finally, the values of the four reaction-wise components can be approximated by averaging the maximum and minimum estimates:

$$\begin{aligned}
 \Delta\rho_L &= \frac{1}{2}(\Delta\rho_{L,\max} + \Delta\rho_{L,\min}) = -\frac{1}{2}\left(\frac{1}{P_0} + \frac{1}{P_1}\right) \cdot \Delta L \\
 \Delta\rho_C &= \frac{1}{2}(\Delta\rho_{C,\max} + \Delta\rho_{C,\min}) = -\frac{1}{2}\left(\frac{1}{P_0} + \frac{1}{P_1}\right) \cdot \Delta C \\
 \Delta\rho_F &= \frac{1}{2}(\Delta\rho_{F,\max} + \Delta\rho_{F,\min}) = -\frac{1}{2}\left(\frac{1}{P_0} + \frac{1}{P_1}\right) \cdot \Delta F \\
 \Delta\rho_P &= \frac{1}{2}(\Delta\rho_{P,\max} + \Delta\rho_{P,\min}) = \frac{1}{2}\left(\frac{1}{P_0 \cdot k_{eff0}} + \frac{1}{P_1 \cdot k_{eff1}}\right) \cdot \Delta P
 \end{aligned}
 \tag{Eq. 3.10}$$

The reaction rates used for the void reactivity decomposition have been obtained using the ERANOS neutron balance module. As already mentioned, the nominal and perturbed state reaction rates need to be correctly normalized to ensure consistency in the decomposition. Often the normalization used is that to the neutron production rate. This, however, effectively corresponds to the same power level in the nominal and perturbed states, and in this case, the production component automatically gets set to zero. An alternative approach is to normalize both cases to the integral flux. The two different normalizations can be expressed in terms of the integral flux (Eq. 3.3) and the one-group core-average cross-section (Eq. 3.4) as follows:

$$\begin{aligned}
 \text{normalization to the production rate : } & v_0 \bar{\Sigma}_{f,0} \Phi_{AC,0} = v_1 \bar{\Sigma}_{f,1} \Phi_{AC,1} \\
 \text{normalization to the integral flux : } & \Phi_{AC,0} = \Phi_{AC,1}
 \end{aligned}
 \tag{Eq. 3.11}$$

Both these approaches have been tried currently. However, the constant integral flux normalization has been found preferable, because, as will be shown later, it reflects the changes of all effective one-group cross-sections (which are independent of the normalization approach).

The decomposition given by Eq. 3.10 can be called reaction-wise. However, the reaction rates can be further divided into contributions of individual isotopes or energy groups. For the capture rate term, for example, the corresponding void reactivity components can be expressed by the following two equations:

$$\begin{aligned}\Delta\rho_c &= -\frac{1}{2}\left(\frac{1}{P_0} + \frac{1}{P_1}\right)\Delta C = -\frac{1}{2}\left(\frac{1}{P_0} + \frac{1}{P_1}\right) \cdot (\Delta C_{\text{U238}} + \Delta C_{\text{Pu239}} + \dots + \Delta C_{\text{Na23}}) \\ \Delta\rho_c &= -\frac{1}{2}\left(\frac{1}{P_0} + \frac{1}{P_1}\right)\Delta C = -\frac{1}{2}\left(\frac{1}{P_0} + \frac{1}{P_1}\right) \cdot (\Delta C_{g1} + \Delta C_{g2} + \dots + \Delta C_{gG})\end{aligned}\tag{Eq. 3.12}$$

where $g1, g2, \dots, gG$ represent the individual energy groups. It may be noted that the ERANOS output options would in principle also allow combined isotope- and group-wise decomposition. Although not generally applied in this doctoral work, such an analysis of individual reaction rate contributions has been carried out in one particular instance, viz. in the next chapter while interpreting the strongly deteriorated breeding gain due to inserted moderator pins.

Clearly, the above presented neutron balance based decomposition method may in general be applied to any given reactivity change. However, it is always important to assess the assumption of monotonic variation beforehand, this being one of the necessary conditions. Finally, it needs to be kept in mind that the neutron balance based decomposition method yields results in terms of the consequences of a certain parametric change, but does not analyze the causes and/or as the sensitivity to individual variables.

3.4.2 Perturbation theory based method and sensitivity coefficients

Perturbation theory can provide complementary information and, as such, is also widely used to decompose reactivity [3.06, 3.07, 3.08]. It requires direct and adjoint flux calculations, and can be used to quantify the sensitivity of a multivariable function to the individual variables. To express the reactivity change introduced by a perturbation, Eq. 3.1 will be firstly simplified by introducing two operators:

$$A(g, r)\Phi(g, r) = \frac{1}{k_{eff}} F(g, r)\Phi(g, r)\tag{Eq. 3.13}$$

where operator A includes all terms on the left-hand side of Eq. 3.1 and the first term on the right-hand side, whereas F is the neutron production operator. Using this nomenclature and omitting the labeling for energy and space dependencies, the reactivity change can be expressed, based on generalized perturbation theory, as follows:

$$\delta\rho = \frac{\int_V \sum_{g=1}^G ((k_T^{-1} \delta F \Phi_T + \delta A \Phi_T) \Phi^+) dV}{\int_V \sum_{g=1}^G (F \Phi_T \Phi^+) dV} = \delta\rho_L + \delta\rho_P + \delta\rho_C + \delta\rho_F + \delta\rho_S \quad \text{Eq. 3.14}$$

where Φ^+ is the adjoint nominal flux and Φ_T is the direct perturbed flux. k_T represents the multiplication factor in the perturbed state. The partial components for leakage $\delta\rho_L$, production $\delta\rho_P$, capture $\delta\rho_C$, fission $\delta\rho_F$ and scattering $\delta\rho_S$ can be obtained by inserting the expression for A from Eq. 3.1 and splitting the integrals into the partial terms. The last four mentioned components relate to perturbation of the corresponding cross-sections in Eq. 3.1.

The application of perturbation theory for assessing the sensitivity of the reactivity effect to individual cross-sections has been done with respect to isotope-specific reactions. Thus, the group dependent sensitivity coefficients of the reactivity effect $S_{ing}(\Delta\rho)$ have been evaluated for a selected reaction type i for an isotope n in an energy group g , according to:

$$S_{ing}(\Delta\rho) = \frac{\delta(\Delta\rho)}{\Delta\rho} \bigg/ \frac{\delta\sigma_{ing}}{\sigma_{ing}} \quad \text{Eq. 3.15}$$

where $\delta(\Delta\rho)$ represents the impact of a variation of the selected cross-section σ_{ing} on the reactivity effect $\Delta\rho$. As discussed later, the void effect sensitivity coefficients obtained in this context for the major neutron absorbing isotopes have been found to be qualitatively consistent with the isotope-wise results of the neutron balance based decomposition.

3.5 Void reactivity decomposition

The major objective of this chapter is the decomposition of the sodium void reactivity using the neutron balance based method. Results obtained applying the perturbation theory based method, including the consideration of sensitivity coefficients, are presented as complementary information. The void reactivity decomposition has been carried out reaction-wise, cross-section-wise, isotope-wise and energy-group-wise. Furthermore, the differences between BOL, BOC and BEC states have been analyzed, with BEC representing the reference case.

3.5.1 Reaction-wise decomposition (neutron balance based method)

The void reactivity has been decomposed reaction-wise into the $\Delta\rho_L$, $\Delta\rho_C$, $\Delta\rho_F$ and $\Delta\rho_P$ components by means of the neutron balance based method using Eq. 3.10. Reaction rates integrated over the active core have been used for the nominal and voided states. For better understanding of the dependency of the reactions on the sodium density, several intermediate points have also been studied. The resulting curves for the integral reaction rates and for their changes at each step are shown for the

BEC state in Figure 3.9a and 3.9b, respectively, Thereby, each reaction rate value has been normalized to the same integral flux Φ_{AC} (see Eq. 3.3), corresponding to the nominal situation of 3600 MWth with 100% sodium density.

From Figure 3.9a, it is found that the dependency of the reaction rates on the sodium density is not strong. One can see from Figure 3.9b that the leakage rate shows the lowest variation and is increased in the voided core; the other three rates are decreased, with the capture rate showing the highest variation. The most important finding is that all reaction rates are almost linearly correlated to the sodium density.

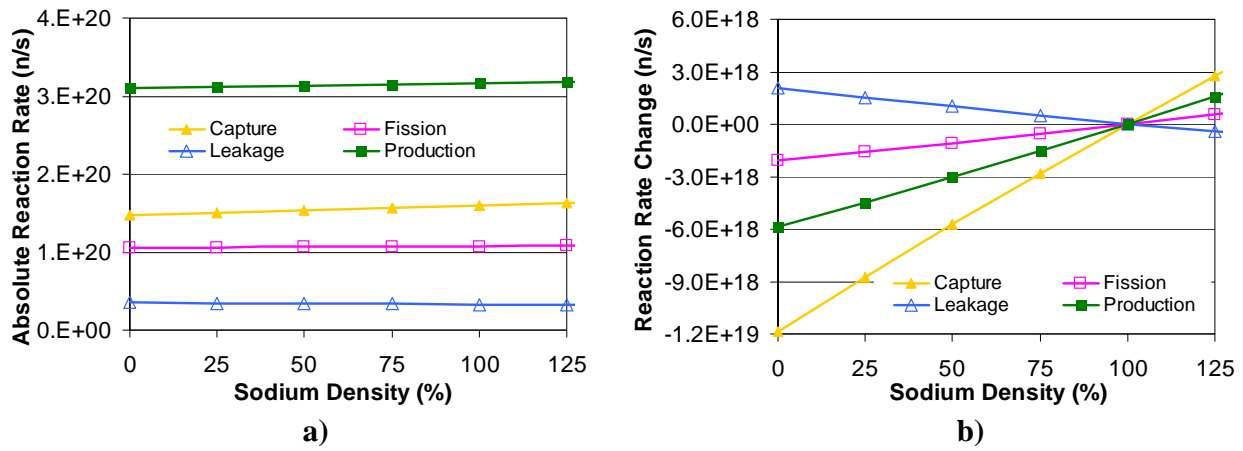


Figure 3.9. Dependence of a) integral reaction rates and b) their absolute changes on the sodium density for the BEC state.

Table 3.4 presents the reaction rates for the nominal (100% sodium density) and voided (almost 0% density) cores at BEC for the two different normalizations defined by Eq. 3.11. In addition, the table presents the one-group effective cross-sections, which are independent of the normalization. It is seen that the effective capture, fission and production cross-sections are all decreased in the voided core. The decrease of the fission and production cross-sections is not reflected by the reaction rates, if the calculation is normalized to production. On the other hand, in the case of normalization to the integral flux, the reaction rates show the appropriate changes for all four reactions (see the relative differences in Table 3.4). This clearly provides an important justification for choosing the latter normalization for all subsequent calculations.

For both the nominal and voided cores, there is about a 200 pcm difference for the reactivity result as obtained from the reaction rates using Eq. 3.5 and that derived directly from the ERANOS k_{eff} values. This is explained by the fact that the (n,2n) reaction rates are not available in the output of the ERANOS neutron balance module. Thus, the impact of (n,2n) reactions has been neglected in formulating Eq. 3.5. Differently, in the case of the directly derived ERANOS k_{eff} value, (n,2n) events

Chapter 3: Void Reactivity Decomposition and Analysis

are taken into account by considering them in terms of negative captures, which is roughly a 200 pcm influence on the nominal reactivity. Nevertheless, the excellent agreement between the two different void reactivity values shown in Table 3.4 clearly confirms that the impact on the sodium void effect of neglecting (n,2n) reactions is quite insignificant.

Table 3.4. Reaction rates (with different normalizations) and one-group effective cross-sections for the nominal and voided core at BEC.

BEC state	Nominal core			Voided core			Relative difference		
Variable	rate (s ⁻¹)	rate (s ⁻¹)	$\bar{\Sigma}_X$ (cm ⁻¹)	rate (s ⁻¹)	rate (s ⁻¹)	$\bar{\Sigma}_X$ (cm ⁻¹)	Δ (%)	Δ (%)	$\Delta \bar{\Sigma}_X$ (%)
Normalization to	Φ_{AC}	production	-	Φ_{AC}	production	-	Φ_{AC}	production	-
Production	3.16E+20 ¹	1000	8.04E-03	3.10E+20	1000	7.89E-03	-1.9	0.0	-1.9
Leakage	3.29E+19	104.1	8.37E-04	3.50E+19	112.7	8.89E-04	5.9	8.3	5.9
Capture	1.60E+20	505.4	4.06E-03	1.48E+20	476.7	3.76E-03	-8.0	-5.7	-8.0
Fission	1.08E+20	340.5	2.74E-03	1.06E+20	340.3	2.68E-03	-2.0	-0.1	-2.0
Φ_{AC} (n·cm/s)	3.94E+22	1.24E+05	-	3.94E+22	1.27E+05	-	0.0	2.4	-
ρ , Eq. 3.5 (pcm)	$\rho_N = 4994$			$\rho_V = 7039$			$\Delta\rho_V = 2045$		
ρ , ERANOS (pcm)	$\rho_N = 5182$			$\rho_V = 7232$			$\Delta\rho_V = 2050$		

¹ E+x is used for 10^x in certain tables and figures, e.g. 3.16E+20 = 3.16×10²⁰.

Results with normalization to the integral flux, analogous to those in Table 3.4 for BEC, have also been obtained for the BOL and BOC states. In all three cases, transport theory was used for the neutron flux calculation and the control rods were placed in the upper parking position. The reaction-wise decomposition results for the void reactivity at BOL, BOC and BEC, as obtained using Eq. 3.10, are presented in Table 3.5.

Table 3.5. Reaction-wise void reactivity decomposition (units: pcm) by the neutron balance method and comparison of the BOL, BOC and BEC states.

Flux calculation	Transport theory		
Control rod position	Upper parking position		
Fuel cycle state	BOL	BOC	BEC
Decomp. method	Neutron Balance		
Normalization to	Φ_{AC}		
Leakage	-664	-616	-653
Capture	3892	4010	3794
Fission	923	797	666
Production	-2579	-2218	-1762
Component sum	1572	1972	2045

As can be seen, for all three fuel cycle states, the capture term is the most significant positive component of the void reactivity. The production and leakage components provide smaller, negative contributions. It should be noted that a decrease in the capture, fission or leakage rate provides a positive reactivity, whereas a decrease in the production rate leads to negative reactivity; thus, the production component is always of opposite sign to the fission component, although it is $\sim \nu$ -times stronger. The increases in the void reactivity for the BOC and BEC states, relative to BOL, are seen to be caused mainly by the production component. Changes in the leakage and capture components are relatively small.

3.5.2 Cross-section-wise decomposition (perturbation theory based method)

The void reactivity has been decomposed cross-section-wise into the $\delta\rho_L$, $\delta\rho_P$, $\delta\rho_C$, $\delta\rho_F$ and $\delta\rho_S$ components by the perturbation theory based method according to Eq. 3.14. As mentioned earlier, it has been applied using diffusion-theory flux solutions for the core calculation, with the control rods inserted 20 cm to assure criticality. The cross-section-wise components for BOL condition are summarized in Table 3.6a. Shown in Table 3.6b are the neutron balance based reaction-wise results obtained using the same (i.e. diffusion-theory) solution for the direct flux. Before discussing the results, it should be recalled that the perturbation theory and neutron balance based methods basically provide two complementary sets of reactivity components. While the former helps quantify the impact of the various cross-sections and thus provides an understanding of the causes of the reactivity change, the latter provides an understanding of the consequences through the influence on the reaction rates.

The results in Table 3.6 clearly show the consistency of the two decomposition methods in the sum of the individual components. However, the partial components strongly differ. The perturbation theory based method identifies scattering as the largest positive component, which is only partly reduced by the leakage term. This implies that the reduction in scattering cross-section (due to sodium removal) and the resulting spectrum hardening represent the main cause of the sodium void reactivity effect. The neutron balance based decomposition, on the other hand, shows the capture component to be the most important positive contribution to the void reactivity. In this context, the capture rate reduction is to be seen as the most important consequence of the spectrum hardening resulting from the sodium removal, even though, according to the perturbation method, the change of the capture cross-section is relatively small. Both these aspects – cause and consequence – are discussed in greater detail in the following subsections.

Table 3.6. Void reactivity decomposition (units: pcm) at BOL into a) cross-section-wise components using the perturbation method and b) reaction-wise components using the neutron balance method.

a)

Decomp. method	Perturbation
Flux calculation	Diffusion theory
Control rod position	20 cm in the core
Fuel cycle state	BOL
Leakage	-789
Capture	378
Fission+Production	65
Scattering	1757
Component sum	1411

b)

Decomp. method	Neutron Balance
Flux calculation	Diffusion theory
Control rod position	20 cm in the core
Fuel cycle state	BOL
Leakage	-751
Capture	3815
Fission	892
Production	-2534
Component sum	1422

3.5.3 Isotope-wise decomposition (neutron balance based method)

The void reactivity can be further decomposed into isotope-wise components. For the neutron balance based method, this is accomplished by applying Eq. 3.12. The decomposition is based on the individual isotopic reaction rates for capture, fission and production. These rates at BEC are shown in Figure 3.10a for several key isotopes. The production rate is seen to have the largest value for ^{239}Pu , which is the main fissile isotope. Since the reaction rates in Figure 3.10a correspond to the equilibrium closed cycle state, the ^{238}U capture rate – as the “producer” reaction for ^{239}Pu – is practically equal to the ^{239}Pu destruction rate (via fission and capture), the equilibrium SFR core’s behavior being nearly that of an iso-breeder with account for fuel reprocessing and refueling time.

Figure 3.10b shows the changes in the isotopic reaction rates caused by the voiding of the core at BEC. The ^{238}U capture rate is seen to have the largest reduction. ^{239}Pu , as the other principal nuclide, shows significant changes in all three reaction rates.

Chapter 3: Void Reactivity Decomposition and Analysis

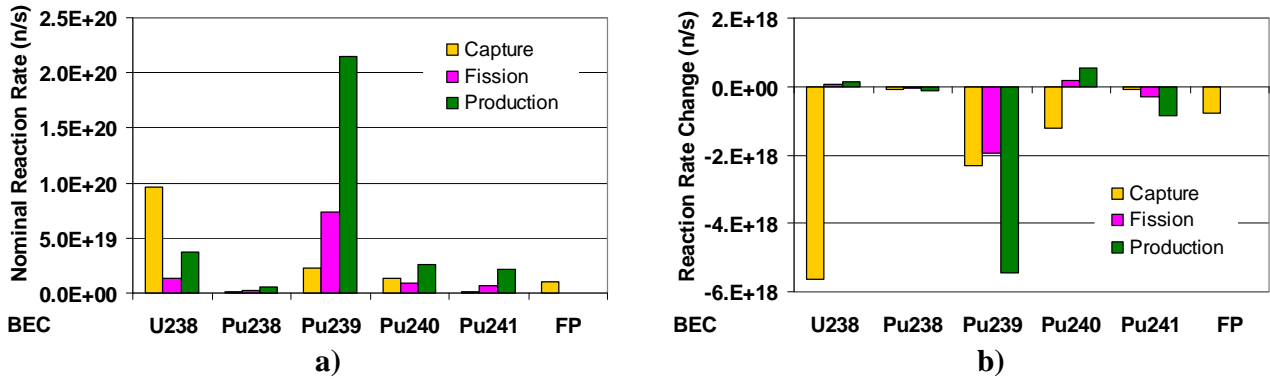


Figure 3.10. Isotope-wise a) reaction rates in the nominal core at BEC and b) reaction rate changes caused by the core voiding.

Isotopic reaction rate results analogous to those for BEC were also obtained for BOL and BOC. All three sets were then used for the isotope-wise void reactivity decomposition. The leakage component clearly does not warrant further decomposition in the current context, so that the global isotope-specific impact can be written as $\Delta\rho_{P,C,F} = \Delta\rho_P + \Delta\rho_C + \Delta\rho_F$. The isotope-wise decomposition for this global impact is presented in Table 3.7, together with the corresponding value of the component expressed per unit mass of the isotope in the given fuel cycle state.

Table 3.7. Global isotope-wise void reactivity decomposition for BOL, BOC and BEC states.

State	BOL			BOC			BEC		
Variable	mass, m	$\Delta\rho_{P,C,F}$	$\Delta\rho_{P,C,F}/m$	mass, m	$\Delta\rho_{P,C,F}$	$\Delta\rho_{P,C,F}/m$	mass, m	$\Delta\rho_{P,C,F}$	$\Delta\rho_{P,C,F}/m$
(units)	(t)	(pcm)	(pcm/t)	(t)	(pcm)	(pcm/t)	(t)	(pcm)	(pcm/t)
U235	0.15	-25.6	-232.7	0.11	-19.6	-178.2	0.08	-10.2	-127.5
U238	61.83	2108.1	35.9	58.70	2020.0	34.4	57.46	1830.8	31.9
Pu238	0.42	-2.3	-6.8	0.34	-5.4	-15.9	0.26	2.5	9.6
Pu239	5.51	-496.0	-82.0	6.05	-384.2	-63.5	6.97	-280.5	-40.2
Pu240	3.45	463.0	132.7	3.49	446.9	128.1	4.29	491.6	114.6
Pu241	0.96	-377.5	-490.3	0.77	-289.6	-376.1	0.46	-129.2	-280.9
Pu242	1.21	123.1	108.0	1.14	110.4	96.8	0.43	39.3	91.4
MA	0.09	26.2	97.0	0.27	63.2	234.1	0.90	137.9	153.2
FP	0.00	0.0	0.0	2.76	241.0	87.3	2.74	246.5	90.0
O16	9.79	-2.1	-0.2	9.79	-2.1	-0.2	9.79	-2.7	-0.3
Na23	4.03	135.3	33.6	4.03	132.8	33.0	4.03	122.0	30.3
Steel	22.98	283.2	12.3	22.98	275.1	12.0	22.98	250.3	10.9
SUM	110.4	2235.4	20.2	110.4	2588.5	23.4	110.4	2698.3	24.4

Chapter 3: Void Reactivity Decomposition and Analysis

It is seen that, for all three fuel cycle states, the fertile isotope ^{238}U provides the largest positive reactivity component. The two other less strongly fissionable isotopes, ^{240}Pu and ^{242}Pu , increase the void reactivity as well. Conversely, the fissile isotopes ^{239}Pu and ^{241}Pu reduce the void effect. It is interesting to note that, in terms of the effect per unit mass, ^{241}Pu is found to be the most favorable isotope for the void effect reduction, while the MA are the most detrimental. The difference in void reactivity between BOL, BOC and BEC results from various effects, and these are discussed separately later in the context of the more detailed decomposition presented below.

The isotope-wise reaction rates provided by ERANOS are also divided reaction-wise. This enables one to achieve a more detailed decomposition of the void reactivity, viz. both reaction- and isotope-wise. The resulting isotope-wise decomposition of each of the three reaction rate components – $\Delta\rho_P$, $\Delta\rho_C$ and $\Delta\rho_F$ – are shown in Table 3.8 for all three studied fuel cycle states.

Table 3.8. Reaction- and isotope-wise void reactivity decomposition for BOL, BOC and BEC.

State	BOL			BOC			BEC		
Variable (units)	$\Delta\rho_P$ (pcm)	$\Delta\rho_C$ (pcm)	$\Delta\rho_F$ (pcm)	$\Delta\rho_P$ (pcm)	$\Delta\rho_C$ (pcm)	$\Delta\rho_F$ (pcm)	$\Delta\rho_P$ (pcm)	$\Delta\rho_C$ (pcm)	$\Delta\rho_F$ (pcm)
U235	-76.6	18.9	32.1	-56.0	13.0	23.4	-32.7	8.2	14.3
U238	36.7	2083.5	-12.1	24.9	2003.0	-7.9	44.2	1802.3	-15.7
Pu238	-80.8	49.7	28.8	-66.5	37.5	23.6	-35.4	24.6	13.3
Pu239	-1903.9	728.1	679.8	-1739.7	731.9	623.6	-1636.9	740.3	616.1
Pu240	109.5	390.6	-37.1	118.5	368.4	-40.0	157.0	390.0	-55.4
Pu241	-700.3	79.2	243.6	-535.1	59.5	186.0	-252.3	30.9	92.2
Pu242	35.0	99.9	-11.8	31.5	89.6	-10.7	14.0	30.2	-4.9
MA	1.1	25.5	-0.4	4.4	60.3	-1.5	-19.6	151.8	5.7
FP	-	0.0	-	-	241.0	-	-	246.5	-
O16	-	-2.1	-	-	-2.1	-	-	-2.7	-
Na23	-	135.3	-	-	132.8	-	-	122.0	-
Steel	-	283.2	-	-	275.1	-	-	250.3	-
SUM	-2579.3	3891.8	922.9	-2218.0	4010.0	796.5	-1761.7	3794.4	665.6

It is seen that the capture component is positive for each of the fuel isotopes, consistent with the earlier noted fact that the overall capture rate is reduced in the voided core. In this context, the ^{238}U capture term is the most important single component and, as such, represents the major contribution to the positive void reactivity.

It can also be seen that the fissile isotopes all have positive fission components, which means that each of these fission rates is reduced in the voided core. The corresponding production components are negative and ν -times stronger; furthermore, each of these production components is also stronger than

the corresponding capture term. Accordingly, the net impact on the void reactivity of each of the fissile isotopes (principally, ^{239}Pu and ^{241}Pu) is negative.

Differently, the less strongly fissionable isotopes show negative fission, and thus positive production, components. In addition, they also have their positive capture components, so that their overall impact is positive. To this group belong ^{240}Pu and ^{242}Pu , as also the already discussed ^{238}U with its very strong capture component. Regarding the non-fuel materials, the capture reactivity component for steel is twice higher than that for the void effect steering isotope ^{23}Na , which has only minor impact. At BOC and BEC, there is also a significant positive capture term for the FP.

Table 3.8 also shows in detail the origin of the void reactivity differences between the BOL, BOC and BEC states. Before discussing the various individual effects, it is instructive to first compare the differences in the nominal reaction rates between BOC and BOL, and between BEC and BOC. From the results shown in Figure 3.11a, it is seen that the BOC reaction rates differ from the BOL values mainly in terms of the higher (newly appearing) FP, lower ^{238}U capture, higher ^{239}Pu and lower ^{241}Pu fission (along with the corresponding production differences). The reaction rate differences between the BEC and BOC states shown in Figure 3.11b indicate that the ^{238}U capture rate is significantly lower at BEC. The fission rate (and related production) is higher for ^{239}Pu and ^{240}Pu , and lower for ^{241}Pu .

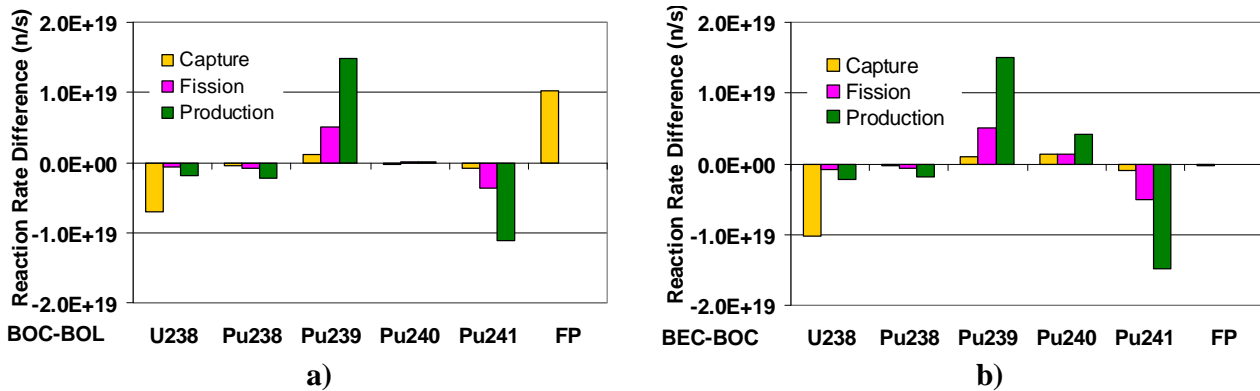


Figure 3.11. Differences in nominal reaction rates between a) BOC and BOL, and between b) BEC and BOC.

The above fuel cycle specific differences in the nominal state of the SFR core are, as to be expected, somewhat different when one considers the changes caused by voiding. These differences clearly, in turn, influence the trend one sees for the void reactivity between BOL, BOC and BEC.

As presented in Table 3.2, the void reactivity increases from 1578 pcm at BOL to 1978 pcm at BOC, and then further to 2050 pcm at BEC. Thus, the differences are 400 pcm between BOC and BOL, and only 72 pcm between BEC and BOC. The corresponding differences in the leakage component of the void reactivity (see Table 3.5) are only 48 pcm and -37 pcm. Accordingly, the remaining three

reactions (production, capture and fission) should contribute 352 pcm and 109 pcm to the former and latter differences, respectively. These values are quite consistent with the decomposition comparisons made in Table 3.7, between BOL, BOC and BEC: the differences in the sum of the production, capture and fission components of the void reactivity are seen to be 353 pcm between BOC and BOL, and 110 pcm between BEC and BOC.

Table 3.9 presents the decompositions of Table 3.8 in another form, viz. in terms of the differences in the reaction- and isotope-wise components between the three studied fuel cycle states. Thereby, it is seen that the net (BOC-BOL) difference of 353 pcm is mainly caused by the appearance of FP capture (241 pcm), and the smaller negative contributions from ^{239}Pu production (164 pcm) and ^{241}Pu production (165 pcm). The smaller negative ^{239}Pu production contribution at BOC appears to be in contradiction to the fact that the ^{239}Pu mass is increased at BOC (see Table 3.9 and Figure 3.11a). This is a consequence of the relatively strong neutron spectrum change between the nominal conditions of these two fuel cycle states. The fourth largest component of the (BOC-BOL) difference in void reactivity is the ^{238}U capture (-81 pcm). The mass of ^{238}U is decreased at BOC, which, in this case, is qualitatively consistent with its reduced positive contribution to the void reactivity.

Table 3.9. Differences of isotope-wise void reactivity components between the BOL and BOC, and between the BOC and BEC, states.

Difference	BOC-BOL					BEC-BOC				
Variable (units)	Mass (t)	$\Delta\rho_P$ (pcm)	$\Delta\rho_C$ (pcm)	$\Delta\rho_F$ (pcm)	$\Delta\rho_{P,C,F}$ (pcm)	Mass (t)	$\Delta\rho_P$ (pcm)	$\Delta\rho_C$ (pcm)	$\Delta\rho_F$ (pcm)	$\Delta\rho_{P,C,F}$ (pcm)
U235	-0.04	20.6	-5.9	-8.7	6.0	-0.03	23.3	-4.8	-9.1	9.4
U238	-3.13	-11.8	-80.5	4.2	-88.1	-1.24	19.3	-200.7	-7.8	-189.2
Pu238	-0.08	14.3	-12.2	-5.2	-3.1	-0.08	31.1	-12.9	-10.3	7.9
Pu239	0.54	164.2	3.8	-56.2	111.8	0.92	102.8	8.4	-7.5	103.7
Pu240	0.04	9.0	-22.2	-2.9	-16.1	0.80	38.5	21.6	-15.4	44.7
Pu241	-0.19	165.2	-19.7	-57.6	87.9	-0.31	282.8	-28.6	-93.8	160.4
Pu242	-0.07	-3.5	-10.3	1.1	-12.7	-0.71	-17.5	-59.4	5.8	-71.1
MA	0.18	3.3	34.8	-1.1	37.0	0.63	-24.0	91.5	7.2	74.7
FP	2.76	-	241.0	-	241.0	-0.02	-	5.5	-	5.5
O16	0.00	-	0.0	-	0.0	0.00	-	-0.6	-	-0.6
Na23	0.00	-	-2.5	-	-2.5	0.00	-	-10.8	-	-10.8
Steel	0.00	-	-8.1	-	-8.1	0.00	-	-24.8	-	-24.8
SUM	0.00	361.3	118.2	-126.4	353.1	0.00	456.3	-215.6	-130.9	109.8

As regards the (BEC-BOC) void reactivity difference of 110 pcm, Table 3.9 shows that this has several components of comparable magnitude. First of all, the ^{238}U mass is further reduced and simultaneously the spectrum is changed, with the result that the total ^{238}U impact is -189 pcm (-201

pcm from its capture). The ^{241}Pu mass is also further decreased, the resulting positive effect of the production component being 283 pcm. The third most important component is the production term of ^{239}Pu (103 pcm). Its negative contribution to the void effect is reduced, again in apparent contradiction to its mass increase.

3.5.4 Isotope-wise sensitivity coefficients (perturbation theory based method)

With the perturbation theory based method, an isotope-wise consideration of the reactivity change consistent with the neutron balance method is best achieved by quantifying the corresponding sensitivity coefficients. For a given isotope n and reaction type i , the group dependent sensitivity coefficient is obtained by applying Eq. 3.15. Clearly, the energy integrated sensitivity coefficients (obtained from the sum of the group dependent values for a given reaction) can not be directly compared with the corresponding reactivity components obtained from the neutron balance based method. Accordingly, in order to achieve a qualitative comparison of the sensitivity coefficients and the reactivity decomposition components, the results for the two sets of parameters have first been normalized internally, the ^{238}U capture cross-section or reaction rate being selected as the respective reference in each case. Furthermore, one should note that – for the type of comparison being made here – the perturbation theory based result for the sensitivity to a specific fission cross-section needs to be compared with the sum of the corresponding fission and production terms obtained from the neutron balance based method.

Table 3.10 shows the two sets of normalized results (with the value for the ^{238}U capture component set at 100 in each case), in terms of values for the individual isotopes. The important sensitivity coefficient with respect to scattering is not considered here, since there is no corresponding term to be compared with in the neutron balance context.

The two sets of numbers in Table 3.10 are, surprisingly, quite consistent, even though the coefficients serve to quantify the sensitivity of the void reactivity to the cross-section for a given reaction, while the neutron balance based decomposition quantifies the impact of that reaction (i.e. provides a measure of consequence). The explanation is to be found in the nature of the sodium void effect. Due to the reduced ^{23}Na scattering, the spectrum is hardened quite significantly upon voiding of the core. This has a high impact on all reaction rates. In the energy region where the spectrum changes most strongly, the neutron flux is increased or decreased considerably, but the multi-group cross-sections for capture and fission stay practically constant. Accordingly, the importance of both sensitivity coefficients and neutron balance based components is simply proportional to the value of the cross-section for the corresponding reaction. This aspect is discussed further in the next subsection, which considers the neutron balance based energy-group-wise decomposition of the void reactivity.

As regards the role of sodium itself, it is clear that the contribution of ^{23}Na capture is of little significance. The sensitivity coefficient and neutron balance based component for this reaction are seen in Table 3.10 to be only 9% and 6%, respectively, of the corresponding ^{238}U capture value. On the other hand, the values of the sensitivity coefficients with respect to sodium elastic and inelastic

scattering have been found to be as high as about 75% and 44%, respectively, relative to the value for the important ^{238}U capture reaction. This of course corresponds to the high impact mentioned above, which the spectrum hardening due to sodium removal has on all reaction rates.

Table 3.10. Normalized isotope-wise results for a) void reactivity sensitivity coefficients to capture and fission cross-sections, b) neutron balance based, void reactivity decomposition components for capture and for the sum of fission and production; normalization, in each case, is to a value of 100 for the ^{238}U capture component.

a)

Void reactivity sensitivity coefficients, normalized to value for ^{238}U capture		
Isotope	$S\sigma_c$	$S\sigma_f$
U235	1.0	-2.9
U238	100.0	4.5
Pu238	2.8	-3.1
Pu239	40.9	-74.0
Pu240	20.4	8.4
Pu241	4.4	-32.9
Pu242	5.5	2.6
MA	1.5	0.1
O16	-1.3	-
Na23	8.7	-
Steel	2.0	-
SUM	185.8	-97.4

b)

Neutron balance based components, normalized to value for ^{238}U capture		
Isotope	$\Delta\rho_c$	$\Delta\rho_f + \Delta\rho_p$
U235	0.9	-2.2
U238	100.0	1.7
Pu238	2.4	-2.5
Pu239	34.8	-59.8
Pu240	18.7	3.7
Pu241	3.8	-22.5
Pu242	4.8	1.2
MA	1.2	0.04
O16	-0.1	-
Na23	6.4	-
Steel	13.5	-
SUM	186.4	-80.2

In summary, the reaction- and isotope-wise breakdown of the void effect – using the complementary, neutron balance based reactivity components and perturbation theory based sensitivity coefficients – have clearly underlined the role of ^{238}U capture as the most important single reaction rate, from both the neutron balance and sensitivity analysis viewpoints. Furthermore, ^{239}Pu and ^{241}Pu fission (in conjunction with the corresponding production terms) contribute significant negative components. Finally, the important role of sodium is manifested, not directly in the neutron balance based decomposition (i.e. does not appear as important “consequence”), but rather via the scattering term as indicated by the perturbation theory based decomposition (which provides a measure of “cause”). The high sensitivity is clearly linked to its large influence on the neutron spectrum. This aspect is further discussed in the following subsection.

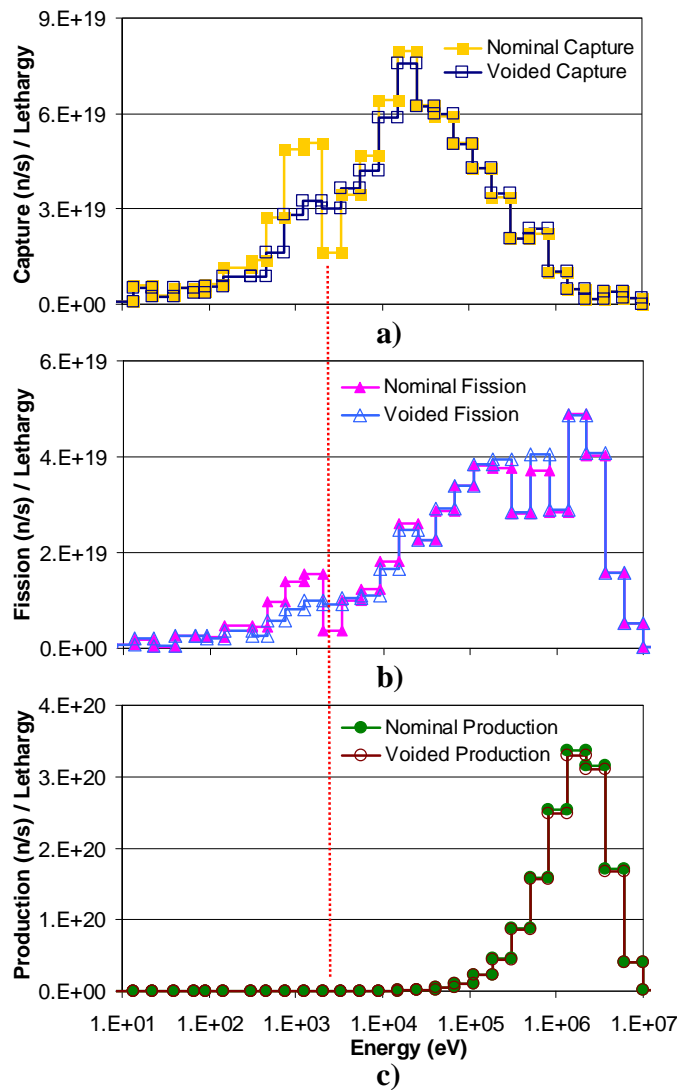


Figure 3.12. Group-wise distributions for a) capture, b) fission and c) production rates at BEC. The dotted red line marks the position of the ^{23}Na scattering resonance at ~ 3 keV.

3.5.5 Energy-group-wise decomposition (neutron balance based method)

To better understand the relationship between the reduced scattering (due to sodium removal) and the decreased ^{238}U capture in the voided core, the necessary group-wise reaction rates were obtained from ERANOS and the group-wise decomposition of the void reactivity has been carried out applying the neutron balance method according to Eq. 3.12.

Figure 3.12 first presents the energy dependence of the capture, fission and production rates in the nominal (100% sodium density) and voided (almost 0% density) cores at BEC. It is clearly seen from Figure 3.12a and 3.12b that the energy distributions for the capture and fission rates differ quite significantly between the two cases, the strongest variation being at and below the ^{23}Na scattering resonance at ~ 3 keV. As regards the production rate, illustrated in Figure 3.12c, this is slightly lower in the voided core than in the nominal state, but the energy distribution – being determined by the fission spectrum – is almost identical.

In order to better understand the changes in the capture and fission rate energy distributions, the neutron spectra for the nominal and voided states have been examined more closely, along with the cross-sections for ^{238}U capture, ^{239}Pu fission and ^{23}Na elastic scattering. It should be noted that the presented 1968 energy-group spectra were obtained by cell calculations for the ESFR fuel lattice, using the ERANOS module ECCO, and were verified via comparisons with the SERPENT Monte Carlo code (see Appendix A). It is clearly seen from Figure 3.13 that, in the nominal case, the strong sodium elastic scattering suppresses the neutron flux at higher energies and increases it significantly in the lower energy region. The spectrum in the nominal state is thus effectively shifted to an energy range with higher ^{238}U capture and ^{239}Pu fission cross-sections. In the voided core, this spectral shift disappears, and these reaction rates are reduced correspondingly.

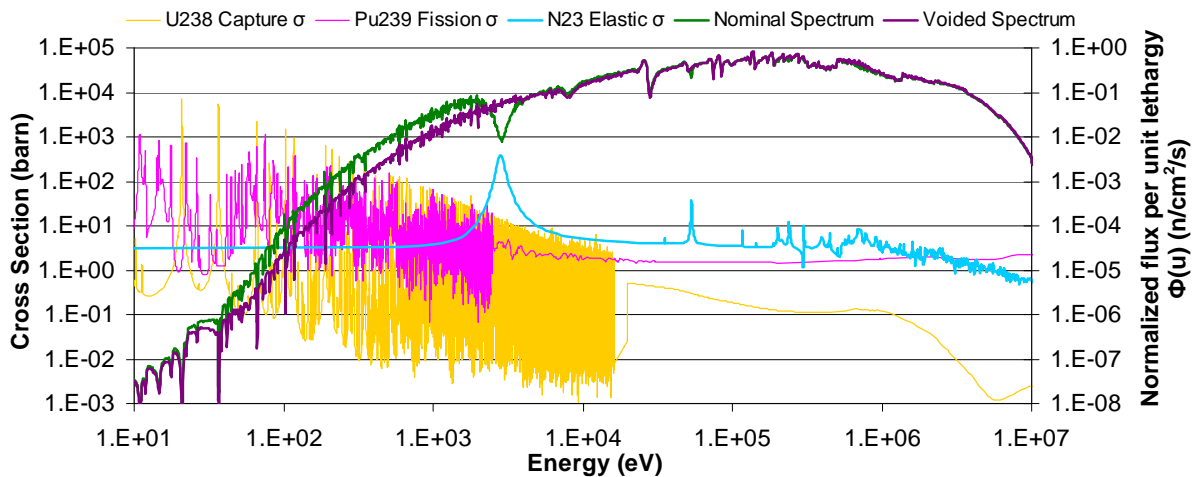


Figure 3.13. Nominal and voided ESFR spectra, along with ^{238}U , ^{239}Pu and ^{23}Na cross-sections.

The group-wise void reactivity decomposition for the BEC state is illustrated in Figure 3.14. As shown, the production component, which relates to fission, provides solely negative reactivity contributions and is distributed according to the fission spectrum. The capture and fission components, on the other hand, correspond to both negative and positive reactivity values. Furthermore, these two sets of components behave consistently within each group. The most conspicuous fluctuation in sign occurs between the 18th and 19th energy group, i.e. in the region of the ^{23}Na scattering resonance where the neutron spectrum difference also changes sign (see the blue plot in Figure 3.14). This is just a local perturbation of the general spectrum softening trend.

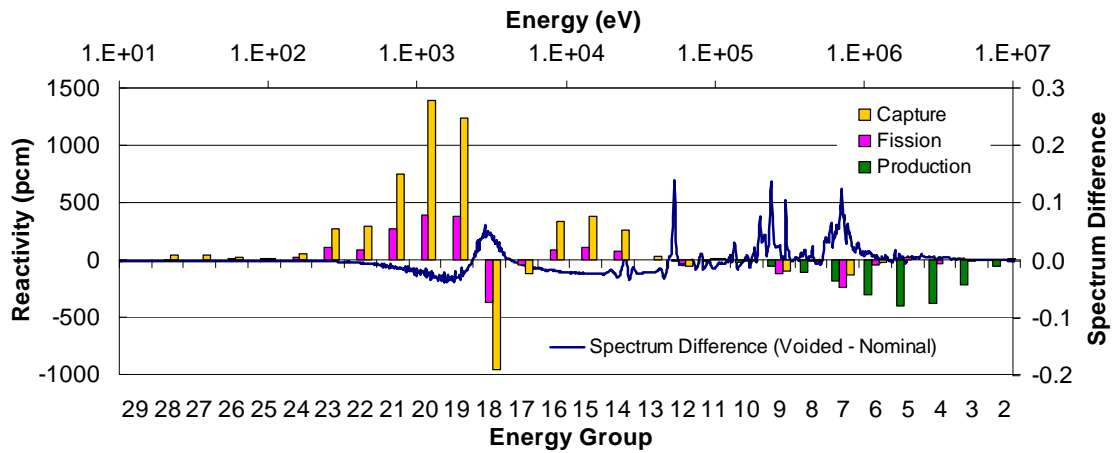


Figure 3.14. Group-wise void reactivity decomposition at BEC, together with the change in neutron spectrum.

From the above discussion, it is clearly seen that the void effect is mainly driven by the spectrum shift caused by the sodium removal. Thereby, it is the sodium elastic scattering that plays the key role, largely determining the influence on the capture and fission rates, and hence the corresponding void reactivity components. The reduced capture rate in the resonance energy range, in particular that of ^{238}U , results in being the main consequence, even though the capture cross-section in these energy groups does not change much.

It should be pointed out that, in a recent, very relevant publication [3.11], 33-energy-group sodium void sensitivity profiles have been presented with respect to capture and fission in the individual major actinides, i.e. ^{238}U , ^{239}Pu , ^{240}Pu , and ^{241}Pu . Interestingly, the reported shapes of the capture sensitivity profiles are quite similar for the various heavy nuclides and largely follow the distribution of the group-wise capture components shown in Figure 3.14. However, the shapes of the fission sensitivity profiles for the fissile isotopes, i.e. ^{239}Pu and ^{241}Pu , are found to be inversed images of the group-wise fission components shown in Figure 3.14. This is because the fission components in [3.11] have been combined with the corresponding production terms (opposite in sign to fission, but $\sim \nu$ times stronger). In addition, the sensitivity profiles presented in [3.11] clearly confirm ^{238}U capture to be the reaction

which is most strongly influenced by sodium voiding. Effectively, the perturbation theory based sensitivity results reported in [3.11] provide important justification for the current, neutron balance based group-wise void reactivity decomposition, as also – in more general terms – for the present detailed interpretation of the SFR void effect.

3.6 Chapter summary

The sodium void effect for the ESFR has been studied in this chapter, emphasis being placed on an asymptotic core state corresponding to the equilibrium closed fuel cycle. Partial validation of the deterministic calculations, carried out using ERANOS, has been achieved via code-to-code comparisons with the Monte Carlo code SERPENT, very good agreement being observed for the sodium void reactivity computation. Voiding of the active core (both inner and outer fuel zones) was chosen as the reference voiding scenario, the void effect in this region having been found to be spatially additive. It has also been shown that the spatial distributions of flux worth and void reactivity importance are strongly correlated.

The void reactivity for the reference voiding case has been decomposed using a methodology based on the neutron balance equation. This was done in terms of the corresponding leakage, fission, capture and production terms, as well as isotope-wise and energy-group-wise. It has been shown that the dominating component of the void reactivity is the strongly positive absorption term, whereas the negative production and leakage terms are relatively weaker. ^{238}U capture is the dominating reaction rate. ^{239}Pu , as the second most important nuclide, yields significant contributions due to changes in both production and absorption. However, these two partly compensate each other, and the overall negative effect is significantly smaller in magnitude than the ^{238}U capture effect. It is necessary to note that the impact of ^{23}Na capture is negligible. In terms of the impact per unit mass, ^{241}Pu has been found to be the most favorable isotope for reduction of the void reactivity.

The void effect is driven mainly by the strong ^{23}Na elastic scattering, which in the nominal case suppresses the neutron flux at higher energies and increases it significantly in the lower energy region. The spectrum is thus shifted to the energy range with higher ^{238}U capture and ^{239}Pu fission cross-sections. In the voided core, this spectral shift disappears, resulting in the reduction of both ^{238}U capture and ^{239}Pu production (in conjunction with fission), and yielding the corresponding important contributions to the reactivity change.

The cross-section-wise decomposition results obtained applying the perturbation theory based method have confirmed the key role played by ^{23}Na scattering. In addition, the isotope-wise sensitivity analysis results for capture, fission and production have been found to be quite consistent, in relative terms, with the corresponding components obtained from the isotope-wise neutron balance based decomposition.

Chapter 3: Void Reactivity Decomposition and Analysis

As compared to the beginning-of-life (BOL) void reactivity value of ~ 1578 pcm for the considered ESFR core, the influences of equilibrium closed and open fuel cycles on the void reactivity correspond to increases of ~ 472 pcm (BEC) and ~ 400 pcm (BOC), respectively. The four most important isotope-wise contributions to these influences are those of the fission products, ^{238}U , ^{241}Pu and ^{239}Pu , the overall impact of the minor actinides not being very significant.

Finally, it is clear that the reactivity decomposition methodology, which has been developed and applied in this chapter for achieving a better understanding of the SFR void effect, can also be a valuable tool for optimization studies. Thus, two important potential orientations have been indicated for neutronics optimization, viz. leakage related and spectrum related. The former, for example, can be considered via the introduction of an upper sodium plenum above the core and/or variation of the core's height-to-diameter ratio, whereas the latter can be influenced by introduction of moderator pins into the fuel assembly and/or change of the loaded plutonium vector. Details of the optimization work currently carried out are presented in the next chapter.

References

- [3.01] R. Jacqmin and J-P Both. ECCO/ERANOS validation studies. Technical report, JEF/DOC-647, NJOY/JACQMIN-01, 1996.
- [3.02] J. Krepel, S. Pelloni, K. Mikityuk, P. Coddington. EQL3D: ERANOS based equilibrium fuel cycle procedure for fast reactors. *Annals of Nuclear Energy*, vol. 36(5): pp. 550-561, 2009.
- [3.03] J. Krepel, K. Mikityuk, K. Sun, G. Rimpault. SFR equilibrium cycle analysis with the EQL3D procedure. In ICAPP 2009, Paper 9226.
- [3.04] R. Chawla, F. Jatuff, F. Tani. Diagnostic analysis of pin-removal reactivity worth experiments in a SVEA-96+ test lattice. *Annals of Nuclear Energy*, vol. 35(3): pp. 495-502, 2008.
- [3.05] S. G. Hong, Y. Kim, F. Venneri. Neutronic characterization of sodium-cooled fast reactor in an MHR-SFR synergy for TRU transmutation. In ICAPP 2007, Paper 7308.
- [3.06] S. Pelloni, P. Coddington. On using alternative perturbation theory methodologies in the evaluation of reactivity effects in ADS cores. *Annals of Nuclear Energy*, vol. 33(17-18): pp. 1360-1367, 2006.
- [3.07] L. Buiron, Ph. Dufour, G. Rimpault, G. Prulhiere, C. Thevenot, J. Tommasi, F. Varaine, A. Zaetta. Innovative Core Design for Generation IV Sodium-cooled Fast Reactors. In ICAPP 2007, paper 7383.
- [3.08] Y. Fukaya, Y. Nakano, T. Okubo. Study on characteristics of void reactivity coefficients for high-conversion-type core of FLWR for MA recycling. *Journal of Nuclear Science and Technology*, vol. 46(8): pp. 819-830, 2009.
- [3.09] K. Sun, J. Krepel, K. Mikityuk, S. Pelloni, R. Chawla. Void reactivity decomposition for Sodium-cooled Fast Reactor in equilibrium fuel cycle. *Annals of Nuclear Energy*, vol. 38(7): pp. 1645-1657, 2011.
- [3.10] J. Krepel, J. Saliba, K. Mikityuk, R. Chawla. Comparison of safety related parameters of Generation-IV fast reactors in equilibrium closed cycle. In GLOBAL 2011, Paper 386009.
- [3.11] J. Tommasi, P. Archier, J. M. Ruggieri. Validation of the sodium void reactivity effect prediction using JEFF-3.1 nuclear data. *Annals of Nuclear Energy*, vol. 37(11): pp. 1534-1553, 2010.

Chapter 4

Neutronics Optimization of the ESFR Core

The neutronics optimization study, which has been carried out currently on the basis of the ESFR reference core design, is presented in this chapter. Section 4.1 principally describes the considered optimization options, as also the key safety and performance parameters taken into account. Also included in this section is a brief review of the neutron balance based decomposition method for the void effect analysis (main content of Chapter 3), as well as of the ERANOS based EQL3D procedure for simulating the equilibrium fuel cycle. Sections 4.2 and 4.3 present the results of the optimization study for BOL and BEC states, respectively, in relation to each optimization option. A discussion of the main findings is presented in Section 4.4, along with the description of two “synthesis” core concepts corresponding to certain combinations of the different analyzed options. Finally, Section 4.5 gives a chapter summary.

It should be noted that the present optimization study mainly focuses on the sodium void effect, which is the most crucial neutronics drawback of the SFR. The other considered parameters are viewed more in terms of having to meet certain necessary requirements.

4.1 Considered optimization options and parameters

There are various possible optimization options which have been proposed in the literature for an SFR core [4.01, 4.02, 4.03, 4.04]. In particular, [4.03], published in 2008, considered a large number of possible modifications aimed at improving SFR safety and performance, e.g. reducing the sodium fraction in the fuel assembly, adding high energy absorbers, adding moderator, using dense fuels, reducing the core volume, introducing an upper sodium plenum, reducing the core’s height-to-diameter ratio, changing the fuel assembly heterogeneity, etc. Most of these possible options were considered in a preliminary phase of the present study.

It needs to be mentioned that, in parallel to the current doctoral research, several other SFR optimization studies have been under way internationally, emphasis on void reactivity reduction being a common feature. Thus, for example, [4.04] reports on a recent investigation carried out jointly by the French CEA, EDF and Areva in which the possibility has been suggested of achieving an evolutionary core design (viz. the CFV^{4.1}) with negative sodium void effect. This design corresponds to a thermal

^{4.1} CFV is a French acronym for Low Void effect Core [4.03].

power of 2400 MW (i.e. two-thirds of the reference ESFR core) and combines various types of geometrical options which are favorable to sodium void effect reduction, viz. internal blanket region (to increase the neutron flux level in the upper part of the core), two different core heights for the inner and outer fuel zones (to increase the interface between the core and the sodium plenum), etc. Thus, the SFR core proposed in [4.04] is characterized by a very high level of heterogeneity. Moreover, with the changes in various geometrical parameters having been made simultaneously, it is difficult to analyze the impact of the different contributing effects. In the present study, individual optimization options have first been investigated separately. Furthermore, the study is closely combined with fuel cycle analysis. Accordingly – in order to avoid the need to consider complex fuel management schemes during the recycling – a high level of heterogeneity has not been chosen for the finally proposed core designs.

After careful evaluation, four different optimization options were finally down-selected for in-depth consideration, viz. introducing an upper sodium plenum and boron layer, varying the core's height-to-diameter ratio, introducing moderator pins into the fuel assembly, and modifying the initially loaded plutonium content. Each of these options can significantly influence one or several safety and/or performance parameters. Systematic sensitivity analysis of each considered parameter has accordingly been carried out. Finally, based on the obtained results, two synthesis core concepts – combining the analyzed optimization options in different ways – are proposed and discussed in Subsection 4.4.2.

4.1.1 Leakage oriented optimization options

As indicated in the previous chapter, one potential orientation for optimization of the sodium void effect is through the leakage component. The following two options aim at enhancing the neutron leakage in the voided state.

Introducing an upper sodium plenum and boron layer

The first investigated leakage oriented optimization option is to introduce an upper sodium plenum with a boron layer above it. The former consists of 92% sodium and 8% steel, whereas the latter is assumed to have the same composition as the control rod region (i.e. B₄C with 20% ¹⁰B enrichment and a sodium volume fraction of 50%), both regions being modeled homogeneously in the ERANOS calculations. A schematic of the core with the sodium plenum and boron layer is shown in Figure 4.1. In this context, one may evaluate the void reactivity in two different ways: 1) reference void (voiding of only the fuel zone) and 2) extended void (voiding of the fuel zone plus the sodium plenum). For each of these voiding scenarios, the sensitivity of the void reactivity has been assessed while varying the heights of the upper sodium plenum and boron layer.

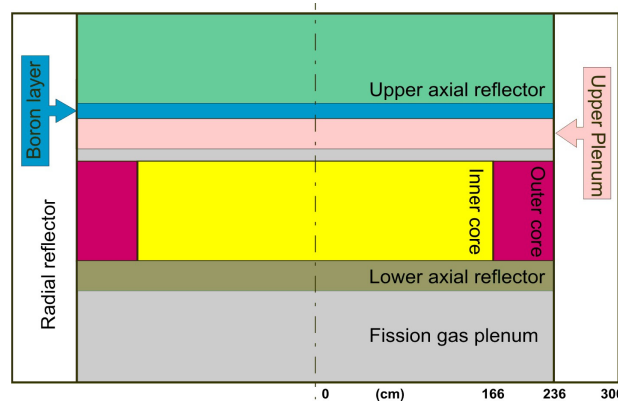


Figure 4.1. Vertical cross-section of the SFR core with the introduced upper sodium plenum and boron layer.

Varying the core height-to-diameter (H/D) ratio

The second discussed option is to test different height-to-diameter ratios for the core, the original ratio being 1.0 m to 4.7 m, i.e. $H/D = 0.213$. The alternative H/D ratios correspond to slightly modified fuel assembly design. In the studied ESFR core, the reference fuel assembly is with 10 rings of fuel pins, i.e. 271 pins in total. One may change the number of rings to 11 or 9, in order to have 331 or 217 fuel pins in a fuel assembly, respectively (see Figure 4.2). At the same time, to maintain the constant fuel mass, the core height needs to be adjusted to 0.82 m and to 1.25 m, respectively. The wrapper thickness is also changed correspondingly, in order to preserve the material balance. With these modifications, the two alternative H/D ratios arrived at are 0.158 (331 pins per fuel assembly) and 0.297 (217 pins per fuel assembly).

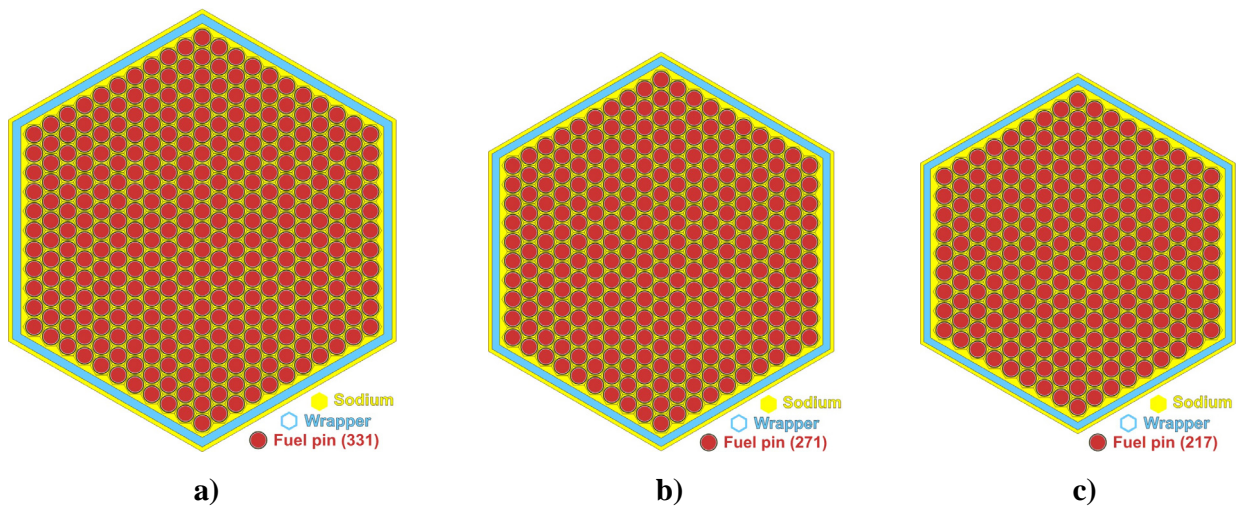


Figure 4.2. Illustration of the fuel assemblies with different numbers of pins, a) 331 pins, b) 271 pins (reference design) and c) 217 pins.

4.1.2 Spectrum oriented optimization options

The other potential orientation for the sodium void effect optimization is in relation to the neutron spectrum. The following two options aim at influencing the void reactivity via modification of the spectrum in the SFR core.

Introducing moderator pins

The first investigated spectrum related option is to introduce moderator pins into the fuel assemblies, ZrH_2 being selected as the moderator material. Up to 13 moderator pins have been introduced group-wise – the positions of the three different groups, corresponding to 3, 4 and 6 pins, respectively, being indicated in Figure 4.3. It should be noted that, in order to compensate for the replaced fuel pins, the height of the fuel assembly was correspondingly increased in each case, e.g. in the case of 13 moderator pins, the core height was increased by 5.04%.

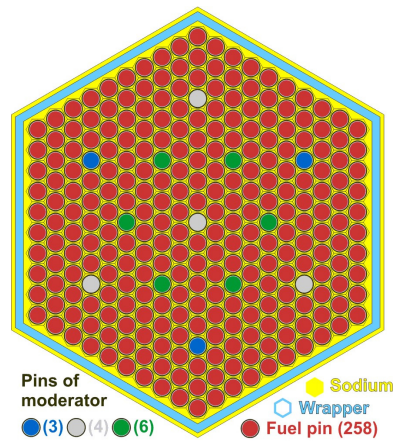


Figure 4.3. Horizontal cross-section of the fuel assembly with the introduced moderator pins.

Varying the initial plutonium content

The second option considered here is to modify the initially loaded plutonium content. The average content for the reference core is 15.8%, with 14.6% and 17.0% as the separate values for inner and outer fuel zones, respectively. In the present study, the effects of varying the average plutonium content have been investigated in terms of either an increase of the reference core value to 16.7% (15.8% for the inner, and 17.7% for the outer zone), or a decrease to 14.9% (13.4% for the inner, and 16.3% for the outer). It should be noted that, in order to preserve the power distribution of the reference ESFR core design, the changes in the inner and outer fuel zones are not proportional.

4.1.3 Considered safety and performance parameters

The principally considered safety related parameters are the void reactivity ($\Delta\rho_v$) and the Doppler constant (DC), nominal reactivity (ρ) and breeding gain (BG) being employed as the simultaneously assessed performance parameters. It should be mentioned that the BG value (see Subsection 2.2.1 for its definition) varies during the irradiation history of a given fuel batch, sometimes even with a change of sign. Clearly, it is the average value which is meaningful for interpreting core performance. Accordingly, all the BG values reported here correspond to the average breeding gain between the initial and final fuel states ($\overline{\text{BG}}$ in Eq. 4.4). The various parameters considered are defined as follows:

$$\rho = 1 - \frac{1}{k_{eff}} \quad \text{Eq. 4.1}$$

$$\Delta\rho_v = \rho_v - \rho_N \quad \text{Eq. 4.2}$$

$$\text{DC} = \frac{\rho(T_N + 1000) - \rho(T_N)}{\ln\left(\frac{T_N + 1000}{T_N}\right)} \quad \text{Eq. 4.3}$$

$$\overline{\text{BG}} = \frac{\text{BG}_{\text{ini}} + \text{BG}_{\text{fin}}}{2} \quad \text{Eq. 4.4}$$

where k_{eff} is the multiplication factor, the subscripts N and V indicate the nominal and voided states, respectively, T is the fuel temperature in Kelvin, the subscripts “ini” and “fin” represent the initial and final states of a fuel batch, respectively.

4.1.4 Void reactivity decomposition and equilibrium fuel cycle methodologies

This subsection briefly recalls the neutron balance based decomposition method for analyzing the sodium void effect, as also the ERANOS based EQL3D procedure for simulating the equilibrium fuel cycle.

The void reactivity can be decomposed on the basis of the neutron balance equation using the methodology described extensively in Subsection 3.4.1. The method essentially considers the integral neutron reaction rates in the reactor core, so that the reactivity is decomposed into the corresponding leakage, fission, capture and production components. Further decomposition can be done both isotope-wise and energy-group-wise. Application of this method in the present chapter is aimed at achieving a clear understanding of the physical mechanisms involved in the void reactivity optimization.

Although the ERANOS output options also allow combined isotope- and energy-group-wise decomposition, this has not generally been applied here. One exception is the case with inserted moderator pins, for which such an analysis of individual reaction rate contributions has been carried out to understand the strong deterioration of the breeding gain.

As indicated previously, the present optimization study focuses not only on the BOL state of the core, but also on the BEC state. The BOL state, i.e. the ESFR core with its design-specific fresh fuel composition, is considered as the reference state, and the BEC state is evaluated in order to quantify the impact of the optimization on the equilibrium closed fuel cycle. The methodology applied for carrying out the equilibrium cycle calculations is the ERANOS based EQL3D procedure [4.05], a more detailed description being given in Subsection 2.2.1. In particular, the equilibrium of a closed fuel cycle corresponds to the asymptotic state of a reactor with a fixed fuel management scheme involving recycling of its own fuel. Explicit cycle-by-cycle reactor operation, under the constant feed of natural uranium, is simulated until the equilibrium state is reached. The fundamental assumptions of the methodology are to keep the actinides mass in the manufactured fuel constant and to impose constant reactor power.

4.2 Optimization study at BOL

In this section, the considered safety and performance parameters for each optimization option are discussed successively, for the case of the reference BOL fuel cycle state. In particular, the corresponding void reactivity components, as obtained by the neutron balance based decomposition method, are presented as complementary information.

4.2.1 Upper sodium plenum and boron layer

The sodium plenum and boron layer – located above the upper fission gas plenum – are introduced into the reference ESFR core design. The effects of varying their heights on the void reactivity have been assessed, with both reference and extended voiding scenarios (see definitions in Subsection 4.1.1) being simulated for the purpose.

ERANOS verification

The prediction of the void effect in the upper sodium plenum region using a deterministic code (e.g. ERANOS) requires an accurate solution of the neutron transport (or diffusion) equation, since it largely depends on an adequate interpretation of changes in the leakage term. The ERANOS module TGV/VARIANT, which uses the variational nodal method (see Subsection 2.2.1), has been selected in almost all the reactor core calculations carried out in the present doctoral research. Different flux solving options are available in this module, viz. diffusion theory, transport theory with simplified spherical harmonics, and a full transport solution. In order to evaluate the accuracy of the ERANOS predictions of the sodium plenum effect (i.e. the reactivity effect caused by sodium plenum voiding), code-to-code comparisons have been carried out using the SERPENT Monte Carlo code (see Subsection 2.2.2) for the verification. Three different voiding scenarios have been considered for the benchmark comparisons: reference voiding, extended voiding, and plenum voiding.

It should be noted that the reference ERANOS model has a heterogeneous description for the inner and outer fuel zones only, the remaining components – including the upper sodium plenum – being simulated homogeneously. The reference SERPENT model, on the other hand, has a heterogeneous description for the whole core. In order to evaluate the corresponding influence on the treatment of neutron streaming effects in the extended and plenum voiding scenarios, usage has also been made of an alternative SERPENT model in which a homogenized upper sodium plenum is adopted. Table 4.1 presents the comparisons made for the different cases, the heights assumed for the sodium plenum and boron layer being 30 cm and 15 cm, respectively.

Table 4.1. ERANOS to SERPENT benchmark comparisons for reactivity effect results (units: pcm) in the case of reference, extended and plenum voiding scenarios (with 90% voidage)

Computation code	ERANOS	ERANOS	ERANOS	SERPENT	SERPENT
Sodium plenum mode	Homogeneous	Homogeneous	Homogeneous	Homogeneous	Heterogeneous
ERANOS flux solving option	Diffusion	Simpl. transport	Transport	-	-
Reference $\Delta\rho_v$ (90% voided)	1433	1463	1463	1441 ± 7	1442 ± 7
Extended $\Delta\rho_v$ (90% voided)	832	869	928	854 ± 7	821 ± 7
Plenum $\Delta\rho_v$ (90% voided)	-516	-512	-462	-501 ± 7	-531 ± 7

As seen from the tabulated results, the different flux solving options in ERANOS generally agree with each other for all the considered voiding scenarios. It is found that diffusion theory underestimates the reference void reactivity slightly (by ~ 30 pcm). Relative to the full transport solution, results for voiding of the plenum by itself are ~ 50 pcm more negative (i.e. less conservative) for both diffusion theory and simplified transport.

From the two sets of SERPENT results shown in Table 4.1, one can see that homogenization of the upper sodium plenum has negligible influence on the reference void reactivity prediction. However, in both the other two cases, the heterogeneous calculation is seen to yield a slightly more negative effect of voiding the sodium plenum. This is clearly due to the reduction of the streaming effect in the homogeneous calculation. Nevertheless, this reduction may be considered insignificant (~ 30 pcm), in comparison to the global leakage enhancing effect of the sodium plenum voiding (~ 500 pcm).

Due to the fact that the homogenized sodium plenum modeling slightly underestimates the plenum effect, i.e. is somewhat conservative, adopting the option of simplified transport theory in ERANOS would be a reasonable compromise. Moreover, considering the relatively large number of cases simulated in the sensitivity study presented below, this choice is also in favor of computational efficiency and has accordingly been used as the reference flux solving option for all subsequent calculations.

Influence of heights of sodium plenum and boron layer

Figure 4.4 shows the sensitivity of the void reactivity on the assumed size of the sodium plenum and boron layer. It is seen that only a limited sodium plenum effect is obtained when the voiding is assumed to occur only in the fuel region (i.e. for the reference voiding scenario). However, for the more realistic case of simultaneous voiding of the sodium plenum, i.e. for the extended voiding scenario, it is seen that the void reactivity can indeed be reduced significantly. Although Figure 4.4 shows that the maximum reduction of the void reactivity (more than 800 pcm) is achieved for the case with 60 cm sodium plenum and 15 cm boron layer, a clear “saturation” effect can be observed. The final choice for the size of the sodium plenum and boron layer would, of course, need to be based also on other considerations, e.g. thermal-hydraulics and economics.

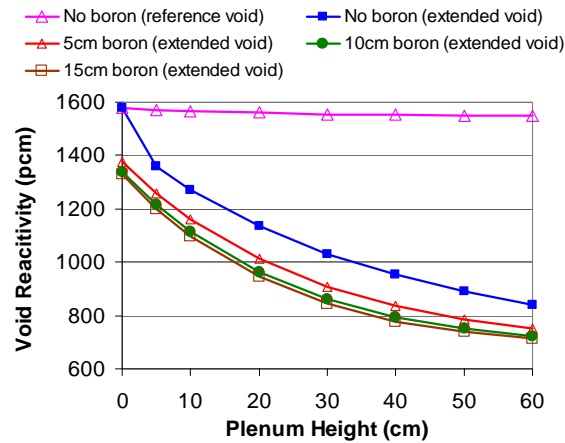


Figure 4.4. Sensitivity of the void reactivity on the size of sodium plenum and boron layer.

The impact of the sodium plenum and boron layer on the various considered safety and performance parameters is presented in Table 4.2. As can be seen, the variations in both the Doppler constant and the breeding gain are very limited. The sodium plenum and boron layer have nearly no influence on them. The nominal reactivity value goes down slightly, but the decrease is not very significant, even for the 60 cm sodium plenum case considered. Thus, the sodium plenum along with boron layer can be regarded as an optimization option with just one main effect, viz. a favorable void reactivity reduction.

Table 4.2. Safety and performance parameters at BOL for the cases with 60 cm sodium plenum, with and without a 15 cm boron layer, as also for the reference core

	$\Delta\rho_V(\text{pcm})$	DC (pcm)	ρ (pcm)	BG
Reference	1578	-1204	934	0.0644
with sodium plenum	842*	-1204	751	0.0632
and with boron layer	714*	-1202	718	0.0633

* for the extended voiding scenario

Sodium void reactivity decomposition

The void reactivity for the above selected cases has been decomposed reaction-wise according to Eq. 3.6, using integral reaction rates calculated by ERANOS. The results are presented in Table 4.3. It should be firstly noted that the sum of the components for each voiding scenario (see the last column of Table 4.3) is slightly different from the void reactivity result obtained directly from the ERANOS calculation (see the second column of Table 4.2). This is largely because the (n,2n) reaction rates – as discussed previously in Subsection 3.5.1 – are not provided in the output of the ERANOS neutron balance module and have been neglected in the reactivity decomposition. The effects are small, as can be seen also in the decomposition results for the later described optimization options.

Table 4.3. Reaction-wise void reactivity decomposition at BOL for the cases with 60 cm sodium plenum, with and without a 15 cm boron layer, as also for the reference core

Voiding scenario	$\Delta\rho_P$	$\Delta\rho_L$	$\Delta\rho_C$	$\Delta\rho_F$	$\sum_{P,L,C,F} \Delta\rho$
Reference	-2579	-664	3892	923	1572
with sodium plenum	-3062	-1735	4540	1091	833
and with boron layer	-3035	-1943	4600	1082	704

Comparing the void effect decomposition for the reference and extended voiding scenarios, larger negative leakage components are found in the latter, confirming that the sodium removal from the plenum region enhances the neutron leakage from the fuel zone. Furthermore, the introduction of the boron layer ensures that leaking neutrons are absorbed, rather than reflected, thus strengthening the leakage effect caused by the voiding of the sodium plenum (see Table 4.3). The three other components (viz. production, capture and fission) are also seen to become more significant in the extended voiding cases (although the effects are not as strong as for leakage). These changes result from the stronger spectral shift caused by the additional sodium voiding, i.e. that in the upper sodium plenum region.

4.2.2 Core H/D ratio

The original H/D ratio of the ESFR core is 0.213. The considered optimization test consists in varying the ratio in both directions while keeping the core volume, as well as its composition, constant. An overview of the influence on the four safety and performance parameters for each of the simulated core H/D values is presented in Table 4.4.

Table 4.4. Safety and performance parameters at BOL for the different core H/D ratios

H/D ratio	$\Delta\rho_v$ (pcm)	DC (pcm)	ρ (pcm)	BG
0.158	1321	-1190	-1405	0.0504
0.213 (reference)	1578	-1204	934	0.0644
0.297	1796	-1188	2889	0.0776

A lower void reactivity is obtained with the smaller H/D ratio, and a higher void reactivity with the larger value. The indicated void reactivity changes are analyzed below using the decomposition method. It should be mentioned, moreover, that the flatter core can also be expected to enhance the favorable void reactivity reduction effect of the sodium plenum, and that the inverse is to be expected for the larger H/D ratio.

From Table 4.4, one sees, however, that the smaller core H/D ratio results in a considerable decrease in the nominal reactivity, so that the reactor in fact becomes sub-critical, i.e. violates the constraint of a positive nominal reactivity. Clearly, other changes would be necessary in order to realize a core with the smaller H/D ratio considered here, e.g. increase in the plutonium content of the fuel (see Subsection 4.2.4).

As regards the breeding gain, this is found to remain positive for the two changed H/D values, the lowest value shown in Table 4.4 staying greater than 0.05. Nevertheless, a lower breeding ability is observed for the flatter core. The result for the Doppler constant shows that this important safety parameter is almost unchanged while varying the core H/D ratio.

Although, as mentioned, the core with the lower H/D ratio would require other changes to be viable, i.e. to have a positive nominal reactivity, the void reactivity decomposition has been carried out for the three considered cases without modification, simply in order to assess the relative importance of the individual components (see Table 4.5). From the decomposition, it is seen that the leakage term has the most notable relative change when the H/D ratio is varied. This is consistent with the fact that – with the picture of a bare cylindrical core in mind – the main effect of changing the H/D value is to change the value of the geometrical buckling. Considering that the reference core design is already quite flat, a further decrease in the H/D ratio would correspond to an increase in the geometrical buckling, and hence to the leakage effect. Furthermore, the other components, viz. the production, capture and

fission terms – which are modified due to the leakage-related changes in neutron spectrum – compensate each other partially. Therefore, the total spectral effect on the void reactivity of varying the core H/D ratio, i.e. the sum of the variations of the production, capture and fission terms, is significantly smaller than the leakage effect itself.

Table 4.5. Reaction-wise void reactivity decomposition at BOL for the reference core and the two cases with modified H/D ratios

H/D ratio	$\Delta\rho_P$	$\Delta\rho_L$	$\Delta\rho_C$	$\Delta\rho_F$	$\sum_{P,L,C,F} \Delta\rho$
0.158	-2714	-843	3912	960	1315
0.213 (reference)	-2579	-664	3892	923	1572
0.297	-2432	-532	3864	890	1789

4.2.3 Moderator pins

In this subsection, the effects of the introduction of moderator pins into the fuel assembly are discussed. As mentioned earlier, up to 13 of the original 271 fuel pins in each assembly have been replaced by ZrH_2 moderator pins, the height of the fuel assembly being increased appropriately for each considered case such as to conserve the fuel mass.

Table 4.6. Safety and performance parameters at BOL for the cases with inserted moderator (ZrH_2) pins

Moderator	$\Delta\rho_V(\text{pcm})$	DC (pcm)	ρ (pcm)	BG
0 (reference)	1578	-1204	934	0.0644
3 pins	1504	-1607	832	0.0304
7 pins	1416	-2022	792	-0.0009
13 pins	1352	-2421	995	-0.0677

An overview of the moderation effects on the considered safety and performance parameters is presented in Table 4.6. This again is currently done for the BOL state. As can be seen, both safety parameters are improved by introducing the moderator: the void reactivity is slightly reduced, while the Doppler constant becomes much stronger. Concerning the performance parameters, on the one hand, the breeding ability is strongly affected. Thus, for example, the breeding gain at BOL is seen to become negative with as little as 7 moderator pins in the fuel assembly. On the other hand, the nominal reactivity first shows a decrease and then an increase. This is a consequence of the two different, simultaneous changes made: additional moderation and increased core height (the mechanism

employed for conserving the fuel mass); the former change provides a negative contribution to the nominal reactivity, while the latter has a positive effect.

The influence of the moderator on the void reactivity has been decomposed reaction-wise. The components corresponding to production, leakage, capture and fission are presented in Table 4.7. As seen, the leakage term becomes less negative when increasing the number of ZrH_2 pins, this being explained by the shorter diffusion length due to the added moderator. The magnitude of each of the other three terms, i.e. production, capture and fission, is also reduced. As already indicated, these three components represent the consequences of the spectral hardening caused by the sodium removal, and the introduced moderator may indeed be expected to mitigate these effects. All in all, the introduction of moderator pins reduces the positive terms (capture, fission) somewhat more strongly than the negative terms (leakage and production), leading to a slight decrease in the magnitude of the positive sodium void effect.

Table 4.7. Reaction-wise void reactivity decomposition at BOL for the cases with inserted moderator pins

Moderator	$\Delta\rho_P$	$\Delta\rho_L$	$\Delta\rho_C$	$\Delta\rho_F$	$\sum_{P,L,C,F} \Delta\rho$
0 (reference)	-2579	-664	3892	923	1572
3 pins	-2404	-536	3578	859	1498
7 pins	-2212	-493	3323	791	1409
13 pins	-1928	-441	3022	692	1345

It was shown in the previous chapter (see also [4.06]) how sodium elastic scattering plays a key role in determining the important spectrum-change related void reactivity components. The energy-group-wise capture, fission and production void reactivity components for the reference case (i.e. with original fuel assembly) is illustrated in Figure 4.5a. As shown, on the one hand, the production component (which relates to fission) consists solely of negative contributions and is distributed according to the fission spectrum. On the other hand, the capture and fission components (i.e. the absorption terms) correspond to both negative and positive contributions. Furthermore, these two sets of energy-dependent contributions behave consistently within each group.

Figure 4.5b shows the energy-group-wise results for the case with 13 moderator pins in the fuel assembly. One can see that the energy dependence of the reactivity components is almost the same as for the reference case (see Figure 4.5a), but the values are mostly smaller in magnitude. The capture and fission terms are mitigated by the moderation and become less positive. The latter further implies a less negative production term in the high energy range. However, this effect is not large enough to compensate the total negative impact of the absorption terms, which still dominates the moderation effect. In summary, the energy-group-wise analysis provides valuable insights into the manner in

which introducing moderator pins into the fuel assembly is able to diminish the positive void reactivity as a whole.

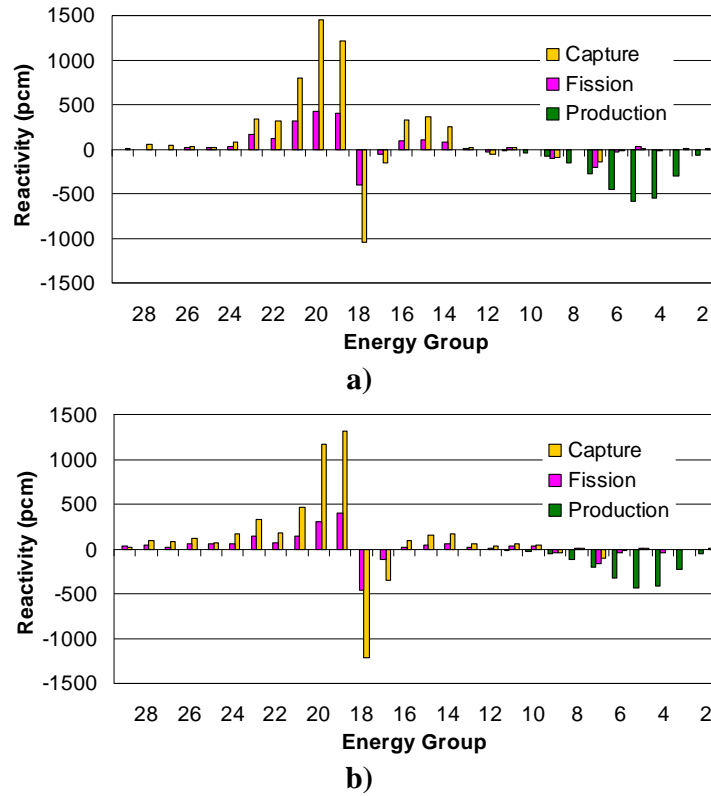


Figure 4.5. Energy dependence of the capture, fission and production components of the void reactivity for a) the reference case and b) the case with 13 moderator pins.

As a further illustration of the effectiveness of the decomposition methodology for pinpointing the physical causes of specific changes, a combined isotope- and energy-group-wise reaction rate decomposition has been carried out for understanding the strong deterioration of the breeding gain upon introduction of the moderator. Firstly, the group-wise total capture rate is shown in Figure 4.6a, for both the reference and moderator (13-pin) cases. For this particular investigation, the neutron balance normalization has been done with respect to the reactor power, i.e. approximately to the same neutron production rate. It is found that the total capture rates, in the two cases, are almost the same; however, due to the introduced moderator, the energy distribution is generally shifted towards lower energies.

The energy distribution of capture rates in Figure 4.6a has been split further into individual isotopes, the group-wise capture rates in ^{238}U and ^{239}Pu being presented in Figures 4.6b and 4.6c, respectively. For the moderator case, the major part of the decrease in total captures at higher energies (i.e. above 5 keV) is seen to come from ^{238}U . On the contrary, the compensating increase in total captures in the

lower energy range is caused not only by ^{238}U but also by the fissile isotopes, principally ^{239}Pu . This implies that, in the moderator case, the total capture rate of ^{238}U is decreased, whereas that of ^{239}Pu is increased. Overall, the effect is that a certain fraction of neutrons, which were earlier captured by fertile material, are now “shared” by absorption in fertile and fissile isotopes. This qualitatively explains the strong negative effect of the moderator on the breeding gain.

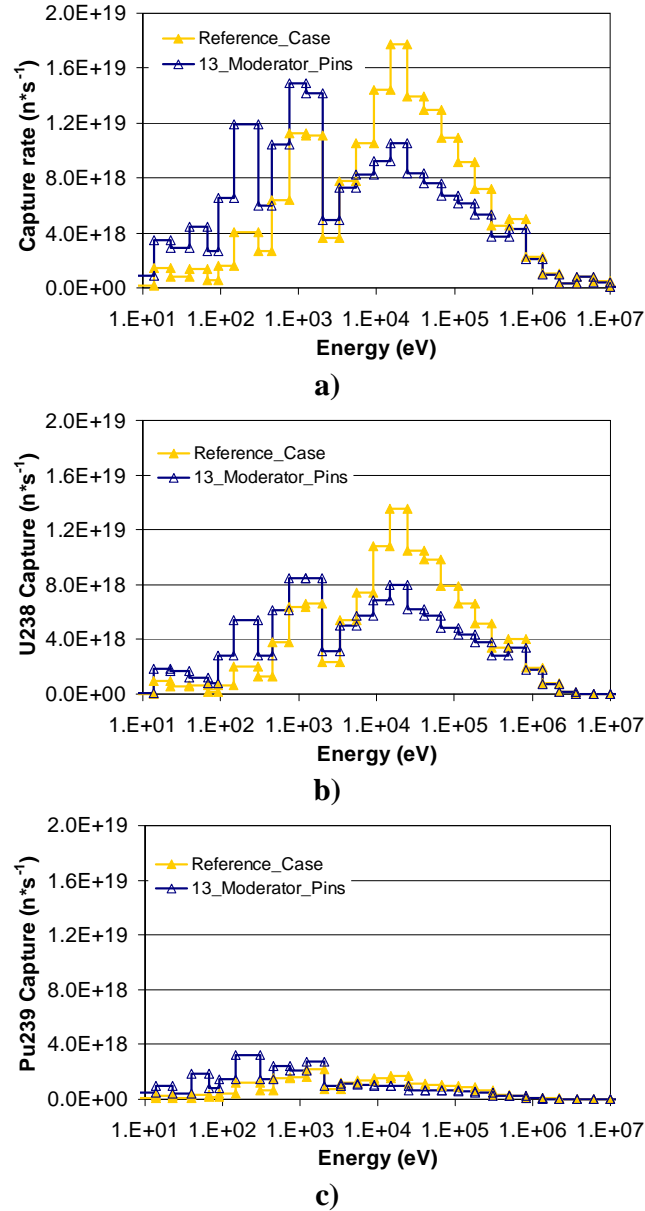


Figure 4.6. Energy-group-wise reaction rate distributions in the reference and moderator (13-pin) cases, for a) total capture, b) ^{238}U capture and c) ^{239}Pu capture.

4.2.4 Initial plutonium content

As mentioned earlier, if a particular optimization option (e.g. the smaller H/D ratio considered in Subsection 4.2.2) makes the core sub-critical, increasing the plutonium content of the fresh fuel would clearly be a possible measure to consider. In this subsection, the corresponding sensitivity analysis has been carried out using increased or decreased values for the initially loaded plutonium content. The average plutonium content of the reference core design is 15.8%, and the values of the two tested cases have been chosen to be 16.7% and 14.9%. It should be noted that, in order to preserve a similar power distribution as in the reference core design, the modifications in the inner and outer fuel zones are not equal. Further information on the modifications made can be found in Subsection 4.1.2.

Table 4.8 gives an overview of the considered safety and performance parameters, for the different plutonium contents of the initially loaded fuel. It can be seen, on the one hand, that better safety related parameters can be obtained with less plutonium in the core; however, the improvement is not very significant. On the other hand, with more plutonium in the core, the nominal reactivity is strongly increased, but at the same time, the breeding ability is considerably reduced. The deterioration in breeding gain is, of course, simply due to the fuel composition change, no other core design modification having been made.

Table 4.8. Safety and performance parameters at BOL for the cases with different initial plutonium contents

Pu content	$\Delta\rho_v(\text{pcm})$	DC (pcm)	ρ (pcm)	BG
14.9%	1499	-1292	-2367	0.1208
15.8% (reference)	1578	-1204	934	0.0644
16.7%	1627	-1112	4144	0.0081

The reaction-wise void reactivity decomposition is presented in Table 4.9. As seen, there are mainly two reaction-wise effects when one has a higher plutonium content in the core. On the one hand, the production term is less negative, and on the other hand, the absorption terms are less positive. The former change is stronger than the latter, which yields a slightly more positive overall void reactivity (the change in the leakage component being relatively small).

The fact that the change in the production term is smaller is basically because the core with a higher plutonium content has a harder spectrum in the nominal state. As a result, the spectral shift leads to a more significant fission rate increase in the energy range between 0.1 MeV and 10 MeV, where the η value (i.e. $\nu\sigma_f/\sigma_a$) of ^{239}Pu is relatively high. This implies a stronger positive production contribution in this upper energy range. When the sodium elastic scattering is no longer present due to core voiding, the overall negative production term (mainly due to the reduced fission rate at lower energies) is of somewhat lower importance due to the enhanced fission rate in the upper energy range.

Table 4.9. Reaction-wise void reactivity decomposition at BOL for the cases with different plutonium contents.

Pu content	$\Delta\rho_P$	$\Delta\rho_L$	$\Delta\rho_C$	$\Delta\rho_F$	$\sum_{P,L,C,F} \Delta\rho$
14.9%	-2870	-682	4053	991	1492
15.8% (reference)	-2579	-664	3892	923	1572
16.7%	-2304	-660	3730	855	1621

In order to obtain a deeper understanding of the plutonium content effect on the void reactivity, an isotope-wise decomposition is useful, and the results obtained for the reference and increased plutonium cases are shown in Table 4.10.

Table 4.10. Reaction- and isotope-wise void reactivity decomposition at BOL for the cases with a) 15.8% Pu content (reference case), and b) 16.7% Pu content.

a)				
15.8% Pu	$\Delta\rho_P$	$\Delta\rho_C$	$\Delta\rho_F$	$\sum_{P,C,F} \Delta\rho$
U238	37	2084	-12	2109
Pu239	-1904	728	680	-496
Pu240	110	391	-37	464
Pu241	-700	79	244	-377

b)				
16.7% Pu	$\Delta\rho_P$	$\Delta\rho_C$	$\Delta\rho_F$	$\sum_{P,C,F} \Delta\rho$
U238	44	1981	-15	2010
Pu239	-1717	709	635	-373
Pu240	122	380	-43	459
Pu241	-651	77	235	-339

As discussed in the previous chapter, the less strongly fissionable isotopes, e.g. ^{238}U and ^{240}Pu , increase the void reactivity through their positive capture terms. Conversely, the fissile isotopes, e.g. ^{239}Pu and ^{241}Pu , are able to reduce the void effect due to their significantly negative production components. Tables 4.10a and 4.10b reflect these factors. Comparing the two tables, one notes that the positive ^{238}U capture term is decreased notably. This is because of the lower uranium mass in the fuel, as also the lower flux level. At the same time, one observes that – in spite of the higher plutonium content – the negative ^{239}Pu production term is decreased significantly. This has been discussed in the

previous paragraph as being a consequence of the spectrum hardening in the nominal state. With the effect from ^{239}Pu being larger than that from ^{238}U , a slightly more positive total void reactivity results.

4.3 Results for the equilibrium fuel cycle

In this section, equilibrium fuel cycle calculations have been carried out. For each of the studied cases, the core has been considered with normal sodium density (zero void) during burnup, and results are shown for the evolution of k_{eff} while approaching the equilibrium closed fuel cycle. To be noted is that the final equilibrium state is independent of the path adopted for approaching equilibrium, so that the path itself is of secondary importance in the present study. The considered safety and performance parameters for each core at equilibrium have been assessed using the fuel composition obtained for the corresponding BEC state.

4.3.1 Upper sodium plenum and boron layer

Figure 4.7 shows the k_{eff} evolution with time for the cases with sodium plenum and boron layer, as well as for the reference core. The approaching paths to the final equilibrium state are seen to be very similar for the different cases. Effectively, it is seen that one can almost neglect the impact of the sodium plenum and boron layer on the fuel cycle.

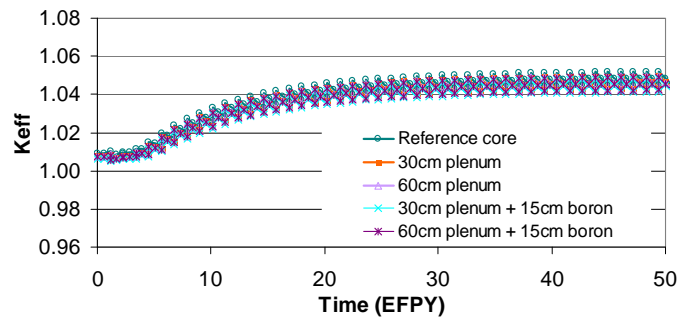


Figure 4.7. Evolution of k_{eff} while approaching the equilibrium closed fuel cycle for the cases with sodium plenum and boron layer, as well as for the reference core. EFPY represents Equivalent Full Power Years.

Table 4.11 compares the BEC results for the cases with 60 cm sodium plenum, with and without a 15 cm boron layer, with the corresponding results for the reference core. Firstly, one sees that the nominal reactivity is significantly higher in the equilibrium state than that at BOL, the same observation having been made in the fuel cycle analysis in Section 3.2. This is due to the core breeding. Furthermore, there is only a small difference in the nominal reactivity (less than 300 pcm) between the reference case and the case with sodium plenum plus boron layer, which confirms the negligible impact of the

analyzed options on the fuel cycle. The equilibrium state also implies iso-breeding per definition, so that the breeding gain value at this state effectively represents the reactivity swing within one batch (along with the effect of the ^{241}Pu decay during reprocessing). Accordingly, it is easy to understand that the BEC breeding gain values for the studied cases (with or without sodium plenum and boron layer) are almost identical.

Table 4.11. Safety and performance parameters at BEC for the cases with 60 cm sodium plenum, with and without a 15 cm boron layer, as also for the reference core.

	$\Delta\rho_V(\text{pcm})$	DC (pcm)	$\rho(\text{pcm})$	BG
Reference	2050	-795	5182	0.0316
with sodium plenum	1401*	-797	4957	0.0316
and with boron layer	1292*	-797	4929	0.0315

* for the extended voiding scenario

The Doppler effect in the equilibrium state is seen to be significantly reduced, as compared to that at BOL. This is mainly caused by the spectral change and the reduction of ^{238}U (due to its transmutation to plutonium and minor actinides) in the equilibrium fuel composition. The differences in the Doppler constant between the considered individual cases are negligible. The positive void reactivity values at BEC are generally higher than those at BOL, which is mainly due to the appearance of fission products and the reduction of the ^{241}Pu amount. Last but not least, the sodium plenum and the boron layer retain their favorable void reactivity reduction effect in the equilibrium state.

4.3.2 Core H/D ratio

Figure 4.8 presents the k_{eff} evolution for the three cores with different H/D ratios. One can see that the k_{eff} value of the reference core remains more or less constant over the first few batches, while the cores with higher and lower H/D ratio act as breeder and burner, respectively. Nevertheless, after about a four-year operation, all the three cores work as breeders, i.e. the k_{eff} value increases in each case until equilibrium is reached. Once again, the path adopted for approaching equilibrium is of secondary importance. In this sense, the most significant results from the equilibrium calculation are the final stabilized k_{eff} level and the fuel composition at the BEC state. As seen in Figure 4.8, the core with larger H/D ratio has a k_{eff} value stabilized at a higher level, the situation being reversed for the smaller H/D. This is related to the breeding ability, which implies a higher or a lower effective amount of fissile material in the equilibrium state.

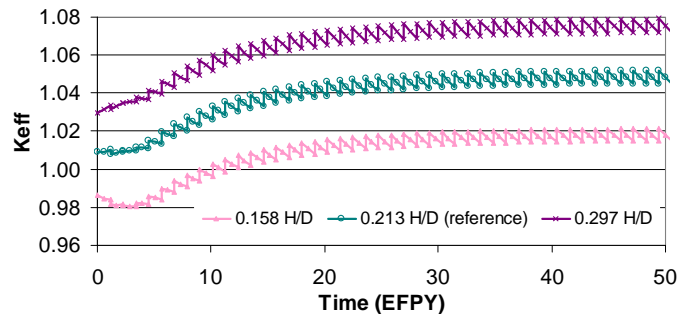


Figure 4.8. Evolution of k_{eff} while approaching the equilibrium closed fuel cycle for the three cores with different core H/D ratios.

The safety and performance parameter results at BEC are listed in Table 4.12. The influence of the core shape on the void reactivity becomes weaker, as compared to that at BOL. Slightly larger differences in the Doppler constant are observed between the different core shapes. These can be explained by the different fuel compositions at BEC. The nominal reactivity remains positive at BEC with a flatter core, but is significantly smaller than for the higher H/D case. The breeding gain values at equilibrium are almost the same for the three different H/D cores which, once again, implies that their reactivity swings within one batch (along with the ^{241}Pu decay effect during reprocessing) are of the same magnitude.

Table 4.12. Safety and performance parameters at BEC for the different core H/D ratios.

H/D ratio	$\Delta\rho_v$ (pcm)	DC (pcm)	ρ (pcm)	BG
0.158	1836	-818	2360	0.0313
0.213 (reference)	2050	-795	5182	0.0316
0.297	2175	-758	7572	0.0317

4.3.3 Moderator pins

In Figure 4.9, the k_{eff} evolutions for each of the different moderator cases are shown, along with that for the reference case. Although all the four curves start at approximately the same point, they are separated almost immediately thereafter. Furthermore, it is found that the case with 13 moderator pins in the fuel assembly effectively fails to reach criticality for the equilibrium closed fuel cycle. For the other two moderator cases, i.e. fuel assembly with 3 and 7 moderator pins, the equilibrium state can be considered feasible, even though the nominal reactivity margin is significantly reduced compared to the reference case.

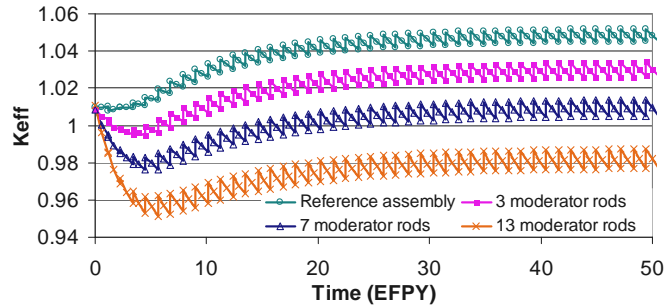


Figure 4.9. Evolution of k_{eff} while approaching the equilibrium closed fuel cycle for the different moderator cases.

The considered safety and performance parameters at BEC have been assessed for each moderation step (see Table 4.13). Similarly as seen earlier, the safety parameters, i.e. void reactivity and Doppler constant, are found to deteriorate in comparison to values at BOL. Nevertheless, also at BEC, the presence of moderator continues to have favorable effects on them. It is confirmed here that, with 13 moderator pins in the fuel assembly, the nominal reactivity is negative at BEC, so that the core is not feasible in this state. The highest breeding gain value is found for this hypothetical case, consistent with the fact that it corresponds to the strongest reactivity swing within one batch (and the greatest ^{241}Pu decay during reprocessing in the equilibrium state).

Table 4.13. Safety and performance parameters at BEC for the cases with inserted moderator pins.

Moderator	$\Delta\rho_V(\text{pcm})$	DC (pcm)	ρ (pcm)	BG
0 (reference)	2050	-795	5182	0.0316
3 pins	1992	-1091	3573	0.0371
7 pins	1911	-1418	1706	0.0431
13 pins	1839	-1787	-880	0.0493

4.3.4 Initial plutonium content

Finally, the equilibrium fuel cycle calculations are reported for the cases with different BOL plutonium contents of the fuel. As can be seen in Figure 4.10, the three k_{eff} evolution curves start from different initial states and then converge after about 10 years operation. In the end, they reach a consistent equilibrium state. It has been mentioned in [4.07] that the final equilibrium state is dependent on the core geometry, feed composition and fuel management, but independent of the initial fuel composition, which is consistent with the results shown here. This feature clearly provides considerable flexibility in the choice of the BOL fuel composition and the corresponding refueling scheme during the first few fuel cycles.

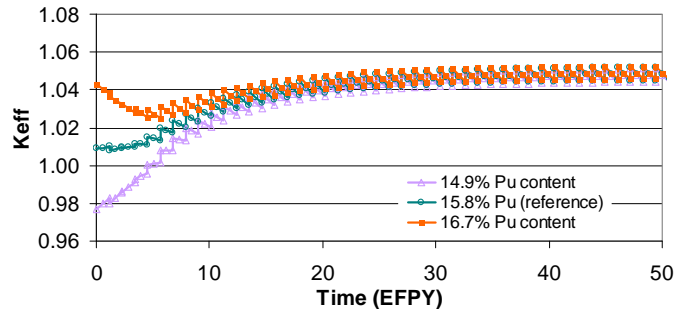


Figure 4.10. Evolution of k_{eff} while approaching the equilibrium closed fuel cycle for the different initial plutonium content cases.

Since a consistent equilibrium state is reached for the three initial plutonium loading cases, their safety and performance parameters at BEC are, as to be expected, also very consistent (see Table 4.14).

Table 4.14. Safety and performance parameters at BEC for the cases with different initial plutonium contents.

Pu content	$\Delta\rho_V(\text{pcm})$	DC (pcm)	ρ (pcm)	BG
14.9%	2050	-797	5180	0.0317
15.8% (reference)	2050	-795	5182	0.0316
16.7%	2051	-795	5183	0.0316

4.4 Main findings and proposed optimized cores

4.4.1 Summarized discussion of the results

The four currently studied optimization options for the SFR have been: a) introducing an upper sodium plenum and boron layer, b) varying the core H/D ratio, c) introducing moderator pins into the fuel assembly, and d) modifying the initially loaded plutonium content.

Figure 4.11 provides a summarized representation of the results obtained from the sensitivity studies which have been carried out. First of all, it is seen that the sodium plenum (along with boron layer) has the favorable effect of void reactivity reduction – with the extended voiding scenario considered as basis – without any significant side effect. This is found to be the case for both BOL and BEC states (see Figure 4.11a). Secondly, a lower H/D ratio can reduce the void reactivity, but both nominal reactivity and breeding ability are deteriorated, the influence on the former being particularly strong (see Figure 4.11b). Thirdly, introducing moderator pins into the fuel assembly can improve both the safety related parameters (see Figure 4.11c). However, this option significantly decreases the breeding

Chapter 4: Neutronics Optimization of the ESFR Core

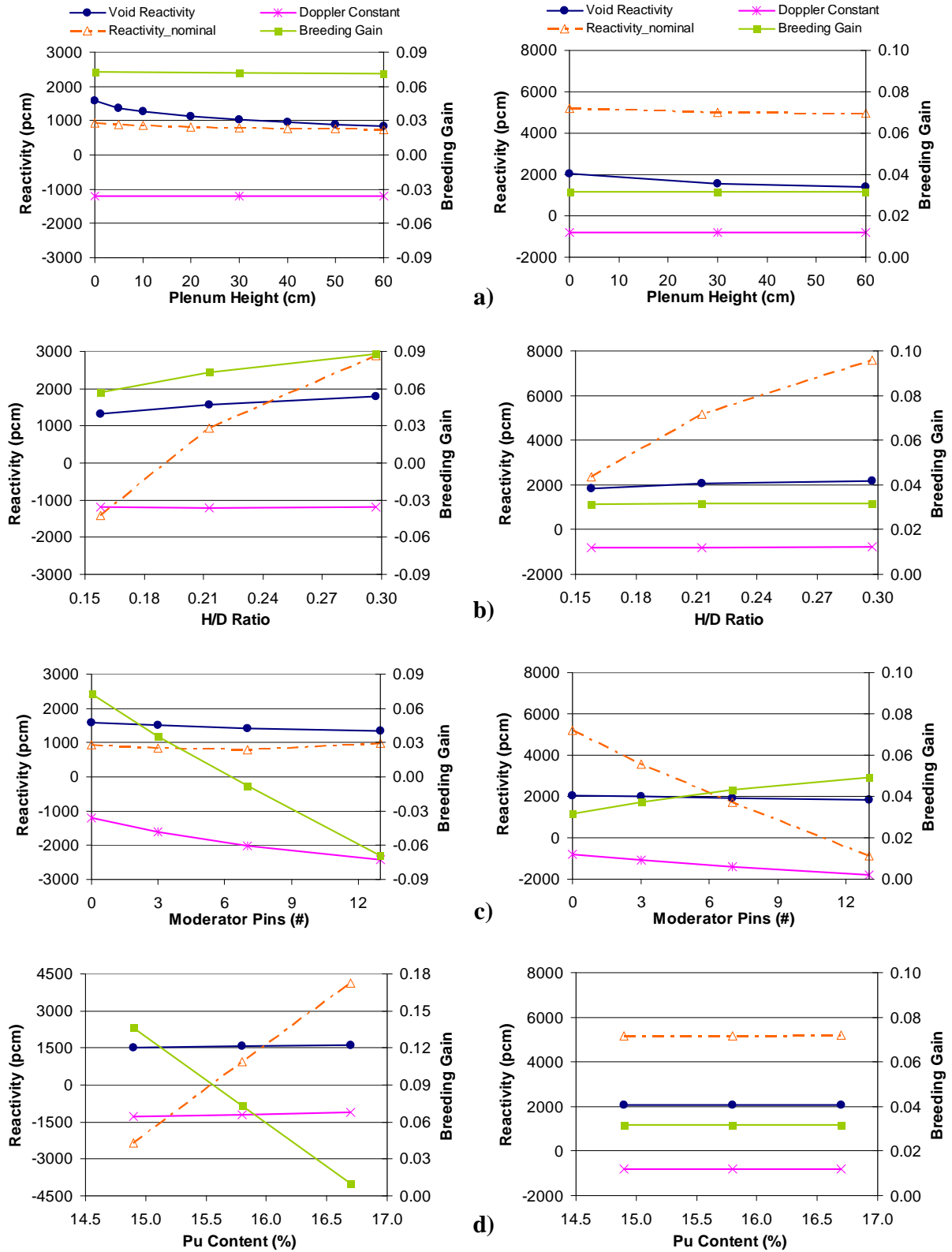


Figure 4.11. Sensitivity of the considered safety and performance parameters, at BOL (left) and BEC (right), to a) sodium plenum, b) H/D ratio, c) moderator and d) BOL fuel plutonium content.

gain at BOL and, if more than seven moderator pins are inserted into the fuel assembly, not enough reactivity margins are available for the BEC state. Thus, with lower H/D ratio or with introduced moderator, there can be an initial phase at the beginning of the path approaching equilibrium (see Figures 4.8 and 4.9), during which the fuel cycle becomes unfeasible (due to the occurrence of sub-criticality) unless other compensatory changes are made. Increasing the plutonium content of the fresh fuel is clearly such a measure, as is seen clearly in Figure 4.11d, which shows the effects of this last considered optimization option. As to be expected, the nominal reactivity increases strongly, while the breeding gain decreases; the equilibrium fuel cycle state reached, however, is the same as for the reference core.

Table 4.15 presents a simplified “score table” for the four studied optimization options. Thereby, each of the considered safety and performance parameters is provided with a certain type of arrow, corresponding to improvement (\nearrow), deterioration (\searrow) or little effect (\rightarrow), the number of arrows (1 to 3) in the first two cases indicating the magnitude of the effect. It should be noted that some of the findings of the present study are qualitatively quite similar to those of [4.03].

Table 4.15. A score table evaluating the impact of the four different optimization options on the considered safety and performance parameters at BOL and BEC, respectively.

Optimization Option	BOL Parameters				BEC Parameters			
	$\Delta\rho_v$	DC	ρ	BG	$\Delta\rho_v$	DC	ρ	BG
Sodium plenum & boron layer	$\nearrow\nearrow$	\rightarrow	\searrow	\rightarrow	$\nearrow\nearrow$	\rightarrow	\searrow	\rightarrow
Decreasing H/D ratio	\nearrow	\rightarrow	$\searrow\searrow\searrow$	\searrow	\nearrow	\rightarrow	$\searrow\searrow\searrow$	\rightarrow
Adding moderator	\nearrow	$\nearrow\nearrow\nearrow$	\rightarrow	$\searrow\searrow\searrow$	\nearrow	$\nearrow\nearrow\nearrow$	$\searrow\searrow\searrow$	\rightarrow
Increasing initial plutonium content	\rightarrow	\rightarrow	$\nearrow\nearrow\nearrow$	$\searrow\searrow$	\rightarrow	\rightarrow	\rightarrow	\rightarrow

4.4.2 Proposed optimized cores

Two different combinations of the considered optimization options are proposed in the following as possible “synthesis” core concepts, which merit further, more detailed study. In each case, having a positive nominal reactivity at the End of Equilibrium closed fuel Cycle (EEC) has been set as boundary condition. Furthermore, the upper sodium plenum thickness that has been considered is 30 cm, rather than 60. This is based on a compromise between neutronics and thermal-hydraulics aspects. On the one hand, the larger the sodium plenum the stronger the void effect reduction (see Figure 4.4) and the greater the expected hydraulic stability of sodium boiling phenomena (according to [4.08]). On the other hand, from the viewpoint of a hypothetical ULOF accident scenario, violent

oscillations can occur if the neutronics/thermal-hydraulics coupling becomes too strong due to an over-dimensioned plenum size (see Appendix B for a more detailed discussion). Furthermore, the sodium plenum is only partly voided under pre-dryout conditions and one cannot take advantage of the boron layer unless the sodium plenum is of limited height. Accordingly, 30 cm has been considered to be more appropriate as plenum thickness than 60, and the two possible optimized SFR cores proposed are:

- Synthesis Core 1 (SC1) characterized by - lowest void reactivity: introduction of a 30 cm upper sodium plenum, along with a 15 cm boron layer; H/D ratio of the core reduced to 0.158 (with 11 rings of fuel pins in the fuel assembly); average BOL fuel plutonium content increased to 16.7%.
- Synthesis Core 2 (SC2) characterized by - joint optimization of both safety parameters: introduction of a 30 cm upper sodium plenum, along with a 15 cm boron layer; H/D ratio of the core increased to 0.297 (with 9 rings of fuel pins in the fuel assembly); introduction of 9 moderator pins into the fuel assembly (increasing the fuel assembly height correspondingly).

Table 4.16 presents the calculated safety and performance parameters for the two proposed synthesis cores, as well as for the reference ESFR core. It is seen that SC1 has a void reactivity as low as 321 pcm at BOL (for the extended voiding scenario, i.e. with voiding assumed for the sodium plenum as well as the core). The Doppler constant is similar to that for the reference core. In the case of SC2, the void reactivity is also reduced in comparison with the reference ESFR core, although less significantly than with SC1. However, the Doppler constant is much stronger.

Table 4.16. Safety and performance parameters at different fuel cycle states, for the two proposed synthesis cores as well as the reference ESFR core.

	BOL				BEC				EEC	
	$\Delta\rho_V(\text{pcm})$	DC (pcm)	$\rho(\text{pcm})$	BG	$\Delta\rho_V(\text{pcm})$	DC (pcm)	$\rho(\text{pcm})$	BG	$\rho(\text{pcm})$	ρ -swing
ref SFR	1578	-1204	934	0.0644	2050	-795	5182	0.0316	4586	596
SC1	321*	-1106	1187	-0.0029	854*	-816	1779	0.0316	1182	597
SC2	1038*	-2343	2335	-0.0418	1511*	-1666	1519	0.0479	478	1041

* for the extended voiding scenario

In the BEC state, the safety parameters, viz. void reactivity and Doppler constant, are both seen to be significantly deteriorated, relative to BOL, the degree of deterioration being quite similar in all three cores. Clearly, appropriate safety margins need to be applied for the equilibrium state, when designing an SFR core on the basis of its BOL fuel composition. Nevertheless, the SC1 core is seen to have a relatively low void reactivity even at BEC, while the magnitude of the Doppler constant at BEC is the largest in the case of SC2. Furthermore, it is seen that the breeding gain is positive for all three cores at BEC. As indicated earlier, its magnitude in the equilibrium cycle is correlated with the reactivity swing

within one batch (along with the ^{241}Pu decay effect during processing). Last but not least, having been set as the boundary condition, a positive nominal reactivity is observed at EEC for both synthesis cores.

4.5 Chapter summary

Certain promising optimization options for the core of a large SFR have been studied quantitatively in this chapter, with discussion the trade-offs between the considered safety and performance parameters. A principal aim has been to achieve a reduction of the positive sodium void reactivity – the one dominating neutronics drawback of SFRs. In this context, the introduction of an upper sodium plenum, along with a boron layer, has been found to be the most effective option, with further improvements also achievable via a reduction of the H/D ratio and/or the introduction of moderator pins into the fuel assembly. The latter two options, however, reduce the nominal reactivity in the first few fuel cycles, and an increase in the plutonium content of the fresh fuel can become necessary.

Both BOL and BEC conditions have been considered, and emphasis has been placed on obtaining a physical understanding of the impact of the different optimization options on the void reactivity. The latter has been achieved by applying the neutron balance based reactivity decomposition methodology described in the previous chapter.

Based on the sensitivity studies carried out, two different synthesis core concepts have been proposed. The following chapter assesses the impact of the implemented design improvements on the core dynamic behavior, with a representative unprotected loss-of-flow accident being selected as basis for comparison. Although the emphasis in the current research is clearly on neutronics aspects, certain thermal-hydraulics optimizations – in the context of the coupled neutronics/thermal-hydraulics phenomena involved – will also be presented there.

References

- [4.01] H. S. Khalil and R. N. Hill. Evaluation of Liquid-Metal Reactor Design Options for Reduction of Sodium Void Worth. *Nuclear Science and Engineering*, vol. 109: pp. 221-266, 1991.
- [4.02] Y. I. Kim, R. Hill, K. Grimm, G. Rimpault, T. Newton, Z. Li, A. Rineiski, P. Mohanakrishnan, M. Ishikawa, K. B. Lee, A. Danilytchev, V. Stogov. BN-600 Full MOX Core Benchmark Analysis. In *PHYSOR 2004*, paper 95579.
- [4.03] L. Buiron, Ph. Dufour, G. Rimpault, G. Prulhiere, C. Thevenot, J. Tommasi, F. Varaine, A. Zaetta. Innovative Core Design for Generation IV Sodium-cooled Fast Reactors. In *ICAPP 2007*, paper 7383.
- [4.04] P. Sciora, D. Blanchet, L. Buiron, B. Fontaine, M. Vanier, F. Varaine, C. Venard, S. Massara, A.C. Scholer, D. Verrier. Low void effect core design applied on 2400 MWth SFR reactor. In *ICAPP 2011*, paper 11048, 2011.
- [4.05] J. Krepel, S. Pelloni, K. Mikityuk, P. Coddington. EQL3D: ERANOS based equilibrium fuel cycle procedure for fast reactors. *Annals of Nuclear Energy*, vol. 36: pp. 550-561, 2009.
- [4.06] K. Sun, J. Krepel, K. Mikityuk, S. Pelloni, R. Chawla. Void reactivity decomposition for Sodium-cooled Fast Reactor in equilibrium fuel cycle. *Annals of Nuclear Energy*, vol. 38: pp. 1645-1657, 2011.
- [4.07] J. Krepel, K. Mikityuk, K. Sun, G. Rimpault. SFR equilibrium cycle analysis with the EQL3D procedure. In *ICAPP 2009*, paper 9226.
- [4.08] J. M. Seiler, D. Juhel, Ph. Dufour. Sodium boiling stabilization in a fast breeder subassembly during an unprotected loss of flow accident. *Nuclear Engineering and Design*, vol. 240: pp. 3329-3335, 2010.

Chapter 5

Impact of Optimization on Transient Behavior

The proposal of two alternative, optimized “synthesis” cores in Chapter 4 has been made purely on the basis of reactor statics considerations. The current chapter focuses on their dynamic behavior during a representative unprotected loss-of-flow (ULOF) accident scenario in which sodium boiling occurs. It is found that the neutronics optimization carried out in the previous chapter is not – on its own – sufficient to prevent fuel damage^{5.1} during the postulated event and that the implementation of certain thermal-hydraulics related improvements are needed.

The coupled PARCS/TRACE model employed for the multi-physics simulations, as well as the selected transient, are described in Section 5.1. The behavior of the reference ESFR core at BOL is presented in Section 5.2 as the starting point of the study. A comparative analysis of the two proposed optimized cores (i.e. SC1 and SC2; see Subsection 4.4.2) is also reported in this section. In spite of certain improvements being observed with the optimized cores, it is found that sodium flow blockage – which leads to fuel failure – cannot be prevented.

For overcoming this difficulty, an innovative wrapper design for the fuel assembly is proposed in Section 5.3, and the behavior of the optimized cores is re-analyzed. On the one hand, it is found that – at BEC – a positive total reactivity feedback cannot be avoided over the entire transient in the case of the SC2 core, which then justifies the decision not to consider this core design further. On the other hand, the SC1 core maintains a negative total reactivity feedback at both BOL and BEC; however strong coolant flow instability – related to sodium vaporization/condensation oscillations in the upper plenum – is observed. Section 5.4 describes the implementation and analysis of a second thermal-hydraulics improvement, viz. an alternative plenum design, which effectively amounts to replacing the original sodium plenum by an extended fission gas plenum. With this final variation of the SC1 core design, it is shown that one can indeed prevent cladding and fuel from melting during the selected ULOF accident scenario, at BOL as well as at BEC^{5.2}. A chapter summary is provided in Section 5.5.

^{5.1} Since detailed thermal-mechanical modeling has not been carried out currently, reaching the melting temperature of either fuel or cladding is considered as the criterion for fuel failure.

^{5.2} For the sake of simplicity, the fuel and cladding melting temperatures are assumed to be independent of the fuel cycle state.

5.1 The PARCS/TRACE model and selected transient

The present SFR dynamics study has been conducted using a coupled PARCS/TRACE model. A representative ULOF transient, i.e. flow run-down without SCRAM, in which sodium boiling is anticipated to occur, has been selected as the considered accident scenario. It should be noted that the specific ULOF scenario chosen in the current study is mainly intended to demonstrate the effectiveness of the ESFR design improvements which are being proposed, a detailed SFR safety analysis being clearly beyond the scope of the present doctoral research.

5.1.1 Description of the PARCS/TRACE model

In this subsection, the adopted PARCS and TRACE models are described respectively. The mapping scheme, which connects the two models, is also presented.

PARCS model

As described in Subsection 2.2.1, the 33-group macroscopic cross-sections of the nominal core state and their corresponding derivatives are prepared for the PARCS code using the ECCO module in ERANOS, the format being processed with the in-house routine ERANOS2PARCS. PARCS takes the reactivity feedbacks into account through these basic cross-sections and derivatives. In the current study, four reactivity components are considered: the coolant density effect (including the void effect), the Doppler effect, and the effects of thermal expansion of fuel (axial expansion) and core diagrid (radial expansion).

A 60-degree symmetry is considered in the PARCS model, so that only one sixth of the studied SFR core needs to be simulated; this consists of 85 fuel assemblies, 60 reflector channels, and 7 control and safety rods. Radially, the size of the node corresponds to the fuel assembly pitch, i.e. 21 cm, while the size of the axial mesh largely depends on the actual height of the corresponding zones, but is always of the order of 10 cm. It should be mentioned that the computational nodes in PARCS are homogenized in hexagonal geometry.

TRACE model

The TRACE model represents 1/12 of the studied SFR core. Thereby, it consists of 52 parallel channels (PIPEs): 45 fuel channels, 5 control rod channels, 1 safety rod channel, and 1 channel to represent all the vertical bypasses including inter-assembly gaps and reflectors (see Figure 5.1a). From the bottom to top, the channels are divided into different zones corresponding to: lower fission gas plenum, lower reflector, fuel region, upper fission gas plenum, and upper reflector. In particular, each fuel region of the channels is represented by a heat structure (HTSTR), where the power generation is simulated. A schematic view of the TRACE model is shown in Figure 5.1b.

As mentioned earlier, the transient analysis is carried out for both BOL and BEC conditions. For the sake of simplicity, however, the material properties employed in the TRACE fuel rod model are assumed to be the same for both fuel cycle states.

Since the principal purpose of the present transient study is to demonstrate the effectiveness of the proposed ESFR core design improvements, only the reactor core region is explicitly described in the current TRACE model. Accordingly, appropriate boundary conditions have been applied at the inlet for coolant temperature and mass flow rate, and at the outlet for the pressure.

Mapping scheme

The PARCS and TRACE models have been coupled via an appropriate mapping scheme, linking the neutronics nodes to the corresponding thermal-hydraulics channels and heat-structure components. In order to facilitate the mapping, the nodalization schemes in the PARCS and TRACE models have been chosen to be as close as possible.

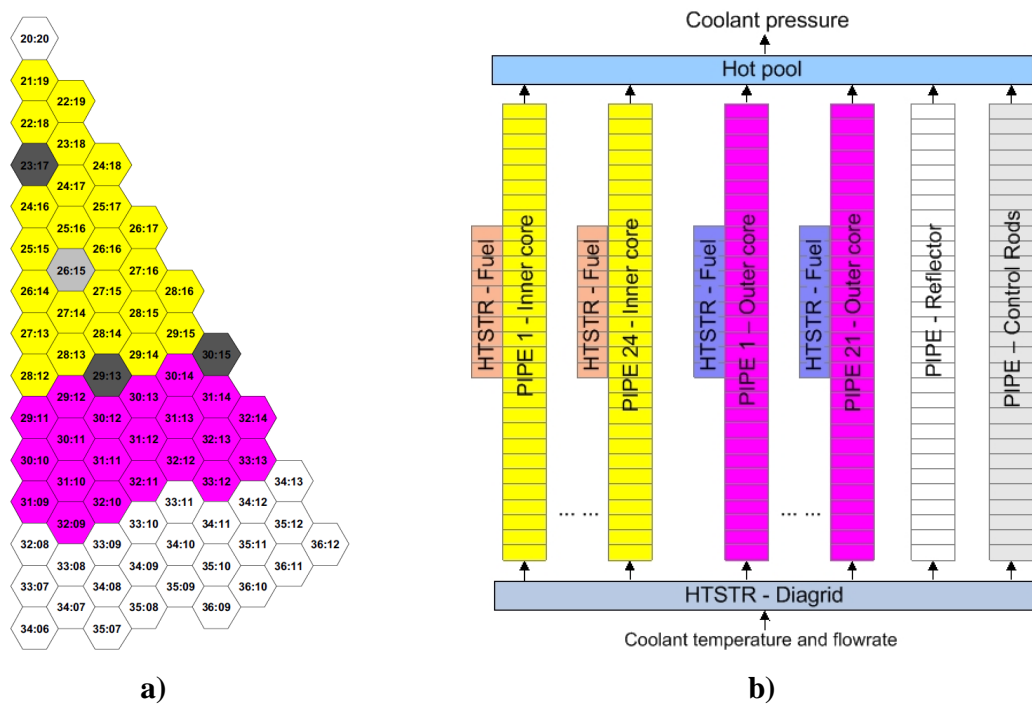


Figure 5.1. a) 1/12 of the SFR core modeled in TRACE and b) schematic of the TRACE model.

5.1.2 Verification of the PARCS/TRACE model

The coupled PARCS/TRACE model has been verified by code-to-code comparisons against reference static ERANOS calculations for the BOL state.

First, the comparisons have been carried out in terms of nominal core state reactivity, Doppler effect (DOP), axial expansion effect (AXI), radial expansion effect (RAD), coolant density effect in the active core (DAC) and void effect in the same region (VAC). For this stage, diffusion theory has been adopted as the flux solving option in both PARCS/TRACE and ERANOS. It should be pointed out that results from this part of the study were reported in [5.02]. As the next step, the coolant density effect and the void effect in the upper sodium plenum region (DSP and VSP) have been verified in particular. Here, not only diffusion theory, but also the transport theory options (simplified spherical harmonics and full transport solution) have been used in ERANOS. This more detailed consideration is necessary because the coolant density reactivity feedback in the upper sodium plenum region – as discussed in Chapter 4 – is largely dominated by the leakage effect, which renders the comparison with transport theory more important.

For the PARCS/TRACE nominal state, the fuel is assumed to be at room temperature (i.e. 20 °C) and the sodium has a density of 950 kg/m³. For each of the perturbed core states considered, only a single variable is changed. Thus, the DOP state has an increased fuel temperature of 727 °C, the AXI state has an increase in fuel height of 2.197 cm (while considering that the fuel and cladding are not bound), the RAD state has an increase of fuel assembly pitch by 0.170 cm (due to thermal expansion of the diagrid), the DAC and DSP states have the coolant density reduced to 777 kg/m³ in the corresponding regions, and the VAC and VSP states focus on the sodium void effect (i.e. the coolant density reduced to almost zero).

The macroscopic cross-sections for the nominal and perturbed states, generated by the ECCO module in ERANOS, have been used both in the VARIANT module of ERANOS and in the coupled PARCS/TRACE model. Strictly speaking, the latter uses the individual cross-section derivatives to simulate the perturbed states. The nominal reactivity obtained with ERANOS is 3244 pcm, whereas with PARCS/TRACE it is 3010 pcm. Even though both sets of neutronics calculations adopt diffusion theory, the latter result is 234 pcm lower than the former. This difference may be due to, at least in part, the different nodal schemes employed. VARIANT uses a variational nodal method based on the even-parity form of the transport equation [5.03], whereas PARCS uses the Triangle-based Polynomial Nodal (TPEN) method [5.04].

The comparisons of reactivity feedback effects in the active core region (viz. DOP, AXI, RAD, DAC and VAC) are shown in Figure 5.2a. Even though a slight difference has been found in the nominal reactivity comparison, the reactivity feedbacks predicted by the two codes are generally in very good agreement. One notes a relatively large discrepancy in the AXI values. This is because the control rod treatment in the two codes is different. When the fuel expands in ERANOS, the control rod position is correspondingly shifted upwards, while in PARCS/TRACE the control rod position remains the same. The resulting overlapping between the fuel and control rod nodes makes the axial expansion effect more negative in the latter case. However, as to be seen later, the reactivity effect contribution from axial expansion is generally not dominant during the considered ULOF transient. Thus, its overall influence on the core behavior is not very significant.

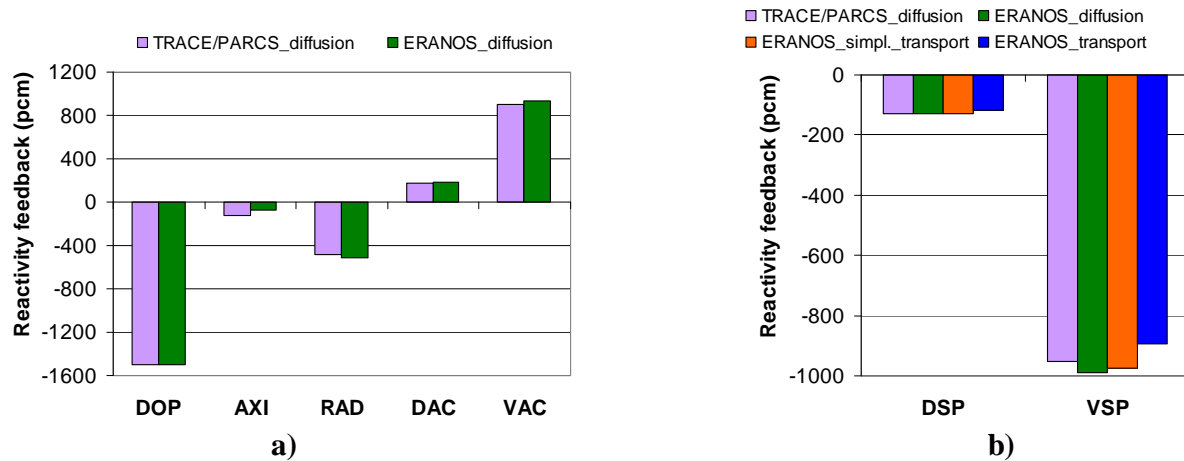


Figure 5.2. Comparisons of the reactivity feedbacks calculated by ERANOS and PARCS/TRACE:
a) active core region feedbacks, b) upper sodium plenum region feedbacks.

As mentioned earlier, the transient analysis carried out in the current doctoral research has been restricted to a simulation of just the core region in the primary circuit. Consequently, the present PARCS/TRACE model is not able to catch the response of the secondary circuit during the transient. Instead, the core inlet temperature has been assumed to be constant. Thus, even though the radial thermal expansion effect – which is induced by the diagrid temperature change and normally provides a large negative reactivity feedback when the inlet temperature is increased – has been calculated and verified, it is actually not taken into account due to the above mentioned restriction. This of course renders the currently obtained results for the transient somewhat conservative.

Figure 5.2b shows the comparisons of reactivity feedbacks caused by the coolant density variation in the upper sodium plenum region (i.e. the DSP and VSP cases). While the diffusion theory option is maintained in PARCS/TRACE, the ERANOS results include those with its two transport options. As can be seen, the four sets of result are generally in good agreement. The full transport solution gives the most conservative prediction of the negative sodium plenum effect. However, considering that the calculated reactivity feedback is for the voiding of the entire upper sodium plenum, the PARCS/TRACE overestimation is relatively small, viz. only 36 pcm. Accordingly, it can be concluded that the coupled PARCS/TRACE model predictions of static neutronic parameters are quite satisfactory for reactivity feedback effects, not only in the active core but also in the upper sodium plenum region.

5.1.3 Description of the ULOF transient

A simple coolant flow run-down curve has been chosen as basis for defining the reference ULOF accident scenario in the present doctoral research. In principle, the corresponding parameters should be defined while considering the primary pump characteristics and the primary circuit layout; however, the exact features of the reference ESFR primary system are still unknown. By making reasonable

estimations for the flow run-down, the inlet mass flow rate can be derived according to the following equations:

$$\frac{\dot{m}(t)}{\dot{m}_0} = \left(1 - \frac{\dot{m}_\infty}{\dot{m}_0}\right) \cdot \exp(-at) + \frac{\dot{m}_\infty}{\dot{m}_0} \quad \text{Eq. 5.1}$$

$$a = \frac{1}{t_{1/2}} \cdot \ln \left(\frac{1 - \frac{\dot{m}_\infty}{\dot{m}_0}}{\frac{1}{2} - \frac{\dot{m}_\infty}{\dot{m}_0}} \right) \quad \text{Eq. 5.2}$$

where \dot{m}_0 represents the initial mass flow rate at steady state and an asymptotic level of 20% is assumed for \dot{m}_∞ . a is a parameter characterizing the half-time $t_{1/2}$, i.e. the time after which the flow is reduced by 50%. During such a hypothetical accident, sodium boiling is anticipated to occur and, as such, its consideration is crucial for assessing SFR safety. Once again, it should be noted that the specific ULOF accident scenario chosen here is mainly intended to demonstrate the effectiveness of the ESFR design improvements which are being proposed, a detailed SFR safety analysis being clearly beyond the scope of the present doctoral research. The transient starts always at 400s in this study, the normalized inlet mass flow rate as function of time being shown in Figure 5.3.

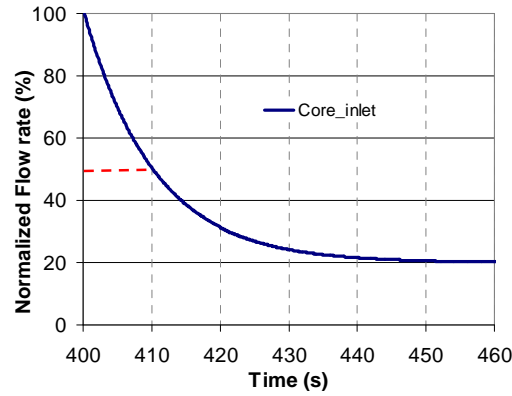


Figure 5.3. Evolution of the normalized coolant flow rate at the core inlet during the ULOF.

5.2 Core behavior during the ULOF transient at BOL

As mentioned, the core response to a ULOF transient of the type considered is of prime importance for the safety demonstration of an SFR. Since sodium boiling is anticipated to occur, this may lead to a severe accident situation, in which both fuel and cladding melt and relocate. In this section, the core behavior during the selected ULOF accident scenario is analyzed for the reference ESFR core design

and for the two optimized cores (SC1 and SC2) proposed in the previous chapter. BOL has been chosen as the reference fuel cycle state for the start of the transient study, with BEC conditions also being considered later.

5.2.1 The reference ESRF core behavior at BOL

In this subsection, the case of the reference ESRF core at BOL is presented as the starting point for the core behavior investigations. First of all, one can see the power evolution in Figure 5.4a. It is found that the core power decreases slightly during the first 30s of the transient, down to about 90% of the initial value. Thereafter, a clear sharp increase occurs, in combination with slight oscillations (with a frequency of the order of 1 Hz). Within about 10s, the core power reaches 220% of the initial value. It should be noted here that sodium boiling onset occurs at 427s, only a few seconds ahead of the turning point of the power curve.

The responses of the fuel and cladding temperature in the hottest nodes, together with the melting temperatures of MOX (the fuel) and Fe-Cr based ODS (the steel type adopted for the cladding) [5.05], are presented in Figure 5.4b. During the first 30s of the transient, a slight increase of the maximum fuel temperature (i.e. centerline fuel temperature in the hottest channel) is found to occur, even though the core power decreases a little. Meanwhile, the cladding temperature increases because the significant reduction of the coolant flow rate makes the heat transfer at the cladding surface less efficient. After the boiling onset at 427s, the response of the cladding temperature comes first, and the cladding reaches its melting temperature at about 440s. The rise in the fuel temperature occurs somewhat later, since this is dominantly driven by the core power which jumps up shortly after 430s. Nevertheless, the fuel starts to melt several seconds earlier than the cladding.

The explanation of the power evolution during the ULOF accident can be drawn from the development of the total reactivity and its decomposition. After the transient starts, both coolant and fuel become hotter. The former introduces positive reactivity feedback due to the decreased coolant density, whereas the latter brings in a negative reactivity contribution because of the Doppler effect and axial thermal expansion of fuel. As seen in Figure 5.4c, the total reactivity is found to be slightly negative during the first 30s, with the sum of Doppler and axial expansion effects being somewhat stronger than the compensating coolant density effect. Consequently, the core power decreases slightly during this period. However, after the sodium boiling onset, the reactivity feedback from the coolant density effect becomes much more dominant which drives the total reactivity positive. As a result, the core power is sharply increased. (It should be noted here, once again, that – even though the radial thermal expansion effect has been calculated and verified (see Subsection 5.1.2) – it is actually not taken into account due to the current restriction on simulating primary/secondary circuit interaction.)

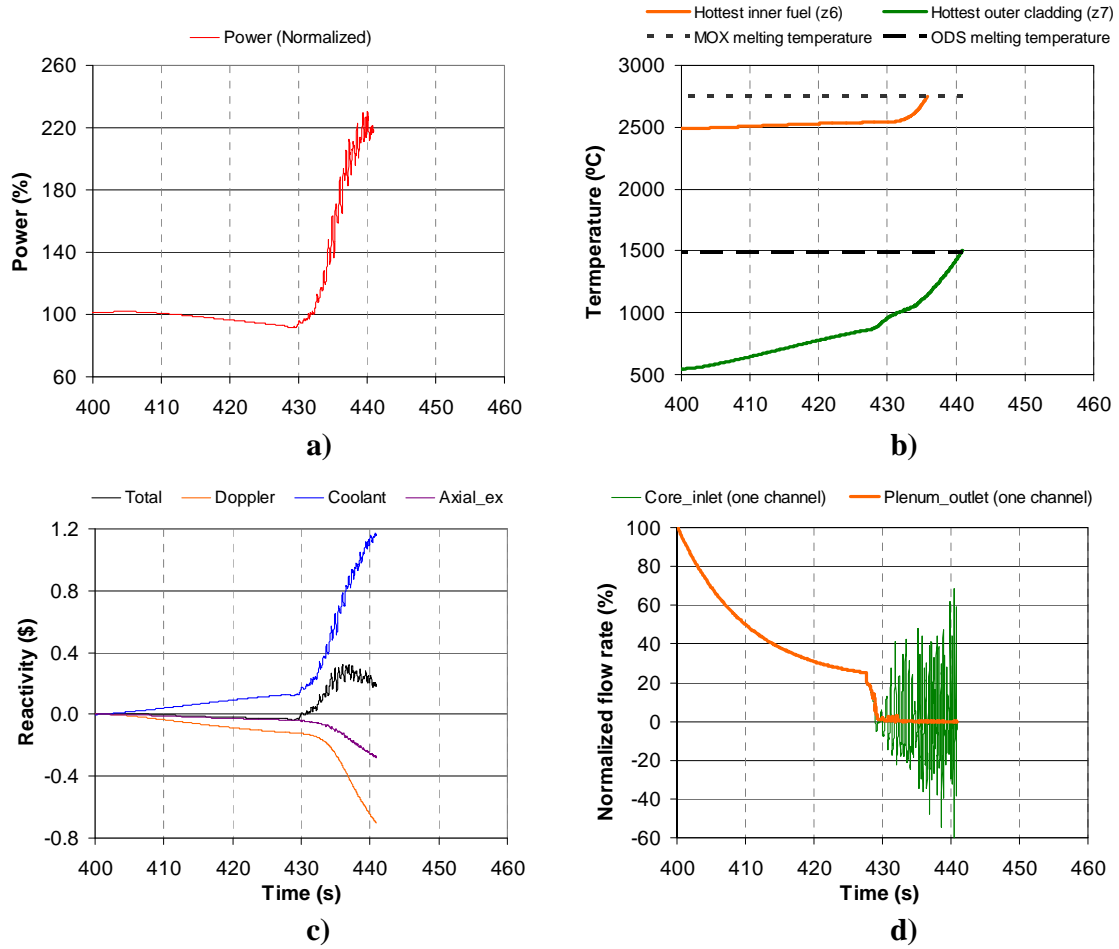


Figure 5.4. ULOF for the reference ESFR core at BOL: evolutions of a) power, b) fuel and cladding temperatures in the hottest channel (in which sodium boiling starts), c) total reactivity and its decomposition, d) normalized inlet and outlet flow rates in the hottest channel.

Finally, the flow rates in the hottest channel, at the core inlet and at the upper fission gas plenum outlet, respectively, are presented in Figure 5.4d. It is seen that the flow rate in this specific channel largely follows the overall flow rate change before the boiling onset at 427s. After that, significant oscillations around zero are observed at the core inlet, with the amplitude increasing with time. On the contrary, almost no flow reaches the plenum outlet following the start of boiling. Thus, a large dryout region in between is indicated, and this can be confirmed by the snapshot of the most developed void map presented in Figure 5.5c. As seen therein, a large dryout region, covering the major part of the outer core and the upper regions, is indeed observed, which explains the near-to-zero flow rate at the upper fission gas plenum outlet. Consequently, the corresponding fuel channels are fully blocked by vapor. Moreover, the vaporization/condensation process at the periphery of the dryout region can lead to significant flow rate oscillations, e.g. those shown in Figure 5.4d for the core inlet of the channel in which boiling starts.

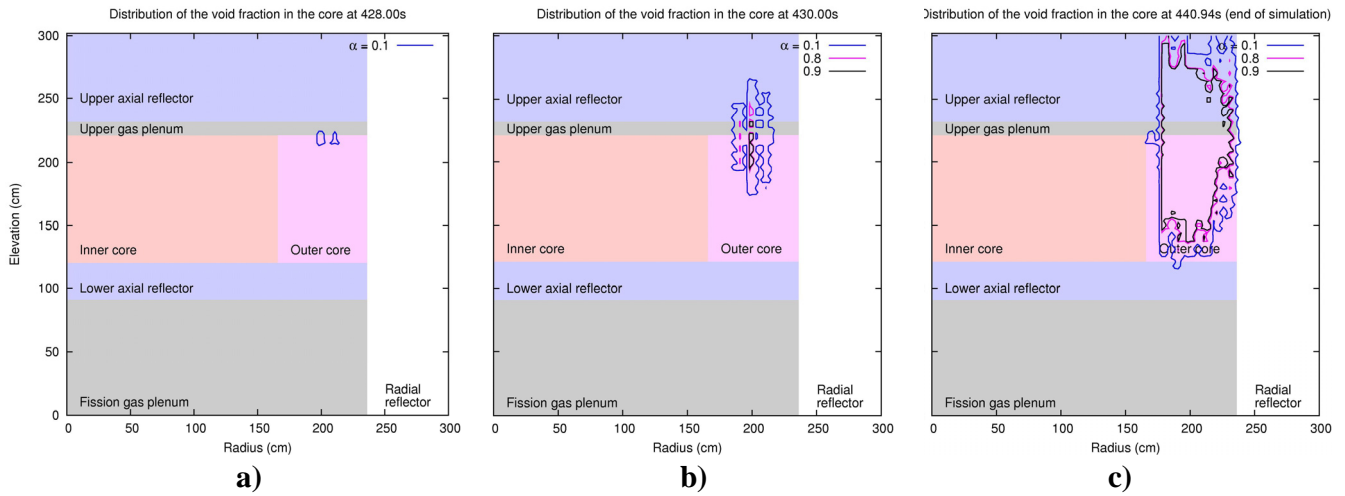


Figure 5.5. Evolution of the void region in the reference core after the sodium boiling onset from a) 428s to b) 430s, and further to c) 441s.

The full evolution of the void region in the reference core is shown in Figure 5.5. It is seen that the sodium boiling starts at the top of the outer core, where the power peak is located for the BOL fuel cycle state (see Figure 5.5a). Thereafter, the void region expands upwards and downwards simultaneously within the same channels, while also propagating radially to the neighboring fuel assemblies (see Figure 5.5b) due to the power increase. One needs to bear in mind that the boiling propagation downward in the fuel region implies a significantly positive coolant density reactivity effect, especially when the sodium void penetrates to the axial center of the core. At the end of the simulation (which is terminated by the occurrence of cladding/fuel melting), the most developed void map – as already discussed above – shows a large dryout region covering the entire upper part of the outer core (see Figure 5.5c).

5.2.2 Behavior of the SC1 core at BOL

The neutronics optimization study carried out in the previous chapter resulted in the proposal of two “synthesis” core designs based on different combinations of optimization options, viz. SC1 and SC2. In particular, the extended void reactivity of the SC1 core is as low as 321 pcm at BOL (SC1 has a 30 cm upper sodium plenum, together with a 15 cm boron layer above it; the H/D ratio of the core is reduced to 0.158; the average BOL plutonium content of the fuel is increased to 16.7%). Thus, SC1 can be expected to provide a significantly better core behavior during the considered ULOF accident than the reference SFR design. The analogous set of results as discussed for the reference case is shown in Figure 5.6.

It should first be mentioned that the boiling onset now occurs at 432s, which is about four seconds later than that in the reference case. This delay can be explained by the power evolution curve in Figure 5.6a. As a result of the core design modifications, the reduced coolant density reactivity effect

makes the initial power reduction somewhat more significant, viz. more than 10% during the first 30s of the transient. After boiling starts, the power reacts, firstly with a sharp decrease (within less than two seconds) and then with significant oscillations between 75% and 100% of the initial power level. One can easily distinguish two different frequencies for these oscillations, viz. a higher value of the order of 1 Hz (also observed in the reference case) and a lower value of about 0.1 Hz.

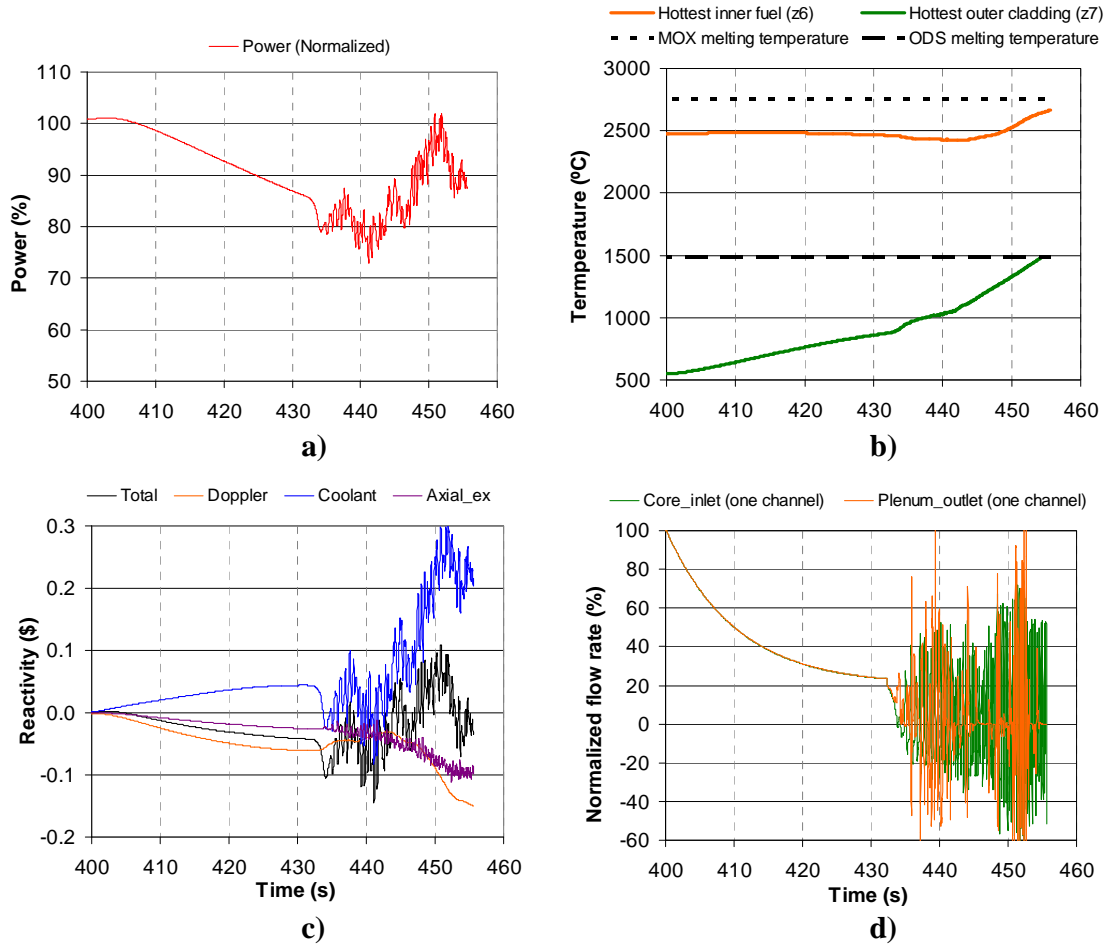


Figure 5.6. ULOF for the SC1 core at BOL: evolutions of a) power, b) fuel and cladding temperatures in the hottest channel, c) total reactivity and its decomposition, d) normalized inlet and outlet flow rates in the hottest channel.

The response of the fuel and cladding temperatures is shown in Figure 5.6b. Thanks to the moderate power level, which is not like the sharp increase in the reference case, the fuel temperature in the hottest node is kept under the melting point throughout the simulation period. However, it can be seen that one still has a clear increasing trend, so that fuel melting can be expected to occur later in the transient. Moreover, in this case, the cladding reaches its melting temperature sooner than the fuel. Its melting and consequent relocation can result in a reduction in neutron absorption, and hence in a

corresponding positive reactivity feedback. The material relocations are not, however, simulated in the current study. Nevertheless, compared to the reference case, the definitive cladding melting occurs more than ten seconds later. This is largely related to the fact that the core design modifications to improve the neutronic safety parameters (mainly to reduce the void reactivity) do yield a beneficial effect in particular, viz. a notable power decrease immediately after the boiling onset at 432s.

As seen from the reactivity decomposition in Figure 5.6c, the initial decrease in power results from a significant decrease of the coolant density reactivity effect (even a negative level is reached at a certain moment), which causes the total reactivity to become more negative. Nevertheless, within less than two seconds, it increases again and remains mostly positive during the rest of the transient, even though not as high as in the reference case, but still large enough to make the total reactivity positive.

The flow rates in the hottest channel are presented in Figure 5.6d, at the level of core inlet and upper sodium plenum outlet. It is found that, this time, the flow oscillations at plenum outlet are even more significant than those at core inlet. The reason is that the large quantity of sodium contained in the upper sodium plenum region cannot be strongly voided that easily. It is the resulting strong vaporization/condensation process, which leads to the large oscillations. As discussed later, reducing the sodium fraction in the plenum region can help to stabilize the coolant flow.

5.2.3 Behavior of the SC2 core at BOL

The SC2 core represents a combined optimization of void and Doppler effects (SC2 has a 30 cm upper sodium plenum and 15 cm boron layer; the H/D ratio of the core is increased to 0.297; it also has 9 moderator pins in the fuel assembly). Although the void reactivity in SC2 is not as significantly reduced as in the case of SC1, its Doppler constant at BOL is twice as strong as in the reference core design. Thus, the core behavior improvement resulting from a stronger Doppler effect is of prime interest here. The same ULOF transient has been simulated, and the analogous set of results as before is shown in Figure 5.7.

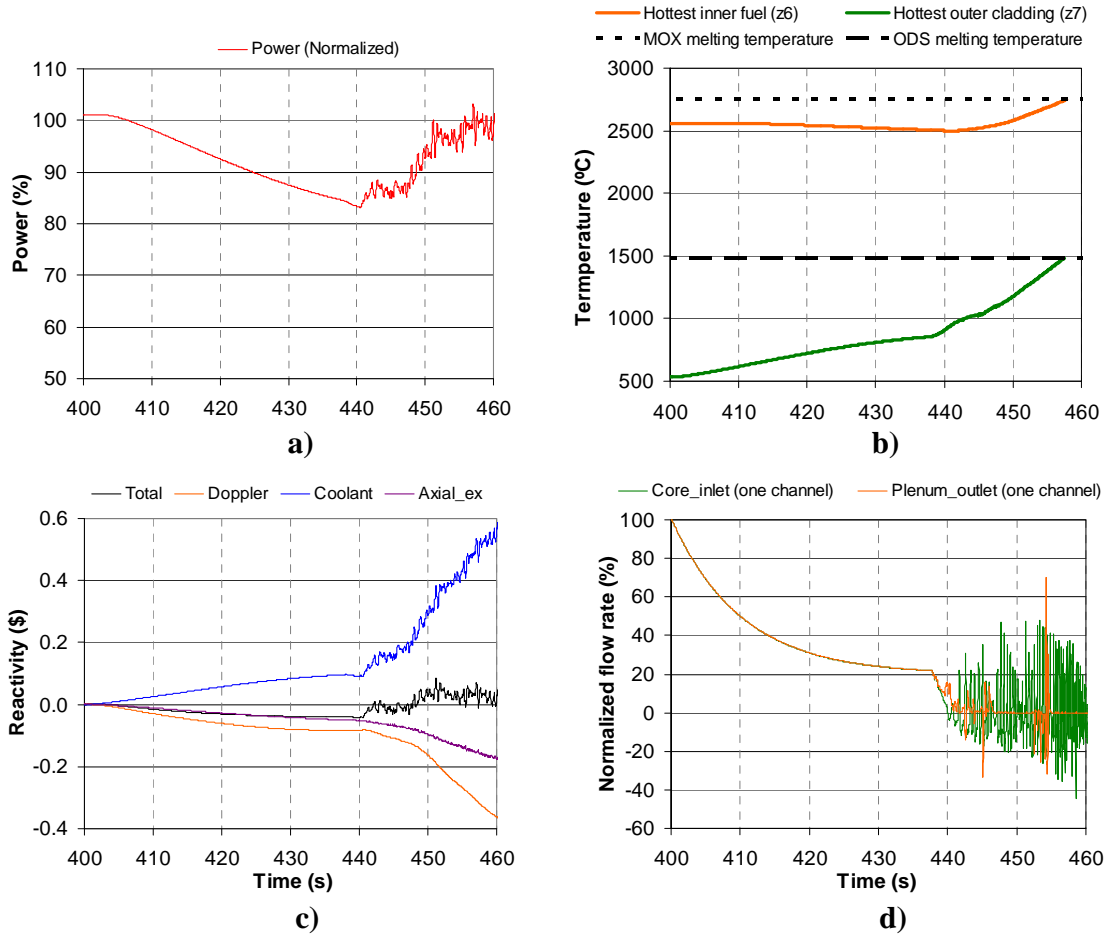


Figure 5.7. ULOF for the SC2 core at BOL: evolutions of a) power, b) fuel and cladding temperatures in the hottest channel, c) total reactivity and its decomposition, d) normalized inlet and outlet flow rates in the hottest channel.

One notes that the core behavior for SC2 is qualitatively similar to that of the reference ESRF core, but the transient develops somewhat slower. The sodium boiling onset is at 437s, which is about ten seconds later than that in the reference case. Thereafter, a power increase (even though not as sharp as in the reference case), combined with local oscillations (similar frequency of the order of 1 Hz), is observed. This is caused by the increase in total reactivity – dominated by the significant positive coolant density feedback – which follows the boiling onset. Both fuel and cladding are seen to melt at around 457s. This represents a delay relative to the reference case, and even relative to the SC1 core. As regards the coolant flow rate, one sees once again that, following the start of boiling, significant oscillations around zero are observed at the core inlet, whereas almost no flow reaches the plenum outlet. A large dryout region in between is thus clearly indicated also in this case.

5.2.4 Summary and discussion

It has been seen that – for the selected ULOF accident scenario – it is not only the core behavior of the reference ESFR design which is unsatisfactory, but also that of the two proposed cores with optimized neutronic characteristics. Neither the reduced void reactivity nor the enhanced Doppler effect appears to be capable of preventing the cladding and fuel from melting, even at BOL. Accordingly, the current investigation has not been extended to the equilibrium fuel cycle states, where the safety parameters are deteriorated. At the current stage, a deeper analysis and further optimization is clearly necessary.

It is worthwhile to recall that – for the SC1 core (see Subsection 5.2.2) – there is a short period during the transient when the coolant density reactivity effect is negative. This is at about two seconds after the sodium boiling onset. From Figure 5.8a, it is seen that, at this time, the sodium void is distributed in the upper fuel region of the hot channels and the corresponding sodium plenum region above. If this void map could be preserved long enough without propagating towards the core center, the reactor power, as well as the fuel temperature, would effectively decrease. Unfortunately, this is not the case in the considered core designs. The sodium void expands rapidly, especially downwards to the core center. In the end, a large dryout occurs in the hot zone and the fuel channels are blocked by sodium vapor (see Figure 5.8b).

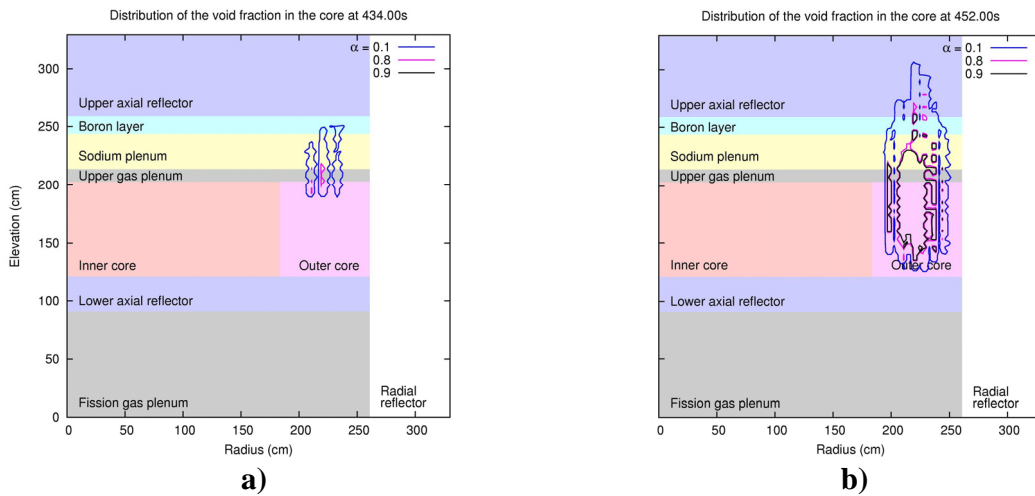


Figure 5.8. Void maps of the SC1 core at a) 434s and b) 452s during the ULOF transient at BOL.

Due to the channel blockage, the capability for heat removal from the cladding is lost, and thus it eventually melts. Nevertheless, an important clue has been obtained here: one needs a specific thermal-hydraulics design, which can effectively sustain the sodium vapor in the upper region. This would use the neutronics improvement (achieved through the enhanced leakage effect) to greater advantage. The corresponding thermal-hydraulics optimization is described in the following section.

5.3 Thermal-hydraulics optimization: wrapper openings

An innovative wrapper design for the fuel assembly is proposed for implementing the thermal-hydraulics improvement suggested above. Following a description of the new wrapper design, its effectiveness during the selected ULOF accident scenario is assessed for the two optimized cores, at both BOL and BEC.

5.3.1 Description of the innovative wrapper design

With the conventional wrapper tube design, every fuel assembly is isolated from its neighbors and has its own independent sodium flow rate. The cold sodium from the reactor lower plenum enters the assembly from the bottom, heats up inside and flows out from the assembly top into the reactor upper plenum. Under normal operating conditions, the sodium coolant always remains single-phase, i.e. liquid. However, in certain accidental situations, e.g. the currently considered ULOF scenario, there is a possibility that the sodium temperature reaches the saturation point and the coolant starts to boil. The sodium boiling pattern in such a situation is characterized by a fast formation of large vapor bubbles in the top part of the fuel bundle, where the sodium is the hottest and where the local void reactivity is close to zero or even negative (see, for example, Figure 3.5). These bubbles rapidly expand radially and may thus block the entire flow area of the channel, leading to an abrupt stop of the coolant flow at the fuel assembly inlet. As a result, the stagnant sodium inside the fuel assembly continues to boil off and the vapor propagates downwards to the core center, where the local void reactivity is strongly positive. This, in turn, implies positive total reactivity and power escalation (see Subsection 5.2.1). The rapid rise in power can lead to dryout, and finally to the melting of both cladding and fuel with subsequent release of radioactivity into the coolant. The above generic description clearly underlines the importance of the detailed consideration of SFR accident scenarios in which sodium boiling may occur.

As indicated previously, if the sodium vapor could be sustained in the upper part of the fuel region and the sodium plenum region above it, the reactivity feedback from the coolant density variation would be negative. In this context, a new wrapper design is needed which can prevent the downward void propagation to the core center. The innovative feature proposed is to introduce small openings in each side surface of the conventional wrapper tube. The exact axial location and the area of the openings would depend on the specific core design. For the currently studied SFR cores, the new wrapper considered has openings located at $\frac{3}{4}$ of the fuel region height (from the bottom) and the area of the opening is about 80cm^2 ($10\text{cm} \times 8\text{cm}$). A schematic view of the proposed wrapper design is shown in Figure 5.9a.

This new design of the wrapper tube aims at improving the unsatisfactory SFR core response during the considered ULOF accident scenario. The introduced openings are intended to provide bypasses for the coolant flow when the sodium vapor blocks the flow area at the top of the fuel. Due to these bypasses, the flow rate at the channel inlet should not drop significantly (nor oscillate strongly), so that

the sodium vapor gets prevented from propagating downwards to the core center, where the local void reactivity is strongly positive. Instead, it would propagate radially into the neighboring channels. The resulting void distribution should thus provide a close to zero or even negative coolant density reactivity feedback. Accordingly, the total reactivity can be expected to remain negative, causing the core power to decrease. Moreover, the continued availability of the sodium flow rate in the fuel assembly, where boiling occurs, would prevent dryout since a liquid film of sodium would be maintained on the cladding surface. With sufficient cooling remaining, there would not be any melting of the cladding or fuel.

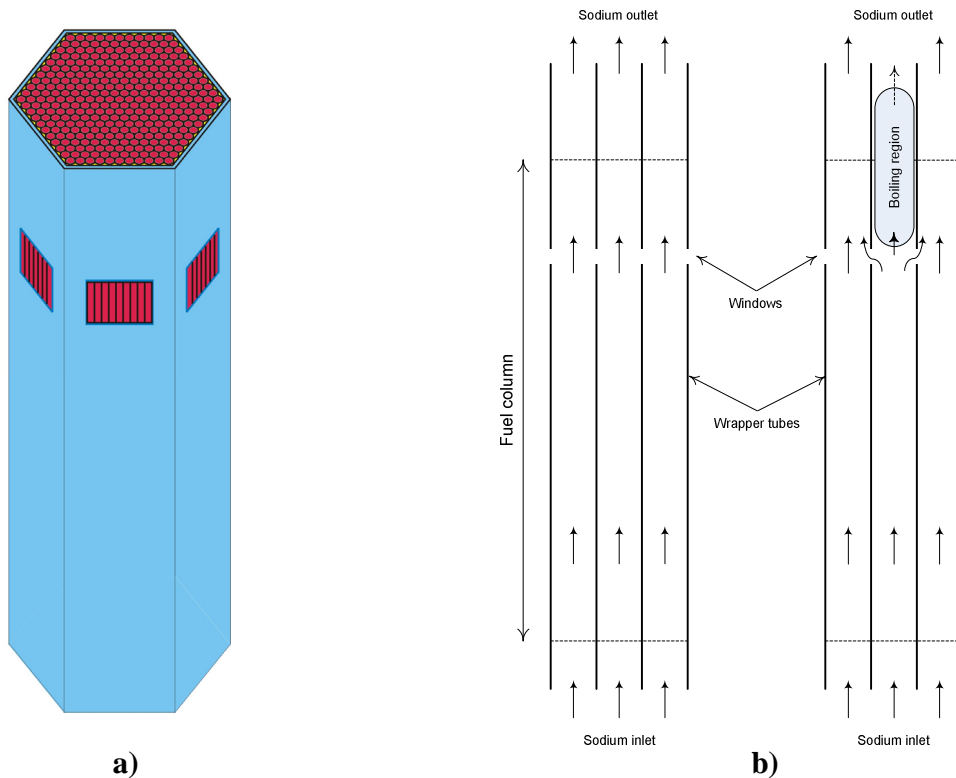


Figure 5.9. a) Schematic view of the wrapper openings and b) the flow patterns during normal operation and in the case of sodium boiling.

The above projected effectiveness of the new wrapper design clearly needs to be tested for the considered ULOF scenario, and this has been done via appropriate PARCS/TRACE simulations, as described in the following subsections. The principal modification made in the TRACE model was the creation of side junctions between all the 45 fuel channels, at $\frac{3}{4}$ of the fuel region height from the bottom. Neighboring channels, according to the mapping scheme, were connected by additional hydraulic components with a flow area of 80cm^2 . It should be mentioned that the thermal-hydraulic impact of sodium flowing between wrappers is neglected by the current TRACE model. In addition, the cross-flow between neighboring fuel assemblies, due to the introduced openings, has been found to be relatively minor in normal operation. Nevertheless, these two features of the TRACE modeling

need to be verified by a detailed CFD (Computational Fluid Dynamics) study. The flow patterns during normal operation and in the case of sodium boiling are illustrated in Figure 5.9b.

Finally, in this subsection, it should be mentioned that a European patent has recently been filed for the new wrapper design, in view of its considerable potential for improving SFR core behavior under sodium boiling conditions [5.06].

5.3.2 Behavior of the SC1 core with wrapper openings at BOL

The core behavior of the SC1 core at BOL has been re-analyzed for the same ULOF accident scenario, but this time in conjunction with the introduced wrapper openings. It is found that, in this case, the sodium boiling onset occurs at 436s, which is about four seconds later than in the case without openings. This postponement can be explained by small cross-flows occurring between neighboring channels during normal operation, which tend to slightly flatten the temperature gradient across the core. As mentioned earlier, such a predicted phenomenon should be checked with CFD calculations.

As seen in Figure 5.10a, the power evolution before the boiling onset is similar to the case with conventional wrapper design, i.e. a smooth decrease down to 85% of the initial power level within about 35s. After this, however, the behavior is quite different. Instead of the significant low-frequency power oscillation that one had in the previous case, a clear reduction is now found to occur, the power level decreasing down to 60% in less than ten seconds. Unfortunately, before a definite trend can be derived, the simulation “crashes” due to numerical non-convergence. Nevertheless, the significant improvement in comparison to the case with the conventional wrapper design, i.e. the power evolution shown in Figure 5.6a, can be clearly seen.

The evolutions of the fuel and cladding temperatures in the hottest node are presented in Figure 5.10b. The maximum fuel temperature curve is relatively flat before the boiling onset at 436s, the effects of the decreased core power and of the reduced coolant flow rate compensating for each other quite closely. Once the sodium starts to boil, the sharp reduction of the core power becomes dominant, so that the fuel temperature decreases significantly. The cladding temperature shows an increase at the beginning of the transient, since it is mainly influenced by the reduced coolant flow. However, the decreased fuel temperature after the boiling onset restricts the rise in cladding temperature. In the end, it seems to be saturated at a little below 1000°C, remaining more than 500°C under the melting point of the Fe-Cr based ODS steel.

The improved core behavior for the case with wrapper openings is mainly due to the total reactivity remaining negative throughout the transient. As seen in Figure 5.10c, the coolant density reactivity effect rapidly drops down to a strongly negative level after the sodium boiling onset at 436s. It is then the dominant component of the negative total reactivity, which finally leads to the power reduction. Even though some oscillations appear afterwards, a decreasing trend is clear. Furthermore, one can also see that the Doppler effect and the axial fuel expansion effect become positive in the later stages

of the transient, the increase being stronger for the former. These changes can be explained by the reduction of core average fuel temperature.

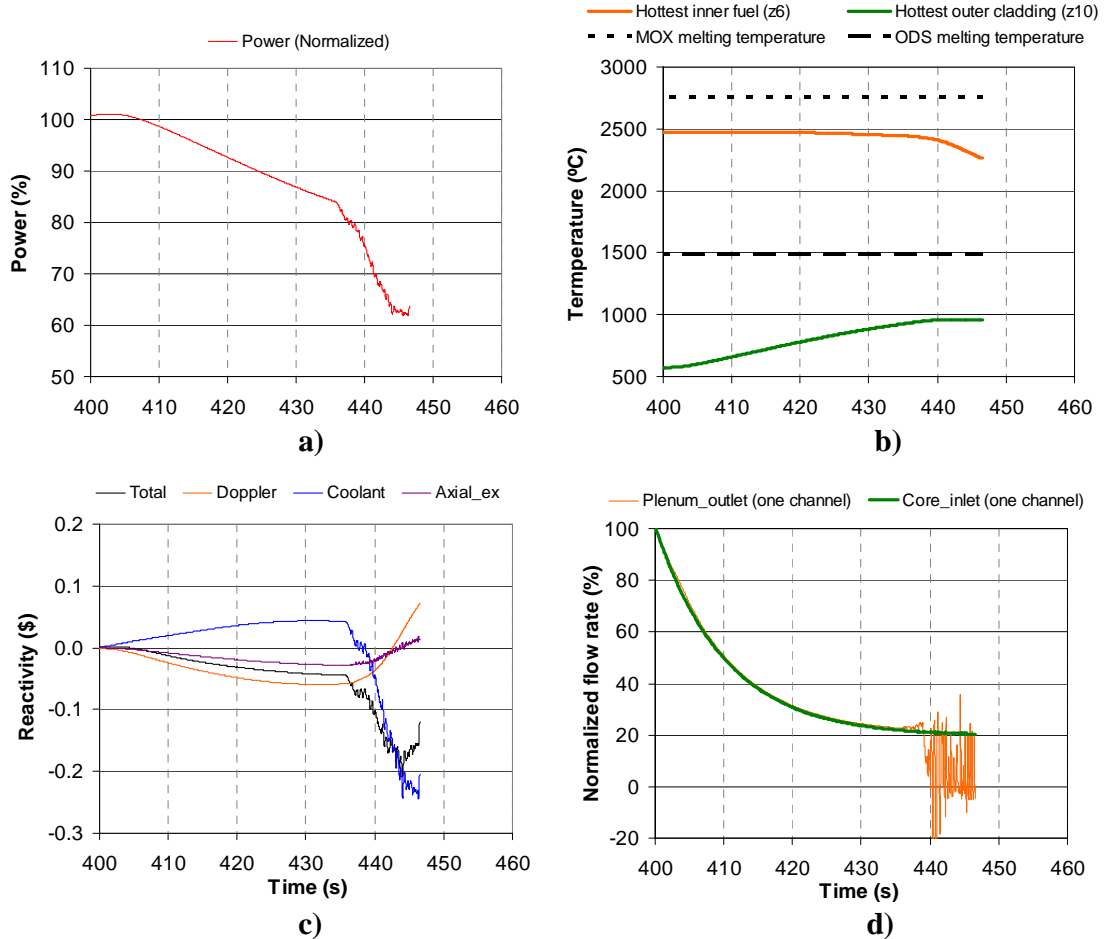


Figure 5.10. ULOF for the SC1 core with wrapper openings at BOL: evolutions of a) power, b) fuel and cladding temperatures in the hottest channel, c) total reactivity and its decomposition, d) normalized inlet and outlet flow rates in the hottest channel.

Thanks to the bypasses through the wrapper openings, there is no channel blockage when sodium boiling develops. It can be seen in Figure 5.10d that the flow rate at the core inlet of the hottest channel follows the overall flow run-down in quite a stable manner. At the upper sodium plenum outlet, however, there are strong flow oscillations. As explained earlier, this is because the large quantity of sodium in the sodium plenum region cannot be fully voided and the resulting vaporization/condensation process leads to a strong oscillatory behavior.

The schematics of the sodium void propagation for the case with wrapper openings are demonstrated in Figure 5.11. When the boiling onset occurs, the first sodium bubble appears at the top of the outer

core (see Figure 5.11a). Thereafter, as seen in Figures 5.11b and 5.11c, the sodium vapor propagates upwards to the sodium plenum and radially into the neighboring channels, the resulting void maps providing negative coolant density reactivity feedback. As compared to the void propagation scheme for the case without wrapper openings (i.e. the void maps shown in Figure 5.8), the downward expansion of the sodium vapor is effectively limited, since bypasses are currently provided for the coolant flow.

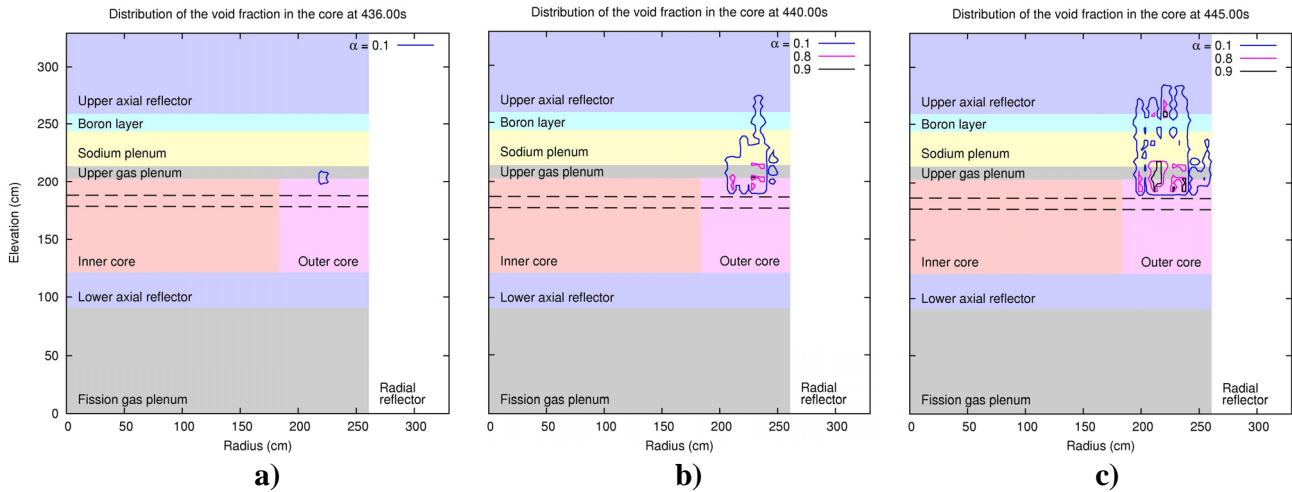


Figure 5.11. Void maps of the SC1 core with wrapper openings at a) 436s, b) 440s and c) 445s, respectively, during the ULOF transient at BOL. The dashed lines indicate the region of introduced wrapper openings.

5.3.3 Behavior of the SC1 core with wrapper openings at BEC

Even though the previous simulation is terminated (due to numerical instability) before a definite trend can be derived, the advantageous impact of the introduced wrapper openings has been successfully demonstrated. At the BOL state, a strong negative coolant density reactivity feedback is observed after the sodium boiling onset. This brings certain expectations that, from the neutronics viewpoint, this core may remain satisfactory during the considered ULOF scenario even under equilibrium fuel cycle conditions, where the safety related parameters are significantly deteriorated. Accordingly, the core behavior of the SC1 core with wrapper opening has been investigated at BEC, the corresponding set of results being shown in Figure 5.12.

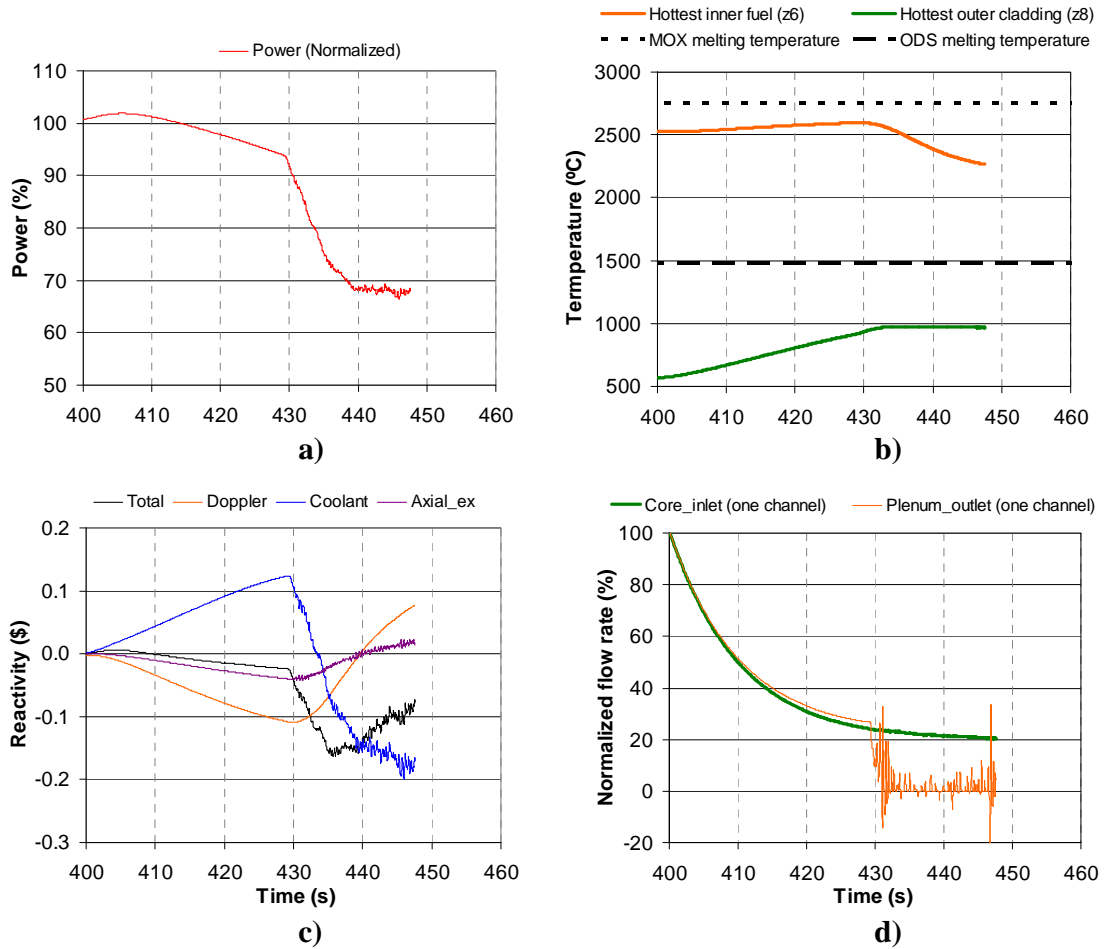


Figure 5.12. ULOF for the SC1 core with wrapper openings at BEC: evolutions of a) power, b) fuel and cladding temperatures in the hottest channel, c) total reactivity and its decomposition, d) normalized inlet and outlet flow rates in the hottest channel.

It can be seen that, generally speaking, the core behaves similarly at BEC as at BOL. In the equilibrium fuel cycle, the core has an increased positive coolant density reactivity feedback in the active core region and a reduced Doppler effect, so that, after the transient starts, the power decreases less rapidly than in the case with fresh fuel (compare Figures 5.12a and 5.10a). Due to the slower power reduction before the sodium boiling onset, the maximum fuel temperature increases slightly in this period, instead of remaining constant as for the case at BOL (compare Figures 5.12b and 5.10b). The deteriorated coolant density reactivity effect in the active core region at BEC is reflected in the overall coolant density effect presented in Figure 5.12c: a more positive level ($> 0.1\$$) is reached before the boiling onset, and thereafter the reduction is somewhat less significant. Last but not least, severe flow rate oscillations are observed at the sodium plenum outlet (as in the BOL case), and the simulation is terminated once again, mainly for this reason.

5.3.4 Behavior of the SC2 core with wrapper openings at BOL

The introduction of wrapper openings has also been applied to the ULOF analysis for the SC2 core at BOL (cf. Subsection 5.2.3), the results obtained being presented in Figure 5.13. One can see that, in this case, the simulation goes through without numerical non-convergence.

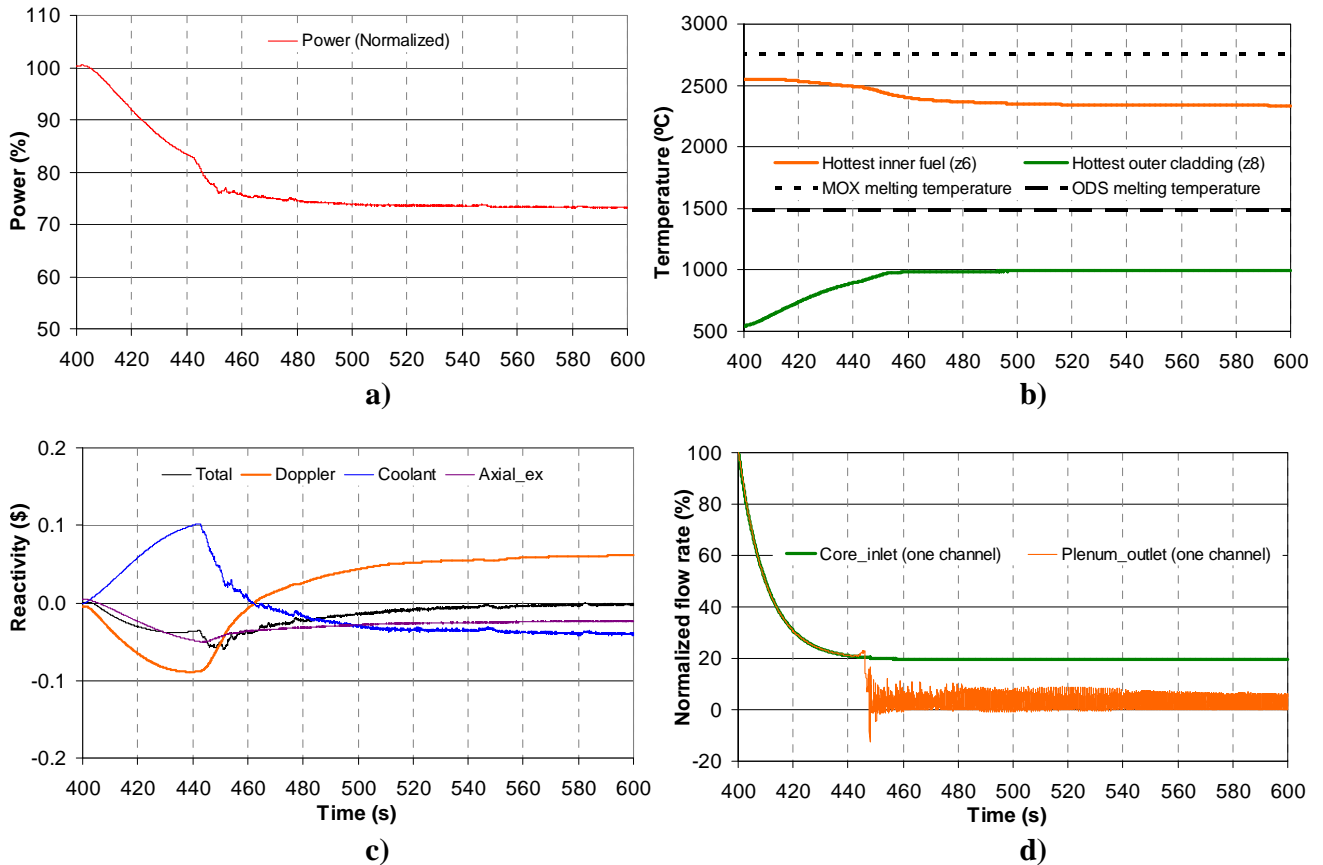


Figure 5.13. ULOF for the SC2 core with wrapper openings at BOL: evolutions of a) power, b) fuel and cladding temperatures in the hottest channel, c) total reactivity and its decomposition, d) normalized inlet and outlet flow rates in the hottest channel.

The power evolution curve (see Figure 5.13a) shows almost a constant decrease during the first 50s of the transient. Thereafter, the reactor power stabilizes, even though some minor oscillations continue to be observed locally. The final stabilized power level is around 75% of the initial value.

Figure 5.13b shows, on the one hand, that the evolution of the maximum fuel temperature largely follows the power evolution. There is a decrease from about 2500°C to 2300°C, with a safety margin of ~ 500°C finally being maintained. On the other hand, the maximum cladding temperature is seen to increase immediately after the transient begins, since it is mainly dominated by the reduced coolant

flow rate. Nevertheless, a new equilibrium is found to be established between the decreased fuel temperature and the reduced mass flow. Accordingly, the rise in cladding temperature flattens out and, in the end, remains $\sim 500^{\circ}\text{C}$ below the melting point.

The power reduction is due to the negative total reactivity, in which the negative Doppler effect is a dominating factor during the first 60s of the transient, whereas the negative coolant density reactivity effect is important later. In the end, the total reactivity asymptotically approaches a zero level (see Figure 5.13c). Due to the less flat core shape and the softer neutron spectrum in SC2, its plenum effect (i.e. void reactivity caused by the sodium plenum voiding) is less negative than in SC1, so that the coolant density reactivity effect eventually levels off at a negative value which is rather small ($\sim -0.04\%$). Since the safety parameters deteriorate in the equilibrium fuel cycle, the coolant density reactivity effect may already be expected to fail to reach a negative level at BEC. The detailed analysis of this case is reported in the next subsection.

Figure 5.13d shows that, as in the SC1 case with wrapper openings, one has a stable flow rate at the inlet of the hottest channel. It follows the overall core flow reduction to 20% of the initial value. At the sodium plenum outlet of the same channel, on the other hand, one has a relatively stable behavior, as compared to the SC1 cases. The flow oscillations – though still quite significant ($\sim 10\%$ of the initial flow rate level) – do not diverge, but stay relatively constant with the flow direction mostly remaining upward. This, in turn, is reflected in the improved stability of the numerical simulation in the present case, the studied transient having been simulated 200s without numerical non-convergence.

The better flow stability at the sodium plenum outlet for SC2 can be explained by the two following facts: 1) the higher H/D ratio of the SC2 core corresponds to an increased core height and a decreased diameter so that, for the same 30 cm sodium plenum, one has a smaller quantity of sodium in comparison to the core of flatter shape (e.g. SC1). Therefore, when boiling occurs in the upper region, the vaporization/condensation process is comparatively less violent. This implies improved flow stability and thus, in turn, more satisfactory computational behavior. 2) The neutronics plenum voiding effect in the SC2 core is not as strong as that in SC1. As a result, the reactivity fluctuations caused by the liquid/vapor transitions of the sodium coolant are less significant, and this mitigates the thermal-hydraulics response. The smoother data exchange during the coupled simulation clearly favors computational stability.

For the current case, it is interesting to make two other specific observations, viz.

- 1) During the first 60s of the transient, there is a slight decrease in the maximum fuel temperature (i.e. the centerline fuel temperature in the hottest channel; see Figure 5.13b); however, the reactivity feedbacks due to both the Doppler and axial fuel expansion effects are negative (see Figure 5.13c).
- 2) In the new steady state, where the total reactivity is around zero, the reactivity feedbacks due to the Doppler and axial fuel expansion effects are of opposite sign, the former having become positive and the latter remaining negative.

Observation 1) above is relatively simple to explain, viz. by noting that the trend for the centerline temperature in the hottest channel is not representative of that for the core average fuel temperature. This can be seen from Figure 5.14a, which shows the variations of the two fuel-temperature-related reactivity feedbacks during the first 60s, in conjunction with the corresponding variation of the core average fuel temperature.

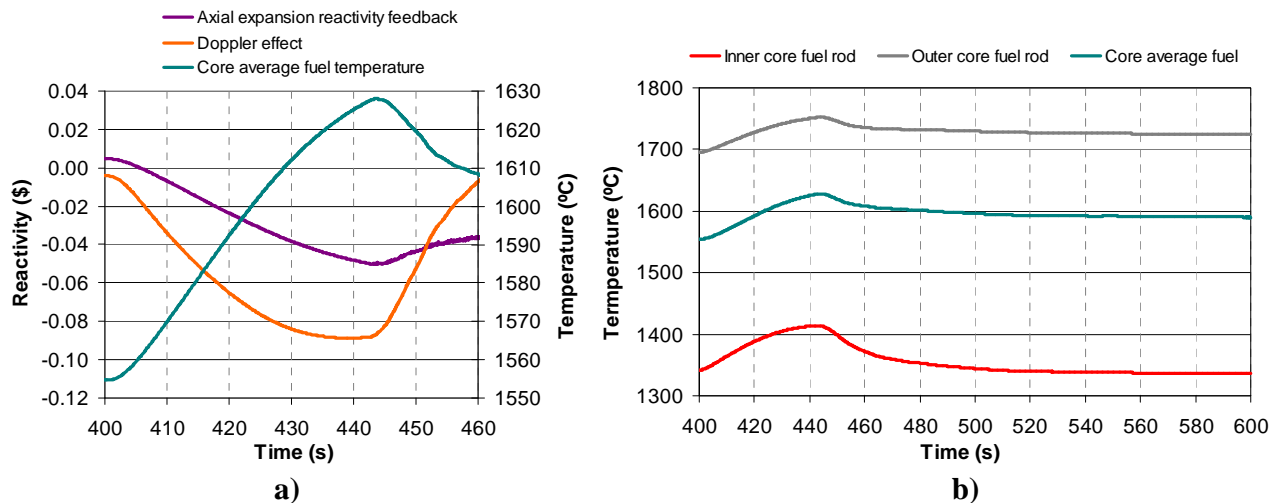


Figure 5.14. a) Doppler and axial thermal expansion reactivity effects, along with the core average fuel temperature, for the SC2 core with wrapper openings at BOL (first 60s), b) evolution (400-600s) of the core average fuel temperature and its spatial components, two representative fuel rods having been selected for the inner and outer fuel zones, respectively.

The explanation for observation 2) above is more complex and is related to the fact that, in this particular case, the variation of the core average fuel temperature needs to be considered in terms of two separate spatial components, viz. the fuel temperature changes in the inner and outer fuel zones, respectively. The fuel temperature evolution for a representative fuel rod from each of the two fuel zones, as well as the core average fuel temperature variation, can be seen in Figure 5.14b. One notes that the core average fuel temperature in the new steady state is slightly higher than that at the beginning of the transient. This difference is a combination of a relatively large increment of the fuel temperature in the outer core and a small reduction of the fuel temperature in the inner core. In the 3D kinetics treatment with PARCS, these opposing variations in the local fuel temperature are – as they should be – “averaged” differently for obtaining the Doppler and axial thermal expansion effects, viz. with a logarithmic dependency on the local fuel temperature variation for the Doppler effect, and a linear dependency for the axial fuel expansion (see Eq. 2.10, Chapter 2). Furthermore, the inner fuel zone has a larger Doppler constant (due to the lower temperature range involved, as well as to the lower plutonium content). The corresponding positive Doppler effect is thus more pronounced than the negative effect in the outer fuel zone. It is for these reasons that here, in the new “steady state”, one

sees a difference in sign for the two, relatively small, fuel-temperature-related feedback effects involved (Doppler and axial thermal expansion).

5.3.5 Behavior of the SC2 core with wrapper openings at BEC

In this subsection, the core behavior of the SC2 core with wrapper openings is analyzed using the fuel composition in the equilibrium closed cycle state, the corresponding set of results being shown in Figure 5.15.

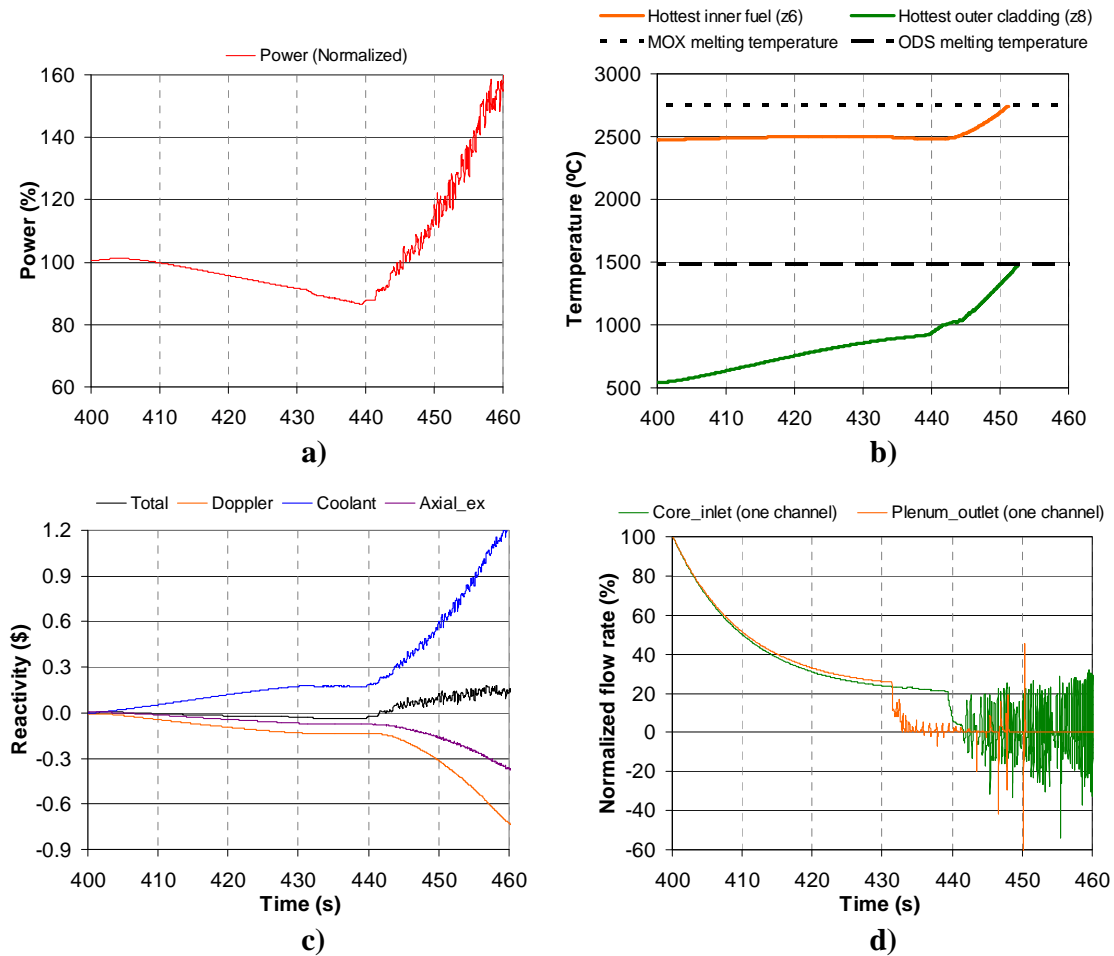


Figure 5.15. ULOF for the SC2 core with wrapper openings at BEC: evolutions of a) power, b) fuel and cladding temperatures in the hottest channel, c) total reactivity and its decomposition, d) normalized inlet and outlet flow rates in the hottest channel.

One should firstly recall the presented parameters in Table 4.16. The extended void reactivity of SC2 is seen to be increased by 473 pcm at BEC, compared to the BOL state. This is mainly caused by

fission product accumulation and ^{241}Pu reduction in the core region. Since the coolant density reactivity feedback at BOL is only slightly negative following the development of sodium vapor in the upper region of the core (see Subsection 5.3.4), the increased extended void reactivity at BEC can be expected to prevent the coolant density reactivity feedback from becoming negative, and this is indeed found to be the case here.

As seen in Figure 5.15c, the coolant density reactivity feedback – after the sodium boiling onset at 431s – remains at a constant positive value for about ten seconds and then starts increasing significantly. As a result, the total reactivity is driven to a positive level, leading to an increase in power (see Figure 5.15a). Flow stagnation is observed at the sodium plenum outlet (see Figure 5.15d), which in turn implies reaching dryout conditions. One has a situation where the melting of the cladding and fuel cannot be prevented (see Figure 5.15b).

The evolution of the void region for the present case is shown in Figure 5.16. It should first be noted that, for the equilibrium fuel cycle, the radial power distribution in normal operation corresponds to the maximum power occurring in the central region and not, as in the BOL case, in the outer core. This can be seen from Figure 3.3, which compares the radial flux distributions at BOL, BOC and BEC for the reference ESFR core, the situation for the optimized cores being quite similar. This explains the trend seen in Figure 5.16, viz. that the sodium boiling onset in the BEC state first occurs in the upper central region of the core and that the void region subsequently propagates from there in all directions.

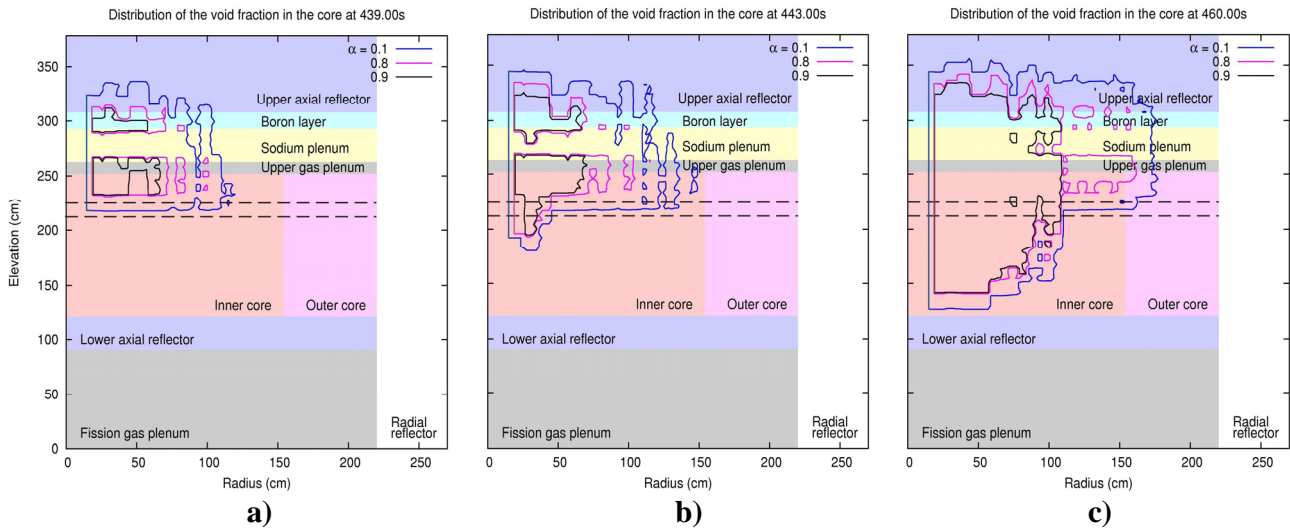


Figure 5.16. Void maps of the SC2 core with wrapper openings at a) 439s, b) 443s and c) 460s, respectively, during the ULOF transient at BEC. The dashed lines indicate the region of introduced wrapper openings.

More precisely, the two-phase sodium mixture establishes itself in the upper part of the inner core and in the corresponding regions above at 439s, i.e. eight seconds after the boiling starts (see Figure

5.16a). Thanks to the wrapper openings, the sodium vapor is initially maintained in the upper core region. However, the void distribution of Figure 5.16a – i.e. one in the inner, rather than in the outer region of the core – is not able to introduce a negative coolant density reactivity effect. As a result, the power remains high and cannot be removed by the reduced coolant flow rate. The sodium void thus starts to penetrate downwards (see Figure 5.16b). A large dryout region develops, covering the major part of the inner core and the corresponding upper regions (see Figure 5.16c). This voiding scenario induces strongly positive coolant density reactivity feedback, accelerating the melting of cladding and fuel even further.

5.3.6 Summary and discussion

In order to employ the neutronics optimization carried out in Chapter 4 to greater advantage, an innovative wrapper design has been proposed for the SFR fuel assemblies. As compared to the conventional wrapper, small openings are introduced in each of the side surfaces, the goal being to provide bypasses for coolant flow when sodium vapor blocks the flow area at the top of the fuel. While adopting the new wrapper design, the core behavior of the SC1 and SC2 cores has been analyzed for both BOL and BEC fuel cycle states.

The SC1 cases demonstrate that the wrapper openings effectively help ensure that the sodium void remains in the upper core region, so that adequately negative coolant density reactivity feedback is introduced following the boiling onset. However, violent flow oscillations occur in the upper sodium plenum and, as a consequence, the simulations do not converge sufficiently for a definite trend to be identifiable. This is of course not just a matter of computational instability, but also has important physical significance: the oscillations imply an unstable state, where uncontrolled void propagation and local dryout can be anticipated to occur. This clearly threatens reactor safety and calls for further design optimization.

Even though, in the SC2 case, there is a trade-off between a less reduced void reactivity and a stronger Doppler effect, the wrapper openings do prevent both cladding and fuel melting for the considered ULOF scenario at BOL. Here, it is found that the transient can be successfully simulated for 200s without numerical non-convergence. The better computational stability results from a less violent vaporization/condensation process in the larger H/D ratio core, in which the sodium plenum has a reduced neutronics effect. The smaller reactivity fluctuations then lead to a smoother data exchange between the coupled codes. In the BEC state, however, the deteriorated safety parameters – particularly the more positive coolant density reactivity effect in the active core – lead to positive total reactivity after the sodium boiling onset and the melting of cladding and fuel cannot be prevented. This clearly underlines the importance of achieving negative coolant density reactivity feedback.

The broad characteristics of the void distribution, which develops during the postulated ULOF transient with the new wrapper design, are in fact more or less fixed: sodium vapor is sustained above the wrapper openings, with the upper part of the active core almost fully voided (~ 90%) and the sodium plenum partly so (~ 50%). According to the axial void importance distribution shown in

Figure 3.5, one can reasonably assume that the reactivity insertion from the largely voided upper active core is approximately equivalent to 4% of the reference void reactivity. The partly voided sodium plenum can be assumed to introduce half of the total plenum reactivity effect. Besides, one needs to take into account the fact that there is a density reduction of the remaining liquid phase sodium in the lower part of the active core (below the wrapper openings). This is caused by the coolant temperature increase during the transient. In the expected new “thermal-hydraulic equilibrium” state, such a decreased density is approximately equivalent to the introduction of about 5% of the reference void reactivity. Thus, in a simplified but reasonable way, the total coolant density reactivity feedback can be represented by the sum of all three of the above contributions, i.e. can be obtained by summing up 9% of the reference void reactivity and 50% of the plenum effect.

Table 5.1 provides a summarized presentation of the reference, extended and plenum void reactivity values for the SC1 and SC2 cores at BOL and BEC, along with the corresponding estimate for the total coolant density reactivity feedback during the ULOF transient. The latter estimates have been obtained on the basis of the simplified considerations made above, i.e. correspond, in each case, to 9% of the reference void reactivity plus 50% of the plenum effect.

Table 5.1. Reference, extended and plenum void reactivity values for the SC1 and SC2 cores at BOL and BEC, along with the corresponding “ULOF” coolant density reactivity feedback based on the simplified considerations made for the “wrapper openings” cases (units: pcm)

Core	$\Delta\rho_v$ at BOL				$\Delta\rho_v$ at BEC			
	Reference	Extended	Plenum	“ULOF”	Reference	Extended	Plenum	“ULOF”
SC1	1332	321	-868	-314	1789	854	-803	-241
SC2	1358	1038	-268	-12	1805	1511	-247	39

It can be seen that – based on the simplified reasoning carried out – the SC1 cases with wrapper openings (for both BOL and BEC states) are expected to have strongly negative reactivity feedback. For the SC2 core, however, only a slightly negative reactivity effect is expected at BOL, while at BEC the feedback becomes positive due to the significantly deteriorated reference void reactivity. Thus, an increase in power can be expected for the SC2 core at BEC.

It needs to be emphasized that the simplified considerations made above are by no means a possible substitute for detailed, 3D coupled simulations of the type made currently using PARCS/TRACE. The latter are, after all, essential for describing the actual void development during the transient. However, the simplified reasoning carried out does provide a useful qualitative assessment for a given core design, as demonstrated here by the clear indication that the behavior of the SC2 core with wrapper openings would not be satisfactory at BEC.

In the overall context of the PARCS/TRACE simulation results for the four cases studied in this section, one can identify two distinct criteria for obtaining satisfactory behavior for the optimized cores with wrapper openings. The first is that – with sodium vapor successfully sustained above the wrapper openings – one has to achieve negative coolant density reactivity feedback, both at BOL and at BEC. The other criterion is that of stability. From among the four cases studied currently, the most satisfactory behavior has been found to be not for the case with the most negative coolant density reactivity feedback (i.e. SC1 at BOL), but rather that for the case in which convergence is reached, (i.e. SC2 at BOL). This underlines the importance of preventing strong physical oscillations during the sodium boiling. Accordingly, the focus in the next section will be placed on the trade-off between the negative neutronics effect in the sodium plenum and stabilization of the coupled neutronics/thermal-hydraulics phenomena.

Finally, it needs to be mentioned here that, even though a successful case has been demonstrated for SC2 at BOL, the positive coolant density reactivity effect at BEC is not acceptable. Accordingly, the SC2 core is not considered any further, and the following section describes the second thermal-hydraulics related improvement carried out, viz. that of the upper plenum design, in the context of SC1 alone.

5.4 Stabilization of conditions in the upper plenum

It has been indicated previously that stabilization of the coupled neutronics/thermal-hydraulics phenomena, which occur in the upper sodium plenum during the transient, is of utmost importance once one has ensured that the reactivity insertion following the sodium boiling onset is negative. The violent vaporization/condensation process which occurs in this region has to be mitigated, so that the mutual feedback between the neutronics and thermal-hydraulics remains smooth. In this context, an alternative plenum design – amounting to the replacement of the original sodium plenum by an extended fission gas plenum – is proposed and analyzed in this section.

5.4.1 The alternative sodium plenum design

The violent vaporization/condensation process in the sodium plenum, which leads to the observed flow instability, is largely due to the very high sodium volume fraction (92%) in this region. Accordingly, a reduction of this high fraction needs to be considered. Clearly, a reduced sodium amount in the plenum region will also lead to a less negative plenum effect from the neutronics viewpoint. Nevertheless, this trade-off is necessary to achieve a smoother mutual feedback in the neutronics/thermal-hydraulics coupling. The most realistic, and also the simplest, way is to replace the original sodium plenum with an extended fission gas plenum. The latter region, in which the sodium fraction is considerably reduced (28%), has the same coolant flow cross-section as the fuel region. The remaining volume fraction is taken up by the helium-filled gas plenum in the upper part of the fuel pins and the corresponding amount of cladding material (ODS steel). Bearing in mind that there is an

11 cm upper fission gas plenum in the reference ESFR core (as also in SC1), one now has $30 + 11 = 41$ cm in total. Such an extended fission gas plenum in SC1 – in place of the earlier 30 cm sodium plenum – yields the final optimized core configuration, which is analyzed here.

Before presenting the results of the PARCS/TRACE simulations for this final core configuration, it is useful to make an analogous simplified consideration of static neutronic parameters as done for the SC1 and SC2 cores in Subsection 5.3.6, in particular to estimate the “ULOF” coolant density reactivity feedback one can expect. The corresponding results obtained for the final core configuration are compared in Table 5.2 with those for the SC1 core (i.e. with the original 30 cm sodium plenum). It should be mentioned here that, due to the lower sodium fraction in the extended fission gas plenum, the void fraction to be expected in this region is higher than that in the original sodium plenum. Accordingly, the fraction of the total plenum effect which has been assumed to be effective in the case of the extended fission gas plenum is 75%, instead of the 50% value assumed for the original sodium plenum.

Table 5.2. Comparison of neutronics parameters for SC1 and the final core configuration at BOL and at BEC (units: pcm)

Core	$\Delta\rho_v$ at BOL					$\Delta\rho_v$ at BEC			
	Nom. ρ	Void reactivity values				Void reactivity values			
		Ref.	Extended	Plenum	“ULOF”	Ref.	Extended	Plenum	“ULOF”
SC1	1187	1332	321	-868	-314	1789	854	-803	-241
Final-configuration	1075	1314	887	-366	-130	1774	1383	-335	-92

One can firstly notice that the nominal reactivity in the final core configuration at BOL, as compared to that in SC1, is reduced by only 112 pcm. This indicates that the neutron economy under normal operating conditions is not much deteriorated. As regards the void reactivity values, these are less than 20 pcm different, at both BOL and BEC, for the reference voiding scenario. The extended void reactivity values, however, differ by more than 520 pcm. This considerable difference is due to the reduced plenum voiding effect in the final core configuration. Nevertheless, the “ULOF” void reactivity, as defined in Section 5.3.6 (but based on a 75% plenum effect, rather than 50%), is seen to remain negative in the final core configuration, at both BOL and BEC. Satisfactory core behavior may thus already be expected from the PARCS/TRACE simulations described in the following subsections.

5.4.2 Final-configuration core behavior at BOL

The standard set of core behavior results, presented in all previous simulations of the selected ULOF accident scenario, are shown in Figure 5.17 for the final core configuration at BOL. It may first be noted that the sodium boiling onset occurs at 435s, which is very close to the timing for the corresponding SC1 case with original sodium plenum. Most important is the observation that the

computation is very satisfactory, 400s of the transient having been simulated successfully, i.e. without numerical non-convergence.

The power evolution curve (see Figure 5.17a) shows that, after a smooth decrease during the first 35s (i.e. before the sodium boiling onset) and a sharper decrease during the next 15s (i.e. after the sodium boiling onset), the reactor power is basically stabilized, even though some minor oscillations continue to be observed. The final stabilized power level is slightly above 60% of the initial value.

As seen in Figure 5.17b, the maximum fuel temperature evolution largely follows the power evolution. One has a decrease from about 2500°C to 2000°C, with more than a 700°C safety margin finally being maintained. Once again, the maximum cladding temperature goes up immediately after the transient starts, this being determined mainly by the reduced coolant flow rate. However, the decrease in the fuel temperature after the boiling onset effectively weakens the cladding temperature increase and, in the end, it remains more than 500°C below the melting point.

The total reactivity remains negative during the first 100s of the transient: during the first 40s, the negative Doppler effect plays the major role, whereas the negative coolant density feedback is the dominant effect later (see Figure 5.17c). The latter eventually stabilizes at a value of $\sim -0.3\%$. The Doppler and the axial expansion effects are also stabilized in the later stages, but both of these feedbacks are positive due to the reduction of the core average fuel temperature. The compensation that occurs between the different reactivity components leads to an asymptotic approach of the total reactivity to a zero value. Thus, a new stable critical state is reached.

In Figure 5.17d, one can see a stable flow rate at the inlet of the hottest channel, which follows the overall core flow reduction to 20% of the initial value. At the channel outlet, the flow direction remains upward almost throughout the transient, even though the flow rate is quite low. This is because of the bypasses through the wrapper openings from the hot channels to the neighboring cold ones. As compared to the SC1 core with original sodium plenum, the outlet flow rate oscillates much less strongly. This clearly indicates a satisfactory level of flow stability, with sufficient mitigation having been achieved for the vaporization/condensation process in the extended fission gas plenum. Combining the latter fact with the reduced void reactivity feedback in the plenum, the data exchange during the coupled neutronics/thermal-hydraulics simulation is much smoother, resulting in satisfactory computational stability for this final core configuration.

One can notice that the oscillations one observed after the sodium boiling onset in the previous cases – for various parameters, e.g. coolant density feedback, reactor power, mass flow rate at the outlet, etc. – are still present in the results shown in Figure 5.17. The amplitudes, however, are significantly smaller. What remains almost the same is the frequency, which is of the order of 1 Hz. Such a frequency is quite characteristic of sodium boiling phenomena in parallel channels, as shown in Appendix C which provides a qualitative comparison with experimental data. Clearly, the observed oscillations – and subsequent non-convergence in the previous simulations – are not simply numerical but rather, are related to the physical sodium boiling phenomena in the upper plenum.

Chapter 5: Impact of Optimization on Transient Behavior

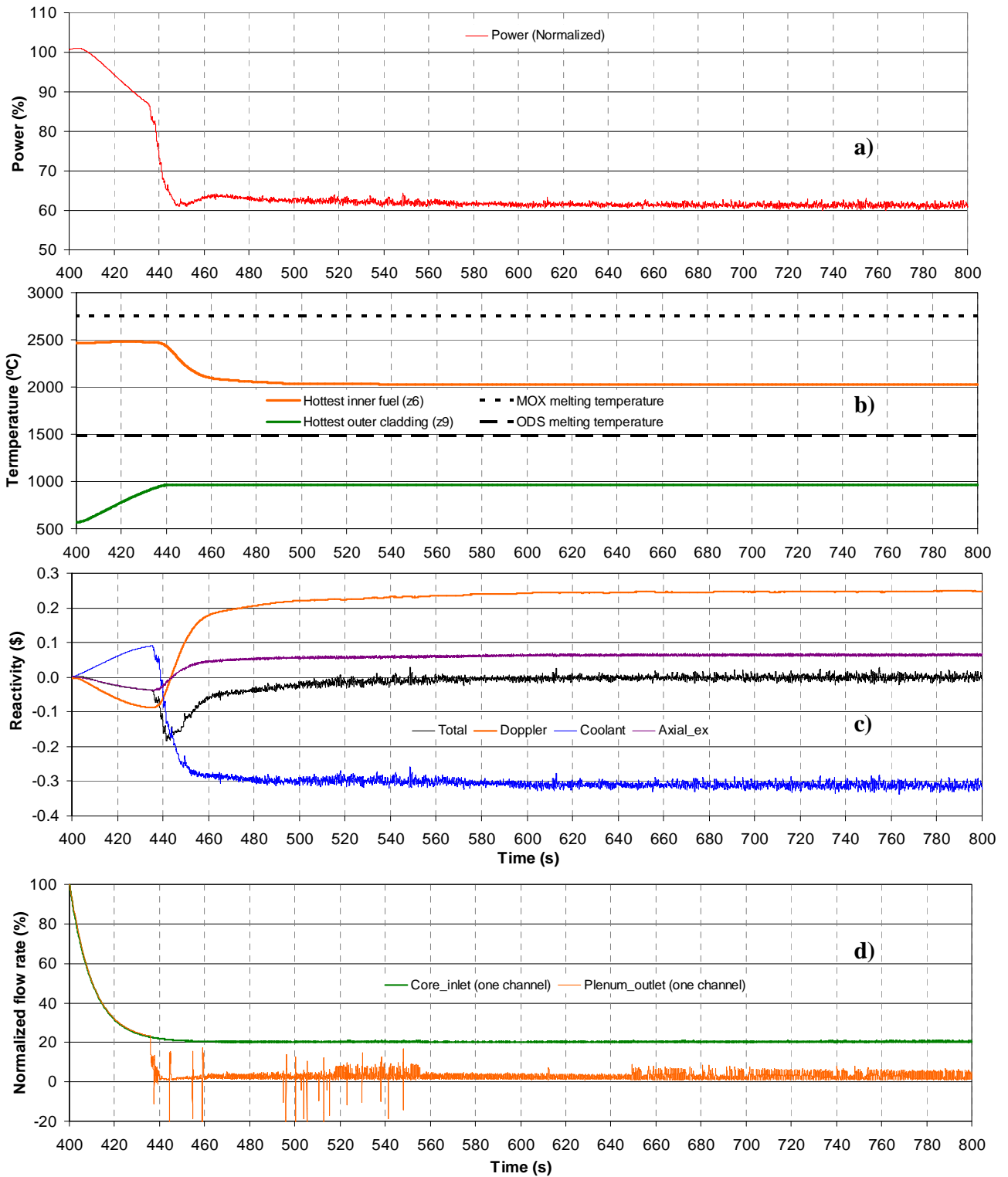


Figure 5.17. ULOF for the final core configuration at BOL: evolutions of a) power, b) fuel and cladding temperatures in the hottest channel, c) total reactivity and its decomposition, d) normalized inlet and outlet flow rates in the hottest channel.

The void maps presented in Figure 5.18 graphically demonstrate the manner in which the new “steady state” with stable boiling is reached during the ULOF in the final core configuration, the snapshots having been taken at 600s, 700s and 800s, respectively. The void region development in the early stage of the transient is not presented here, since it is similar to the SC1 case with wrapper openings at BOL (see Subsection 5.3.2, Figure 5.11). After 200s into the transient (i.e. at time 600s), it is found that the two-phase mixture no longer propagates downwards or radially into the neighboring fuel assemblies but rather, only moderately expands upwards along the upper reflector. The most developed void region at time 800s extends from the upper part of the outer fuel zone (above the wrapper openings), through the large fission gas plenum and boron layer, to the top of the upper reflector. In most of the void region, the vapor quality is lower than 0.9. There are only some small volumes near the top of the active core where the vapor quality is higher, but the values remain below the dryout criterion (viz. with void fraction lower than 0.957). In addition, further upward expansion of the sodium void will not occur since a large common coolant volume for all the fuel channels is located above the upper reflector, so that the rising sodium vapor can be effectively condensed there.

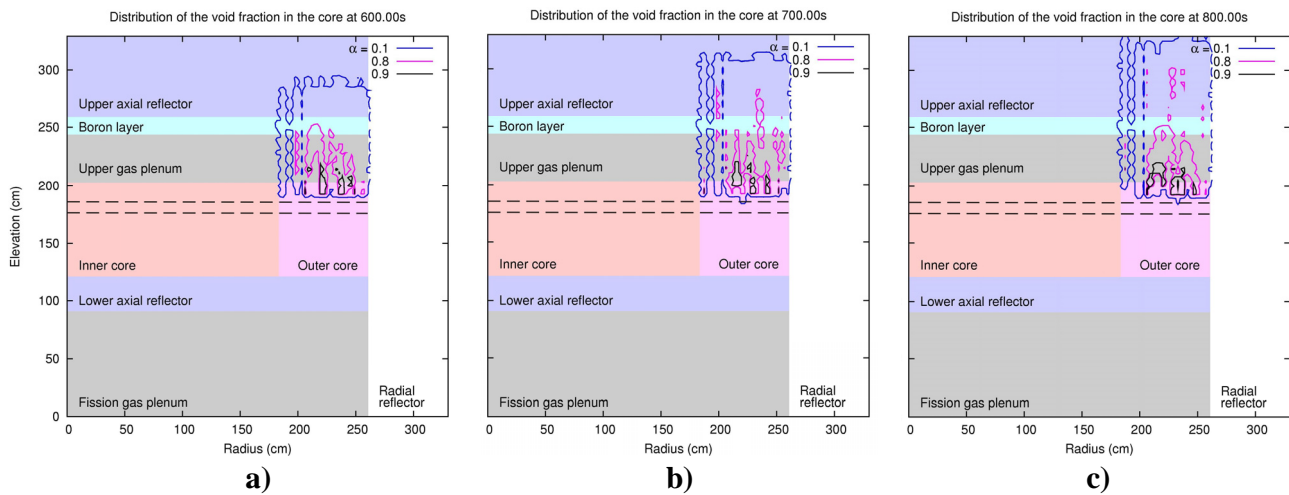


Figure 5.18. Void maps of the final core configuration at BOL at a) 600s, b) 700s and c) 800s, respectively. The dashed lines indicate the region of introduced wrapper openings.

5.4.3 Final-configuration core behavior at BEC

As discussed earlier, the two important differences between BOL and BEC states – from the viewpoint of the core behavior during the ULOF – are: 1) the corresponding safety related parameters (viz. void reactivity, Doppler constant and effective delayed neutron fraction) are deteriorated, and 2) the power peak in the power distribution is shifted from the core periphery to the radial center. Keeping these differences in mind, the PARCS/TRACE simulations for the final core configuration have also been carried out at BEC and are discussed in this subsection.

From the results shown in Figure 5.19, the first impression one has is that the final core configuration behaves similarly at BEC as at BOL, but with stronger oscillations in the presented power and reactivity components. The latter aspect is mainly a consequence of the above mentioned features of the equilibrium fuel cycle. Thus, for example, the reduced effective delay neutron fraction renders the core behavior more sensitive to the reactivity effects, i.e. less stable, in a certain sense. Moreover, the centralized region of maximum power implies that less effective bypasses are provided by the wrapper openings^{5.3} which, in turn, results in a reduced prevention of void propagation. A subsidiary study has shown that the second reason is more important.

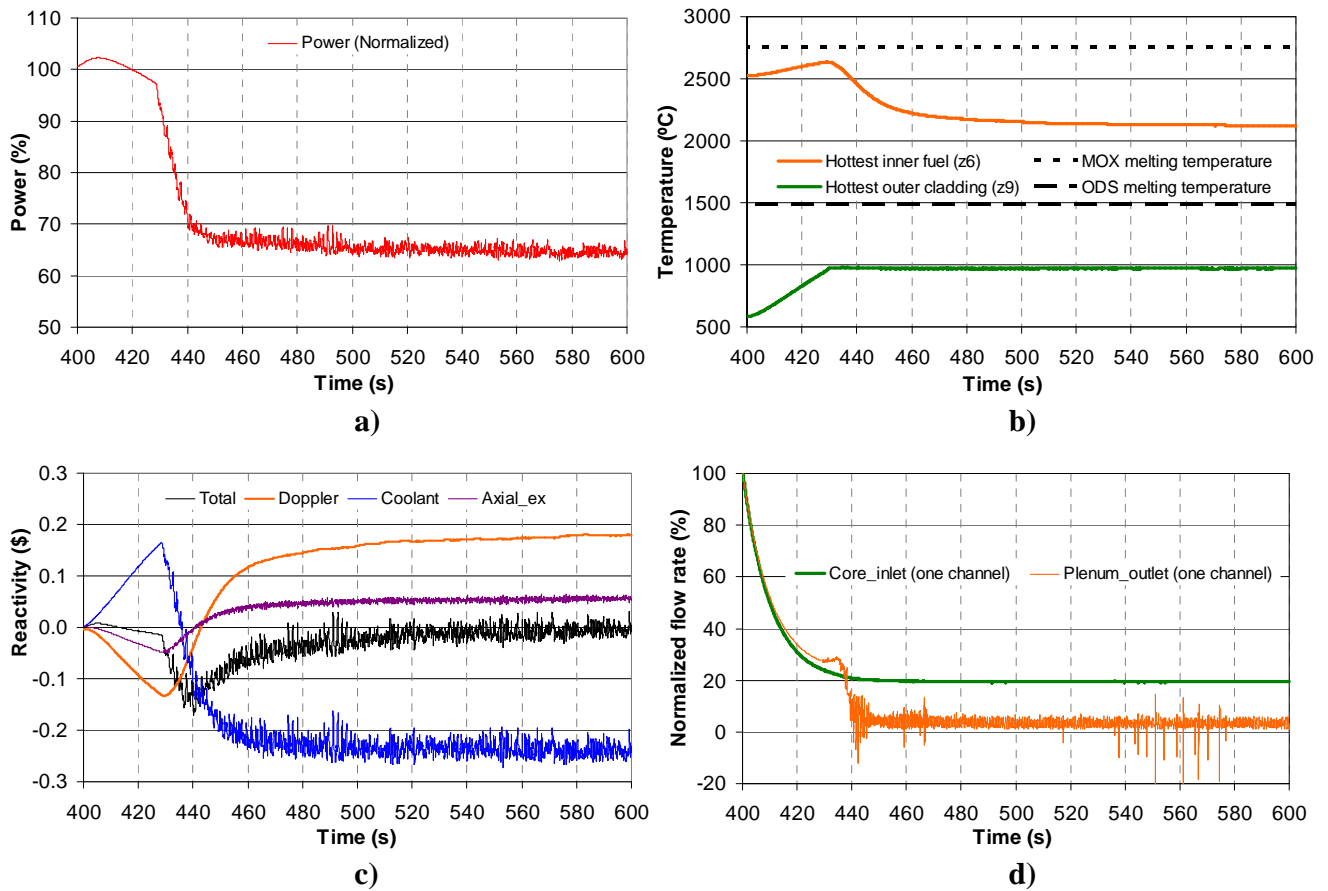


Figure 5.19. ULOF for the final core configuration at BEC: evolutions of a) power, b) fuel and cladding temperatures in the hottest channel, c) total reactivity and its decomposition, d) normalized inlet and outlet flow rates in the hottest channel.

^{5.3} The sodium void can only propagate outwards when the maximum power region is centralized (i.e. at BEC), whereas it can propagate both inwards and outwards when this region is located in the outer core (i.e. at BOL).

Chapter 5: Impact of Optimization on Transient Behavior

The sodium boiling onset occurs at 428s, which is about seven seconds earlier than at BOL. In addition, the core at BEC – with its greater positive coolant density reactivity feedback in the active core region and reduced Doppler effect – exhibits a lower decrease in power during the first 28s, i.e. before the boiling onset (compare Figures 5.19a and 5.17a). Accordingly, the fuel temperature increases more significantly in this period (compare Figures 5.19b and 5.17b) but remains below the melting point. Last but not least, even though the power level oscillates somewhat significantly and the sodium void propagation, which starts from the core center, appears to be more unstable, flow stability in the boiling channels is still maintained at an acceptable level (see Figure 5.19d). The stability of the simulation, as well, is quite satisfactory.

The evolution of the void region in the final core configuration at BEC is shown in Figure 5.20.

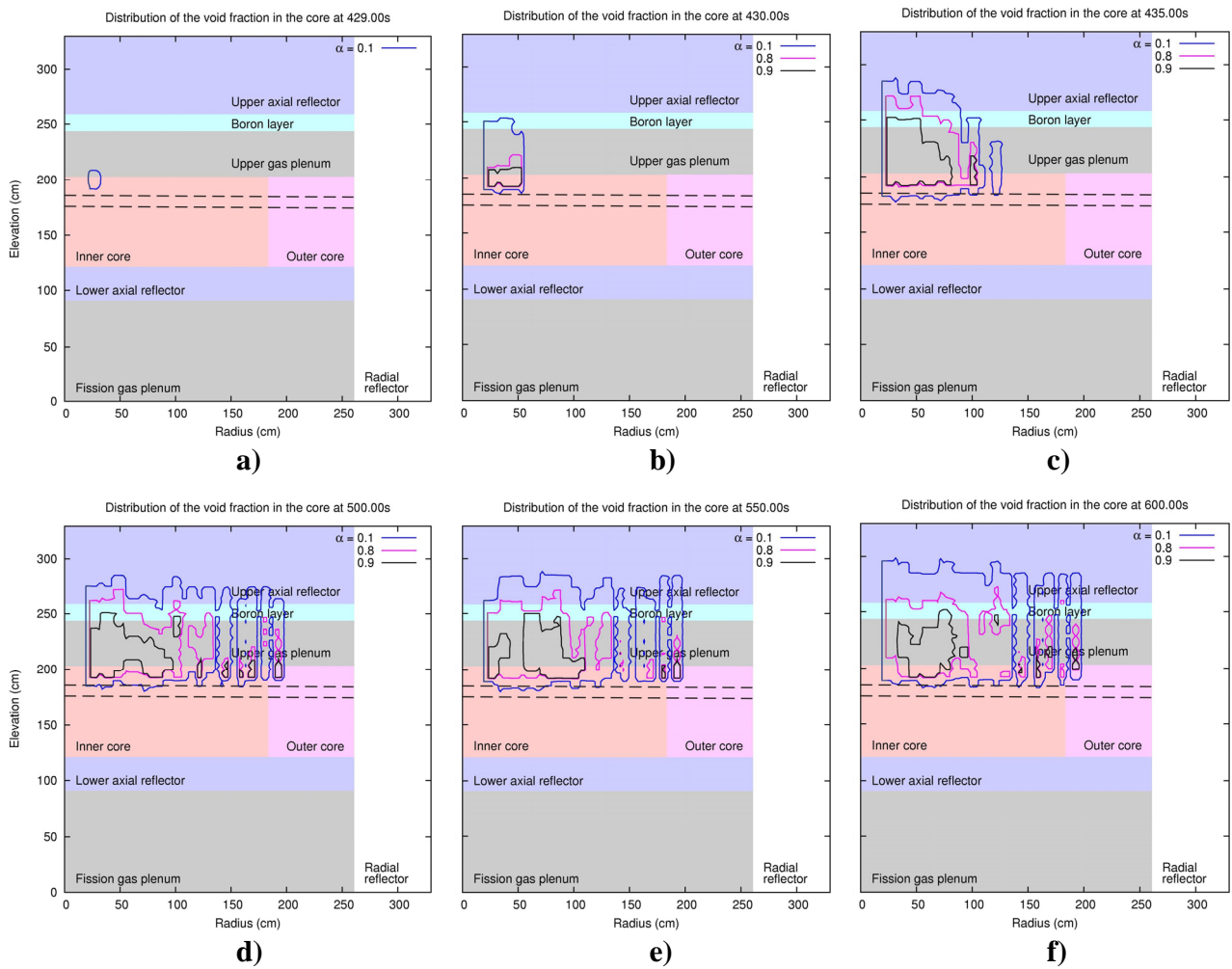


Figure 5.20. Void maps of the final core configuration at BEC at a) 429s, b) 430s, c) 435s, d) 500s, e) 550s and f) 600s, respectively. The dashed lines indicate the region of introduced wrapper openings.

As discussed above, the region of maximum power in the equilibrium fuel cycle is centralized. This is confirmed by the boiling onset position indicated in Figure 5.20a. After the boiling starts, the void region develops in the radial direction and upwards (see Figures 5.20b and 5.20c). The downward propagation is limited by the wrapper openings. After 100s into the transient (i.e. at time 500s), the radial propagation of the two-phase mixture is stopped quite effectively (see Figures 5.20d, 5.20e and 5.20f). There is only a moderate expansion upwards along the upper reflector, similar to the corresponding BOL case (see Figure 5.18). At time 600s, i.e. 200s into the transient, the void distribution covers the upper region of the entire inner core, as well as that of a small part of the outer core (see Figure 5.20f). This voiding scenario corresponds to a steady, negative coolant density reactivity feedback (see Figure 5.19c) which, in turn, ensures the acceptable behavior of the final-configuration core in the BEC state.

5.4.4 Summary and discussion

It can be concluded that the final core configuration – with an extended upper fission gas plenum, in conjunction with the wrapper openings – fulfils the conditions for achieving sufficient coolant flow stability during the reference ULOF accident scenario. The establishing of a new “steady state”, with stable sodium boiling in the upper core region, is able to prevent cladding and fuel melting, at both BOL and BEC.

It is also important to point out that the reduced core height of the final configuration (corresponding to the reduced H/D ratio), in conjunction with the extended upper fission gas plenum, should allow the lower fission gas plenum to be shortened by at least $50\text{ cm}^{5.2}$. This compactness would imply a lower pressure drop across the core, as also a significant reduction in capital costs.

Last but not least, it needs to be underlined that certain passive mechanisms have not been included in the current PARCS/TRACE modeling. In particular, the increase in coolant temperature above the core (by more than 400°C) can be expected to lead to the thermal expansion of control rod drives, which would provide a considerable negative feedback. Such an effect could introduce sufficient negative reactivity for further reducing the core power or even achieving automatic shutdown.

5.5 Chapter summary

In this chapter, the behavior of a 3600 MWth SFR core during a selected ULOF accident scenario has been analyzed via a coupled 3D-neutronics/thermal-hydraulics PARCS/TRACE model. The reference ESFR core behavior at BOL is presented as the starting point of the study. As the next step, the

^{5.2} The total height of the fission gas plenum (sum of the upper and lower plenum heights) is normally proportional to the height of the active core, which corresponds to the amount of gaseous fission products released from the fuel. For the current ESFR design, the ratio is about 1.

analysis for the SC1 and SC2 cores, proposed by the neutronics optimization study in Chapter 4, is carried out.

The reactor power in the reference core is strongly increased during the transient. A large dryout region is created and various channels are blocked by sodium vapor. The system finally suffers melting of both fuel and cladding. It has also been indicated that neither the reduced void reactivity nor the enhanced Doppler effect alone can prevent the severe accident situation that develops, even in the case of BOL conditions, i.e. with fresh fuel in the core. Nevertheless, an important finding was made at this stage: one needs a certain thermal-hydraulics optimization, so that the sodium vapor can effectively be sustained in the upper region for obtaining a negative coolant density reactivity effect. In this context, an innovative wrapper design for the fuel assembly has been proposed.

The innovative feature of this new wrapper design is to introduce small openings in each of the side surfaces of the conventional wrapper tube, the goal being to provide bypasses for the coolant flow when the sodium vapor blocks the flow area at the top of the fuel. While adopting such a wrapper design, the core behavior of the SC1 and SC2 cores has been analyzed, for both BOL and BEC fuel cycle states. The SC1 cases demonstrate that the wrapper openings are indeed able to sustain the sodium void in the upper regions and thus effectively induce negative coolant density reactivity feedback. However, due to violent flow oscillations in the sodium plenum, the simulations are terminated by numerical non-convergence before a definite trend can be derived.

In the SC2 case – even though there is a trade-off between a less reduced void reactivity and a stronger Doppler effect – the wrapper openings do prevent both cladding and fuel melting for the considered ULOF scenario at BOL. A difference here, relative to the SC1 case, is that the transient can be successfully simulated for 200s without numerical non-convergence. The better computational stability results from a less violent vaporization/condensation process in the larger H/D ratio core, in which the sodium plenum has a reduced neutronics effect, leading to a smoother data exchange between during the coupled simulation. In the BEC state for SC2, however, the stronger deterioration of the safety parameters – particularly the more positive coolant density reactivity effect in the active core – leads to positive total reactivity after the sodium boiling onset, and the melting of cladding and fuel cannot be prevented. The SC2 configuration is thus not further considered. However, the insight obtained regarding the mitigation of sodium boiling oscillations via a reduced neutronics effect of the upper sodium plenum leads to the final core configuration: the SC1 core with wrapper openings, but with the original sodium plenum replaced by an extended fission gas plenum.

One can conclude from the behavior of the final core configuration that this fulfils the dual conditions needed for the selected ULOF accident scenario, viz. achieving negative coolant density reactivity feedback, on the one hand, and assuring sufficient coolant flow stability on the other. The establishing of a new “steady state”, with stable sodium boiling in the upper core region, is able to prevent cladding and fuel melting, at both BOL and BEC. Furthermore, it is important to point out that the reduced core height of the final core configuration (smaller H/D ratio, relative to the reference ESFR core) – in conjunction with the proposed extended fission gas plenum – should allow the lower fission gas

plenum to be shortened considerably, implying a lower pressure drop across the core and a reduction in capital costs. Last but not least, it needs to be underlined that certain passive mechanisms have not been included in the present study (e.g. the thermal expansion of the control rod drives). The consideration of such effects could introduce sufficient negative reactivity for achieving a significant further reduction in core power or even an automatic shutdown.

Table 5.3 provides a summary of the key results obtained with the current PARCS/TRACE modeling of the selected ULOF accident scenario. The presentation has been made such as to bring out the step-by-step improvements achieved with the progressive optimization carried out for the BOL state. Tabulated, for the BOL state in each case, are: simulation status, reactor power behavior, cladding and fuel temperature status, coolant density and total reactivity effects, flow rate behavior at core inlet and plenum outlet, fuel channel status, and crucial points.

Table 5.3. Summary of the step-by-step improvements achieved for the SFR core behavior during the ULOF at BOL

	Reference ESFR core	The SC1 core	SC1 with wrapper openings	The final- configuration core
Simulation status	Terminated by melting	Terminated by melting	Terminated by numerical non- convergence	Completed
Power at the end	Increasing	Oscillating	Decreasing	Stabilized
Cladding temperature	Reaches melting point at 440s	Reaches melting point at 454s	Stabilized below melting point	Stabilized below melting point
Fuel temperature	Reaches melting point at 435s	Close to melting point at 455s	Decreasing	Stabilized below melting point
Coolant density reactivity effect	Very positive	Positive	Negative	Negative
Total reactivity effect	Positive	Oscillating around zero	Negative	Negative
Core inlet flow rate (hottest channel)	Strongly oscillating around zero	Strongly oscillating around zero	Smooth & positive	Smooth & positive
Plenum outlet flow rate (hottest channel)	No flow	Strongly oscillating around zero	Oscillating around zero	Smooth & positive
Flow status (hottest channel)	Channel blocked by sodium vapor	Channel blocked by sodium vapor	Strong vaporization/ condensation process	Mitigated vaporization/ condensation process
Crucial points	Power increase	Large dryout	Negative coolant density effect Instability	A new steady state reached with stable sodium boiling

References

- [5.01] K. Sun, A. Chenu, J. Krepel, K. Mikityuk, R. Chawla. Coupled 3D-neutronics/thermal-hydraulics analysis of an unprotected loss-of-flow accident for a 3600 MWth sodium-cooled fast reactor core. In PHYSOR 2012, paper 285.
- [5.02] A. Chenu, K. Mikityuk, R. Chawla. A coupled 3D neutron kinetics / thermal-hydraulics model of the Generation IV sodium-cooled fast reactor. In ICAPP 2010, paper 10281.
- [5.03] G. Palmiotti. VARIANT: Variational anisotropic nodal transport for multi-dimensional cartesian and hexagonal geometry calculations. Technical report, ANL-95/40, Argonne National Laboratory, 2005.
- [5.04] J. Pounders. Calculation of accurate hexagonal discontinuity factors for PARCS. Technical report, B-T-3711, International RELAP5 Users' Seminar, 2007.
- [5.05] Iron-chromium (Fe-Cr) phase diagram, <http://www.calphad.com/iron-chromium.html/>.
- [5.06] European Patent No. 11196146.2–2208. A wrapper tube for a fuel subassembly of a nuclear reactor core and method for protecting fuel against overheating in case of coolant boiling. Filed in 2011.

Chapter 6

Conclusions and Recommendations for Future Work

The goal of the present doctoral research is to improve the safety characteristics of advanced sodium-cooled fast reactor (SFR) core designs, in particular from the viewpoint of the positive sodium void reactivity effect. Starting from the implementation of a neutron balance based methodology for reactivity decomposition, the work carried out addresses the neutronics optimization of a reference core and culminates in the detailed analysis of its dynamic behavior during a hypothetical unprotected loss-of-flow (ULOF) accident scenario, in which sodium boiling occurs. In the latter context, additional improvements are found to be necessary in relation to thermal-hydraulics aspects. Emphasis during the research has been placed not only on the beginning-of-life (BOL) state of the core, but also on the beginning of closed equilibrium fuel cycle (BEC) state.

This concluding chapter starts with a chapter-wise summary of the thesis (Section 6.1). The main achievements of the conducted research are reviewed in Section 6.2, and recommendations for future work are provided in Section 6.3. Finally, certain concluding remarks are made in Section 6.4.

6.1 Chapter-wise summary

Chapter 1 introduces the present doctoral thesis. It starts with the current-day status of nuclear energy and the motivation for the development of fast reactor technology. The SFR – the principal object of the present research – is the Generation IV system for which most practical experience is available. Accordingly, an overview of world-wide SFR activities is provided. Thereafter, the chapter details the goals and scope of the present research and, at the end, gives an outline of the present doctoral thesis.

Chapter 2 provides more specific background information. An important context for the present doctoral research is the 7th European Framework Program's Collaborative Project for a European Sodium Fast Reactor (CP-ESFR). The reference 3600 MW_{th} ESFR core is considered as the starting point for optimization. Its main design features and the detailed project description are presented in this chapter. The employed computational tools, viz. the FAST code system and the Monte Carlo code SERPENT, are also introduced here. More specifically, the major applied codes from the FAST code system consist of the fast-reactor neutronics code ERANOS, the fuel cycle simulating procedure EQL3D (ERANOS based), the 3D spatial kinetics code PARCS, the cross-section format converting

Chapter 6: Conclusions and Recommendations for Future Work

routine ERANOS2PARCS, and the 1D system thermal-hydraulics code TRACE. The use of SERPENT is mainly for benchmarking the ERANOS calculations.

Chapter 3 focuses on the analysis of the positive sodium void reactivity effect. At first, various voiding scenarios and the spatial distribution of void reactivity importance in the core region are investigated. Methods for reactivity decomposition have then been presented, the neutron balance based methodology being the one principally considered in the present research. The ability to breakdown a reactivity change in terms of the contributions of individual reactions, nuclides and/or energy groups has been demonstrated to be most useful in providing a deeper understanding of the physical phenomena underlying the SFR void effect. The perturbation theory method, which considers a reactivity effect in terms of cross-section dependencies, has provided a complementary understanding of the causes of the reactivity change. In addition, it allows analyzing the void effect using sensitivity coefficients. As a whole, the investigations in this chapter have not only helped in achieving a clear understanding of the sodium void reactivity effect, but have also provided a valuable tool for the optimization study which follows.

Chapter 4 presents the static neutronics optimization work carried out for the reference ESRF core design. After a careful down-selection in the preliminary phase, four options oriented towards optimization of the leakage component and/or spectral effects were considered in detail, viz. introducing an upper sodium plenum and boron layer, varying the core height-to-diameter (H/D) ratio, introducing moderator pins into the fuel assemblies, and modifying the initially loaded plutonium content. The sensitivity of the safety and performance parameters – void reactivity, Doppler constant, nominal reactivity and breeding gain – was evaluated with respect to each of the options, focus being placed not only on the BOL conditions, but also on the BEC state. Finally, two synthesis core concepts – representing different selected combinations of the optimization options – have been proposed, a common constraint applied being to have a positive nominal reactivity margin at the end of the equilibrium closed fuel cycle (EEC).

Chapter 5 discusses the dynamic response of the proposed optimized cores to a representative unprotected loss-of-flow (ULOF) accident, in which sodium boiling occurs. Such a hypothetical transient is of prime importance for SFR safety demonstration, since it may lead to a severe accident situation, where both cladding and fuel melt. Certain improvements in the core response are achieved as a result of the static neutronics optimization. However, these are found, in themselves, to be insufficient as regards the prevention of cladding and fuel melting. An additional need is indicated, viz. that for improving the sodium flow behavior during the accident. A certain thermal-hydraulics optimization is thus necessary and, in this context, an innovative wrapper design for the fuel assembly has been proposed, which features small openings in each side of the wrapper tube. This provides bypasses for the sodium flow when the sodium vapor blocks the flow area at the top of the fuel, and the resulting void distribution can induce negative coolant density reactivity feedback. Furthermore, in order to stabilize the coolant flow oscillations, the sodium plenum is replaced by an extended fission gas plenum. Eventually, one succeeds in achieving a final core configuration, where – under stable sodium boiling conditions – melting of neither cladding nor fuel occurs during the stipulated accident

scenario, such satisfactory behavior being confirmed not only for the beginning-of-life state, but also for the equilibrium fuel cycle.

Chapter 6 is the current concluding chapter. The main achievements of the present doctoral research are outlined, along with certain recommendations for future work.

6.2 Main achievements

This section – which reviews the principal findings – is structured according to, effectively, the six main achievements of the present research, viz.

- ***Verification of the neutronics modeling:*** The computational tools employed currently for the neutronics modeling are those of the FAST code system, viz. ERANOS for the cell and reactor static calculations, and PARCS/TRACE for the coupled 3D-neutronics/thermal-hydraulics treatment. Considering that the various analyses carried out are largely related to the reactivity effects of sodium voiding, it has been important that these deterministic codes first be verified via the benchmarking of results against a reference, more accurate methodology. The Monte Carlo code SERPENT has been used in the latter context.
- ***Consideration of the closed equilibrium fuel cycle:*** The closed equilibrium fuel cycle has been simulated with explicit cycle-by-cycle reactor operation under specified periodic fuel management, demonstrating the iso-breeding capabilities of the SFR core with recycling of all minor actinides. The optimization and subsequent transient studies could then be conducted with a view to both beginning-of-life and equilibrium fuel cycle conditions.
- ***Decomposition and analysis of sodium void reactivity:*** The principal phenomena contributing to the sodium void reactivity effect have been identified in a quantitative manner with the use of reactivity decomposition methods, a clearer understanding thus being obtained for the underlying physics.
- ***Neutronics optimization of the ESFR core:*** The potential for neutronics design optimization has been assessed on the basis of a systematic consideration of changes to the reference ESFR core design. Two synthesis core concepts – optimized from the viewpoint of several key safety and performance parameters – have been proposed.
- ***Introduction of an innovative fuel assembly wrapper design:*** In studying the dynamic behavior of the SFR cores with neutronics optimization, it has been found that certain improvements are also needed from the thermal-hydraulics viewpoint, in order to prevent cladding and fuel melting during a selected ULOF accident scenario. The first of these has been the introduction of an innovative wrapper design for the fuel

assembly, so that the sodium boiling in the hot channels can be maintained in the upper core region, thus providing a void distribution with negative reactivity feedback.

- ***Achievement of satisfactory behavior for the final core configuration:*** The second thermal-hydraulics improvement has aimed at mitigating the strong sodium boiling oscillations found to occur in the upper sodium plenum during the postulated accident. By replacing the sodium plenum by an extended fission gas plenum, a final core configuration has been arrived at, for which satisfactory dynamic behavior has been demonstrated.

Verification of the neutronics modeling

In the present doctoral study, the deterministic code system ERANOS has generally been adopted for the static neutronic calculations, the coupled 3D-neutronics/thermal-hydraulics code PARCS/TRACE being used to simulate the dynamic core response. The verification carried out for the accuracy of the results has been presented in Chapters 3, 4 and 5 for the different types of deterministic calculations, Appendix A providing an overall review of the benchmarking against SERPENT.

In Chapter 3, ERANOS results for multiplication factor, void reactivity and Doppler constant – at both cell (assembly) and full core levels – have been compared with the Monte Carlo calculations. It has been seen that SERPENT predicts higher multiplication factor values than those obtained from the ERANOS calculations, the differences being ~ 400 pcm ($1 \text{ pcm} = 10^{-5}$). The discrepancy was found to be mainly due to using different treatments of the unresolved resonances. In this energy region, ECCO derives the effective cross-sections using self-shielding factors with the narrow resonance approximation, whereas SERPENT samples from tables based on probability distribution functions for the different cross-section types. The important finding in the context of the present research is that, even though the ERANOS and SERPENT multiplication factors differ somewhat, the results obtained for both sodium void and Doppler reactivity effects show very good agreement.

In Chapter 4, the emphasis has been on benchmarking the calculated reactivity effects of void production in the proposed, upper sodium plenum region. The deterministic prediction of such effects (dominated by the leakage component) requires an accurate solution of the neutron transport (or diffusion) equation, and it has been important to test the different flux solving options in ERANOS. It has been found that these (diffusion theory, transport theory with simplified spherical harmonics, and full transport) generally agree with each other for different considered voiding scenarios, viz. reference voiding, extended voiding and plenum voiding. In addition, it has been confirmed by the SERPENT calculations that the homogenized modeling of the sodium plenum leads to the prediction of a slightly (~ 30 pcm) less negative plenum voiding effect. This can be explained by the enhanced streaming effect in the upper region with the use of heterogeneous modeling. However, this reduction is rather insignificant, in comparison to the global leakage enhancing effect of the plenum voiding (~ 500 pcm).

In Chapter 5, the coupled PARCS/TRACE modeling has been verified against direct ERANOS calculations, in terms of the various static neutronic parameters. Particular attention has been paid to the void effect in the upper sodium plenum region, the diffusion theory based PARCS/TRACE calculations being compared to ERANOS results obtained using the different flux solving options. Good agreement has been found in general, with the full transport solution in ERANOS giving the most conservative prediction of the negative plenum voiding effect. However, the differences are small, the reactivity effect of voiding the entire upper sodium plenum being overestimated by PARCS/TRACE by only 36 pcm. In practice, a complete voiding of the sodium plenum region is highly unlikely during an accident scenario. For the considered ULOF transient, the overestimation of the plenum voiding effect by PARCS/TRACE can thus be considered to have negligible impact on the predicted core behavior.

It should be mentioned here that the coupled PARCS/TRACE calculational tool has been validated for SFR transient behavior also within the framework of an earlier EPFL doctoral thesis carried out at PSI [6.01]. The context and physical phenomena emphasized were somewhat different, data from a natural convection experiment (forming part of the Phénix end-of-life tests) having been used as validation basis. Apart from this specific testing of the coupled 3D-neutronics/thermal-hydraulics modeling, the same doctoral thesis has also provided experimental validation of the sodium two-phase flow simulation in TRACE. Three different sets of experiments were chosen for the code validation: 1) pressure drop measurements in quasi steady state sodium boiling, 2) dryout measurements in quasi steady state sodium boiling and 3) sodium boiling experiments under loss-of-flow conditions. It has been shown that the sodium two-phase flow model implemented in TRACE is capable of satisfactorily predicting boiling inception, void fraction, radial and axial expansion of the boiling region, pressure evolution, as well as coolant and cladding temperature [6.01].

Consideration of the closed equilibrium fuel cycle

The long-term operation of an SFR core in a closed fuel cycle will lead to an equilibrium state, where both reactivity (or k_{eff}) and fuel mass flow stabilize. This assumes periodic fuel management employing a multi-batch reloading scheme, with recycling of the reactor's own fuel, removal of fission products and a feed of natural or depleted uranium. Similarly, equilibrium can also be obtained for an open (once-through) fuel cycle operation.

It has been found that, for the currently considered reference ESFR core, equilibrium in an open fuel cycle is reached within less than 10 EFPY (Equivalent Full Power Years), whereas the period for the closed fuel cycle is more than 40 EFPY. The nominal reactivity values at BOL and at beginning of equilibrium open fuel cycle (BOC) are quite comparable, the difference observed being a few hundreds of pcm. The BEC reactivity, on the other hand, is more than 4000 pcm higher than the BOL value. This increased nominal reactivity is caused by the higher plutonium content in the equilibrium closed fuel cycle, which is related to the core's breeding capability. As regards the void reactivity, the BOL value (1578 pcm) is found to be significantly lower than the BOC and BEC values, which are close to each other (1978 and 2050 pcm, respectively).

Consideration of the equilibrium fuel cycle has enabled an important broadening of the current SFR optimization and transient studies. Clearly, when designing an SFR core on the basis of its BOL fuel composition, appropriate safety margins need to be applied for the equilibrium fuel cycle states, where both safety parameters (viz. void reactivity and Doppler constant) are deteriorated.

Decomposition and analysis of sodium void reactivity

Neutron balance based and perturbation theory based methods represent the two principal approaches to reactivity decomposition. Both of these have been applied for the sodium void reactivity analysis work carried out currently. From the basic definitions of the two methods, one sees that 1) the neutron balance based method derives the reactivity components in terms of the changes in neutron productions and losses, and thus mainly provides an understanding of the consequences of the void effect, while 2) the reactivity decomposition obtained by the perturbation theory corresponds to the effects of individual reaction cross-sections and thus mainly provides an understanding of the causes. The information obtained from these two methods thus cannot be directly compared, but is strongly complementary.

At first, the void reactivity for the reference voiding case has been decomposed using the neutron balance based method. The components are expressed reaction-wise, i.e. in terms of integral leakage, fission, capture and production, as well as isotope-wise and energy-group-wise. It has been shown that the major component of the void reactivity is the strongly positive absorption term, whereas the negative production and leakage terms are relatively weaker. ^{238}U capture is found to be the dominating reaction rate. ^{239}Pu , as the second most important nuclide, yields significant contributions due to changes in both production (negative) and absorption (positive). However, these two partly compensate each other, and the overall negative effect is significantly smaller in magnitude than the ^{238}U capture effect. It is necessary to note that the impact of ^{23}Na capture is negligible. In terms of the impact per unit mass, ^{241}Pu has been found to be the most favorable isotope for the reduction of void reactivity.

The reference void reactivity has also been decomposed cross-section-wise using the perturbation theory based method. The results have confirmed the key role played by the ^{23}Na elastic scattering cross-section. In addition, the isotope-wise sensitivity analysis results for capture, fission and production have been found to be quite consistent, in relative terms, with the corresponding components obtained from the isotope-wise neutron balance based decomposition.

Combining the understanding obtained from the two different methods, one can conclude that the void effect is driven mainly by the strong ^{23}Na elastic scattering, which in the nominal case suppresses the neutron flux at higher energies and increases it significantly in the lower energy region. The spectrum is thus shifted to the energy range with higher ^{238}U capture and ^{239}Pu fission cross-sections. In the voided core, this spectral shift disappears, resulting in the reduction of both ^{238}U capture and ^{239}Pu production (in conjunction with fission), and yielding the corresponding important contributions to the reactivity change.

As compared to the BOL void reactivity value of ~ 1578 pcm for the considered ESRF core, the influences of equilibrium closed and open fuel cycles on the void reactivity correspond to increases of ~ 472 pcm (BEC) and ~ 400 pcm (BOC), respectively. The four most important isotope-wise contributions to these increases are those of the fission products, ^{238}U , ^{241}Pu and ^{239}Pu , the overall impact of the minor actinides being found to be relatively unimportant.

Neutronics optimization of the ESRF core

Four neutronics optimization options – introducing an upper sodium plenum and boron layer, varying the core H/D ratio, introducing moderator pins into the fuel assemblies, and modifying the initially loaded plutonium content – have been studied quantitatively for the reference ESRF core. The sensitivity to each of these types of changes has been considered for four different safety and performance parameters, viz. void reactivity, Doppler constant, nominal reactivity and breeding gain. In the void reactivity context, the selected options are oriented either towards the leakage component or towards spectral effects. The trade-off between the considered parameters is discussed. Furthermore, as indicated earlier, emphasis has been placed not only on BOL conditions, but also on the BEC state.

First of all, the sodium plenum (along with the boron layer) is found to lead to a favorable void reactivity reduction (extended voiding scenario), without any significant side effect. This is the case for both BOL and BEC states. Secondly, a lower core H/D ratio also improves the void reactivity, but both nominal reactivity and breeding ability are deteriorated, the influence on the former being particularly strong. Thirdly, introducing moderator pins into the fuel assembly can slightly reduce the void effect and significantly improve the Doppler constant. However, the breeding gain at BOL is very sensitive to this option and, if more than seven moderator pins are inserted into the fuel assembly, the reactivity margin available for the BEC state is insufficient. Finally, increasing the plutonium content of the initially loaded fuel is able to compensate for the possibility of sub-criticality during the approach to equilibrium (due to either the lower core H/D ratio or the introduced moderator pins). With this modification, the nominal reactivity increases strongly, while the breeding gain decreases; the equilibrium fuel cycle state reached, however, is the same as for the reference core, since the equilibrium state is independent of the initial fuel composition.

Two different combinations of the considered optimization options have been proposed as possible synthesis core concepts. In each case, having a positive nominal reactivity at EEC has been set as boundary condition. Furthermore, the upper sodium plenum height that has been considered is 30 cm. This is based on a compromise between neutronic and thermal-hydraulic aspects. On the one hand, the larger the sodium plenum, the stronger the void effect reduction (see Figure 4.4) and the greater the expected hydraulic stability of sodium boiling phenomena (according to [6.02]). On the other hand, from the viewpoint of a hypothetical ULOF accident scenario, strong oscillations can occur if the neutronics/thermal-hydraulics coupling becomes intensive due to an over-dimensioned plenum size (see Appendix B). Furthermore, the sodium plenum is only partly voided under pre-dryout conditions and one cannot take advantage of the boron layer unless the sodium plenum is of limited height.

Accordingly, 30 cm has been considered to be appropriate, and the two possible optimized SFR cores proposed are:

- Synthesis Core 1 (SC1) - lowest void reactivity: introduction of a 30 cm upper sodium plenum, along with a 15 cm boron layer; H/D ratio of the core reduced to 0.158 (with 11 rings of fuel pins in the fuel assembly); average BOL fuel plutonium content increased to 16.7%.
- Synthesis Core 2 (SC2) - joint optimization of both safety parameters (viz. void reactivity and Doppler constant): introduction of a 30 cm upper sodium plenum, along with a 15 cm boron layer; H/D ratio of the core increased to 0.297 (with 9 rings of fuel pins in the fuel assembly); introduction of 9 moderator pins into the fuel assembly (increasing the fuel assembly height to preserve constant fuel mass).

The SC1 core has a void reactivity as low as 321 pcm at BOL (for the extended voiding scenario, i.e. with voiding assumed for the sodium plenum as well as the active core). The Doppler constant is similar to that for the reference ESFR core. In the case of SC2, the void reactivity is also reduced in comparison with the reference ESFR core, although less significantly than with SC1. However, the Doppler constant is much stronger in the SC2 core.

In the BEC state, the safety parameters, viz. void reactivity and Doppler constant, are both significantly deteriorated, relative to BOL, the degree of deterioration being quite similar in all the analyzed core configurations. Clearly, appropriate safety margins need to be applied for the equilibrium state, when designing an SFR core on the basis of its BOL fuel composition. Nevertheless, the SC1 core is seen to have a relatively low void reactivity even at BEC, while the magnitude of the Doppler constant at BEC is the largest in the SC2 case.

Introduction of an innovative fuel assembly wrapper design

The dynamic SFR response to an appropriately defined ULOF accident scenario, in which sodium boiling occurs, has been analyzed using the coupled 3D-neutronics/thermal-hydraulics PARCS/TRACE model. The behavior of the reference 3600 MWth ESFR core at BOL has been presented as the starting point. This is followed by analysis of the SC1 and SC2 cores, as proposed by the static neutronics optimization study.

The reactor power in the reference ESFR core is strongly increased during the transient. A large dryout region is created and multiple channels are blocked by sodium vapor. Consequently, both fuel and cladding are predicted to melt. It has also been indicated that neither the reduced void reactivity (i.e. with the SC1) nor the enhanced Doppler effect (i.e. with the SC2) can prevent the severe accident situation, even when the reactor is loaded with fresh fuel. Nevertheless, an important message is obtained: the neutronic improvements need to be combined with thermal-hydraulics optimization. In this context, an innovative wrapper design has been proposed for the fuel assembly [6.03].

The innovative feature of the new wrapper design is the introduction of small openings in each of the side surfaces of the conventional wrapper tube. The goal of these openings is to provide bypasses for the coolant flow when the sodium vapor blocks the flow area at the top of the fuel. The resulting void distribution, which covers the plenum region and the upper part of the core, can effectively induce negative coolant density reactivity feedback.

While adopting such a wrapper design, the behavior of the SC1 and SC2 cores has been re-analyzed, for both BOL and BEC fuel cycle states. The SC1 cases demonstrate that the wrapper openings are able to sustain the sodium void in the upper regions quite adequately; however, due to violent void and flow oscillations in the sodium plenum, the simulations are terminated by numerical non-convergence before a definite trend can be derived. The SC2 trades off a less reduced void reactivity for a stronger Doppler effect. At BOL, the incorporation of the new wrapper with openings effectively prevents the cladding and fuel from melting during the considered ULOF. However, the deteriorated safety parameters in the equilibrium fuel cycle – particularly the more positive coolant density reactivity effect – lead, in the BEC case, to a positive total reactivity after the sodium boiling onset and thus once again result in a severe accident situation.

From the analyzed cases with wrapper openings, two distinct criteria can be identified for obtaining satisfactory ULOF behavior: 1) with sodium vapor successfully sustained above the wrapper openings, negative coolant density reactivity feedback has to be achieved, both at BOL and at BEC, and 2) strong physical oscillations need to be prevented in the upper sodium plenum, so that the strongly coupled neutronics/thermal-hydraulics phenomena there can be stabilized. The second criterion has made a further thermal-hydraulics improvement necessary, viz. a design change for the upper sodium plenum. This, in turn, has yielded the final core configuration discussed below.

Achievement of satisfactory behavior for the final core configuration

The finally proposed core configuration combines the neutronics optimization achieved in SC1 with wrapper openings and an extended fission gas plenum in place of the original sodium plenum. The latter modification helps fulfill the conditions for achieving sufficient coolant flow stability during the void propagation. With the establishing of a new “steady state” – with stable sodium boiling in the upper core region – this final design is able to prevent cladding and fuel from melting under the selected ULOF accident scenario, not only at beginning-of-life, but also in the equilibrium fuel cycle.

It has been pointed out that the reduced core height of the final configuration (smaller H/D ratio, relative to the reference ESFR core) – in conjunction with the extended fission gas plenum – should allow the lower fission gas plenum to be shortened considerably. This would imply a lower pressure drop across the core and a reduction in capital costs.

Finally, it has been underlined that certain passive mechanisms have not been included in the present study (e.g. the thermal expansion of the control rod drives). The consideration of such effects could introduce sufficient, additional negative reactivity for significantly reducing the core power further or

even achieving an automatic shutdown of the reactor during the hypothetical accident scenario in question.

6.3 Recommendations for future work

The conducted doctoral research represents a contribution towards the development of safer SFR core concepts. Improvements and further investigations can be proposed as work to be carried out in the future, and the present section makes four recommendations in this context.

The first two relate to further development and validation of the coupled PARCS/TRACE model, viz.

- 1) Other thermal-mechanical reactivity feedbacks and complete coolant circuits should be implemented in the current PARCS/TRACE model.
- 2) The TRACE modeling of the new wrapper design should be further validated and improved.

The other two recommendations focus on extended applications, viz.

- 3) The neutron balance based method for reactivity decomposition, currently applied to analysis of the static sodium void reactivity effect, should be used in a wider SFR safety context.
- 4) The neutronics and thermal-hydraulics optimization steps currently proposed for the ESFR reference core should be investigated in greater detail within the framework of an industrial prototype project, e.g. the ASTRID reactor, which is planned to be constructed in France by 2020 (see Section 1.4).

Improvement of the PARCS/TRACE model

In the present PARCS model, four SFR reactivity feedback effects are considered: the coolant density effect (including the void effect), the Doppler effect, and the effects of thermal expansion of fuel (axial expansion) and core diagrid (radial expansion). A useful improvement would be to include other thermal-mechanical reactivity feedbacks. Thus, according to the dynamic behavior demonstrated for the final core configuration in Chapter 5, a considerable “grace period” would be available under the selected ULOF accident scenario. During this period, certain passive mechanisms based on the thermal expansion of in-vessel structures could be expected to function. In particular, the increased coolant temperature above the core (more than a 400°C increase) would lead to the thermal expansion of control rod drives and the passive insertion of absorber rods into the active core. It is highly desirable that such effects can be taken into account by PARCS. At the current stage, the PARCS model is already capable of simulating the relative movement of the control rods. It should thus be relatively easy to extend the existing control rod model for meeting the related needs of the transient analysis. Another possible improvement of the present PARCS model is to implement thermal expansion

mechanisms for the cladding (in both axial and radial directions), even though the associated reactivity feedback is expected to be insignificant for the studied accident scenario.

With the present TRACE model, the transient analysis has been restricted to simulation of just the SFR core, with the inlet temperature of the primary coolant assumed to be constant. Consequently, the coupled PARCS/TRACE calculations have not been able to capture the response of the secondary circuit. Thus, even though the radial thermal expansion effect – which is induced by the diagrid temperature change and normally provides a large negative reactivity feedback when the inlet temperature is increased – has been calculated in the PARCS model (and also verified against ERANOS results), it is actually not taken into account during the reactor transient due to the above restrictions. The recommendation is to set up a more complete plant model, so that the interactions between the core and the primary/secondary coolant loops can be simulated more explicitly. Also these modifications are expected to predict a higher safety margin for the considered ULOF transient.

The present doctoral study focuses on the viewpoints of neutronics and thermal-hydraulics. As the next step of the reactor physics analysis in multi-domains, the total coupling of the FAST code system, with additional implementation of the fuel thermal-mechanics FRED model, is recommended. This improvement may allow taking into account 1) the fuel behavior during transient (different fuel and cladding failure criteria may apply) and 2) the influence of the fuel thermal-mechanical properties caused by burnup (e.g. degradation of melting points, thermal conductivities, and etc).

Modeling validation and improvement for the innovative wrapper design

The TRACE model of the SFR core was modified appropriately for the purpose of simulating the proposed wrapper openings. Neighboring channels, according to the mapping scheme, were connected by side junctions at $\frac{3}{4}$ of the fuel region height from the bottom. However, while using of TRACE, i.e. with a 1D thermal-hydraulics modeling of the individual coolant channels, certain simplifications and assumptions had to be made, e.g. the hydraulic impact of the sodium flowing between the wrapper tubes is neglected in the current model. Effectively, the accuracy of the TRACE predictions of the horizontal bypasses between neighboring channels – even for the situation of normal operating conditions, i.e. for single-phase flow – needs more detailed investigation and validation. As a first step, a CFD (Computational Fluid Dynamics) study should be carried out to verify the simulation of the bypasses in the single-phase situation; to the author's knowledge, a reliable CFD simulation of two-phase sodium flow is currently not possible. As the next step, representative flow patterns for sodium boiling should be investigated experimentally, i.e. using configurations of multiple parallel channels with bypasses provided by appropriate wrapper openings.

Extended application of reactivity decomposition methods

In Chapter 3, the neutron balance based reactivity decomposition method has been extensively described and applied to the sodium void reactivity effect. It has been seen how – in conjunction with

complementary studies using perturbation theory based decomposition and sensitivity analysis – a clear understanding of the principal underlying phenomena can be provided for a given type of reactivity change. It would be very useful to broaden the scope of such application in the SFR safety context. Thus, the other principal reactivity effects, viz. Doppler, axial and radial thermal expansion, etc., should be studied in similar manner. Another possible direction is to extend the application in terms of dynamic reactivity decomposition. By implementing the neutron balance based decomposition method into the PARCS kinetics module, it would become possible to follow changes in the contributions of individual reaction-wise, isotope-wise and/or energy-group-wise reactivity components during the course of a given transient.

Investigation of current SFR optimization steps in an industrial context

As mentioned in Section 1.4, a new industrial SFR program – being conducted jointly by CEA, EDF and AREVA – has been underway in France, since 2007. The objective is to develop and implement a prototype reactor with promising innovations representative of a new generation of SFRs by 2020. This prototype, called ASTRID, is expected to serve as the precursor of a first-of-its-kind commercial system, which can largely meet the declared GIF goals. Effectively, the program sets out to demonstrate the progress made in SFR technology on an industrial scale by qualifying innovative options, some of which still remain open in areas requiring improvements, in particular safety.

The major aim of the present doctoral research has been to contribute towards the development of safer advanced SFR concepts through an optimization of the core design. It would be useful to carry out a detailed investigation of the currently proposed neutronic and thermal-hydraulic improvements in the context of an industrial R&D program such as ASTRID. Thus, according to the neutronic analysis, the sodium plenum and boron layer are very favorable to a reduction of the void effect. However, consideration of the thermal-hydraulics has been found to be important for mitigating strong oscillations in the case of sodium boiling. In addition, it has been shown that sodium voiding in the case of an accident should be restricted to the upper region of the core by introducing an innovative wrapper design with openings. It would clearly be beneficial to assess the impact of such changes in the core design for ASTRID.

It needs to be added that, in the present doctoral research, the focus has been on a representative ULOF transient, in order to demonstrate the effectiveness of design improvements from the viewpoint of the sodium void effect. In the context of the suggested investigations, it would be important to broaden the range of studied transients, so that the impact of the proposed design changes can be assessed in a more comprehensive manner. Unprotected Loss-Of-Heat-Sink (ULOHS) and Unprotected Transient Over Power (UTOP) are the transient types that also need consideration. Thus, for example, the Doppler effect – optimization for which has been shown to have relatively little impact on the considered ULOF accident scenario – could play a much more important role during ULOHS and UTOP transients.

6.4 Concluding remarks

The present doctoral research has successfully demonstrated that an advanced SFR core design – with improved safety characteristics from both neutronic and thermal-hydraulic viewpoints – can effectively prevent the cladding and fuel from melting during a selected unprotected loss-of-flow accident scenario, in which sodium boiling occurs. It has been shown that, after a hundred seconds or so into the transient, a new steady state is established with stable sodium boiling involved. To the author's knowledge, such a demonstration of SFR safety, based on coupled 3D-neutronics/thermal-hydraulics modeling, has not been carried out previously.

In summary, a clearer understanding of the principal phenomena contributing to the sodium void reactivity effect has been achieved. The investigation has been carried out using neutron balance and perturbation theory based reactivity decomposition methods. A neutronics optimization study on the basis of the reference ESFR core has been carried out, two optimized core concepts being proposed by combining different analyzed options. The dynamic core behavior during a representative unprotected loss-of-flow accident scenario has been studied using a coupled PARCS/TRACE model. An innovative wrapper design for the fuel assembly has been proposed, in order to provide bypasses for the sodium flow when sodium vapor blocks the flow area at the top of the fuel. The resulting void distribution, which covers the plenum region and the upper part of the active core, can effectively lead to negative coolant density reactivity feedback. By stabilizing the coolant flow oscillations with an innovative plenum design, a final core configuration has been achieved, which is capable to prevent the cladding and fuel from melting during the considered transient, not only for the beginning-of-life state, but also in the equilibrium fuel cycle.

In conclusion, the present doctoral research has analyzed and optimized advanced SFR core designs with improved safety characteristics, particularly from the viewpoint of the positive sodium void reactivity effect and its impact on dynamic core behavior during hypothetical accident scenarios. Recommendations have been made for future investigations.

References

- [6.01] A. Chenu. Single- and two-phase flow modeling for coupled neutronics / thermal-hydraulics transient analysis of advanced sodium-cooled fast reactors. Swiss Federal Institute of Technology, Lausanne (EPFL), doctoral thesis No. 5172 (2011).
- [6.02] J. M. Seiler, D. Juhel, Ph. Dufour. Sodium boiling stabilization in a fast breeder subassembly during an unprotected loss of flow accident. Nuclear Engineering and Design, vol. 240: pp. 3329-3335, 2010.
- [6.03] European Patent No. 11196146.2–2208. A wrapper tube for a fuel subassembly of a nuclear reactor core and method for protecting fuel against overheating in case of coolant boiling. Filed in 2011.

Appendices

Appendix A

Monte Carlo Verification of ERANOS Calculations

In the current appendix, code-to-code benchmark comparisons are presented between the deterministic code system ERANOS and the Monte Carlo code SERPENT. Some of these comparisons have been reported directly in appropriate sections of Chapters 3 and 4, this appendix serving to present the conducted benchmarking in a consolidated and more complete manner.

The background for the study is given in Section A.1. The benchmark results are presented and discussed in Section A.2. A supplementary investigation focusing on the unresolved resonance treatment is performed in Section A.3. Finally, in Section A.4, the conclusions are drawn.

A.1 Background

The deterministic code system ERANOS has generally been adopted in this doctoral research for the steady state neutronic calculations. The constituent data libraries, individual codes and calculation procedures have been developed and validated within the European collaboration on fast reactors over the past 20 years. In particular, ERANOS was initially developed for sodium-cooled fast reactors operating with MOX fuel, so that it can be considered quite appropriate as computational tool for the current ESFR-related research. Nevertheless, a verification study for the ERANOS calculations – particularly in the context of void reactivity predictions – is clearly desirable. A Monte Carlo code, SERPENT, has accordingly been selected for verification purposes.

SERPENT is a 3D continuous-energy burnup calculation code based on the Monte Carlo method. It has been under development at the VTT Technical Research Centre in Finland since 2004. SERPENT reads continuous-energy cross-sections from ACE-format data libraries based on JEF-2.2, JEFF-3.1, JEFF-3.1.1, ENDF/B-VI.8 and ENDFB/B-VII, and then reconstructs them to a uniform lethargy-width energy grid. The nuclear data is available for 432 nuclides at six temperatures between 300K and 1800K. SERPENT uses a universe-based geometry model (similar to MCNP and Keno-VI), which allows the description of practically any 2D or 3D fuel or reactor configuration. The geometry consists of material cells, defined by elementary and derived surface types. The SERPENT geometry routine for the neutron transport simulation is based on a combination of conventional surface-to-surface ray-tracing and the Woodcock delta-tracking method, which has proven efficient and well suited for lattice calculations. The combination of two tracking methods overcomes the efficiency problems normally encountered with delta-tracking in the presence of localized heavy absorbers.

SERPENT is capable of generating homogenized group constants and the predefined energy grid types include the 1968-group and 33-group structures used in ERANOS. This feature enables the comparison of not only the multiplication factors and reactivity effects, but also the neutron spectrum and homogenized group-wise cross-sections.

A.2 Benchmark results

In the present verification study, the same basic nuclear data, viz. JEFF-3.1, have been used in ERANOS and SERPENT for the benchmark calculations. The average material compositions of the fuel pellets, cladding, assembly wrapper, coolant, control rod, reflector, etc. are completely consistent in the models used with the two codes. However, ERANOS has a heterogeneous description for the fuel assembly only (homogeneous descriptions for the rest), whereas SERPENT simulates all the components heterogeneously. The resulting comparison has been carried out on two different scales: 1) at the cell level and 2) at the full reactor core level. For the cell/lattice calculation, both codes select reflective boundary condition in both axial and radial directions (i.e. assuming an infinite lattice) and switch off the B1-method option (buckling search for $k_{eff} = 1$). In ERANOS, the reference computational route is adopted, viz. treatment of the heterogeneous cell geometry using collision probabilities and applying the subgroup method in the fine energy-group structure.

Cell level benchmark

For the cell level benchmark, the neutron spectra (1968 energy groups) generated by ERANOS/ECCO^{A.1} and SERPENT have first been compared. This is followed by the comparison of results for the infinite multiplication factor and the principally considered reactivity effects, viz. void and Doppler. In addition, prediction of the 33-group constants (viz. the homogenized macroscopic cross-sections for fission and capture) is also compared.

A representative comparison of normalized neutron spectra produced by ERANOS/ECCO and SERPENT is made in Figure A.1. As mentioned, the predefined energy grid in both codes adopts the ERANOS 1968-group structure. As seen, the two presented spectra agree very well with each other. The major cross-section resonances of the different isotopes (e.g. the peaks at 3 keV and 50 keV for the ²³Na elastic scattering cross-section, and the peak at 30 keV for the ⁵⁶Fe elastic scattering cross-section, etc.) are interpreted in almost identical manner by the two codes.

^{A.1} The ECCO module is used in ERANOS for the preparation of self-shielded cross-sections and scattering matrices. Its detailed description can be found in Subsection 2.2.1.

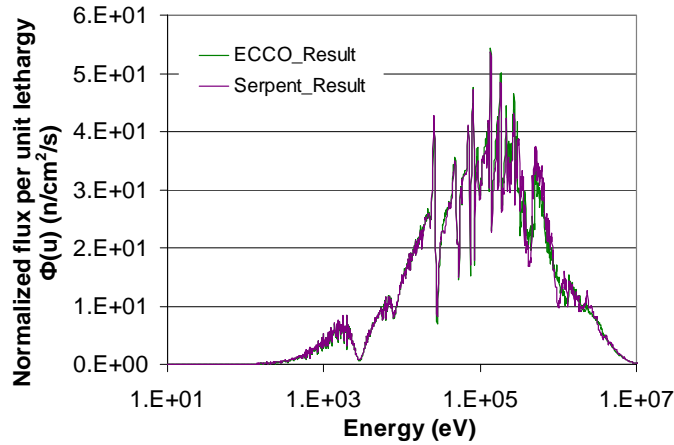


Figure A.1. Comparison of the normalized neutron spectra produced by ERANOS/ECCO and SERPENT for the inner fuel zone of the reference ESFR core.

Table A.1 shows the comparison made at cell level in terms of infinite multiplication factor (k_{inf}), void reactivity ($\Delta\rho_v$) and Doppler constant (DC). It is seen that SERPENT yields significantly higher infinite multiplication factor values than ERANOS/ECCO, the differences being 400 to 500 pcm. This discrepancy may be largely attributed to the different treatments for the unresolved resonance region. In this energy region, ERANOS/ECCO derives effective cross-sections through computing self-shielding factors using the narrow resonance approximation, whereas SERPENT employs probability distributions for the different reaction types. A more detailed discussion of this topic is given in Section A.3. It is important to note here that – even though the infinite multiplication factors computed by SERPENT and ERANOS/ECCO differ significantly – the results obtained for reactivity effects, e.g. void reactivity and Doppler constant, show very good agreement (differences of less than ~105 pcm). This observation provides convincing justification for assuming that ERANOS/ECCO is capable of predicting the principal safety parameters considered in this doctoral research with adequate accuracy.

Table A.1. ERANOS/ECCO and SERPENT results at cell level for multiplication factor, void reactivity and Doppler constant; unit cell calculations for the inner and outer fuel zones of the reference ESFR core

Parameter	SERPENT	ERANOS/ECCO	Difference
Inner fuel k_{inf} (1500K)	1.11237 ± 0.00004	1.10767	470 ± 4 pcm
$\Delta\rho_v$ (90% voided)	2736 ± 6 pcm	2667 pcm	69 ± 6 pcm
DC (1500K→900K)	-1219 ± 11 pcm	-1322 pcm	103 ± 11 pcm
Outer fuel k_{inf} (1500K)	1.20836 ± 0.00004	1.20319	517 ± 4 pcm
$\Delta\rho_v$ (90% voided)	2559 ± 6 pcm	2508 pcm	51 ± 6 pcm
DC (1500K→900K)	-956 ± 11 pcm	-1020 pcm	64 ± 11 pcm

Appendix A: Monte Carlo Verification of ERANOS Calculations

The comparison made of homogenized macroscopic cross-sections for fission and capture is presented in Figure A.2. As indicated earlier, the predefined energy grid for homogenization in both ERANOS/ECCO and SERPENT is the ERANOS 33-group structure. It is seen that the predictions of both fission and capture cross-sections are quite consistent in the energy range shown (above ~ 60 eV, i.e. down to about group No. 25). Relatively large discrepancies have, however, been found in the low energy range below 60 eV (i.e. for groups 26-33). This can largely be explained by the insufficient statistical accuracy of the Monte Carlo results at low energy, which are not relevant to the current SFR investigations, the comparisons being quite adequate for the fast spectrum regions of interest.

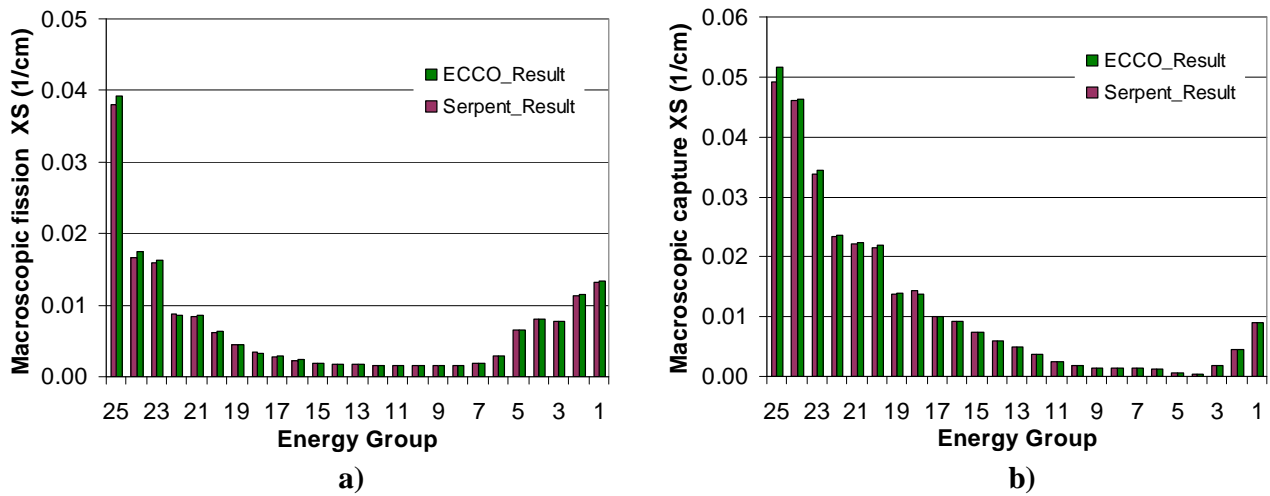


Figure A.2. Comparison of group-wise macroscopic cross-sections for a) fission and b) capture; unit cell calculations for the inner fuel zone of the reference ESFR core

Core level benchmark

The VARIANT module, implemented in ERANOS and using the variational nodal method, has been adopted for most of the core level calculations in this doctoral research. For the core level benchmark, the principal parameters considered are the effective multiplication factor (k_{eff}), void reactivity and Doppler constant.

Table A.2 shows the comparison of the SERPENT and ERANOS results for the reference ESFR core. Here, transport theory with simplified spherical harmonics has been chosen as the reference flux solving option in ERANOS. As in the case of the infinite multiplication factor prediction at the cell level, SERPENT yields a higher value for the effective multiplication factor than ERANOS. This discrepancy is, once again, largely caused by the different unresolved resonance treatments in the two codes. As before, the important point is that a good agreement is obtained for the principal safety parameters, i.e. void reactivity and Doppler constant (differences of less than ~ 50 pcm). This provides convincing evidence for the adequacy of the safety related ERANOS modeling at the full core level.

Table A.2. ERANOS and SERPENT results for the effective multiplication factor, void reactivity and Doppler constant for the reference ESFR core (full core level).

Parameter	SERPENT	ERANOS	Difference
k_{eff} (1500K)	1.01397 ± 0.00005	1.01006	391 ± 5 pcm
$\Delta\rho_v$ (90% voided)	1486 ± 7 pcm	1505 pcm	-19 ± 7 pcm
DC (1500K→900K)	-1284 ± 14 pcm	-1329 pcm	45 ± 14 pcm

As discussed in Chapter 4, one important option to reduce the void effect is introducing an upper sodium plenum and boron layer into the reference ESFR core design. However, the prediction of the void effect in the upper sodium plenum region using a deterministic code (e.g. ERANOS) requires an accurate solution of the neutron transport (or diffusion) equation, since it largely depends on an adequate interpretation of changes in the leakage term. Accordingly, additional emphasis has been placed here for benchmarking the void reactivity corresponding to different voiding scenarios with different flux solving options. Three voiding scenarios are considered: reference voiding, extended voiding, and plenum voiding. In addition, three flux solving options in ERANOS/VARIANT are evaluated, viz. diffusion theory, transport theory with simplified spherical harmonics, and full transport.

It should be noted that the reference ERANOS model has a heterogeneous description for the inner and outer fuel zones only, the remaining components – including the upper sodium plenum – being simulated homogeneously. The reference SERPENT model, on the other hand, has a heterogeneous description for the whole core. In order to evaluate the corresponding influence on the treatment of neutron streaming effects in the extended and plenum voiding scenarios, usage has also been made of an alternative SERPENT model in which a homogenized upper sodium plenum is adopted. Table A.3 presents the comparisons made for the different cases, the heights assumed for the sodium plenum and boron layer being 30 cm and 15 cm, respectively.

Table A.3. ERANOS to SERPENT benchmark for reactivity effect results (units: pcm) in terms of reference, extended and plenum voiding scenarios (with 90% voidage).

Computation code	ERANOS	ERANOS	ERANOS	SERPENT	SERPENT
Sodium plenum mode	Homogeneous	Homogeneous	Homogeneous	Homogeneous	Heterogeneous
ERANOS flux solving option	Diffusion	Simpl. transport	Transport	-	-
Reference $\Delta\rho_v$ (90% voided)	1433	1463	1463	1441 ± 7	1442 ± 7
Extended $\Delta\rho_v$ (90% voided)	832	869	928	854 ± 7	821 ± 7
Plenum $\Delta\rho_v$ (90% voided)	-516	-512	-462	-501 ± 7	-531 ± 7

As seen from the tabulated results, the different flux solving options in ERANOS generally agree with each other for all the considered voiding scenarios. It is found that diffusion theory underestimates the reference void reactivity slightly (by ~ 30 pcm). Relative to the full transport solution, results for voiding of the plenum by itself are ~ 50 pcm more negative (i.e. less conservative) for both diffusion theory and simplified transport.

From the two sets of SERPENT results shown in Table A.3, one can see that homogenization of the upper sodium plenum has negligible influence on the reference void reactivity prediction. However, in both the other two cases, the heterogeneous calculation is seen to yield a slightly more negative effect of voiding the sodium plenum. This is clearly due to the reduction of the streaming effect in the homogeneous calculation. Nevertheless, this reduction may be considered insignificant (~ 30 pcm), in comparison to the global leakage enhancing effect of the sodium plenum voiding (~ 500 pcm).

A.3 Investigation of the unresolved resonance treatments

In the energy range from a few hundred eV to several keV, the resonances of heavy isotopes are located so close together that they can no longer be resolved into separate peaks. However, the strong variations of the cross-sections in this so called “unresolved range” do lead to important effects, e.g. self shielding, particularly in the context of fast-spectrum system applications. In ENDF-format^{A.2} evaluations, the unresolved range is handled by specifying average values for the resonance spacing and the various partial widths, together with probability distributions for the spacing and partial widths [A.01].

In practice, it is not possible to compute simple “cross-section vs. energy” tables in the unresolved range. Instead, for example, ERANOS/ECCO derives the effective cross-section through computing self-shielding factors in the narrow resonance approximation (such an approximation being largely valid for a fast-spectrum system), whereas SERPENT uses probability distributions for the different reaction types. A very relevant study [A.02] has shown that the different unresolved resonance data treatments in Monte Carlo and deterministic codes can, in certain situations, yield discrepancies in multiplication factor of more than 1000 pcm. Thus, the currently observed differences (see Tables A.1 and A.2) seem to be acceptable.

It should be noted that one can choose to switch the unresolved resonance (UR) option in SERPENT on or off, the various results reported above being with the option “on”. The effect induced on the infinite multiplication factor prediction is ~ 400 pcm (see Table A.5). When the UR option is switched off, the SERPENT results appear to be in much better agreement with the ERANOS/ECCO results. This indicates that, when the currently implemented probability distributions of the different types of

^{A.2} ENDF (Evaluated Nuclear Data Format) is used all over the world to encode nuclear data evaluations for use in research and nuclear technology. JEFF-3.1, the cross-section library adopted in the current doctoral work, is written in this format.

cross-sections in the unresolved energy range are not taken into account, SERPENT – somewhat fortuitously – yields very similar multiplication factor results as ERANOS (which adopts the narrow resonance approximation for the unresolved region). This clearly demands further clarification, considering that a reliable unresolved resonance treatment is indeed necessary in fast reactor applications. It needs to be mentioned, in this context, that validation and improvement of the unresolved resonance treatment in SERPENT is a part of the on-going further development activity for the code [A.03].

Table A.5. Effect of the UR^{A.3} option in SERPENT for cell level k_{inf} predictions and comparison to the corresponding ERANOS/ECCO values; calculations for the inner and outer fuel zones of the reference ESFR core at 300K

	SERPENT UR “on”	SERPENT UR “off”	ERANOS/ECCO
Inner fuel k_{inf} (300K)	1.14049 ± 0.00006	1.13609 ± 0.00006	1.13659
Outer fuel k_{inf} (300K)	1.23419 ± 0.00006	1.22995 ± 0.00006	1.22965

A.4 Conclusions

In the present appendix, representative neutronics results obtained using the deterministic code ERANOS – in terms of neutron spectrum, multiplication factor, void reactivity, Doppler constant, and homogenized macroscopic cross-sections for fission and capture – have been verified against Monte Carlo calculations using SERPENT. The comparisons made, at both cell and full core levels, have generally shown very good agreement. This has provided convincing justification for assuming that the ERANOS calculations conducted in this doctoral research are of adequate accuracy.

Particular emphasis in the ERANOS benchmarking against SERPENT has been placed on the prediction of the void reactivity effect in the upper sodium plenum region. Good agreement has been obtained for different voiding scenarios (viz. reference voiding, extended voiding, and plenum voiding), while using different flux solving options in ERANOS, viz. diffusion theory, transport theory with simplified spherical harmonics, and full transport. In addition, it has been confirmed by the SERPENT calculations that the homogeneous modeling of the sodium plenum leads to only a slightly (~ 30 pcm) less negative prediction of the plenum voiding effect.

^{A.3} UR is a SERPENT option, which controls the activation of unresolved resonance probability tables.

References

- [A.01] Introduction to the ENDF formats: <http://t2.lanl.gov/endf/theindex.html>.
- [A.02] R. Jacqmin and J. P. Both. ECCO/ERANOS validation studies. Technical report, NJOY/JACQMIN-01, 1996.
- [A.03] Serpent current status: <http://montecarlo.vtt.fi/development.htm>.

Appendix B

Sensitivity Study with respect to Plenum Height

In the present appendix, the sensitivity of the dynamic core response, during the selected unprotected loss-of-flow (ULOF) accident scenario, has been investigated with respect to the height of the upper plenum. The background information, including the motivation for the current study, is given in Section B.1. The cases studied and results of the sensitivity analysis are reported in Section B.2. Finally, conclusions are drawn in Section B.3.

B.1 Background

It is recalled here that two synthesis core concepts – combining different analyzed optimization options – were proposed in Subsection 4.4.2. The common boundary condition, which was set, is to have a positive nominal reactivity margin at the end of the equilibrium closed fuel cycle. In both optimized core concepts, the upper sodium plenum thickness considered was 30 cm. This was later replaced by an extended fission gas plenum, the length added to the original fission gas plenum height being exactly the same 30 cm. Effectively, a compromise has had to be made between neutronics and thermal-hydraulics aspects associated with the upper plenum region. Thus, even though it has been confirmed by static neutronic calculations that the larger the sodium plenum, the stronger the void effect reduction (see Figure 4.4), from the dynamics point of view, too large a volume of sodium above the core can – during the considered ULOF transient – lead to strong sodium boiling oscillations (see Subsection 5.3.2).

Considering that the final core configuration, proposed in Section 5.4, is the case where a new steady state was shown to be established involving stable sodium boiling, it is clearly important to investigate the impact of varying the plenum height in this configuration. The sensitivity study carried out accordingly employs the final core configuration as basis.

B.2 Studied cases and results

Four different “additional heights” for the extended fission gas plenum have been tested in the present study: 15cm, 30cm (the finally adopted core configuration in Chapter 5), 45cm and 60cm. It should be noted that the original height of the upper fission gas plenum implemented in the reference ESFR core is 11cm, so that one should always add this value to obtain the effective upper fission gas plenum

Appendix B: Sensitivity Study with respect to Plenum Height

height. The same flow run-down curve as described in Subsection 5.1.3 has been chosen here, representing the reference ULOF accident scenario. The PARCS/TRACE results for the evolutions of power and coolant density reactivity feedback during the transient are shown in Figure B.1.

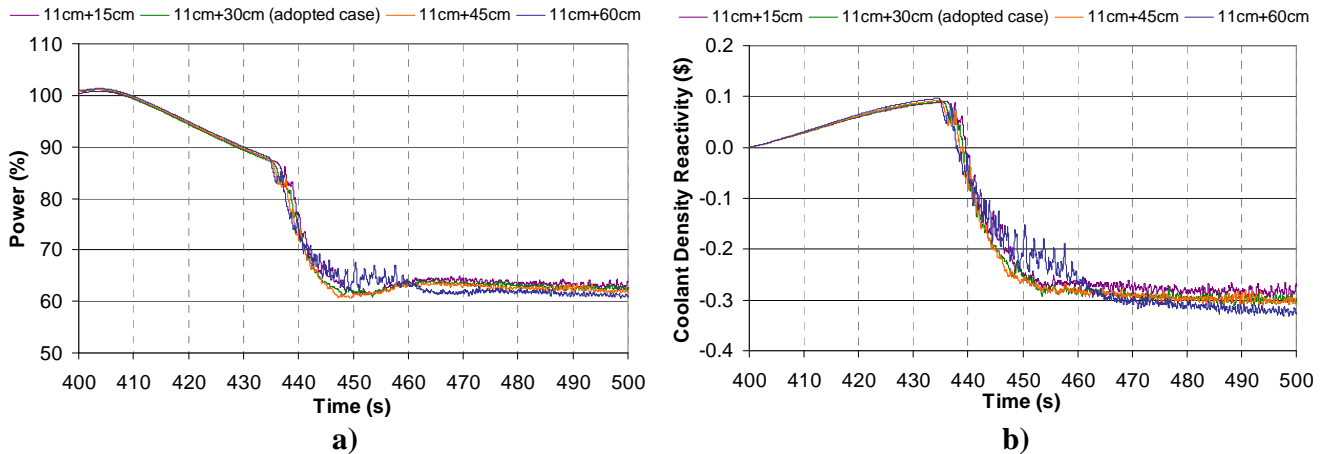


Figure B.1. Evolutions of a) power and b) coolant density reactivity feedback during the ULOF for core configurations with different additional heights for the upper fission gas plenum: 15cm, 30cm, 45cm and 60cm; the original height of the upper fission gas plenum is 11cm.

As seen from the figures, even though the four simulated cases have different plenum heights, the core behaviors during the considered ULOF accident scenario are, in general, quite similar. This indicates that the dynamic response of the final core configuration for this particular transient is not very sensitive to the plenum height. The case with 60 cm additional fission gas plenum height is shows – as to be expected – the most negative coolant density reactivity feedback in the new steady state. However, the difference, as compared to the other three cases, is not significant. Somewhat more important is the observation that, during the period that the sodium boiling propagates (i.e. from the boiling onset until the new steady state), the 60cm case features the strongest oscillations. As mentioned, the greater instability is mainly due to the vaporization/condensation process becoming more violent in the larger volume of sodium above the core, a consequence of the more intensive coupling between neutronics and thermal-hydraulics phenomena.

The presented curves for the other three cases, i.e. with additional fission gas plenum height of 15cm, 30cm and 45cm, respectively, behave very similarly, so that it is difficult to determine the most appropriate plenum height from analysis of the dynamic core response. This, in a way, is a positive observation to make, since it underlines the robustness of the final core configuration design.

B.3 Conclusions

In the present appendix, a sensitivity study with respect to the upper plenum height has been reported for the final SFR core configuration proposed in Section 5.4. It is found that the dynamic core response during the selected ULOF accident scenario is not very sensitive to the additional height of the fission gas plenum, in the range between 15 and 45cm. This, in a way, confirms the robustness of the final core configuration design. If the additional fission gas plenum height is too large (e.g. 60cm), there may be a risk of instability of the sodium flow due to too strong a coupling between neutronics and thermal-hydraulics phenomena. On the other hand, too small a plenum could have a negative impact on the neutron economy (due to the short distance between the fuel region and the boron layer). All in all, the chosen 30 cm additional height is considered as a reasonable compromise from the viewpoints of neutronics, thermal-hydraulics and stability.

Appendix C

Study on Sodium Boiling Oscillations

In most of the simulation cases presented in Chapter 5, one can observe that – following the boiling onset – the coolant flow rate at the outlet starts to oscillate with a frequency of the order of 1 Hz. This is not a numerical effect, but is rather related to physical phenomena, viz. those typical of sodium boiling in multi-channel systems. An auxiliary study, conducted in order to confirm this, is presented in this appendix. Representative PARCS/TRACE simulation results for the coolant flow, as obtained in the present research, are compared qualitatively with certain relevant experimental data.

Section C.1 gives a short description of the theoretical background, while Section C.2 describes the considered experiment. The qualitative comparison of currently obtained simulation results and the experimental data is presented in Section C.3, while Section C.4 gives the conclusions.

C.1 Theoretical background

A stable working point usually exists in the case of sodium boiling. Before analyzing the stability of sodium two-phase flow, the following definitions should be presented [C.01]:

- The *Internal Characteristic (I.C.)* is the variation of pressure drop across the channel induced by single- and/or two-phase flow when the inlet flow rate is varied under constant power, constant outlet pressure, and constant inlet temperature. For low pressure sodium flow, the shape of the I.C. has the form of an S-curve, due to the physical properties of sodium (see Figure C.1).
- The *External Characteristic (E.C.)* is the variation in the pressure drop between the two extremities (inlet and outlet) of the fuel assembly induced by the external loop as a function of the corresponding inlet flow rate. As the fuel assembly is part of a loop, the hydrodynamic conditions at the boundary of the assembly are dependent on this external loop.

The intersection between the I.C. and E.C. corresponds to a working point. The stability of this working point depends on the shapes of the I.C. and E.C. curves. According to the Ledinegg criterion, a stable working point, at mass flow rate Q_0 , can be obtained when:

$$\left(\frac{\partial \Delta P_{EC}}{\partial Q} \right)_{Q_0} < \left(\frac{\partial \Delta P_{IC}}{\partial Q} \right)_{Q_0} \quad \text{Eq. C.1}$$

Appendix C: Study on Sodium Boiling Oscillations

where ΔP_{EC} and ΔP_{IC} represent the E.C. and I.C., respectively, and Q is the inlet flow rate of the channel. It should be mentioned that the Ledinegg criterion is only valid for steady state or slow transient conditions. If the criterion is not satisfied, due to the fact that boiling induces a severe increase of the friction pressure drop, the two-phase flow in the fuel assembly may lead to a flow excursion [C.02]. As shown in Figure C.1, the mass flow will decrease progressively from point B to point C and the vapor will expand into the heated zone. A new stable working point (with high quality boiling) may theoretically be reached, where the Ledinegg criterion is again satisfied. However, for the currently considered high power conditions, dryout is anticipated to occur and stable high quality boiling cannot be reached [C.03].

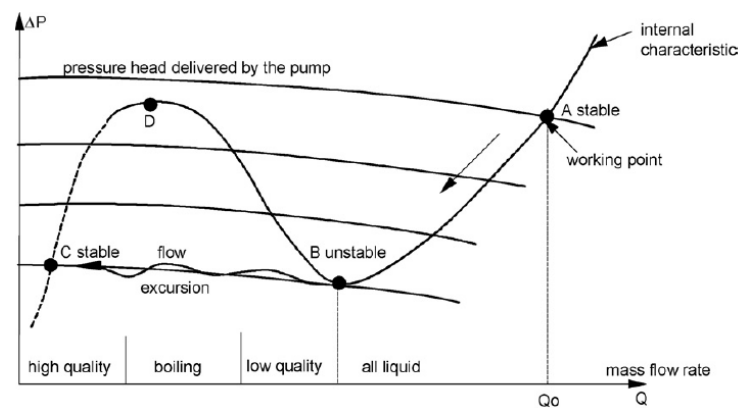


Figure C.1. Typical shapes of the internal characteristic and pressure head curves (external characteristic) for a boiling channel at high power [C.01].

Under typical ULOF transient conditions, the reactor power usually decreases from the nominal level before the sodium boiling onset. In the present doctoral research, the reactor power during the considered ULOF scenario was reduced typically by $\sim 1/6$ at the boiling onset and then leveled off at $\sim 2/3$ of the nominal value. It has been observed in the past [C.04] that, at low power and low flow rates, the two-phase friction pressure drops may become smaller than buoyancy effects, thus leading to stable low quality boiling. For example, the intersection A2 in Figure C.2 is a working point satisfying the Ledinegg criterion and corresponds to stable sodium two-phase flow in a low-quality boiling regime (i.e. without dryout).

It should be noted that Figure C.2 principally depicts the single channel problem, with simply a constant gravity effect taken into account and the friction pressure drop in the cold part of the loop assumed to be negligible. Thus, one sees that E.C. is a fixed, flat (zero derivatives) line. In the present doctoral research, however, the thermal-hydraulics model of the reactor core consists of 45 parallel fuel channels. These are all connected to a common lower plenum. In this sense, mutual hydraulic interactions between neighboring fuel channels can be expected to occur in the case of sodium boiling. Furthermore, for the final core configuration proposed in Chapter 5, the introduced additional hydraulic junctions, representing the wrapper openings, make these mutual interactions even more

significant. Accordingly, the pressure drop in each individual channel is significantly dependent on the other parallel channels. In this context, the E.C. is no longer a fixed curve but rather, as a whole, is shifted up and down due to pressure wave propagation. This, in turn, prevents the working point from maintaining a stationary position, implying that the corresponding mass flow rate behaves in an oscillatory manner.

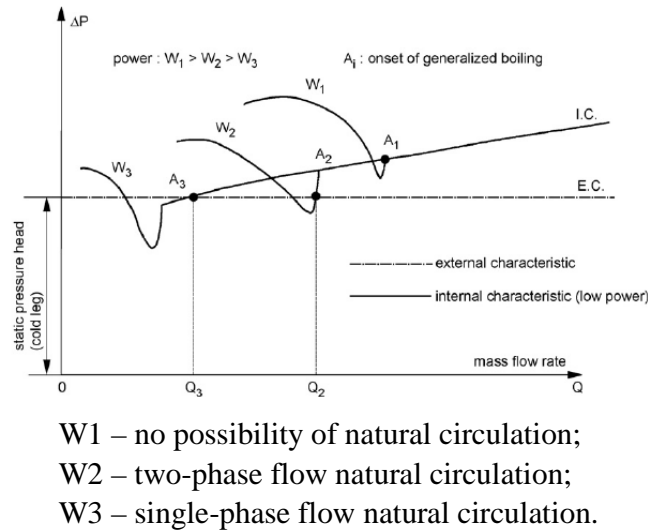
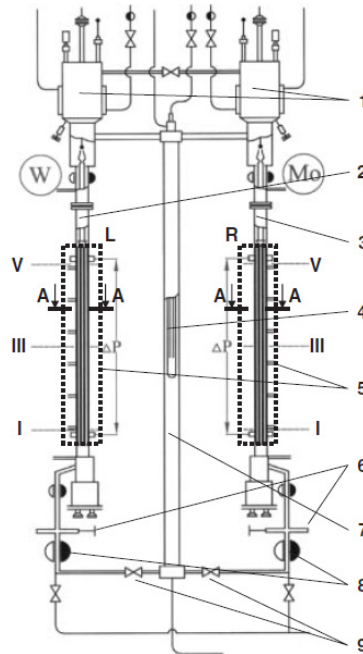


Figure C.2. Internal and external characteristics for sodium boiling at low power [C.01].

C.2 Sodium boiling experiment considered [C.05]

The experiment considered currently was conducted at the AR-1 experimental facility of the Institute of Physics and Power Engineering (IPPE) in Obninsk, Russia. The installation was constructed in order to study sodium boiling inside parallel bundles and is essentially a simplified representation of an SFR core with multi-channel interactions. A Na-K eutectic alloy (22% Na and 78% K) is adopted as the coolant.

The test facility (see Figure C.3) consists of three vertical channels, which are connected to each other at the top and bottom sections. They have a height of three meters. The left and right channels contain the two test sections (i.e. components 2 and 3 in the figure), while the central downcomer (component 7) is made from a 50 mm inner diameter tube. The horizontal sections and the connection at the bottom of the test bundles are made from tubes with an inner diameter of 30 mm. In the test sections, two identical 19-pin simulator assemblies are positioned. The outlet of each assembly is connected to an upper plenum component (i.e. component 1 in Figure C.3), which has a constant pressure of 0.4 bar. The head of the pin assembly is located inside the upper plenum. A cooler (i.e. component 4) is located in the upper section of the downcomer channel.



1: Upper plenum, 2: Left channel, 3: Right channel, 4: Cooler, 5: Test sections, 6: Rods with orifices, 7: Downcomer, 8: Electromagnetic pumps, 9: Globe-valves.

Figure C.3. The AR-1 experimental facility showing the loops with assemblies [C.05].

Even though, at AR-1, there have been various single channel experiments (i.e. using the globe-valves to isolate one of the loops), a parallel channel experiment, utilizing both assemblies under equal heating conditions, is considered here for enabling the desired qualitative comparison with the PARCS/TRACE simulations. The details of this experiment are presented in Table C.1. It was conducted with slow step-wise increases in heating power of the pin simulators. The increment in the heat flux at the pin surface was limited to 10-20 kW/m². After each step increase, a time lag was provided to allow stabilization of the flow parameters. This was judged by flow and temperature measurements. As a consequence of small geometry differences, the inlet coolant temperature in the right bundle was lower than that in the left. A delay of the boiling onset was accordingly observed in the former. For the left bundle, boiling starts at 3480s, while in the right it starts at 3819s. The coolant flow rate oscillates in the parallel bundles during the experiment, providing a basis for analysis of the sodium boiling phenomenon. In the following section, the measured coolant flow rates are qualitatively compared with the PARCS/TRACE simulation results presented in Subsection 5.4.2.

It should be mentioned that a more complete description of the equipment used and the experimental procedure followed can be found in [C.05].

Table C.1. Details of the parallel channel experiment at the AR-1 facility.

Parameter	Used dual channels and conditions	
Channel	Left	Right
Duration (s)	5200	5200
Heater turning off time (s)	5100	5100
Initial heat flux (kW/m^2)	8	8
Outlet pressure of assembly (bar)	0.4 (constant)	0.4 (constant)
Heat flux on the heat-generating element surface (kW/m^2)	100	112
Initial coolant flow rate in the circulation circuit (m^3/h)	0.10	0.20
Maximum coolant flow rate in the circulation circuit (m^3/h)	1.00	0.90
Maximum coolant temperature ($^{\circ}\text{C}$)	761	758

C.3 Comparison of simulated flow rate oscillations with experimental data

The coolant flow rate oscillations in the AR-1 experiment change in character during the course of the experiment and are shown on the right hand side of Figure C.4. As can be seen, during the initial boiling stage (3900s - 4300s), the coolant flow rate oscillations in the two loops possess an in-phase character (see Figure C.4a right). The thermal-hydraulic parameters oscillate with relatively small amplitude and a period of about three seconds. Thereafter, the boiling becomes stronger and the oscillations in the two loops start to depart from each other (see the transition phase in Figure C.4b right). Finally, an equilibrium situation is reached where the oscillations appear to be 180 degrees out-of-phase (see Figure C.4c right). Effectively, the two bundles are driving each other in this condition.

The considered PARCS/TRACE results are from the ULOF simulation for the final core configuration at BOL (see Subsection 5.4.2). In this case, after about 200s into the transient, a new steady state is established with stable sodium boiling involved. For two neighboring channels (in which sodium boiling occurs), the left hand side of Figure C.4 shows the time history of the normalized mass flow rates (with respect to the initial values before the transient starts). It is seen that the period of the oscillations is slightly less than one second, i.e. the frequency is more than three times higher than in AR-1 experiment. It needs to be borne in mind, however, that the oscillation frequency is dependent on a number of factors such as the linear heat generation rate, coolant circuit layout, fuel bundle geometry, etc. These are quite different for the experiment and the simulation which are being compared. Nevertheless, the nature of the oscillations and the manner in which they develop and stabilize are quite similar. In both cases, one can observe the evolution from in-phase oscillations (see

Appendix C: Study on Sodium Boiling Oscillations

Figure C.4a left and right), through a transition phase (Figure C.4b) and finally to 180-degree out-of-phase oscillations (see Figure C.4c).

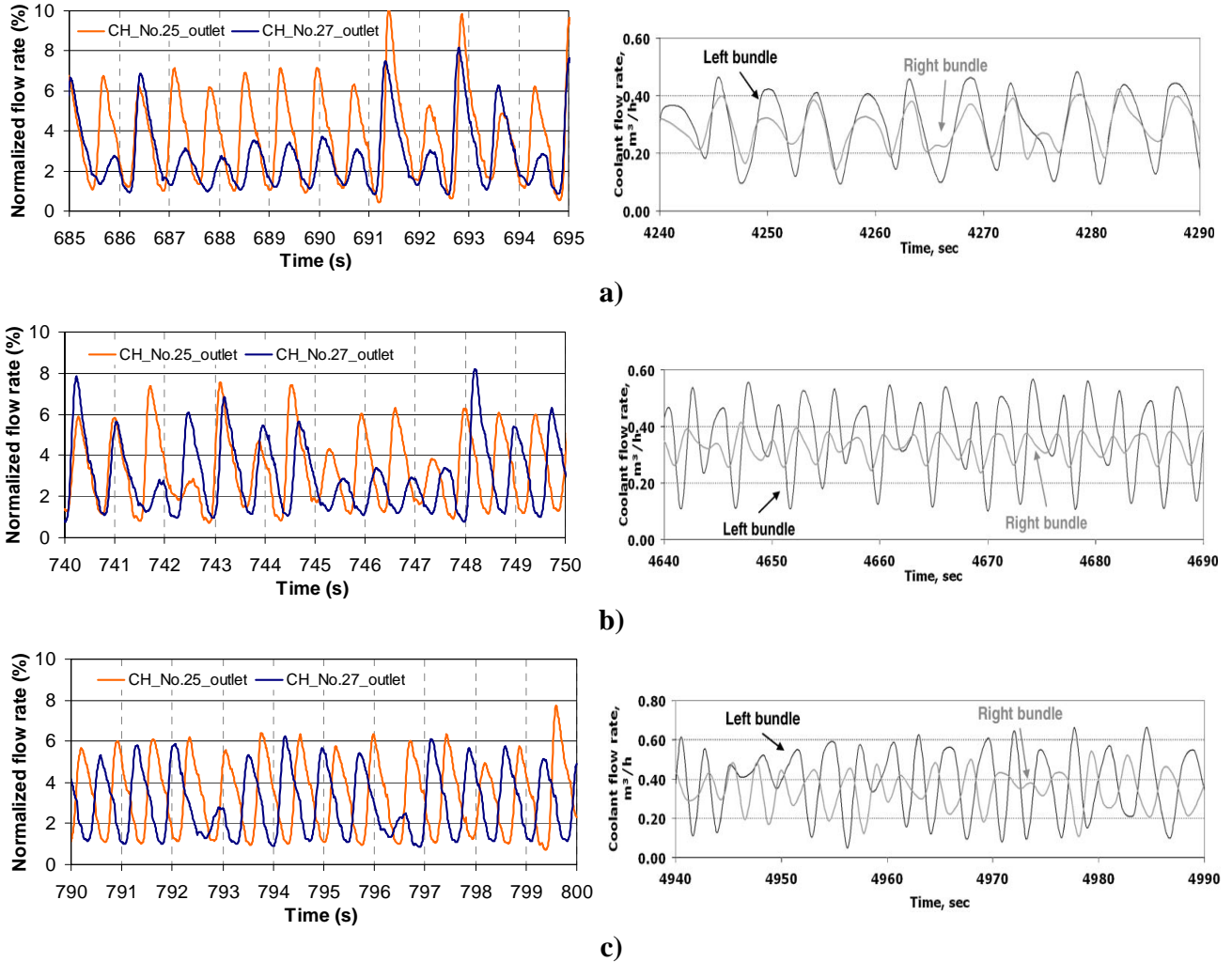


Figure C.4. Qualitative time history comparison of coolant flow rate oscillations between the PARCS/TRACE ULOF simulation for the final core configuration (left) and AR-1 experimental data (right), showing a) in-phase oscillations, b) transition phase and c) out-of-phase oscillations.

C.4 Conclusions

In the present appendix, sodium boiling oscillations in a multi-channel system have been investigated. The theoretical interpretation is that pressure wave propagation, resulting from the hydraulic interaction between the parallel channels, induces the channel-wise mass flow rate to behave in an

Appendix C: Study on Sodium Boiling Oscillations

oscillatory manner. An experiment dedicated to sodium boiling in a parallel channel system (two bundles) has been reviewed to support this message. While considering one of the PARCS/TRACE ULOF simulations carried out in the current research, the time history of the mass flow rates in two neighboring channels of the SFR core (in which boiling occurs) has been qualitatively compared to results from the sodium boiling experiment. The same physical phenomena, involving a transition in the character of the sodium boiling from in-phase oscillations to 180-degree out-of-phase oscillations, have been observed in both cases. Accordingly, one can confirm that the oscillations (of the order of 1 Hz) – which have been observed in the PARCS/TRACE results for reactor power, reactivity components and mass flow rate – are not a numerical effect but rather, correspond to the prediction of physical phenomena related to sodium boiling in multi-channel systems.

References

- [C.01] J. M. Seiler, D. Juhel, P. Dufour. Sodium boiling stabilization in a fast breeder subassembly during an unprotected loss of flow accident. *Nuclear Engineering and Design*, vol. 240: pp. 3329-3335, 2010.
- [C.02] J. Bouré. Review of two-phase instability. In: *ASME-AICHE Heat Transfer Conference*, 1971.
- [C.03] H. M. Kottowski. *Liquid metal thermalhydraulics*. INFORUM Verlag, 1994.
- [C.04] B. Rameau, J. M. Seiler, K. W. Lee. Lower heat flux sodium boiling: Experimental results and analysis; application to natural convection boiling in reactor conditions. *ASME 84-WA/HT-5*, 1984.
- [C.05] G. Sorokin, H. Ninokata, A. Sorokin, H. Endo, E. F. Ivanov. Experimental and numerical study of liquid metal boiling in a system of parallel bundles under natural circulation conditions. *Journal of Nuclear Science and Technology*, vol. 43, No. 6: pp. 623-634, 2006.

Acknowledgements

The present doctoral research has been carried out in the framework of the FAST project, in the Laboratory for Reactor Physics and System Behavior (LRS) at the Paul Scherrer Institute (PSI), and of the Doctoral School in Energy of the Swiss Federal Institute of Technology Lausanne (EPFL). The work, mainly conducted at PSI, was partly supported by the 7th European Framework Program's Collaborative Project for a European Sodium Fast Reactor (CP-ESFR), and the results of the current study constitute an important part of the Swiss contribution. Furthermore, swissnuclear (the nuclear energy section of swisselectric), in the context of promoting young professionals, kindly financed my participation in several international conferences, viz. PHYSOR 2010, ICAPP 2011, and PHYSOR 2012.

This work could not have been realized without the support and contributions of a large number of persons to whom I am particularly grateful:

- Prof. Rakesh Chawla, the director of my thesis, for giving me the opportunity to conduct this doctoral research here in Switzerland, for his helpful guidance and advice throughout the work and for his numerous corrections of all aspects of the present thesis and the various related publications. I really appreciate his great support all these years and wish him all the best for his imminent retirement.
- Dr. Jiří Krepel and Dr. Konstantin Mikityuk, my direct supervisors at PSI, for the patient guidance, enlightening advice and productive discussions. Their abundant knowledge and creative ideas have significantly contributed to this doctoral work. Their kind personalities, remarkable availability and rigorous attitude provided an excellent studious atmosphere. I really learnt a lot during these years. Thank you for the great supervision.
- Dr. Sandro Pelloni of the FAST group, for discussing various technical problems and helping me produce the perturbation theory based results.
- Mr. Martin Zimmermann, the head of LRS at PSI, for his valuable comments on the neutron balance based reactivity decomposition method.
- Dr. Jean-Marc Cavedon, the head of the Nuclear Energy and Safety Research Department (NES) at PSI, for his enlightening suggestions on the innovative fuel assembly design.
- Petr Petkevich, Gaëtan Girardin, Aaron Epiney and Aurélia Chenu – the former FAST PhD students – with whom I shared an office, for the pleasant working atmosphere, for their help with the various official Swiss languages, and for the great leisure time we spent together.
- Ruth Ringele and Philippe Jacquemoud, for their help with all kinds of administrative and computer related problems.

Acknowledgements

- The various Master students who were attached to the FAST group during my PhD study and whom I had the opportunity to help in their research, particularly Levon Ghasabyan, Vladimir Brankov and Dominik Hermann.
- The entire LRS team, with special thanks to my colleagues and friends, Alexander Vasiliev, Omar Zerkak and Konstantin Nikitin for their valuable comments during the preparation of my PhD defense, Davide Bertolotto for his precious advice on career development, Ting Zhu for kindly replacing me from time to time for the supervision of student experiments at EPFL, Tae-Wan Kim, Dominik Rätz, Gregory Perret, William Wieselquist and Oliver Köberl for the nice basketball training we did together, and Jordi Freixa, Victor Petrov and Fabien Devynck for the enjoyable games of ping-pong at the OASE.
- The collaborators in CP-ESFR, in particular Alfredo Vasile and Andrei Rineiski, for the fruitful discussions and valuable comments related to my contributions.

These acknowledgements need to be extended to all the other colleagues and friends that I met at PSI, as well as during business trips. Especially, I would like to thank the members of the PSI Basketball Club and the PSI-Aargau Association of Chinese Students and Scholars. I spent a really good time with you during these four years.

Furthermore, I would like to express my special thanks to my dear friends in China, who have always kept me updated even though I have been so far away. The time we spent together in the past is so memorable that I am sure to join you once again, sooner or later.

My most sincere thanks go to my wife, Xiao Li, as well as to my parents and my parents-in-law, for always being there and giving me unconditional support. Also, thank you, little Xiaohang – my dear two-year-old son – for all the happiness you have brought to our family.

Finally, I would like to thank Prof. Robert Schaller, Prof. Rakesh Chawla, Dr. Jiří Krepel, Dr. Andreas Pautz and Prof. Janne Wallenius for accepting to form the jury for this doctoral thesis.

Curriculum Vitae

Kaichao Sun

Date of birth: 20.12.1984

Place of birth: Beijing, China

Nationality: Chinese

E-mail: sunkaichao@gmail.com

Home Address: DeFengDongXiang 1, 100051, Beijing, China

Education

- Doctoral student,
Energy Doctoral School and **Physics** Section, EPFL (Ecole Polytechnique Fédérale de Lausanne), and
Nuclear Energy and Safety Research Department, PSI (Paul Scherrer Institute),
Switzerland, *Aug. 2008 – present*
- **Master of Science**, Division of **Reactor Physics**,
KTH (Royal Institute of Technology), Stockholm, Sweden, *Aug. 2006 – May 2008*
- **Bachelor of Engineering**, Department of **Engineering Physics**,
Tsinghua University, Beijing, P. R. China, *Sept. 2002 – July 2006*

Research Experience

- **PSI, Switzerland**, *Aug. 2008 – present*, **Doctoral Thesis**
Conducted in the framework of the Collaborative Project for a European Sodium Fast Reactor (CP-ESFR)
Task: Analysis of advanced SFR core designs with improved safety characteristics
Thesis Director: Prof. Rakesh Chawla, EPFL / PSI, Switzerland
- **Westinghouse, Sweden**, *May 2007 – Jan. 2008*, **Master Thesis**
Task: MCNP modeling of VVER fuel bundles and criticality analysis for fuel production safety
Project Manager: Dr. Juan Casal, Westinghouse, Sweden
- **KTH, Sweden**, *Jan. 2007 – May 2007*, Albanova, **Project Work**
Task: Transmutation analysis using MCB
Supervisor: Prof. Janne Wallenius, KTH, Sweden
- **Tsinghua University, China**, *March 2006 – July 2006*, **Bachelor Thesis**
Task: Evaluation of external costs of health effects caused by energy production
Adviser: Prof. Jianping Cheng, Tsinghua University, China

Teaching Experience

- **Laboratory Assistant** for Physics Bachelor students and Nuclear Engineering Master students
Feb. 2009 – present, EPFL, Switzerland
Scope: Reactor experiments and radiation measurements at EPFL's CROCUS reactor

Experience with Codes & Computer Skills

ERANOS, TRACE, PARCS, SERPENT, MCNP, MCB, Matlab, C++, Microsoft Office

Awards & Honors

- **Chinese Government Award** for outstanding self-financed students abroad, 2012.
- **Best 3rd year PhD Paper**, Nuclear Energy and Safety Research Department, PSI, Switzerland, 2011.
- **Scientific Scholarship** of Tongfangweishi, Tsinghua University, P. R. China, 2003.

Membership & Affiliations

- **President**, PSI-Aargau Association of Chinese Students and Scholars, *Jan. 2010 – present*.
- **Member**, STV-Baden Basketball Club, *Nov. 2008 – April 2011*.
- **Deputy President**, Student Union of Tsinghua University, *Sep. 2005 – July 2006*.
- **Member**, Tsinghua University Basketball Team, *March 2005 – July 2006*.

Language Skills

Chinese (native), English (fluent), German (basic), French (basic).

Patent Applications

1. **European Patent No. 11196146.2–2208**. A wrapper tube for a fuel subassembly of a nuclear reactor core and method for protecting fuel against overheating in case of coolant boiling. Filed in 2011.

Journal Publications

1. **K. Sun**, J. Krepel, K. Mikityuk, S. Pelloni, R. Chawla. Void reactivity decomposition for sodium-cooled fast reactor in equilibrium fuel cycle. **Annals of Nuclear Energy**, vol. 38: pp. 1645-1657, 2011.
2. **K. Sun**, J. Krepel, K. Mikityuk, R. Chawla, A neutronics study for improving the safety and performance parameters of a 3600 MWth sodium-cooled fast reactor. **Annals of Nuclear Energy**, under review.
3. **K. Sun**, A. Chenu, J. Krepel, K. Mikityuk, R. Chawla. A coupled 3D-neutronics / thermal-hydraulics optimization study for improving the response of a 3600 MWth SFR core to an unprotected loss-of-flow accident. Submitted to **Nuclear Technology**.

Conference Papers

1. **K. Sun**, A. Chenu, J. Krepel, K. Mikityuk, R. Chawla. Coupled 3D-neutronics / thermal-hydraulics analysis of an unprotected loss-of-flow accident for a 3600 MWth sodium-cooled fast reactor core. Proceedings of **PHYSOR 2012**, Paper 285.
2. **K. Sun**, J. Krepel, K. Mikityuk, R. Chawla. An optimization study for the safety and performance parameters of a 3600 MWth sodium-cooled fast reactor. Proceedings of **ICAPP 2011**, Paper 10304.
3. **K. Sun**, J. Krepel, K. Mikityuk, R. Chawla. Void reactivity decomposition for sodium-cooled fast reactor in equilibrium closed fuel cycle. Proceedings of **PHYSOR 2010**, Paper 157.
4. J. Krepel, **K. Sun**, S. Pelloni, S. Pilarski, K. Mikityuk. Comparison of closed fuel cycles for Generation-IV fast reactors by means of the equilibrium procedure EQL3D. Proceedings of **ICAPP 2010**, Paper 10109.
5. J. Krepel, K. Mikityuk, **K. Sun**, G. Rimpault. Sodium-cooled fast reactor equilibrium cycle analysis with the EQL3D procedure. Proceedings of **ICAPP 2009**, Paper 9226.